

Advanced Direct Drive Shock Ignition Studies

Matthew Ben Khan

Doctor of Philosophy

University of York

Physics

May 2022

Abstract

The shock ignition approach to inertial confinement fusion offers a potential route to ignition and high gain. It proposes a low velocity fuel assembly on a low adiabat, and ignition through the launching of a late timed strong shock. Accurate descriptions of the coupling of laser energy into the capsule are required to model implosions, including driving the highly compressible fuel and the interaction of the shock launching spike with the coronal ablation plasma. Two well diagnosed experiments were performed on the Omega-60 laser facility that isolated key physics issues for the two steps of shock ignition.

The first used a novel conical target to access for the first time the laser-plasma conditions relevant for full-scale shock ignition, in order to characterise the laser-plasma interactions and subsequent supra-thermal hot electrons. The dominant instability was identified as convective stimulated Raman scattering, producing hot electrons of ~ 40 keV with a laser energy conversion efficiency of 1-3%. This is unique and an essential measurement, as inclusion of hot electron generation and propagation in shock ignition simulations is crucial for constructing implosion designs that might be capable of reaching ignition.

The second experiment investigated the implosion dynamics of warm deuterium filled capsules using shaped laser pulses that maintained a reduced shell adiabat and associated high fuel compressibility. A laser drive multiplier was tuned with trajectory measurements from a gated self-emission imager, a significant advancement in the ability to more accurately simulate reduced adiabat designs that are relevant for both shock ignition fuel and conventional central hot spot implosions. Despite significant low mode asymmetries that were identified during the in-flight fuel compression and within the late formed hot spot, the shell trajectory, hot spot morphology and peak neutron emission were well reproduced from one-dimensional simulations. More experiments coupled with predictive modelling are a necessity to determine whether inertial confinement fusion can be a future energy source.

Contents

Abstract	ii
List of Tables	viii
List of Figures	ix
Acknowledgements	xv
Declaration	xvii
Role Of The Author	xviii
1 Introduction	1
1.1 Laser Direct Drive	2
1.2 Thesis Structure	3
1.3 Fusion Reactions	3
1.3.1 Release of Energy	3
1.3.2 Fuel Reactivity	5
1.4 Implosion Metrics	7
1.4.1 Confinement Time	7
1.4.2 Fusion Triple Product	8
1.4.3 Burn-up Fraction	10
1.5 Energy Requirements	11
1.5.1 Shell Implosion Velocity	12
1.6 Hot Spot Ignition	13
1.6.1 Central Hot Spot Approaches	15
1.6.2 Direct Drive Implosion Design	17

1.7	Hydrodynamics	20
1.7.1	Shock Wave Physics	20
1.7.2	Hydrodynamic Efficiency	23
1.8	Inertial Fusion Energy Reactor Requirements	24
1.9	Sources of Degradation	25
1.9.1	Rayleigh-Taylor Instability	26
1.10	Summary	28
2	Shock Ignition	30
2.1	Motivation For Lowering Implosion Velocity	31
2.2	Shock Ignition Principles	33
2.3	Ignitor Shock Launching	37
2.3.1	Hot Electron Influence	39
2.3.2	Implosion Simulations Incorporating Hot Electrons	40
2.4	Propagation of Waves in Plasmas	41
2.4.1	Fundamental Plasma Parameters	41
2.4.2	Electromagnetic Waves	43
2.4.3	Electron Plasma Waves	43
2.4.4	Ion Acoustic Waves	44
2.4.5	Wave Damping	45
2.4.6	Wave Breaking	46
2.5	Parametric Instabilities	46
2.5.1	Stimulated Raman Scattering	48
2.5.2	Two Plasmon Decay	49
2.5.3	Cross-Beam Energy Transfer	51
2.6	Simulating Laser-Plasma Instabilities	51
2.7	Hot Electron Characterisation Experiments	52
2.8	Summary	54
3	Instrumentation and Methods	56
3.1	The Omega Laser Facility	56
3.1.1	Laser Overview	56
3.1.2	Target Alignment and Power Balance	57

3.1.3	Chamber Diagnostics	59
3.2	Beam Smoothing	59
3.2.1	Phase Plates	59
3.2.2	Smoothing by Spectral Dispersion	60
3.3	Sensors	61
3.3.1	Image Plate	61
3.3.2	Scintillators	64
3.3.3	Charge Injection Devices	66
3.3.4	Microchannel Plates	68
3.4	X-ray Diffraction Diagnostics	69
3.4.1	Bragg's Law	71
3.4.2	Zinc von Hamos	72
3.4.3	Spherical Crystal Imager	75
3.5	Hard X-ray Spectrometers	76
3.5.1	Hard X-ray Image Plate	76
3.5.2	Hard X-Ray Detector	78
3.5.3	Filter-Detector Analysis Method	81
3.5.4	Comparison of Diagnostics	84
3.6	Soft X-ray Imagers	85
3.6.1	X-Ray Pinhole Camera	85
3.6.2	Self-Emission Shadography	86
3.6.3	Time Resolved X-ray Imager	88
3.6.4	Kirkpatrick–Baez Framed Microscope	90
3.7	Full Aperture Backscatter Diagnostic	91
3.8	Simulation Codes	91
3.8.1	Radiation-Hydrodynamics Codes	91
3.8.2	Spect3d Post-Processor	92
3.8.3	Geant4 Monte-Carlo Code	92
3.9	Summary	93
4	Laser-Plasma Interactions in Shock Ignition Relevant Conditions	94
4.1	Introduction	94
4.2	Experiment Overview	95

4.3	Experimental Set-Up	96
4.3.1	Target Designs	97
4.3.2	Ablation Plasma Conditions	99
4.3.3	Reference Shot Subtraction	101
4.3.4	Shot Summary	102
4.4	Laser-Plasma Instability Identification	103
4.5	Hot Electron Characterisation	107
4.5.1	Monte-Carlo Simulations of Electron-Target Interactions	108
4.5.2	Hot Electron Bremsstrahlung Detection	109
4.5.3	Time Resolved Hard X-ray Signal	113
4.5.4	Hot Electron Induced Cu K_{α} Emission	115
4.6	Two Temperature Fit	120
4.7	Further Discussions	123
4.7.1	Choice of Electron Energy Distribution Function	124
4.7.2	Thick-Target Model Validity	126
4.7.3	Improvements for Future Experiments	127
4.8	Hot Electron Integrated Radiation-Hydrodynamic Simulations	128
4.9	Conclusion	129
5	Drive Coupling and Low Mode Asymmetries in Reduced Adiabatic Implosions	130
5.1	Introduction	131
5.2	Experimental Set-Up	133
5.3	Implosion Trajectory	136
5.3.1	Radius and Velocity Determination	139
5.3.2	Low Mode Implosion Asymmetries	143
5.4	Hot Spot Offset	145
5.5	Hot Spot Imaging	149
5.5.1	Time Resolved X-ray Imager	150
5.5.2	KB-Framed	154
5.5.3	Gated Monochromatic X-ray Imager	157
5.6	Target Performance	159
5.6.1	Influence of the Stalk Mount on Implosions	160

<i>CONTENTS</i>	vii
5.6.2 Hot Electron Adiat Increase	162
5.7 Discussion	165
5.8 Improved Drive Multiplier	166
5.8.1 Cryogenic-DT Implosions	168
5.9 Conclusion	170
6 Conclusions	172
A <i>n</i>-dimensional Maxwell-Boltzmann Distribution Functions	177
B Sydor Framing Camera Noise Removal Techniques	178
List of References	182

List of Tables

3.1	Table of the composition of layers in the MS-type IP	62
3.2	Table of the filter composition and thickness for the 9-channel HXIP diagnostic	78
3.3	Table of the Hard X-Ray Detector filter combinations and scintillator materials	79
4.1	Table of the shot parameters and target types	103
5.1	Table of the key design features of the laser pulse and targets	136
5.2	Capsule self-emission images captured by the Sydor Framing Camera diagnostic at 16 different times during an implosion	138
5.3	Table of the key parameters from the Time Resolved X-ray Imager diagnostic .	153
5.4	Table of the key metrics for the design and measurements from warm, low- to mid-adiabat implosions	160
5.5	Table of the key implosion metrics from an experimental cryogenic-DT implo- sion and two post-shot simulations that use the previous and optimised drive multipliers	169

List of Figures

1.1	Graph of the binding energy per nucleon as a function of nucleon number	5
1.2	Reactivity of fusions reactions as a function of ion temperature	6
1.3	The conditions required for a self-heating plasma for an isobaric configuration of fuel.	16
1.4	Schematic of the direct drive and indirect drive approaches to laser inertial fusion	16
1.5	Target design and pulse shape for a direct drive implosion with 2.4 MJ of laser energy	18
1.6	Mass density plot of the output from a radiation-hydrodynamics simulation of an igniting direct drive implosion	19
1.7	Ion temperature and mass density against radius of the hot spot and assem- bled fuel from a radiation-hydrodynamics simulation of an implosion at peak compression	19
1.8	The development of a pressure wave into a shock	21
1.9	Density and pressure jump across a shock front	22
1.10	Drive efficiency of the rocket effect from ablation of the outer surface of the shell as a function of the payload fraction.	23
1.11	Representation of the Rayleigh-Taylor hydrodynamic instability for three no- table cases	28
2.1	The laser pulse shape and capsule design for a shock ignition implosion.	34
2.2	Radiation-hydrodynamics simulation of a shock ignition design	35
2.3	Comparison of the temperature and density profiles for the hot spot and com- pressed fuel from shock ignition and central hot spot approaches	36

2.4	Capsule gain for the HiPER baseline shock ignition design as a function of shock launch time demonstrating the ignition window for the spike	38
2.5	Dispersion relations for electromagnetic waves, electron plasma waves, and ion acoustic waves in plasmas	44
2.6	Laser-plasma parametric instabilities	47
2.7	Decay of an incident pump electromagnetic wave into two further waves by the stimulated Raman scattering and two plasmon decay instabilities	50
3.1	Power balance of a shaped Omega pulse	58
3.2	Far field spatial intensity profile from a 380 SG5 phase plate	60
3.3	Schematic of the layers in the MS-type IP	62
3.4	Models for the sensitivity of MS-type Image Plate	64
3.5	Scintillation Emission Spectrum of BaF ₂	66
3.6	Models for the spectral response of CID sensor	67
3.7	Schematic of a Micro-Channel Plate	69
3.8	Spectral response of a Micro-Channel Plate as a function of incident photon energy	70
3.9	Diagram showing the ejection of an inner shell electron and the production of characteristic line emission	70
3.10	A geometric interpretation of Bragg's law of refraction	71
3.11	Schematic of the Zinc von Hamos Diagnostic	73
3.12	Dispersive Crystal in von Hamos Geometry	74
3.13	Alignment of the Spherical Crystal Imager diagnostic and opposing detector	76
3.14	Signal level of an exposed image plate from the Hard X-ray Image Plate diagnostic	77
3.15	Response Functions of Hard X-ray Image Plate channels as a function of incident photon energy	79
3.16	Response Functions of Hard X-Ray Detector channels as a function of incident photon energy	80
3.17	The unfolding process of traces from the Hard X-Ray Detector	81
3.18	The basic geometry of a pinhole camera set up	85
3.19	Time Integrated Emission from the X-Ray Pinhole Camera diagnostic	87
3.20	Schematic of the Sydor Framing Camera diagnostic	88
3.21	Pulse dilation tube concept for Time Resolved X-ray Imager diagnostic	89

3.22	Sensitivity of the KB-Framed diagnostic as a function of photon energy	90
4.1	Schematic of the conical target experiment on Omega	97
4.2	Schematic of four types of target layer compositions	98
4.3	Ablation plasma conditions from radiation-hydrodynamics simulations of laser-target interaction	100
4.4	Plots of the bremsstrahlung hard x-ray signal from the hot electrons from target interactions	102
4.5	Image of the spectrally resolved and temporally streaked backscattered light from laser-plasma instabilities	104
4.6	A comparison of the laser-plasma instability backscattered signals, the hot electron hard x-ray bremsstrahlung emission, and the laser power profiles	106
4.7	Monte-Carlo simulation of hot electron interacting with a conical target	109
4.8	A comparison of the signals recorded by the image plate in the hard x-ray image plate diagnostic and the effect of a proton backlighter	110
4.9	A parameter scan and residual sum minimisation for the fitting of the hot electron temperature and total energy to data from the Hard X-ray Image Plate diagnostic	112
4.10	Hot electron temperature predicted by Hard X-ray Image Plate diagnostic against high beam intensity at the quarter critical density	113
4.11	The time resolved bremsstrahlung hard x-ray signals detected by Hard X-Ray Detector diagnostic	114
4.12	Hot electron temperature predicted by Hard X-Ray Detector diagnostic against high beam intensity at the quarter critical density	115
4.13	Image plate scan, and spectral and spatial profiles from the Zinc von Hamos K_{α} spectrometer	116
4.14	The Zinc von Hamos diagnostic detected spectrum and analysis procedure	118
4.15	Conversion efficiency for laser energy into hot electrons against the laser intensity at quarter critical	119
4.16	Images from the Spherical Crystal Imager diagnostic showing 2D emission of hot electron induced Cu K_{α} from the read side of the target	120
4.17	Two temperature fitting to Hard X-ray Image Plate diagnostic data	122

4.18	Hot electron energy distribution functions for three dimensionalities of Maxwell-Boltzmann's	125
4.19	Simulations of a shock ignition implosion with and without hot electrons, showing the density at peak compression and the pressure generated during the spike	128
5.1	Simulated neutron yield against experimental neutron yield for an ensemble of cryogenic-DT direct drive implosions on Omega as simulated by two radiation-hydrodynamics codes, Lilac and HYADES	132
5.2	Capsule target designs for warm implosions	133
5.3	A schematic and photographs of a capsule mounted on a stalk with a glue joint prior to being shot	134
5.4	Laser pulse template for variable adiabat implosions	135
5.5	Comparison of the data, idealised fit, and post-processed simulation of data from the Sydor Framing Camera diagnostic	141
5.6	The inner radius of implosion as found by the Sydor Framing Camera diagnostic and post-processed radiation-hydrodynamics simulations against time, plotted with the laser power	142
5.7	Inner edge shell radius against time with 3rd order polynomial fits from experimental data and simulations, and their inferred implosion velocities	142
5.8	The percentage deviation of the inner shell radius from the mean radius as a function of angle for Sydor Framing Camera data, and the mode amplitudes from a Fourier transform and fitted Legendre polynomials	144
5.9	The mode-2 amplitude growth and phase angle consistency against capsule radius	145
5.10	The time integrated self emission image of an implosion recorded by the X-Ray Pinhole Camera and the detectors view of the target	146
5.11	Hot spot image and double super-Gaussian fit from X-Ray Pinhole Camera	148
5.12	Fitting and decomposition of elliptical hot spots	150
5.13	A representation of the views of the target and stalk as seen by the Time Resolved X-ray Imager and Kirkpatrick-Baez Framed diagnostics	151
5.14	Hot spot analysis of images from the Time Resolved X-ray Imager diagnostic showing the hot spot emission data and stalk angle, an elliptical 2D super-Gaussian fit, and the difference between the two	151

5.15	The radius of the 1/e contour of a Time Resolved X-ray Imager diagnostic hot spot image and fitted elliptical super-Gaussian as a function of angle from the semi-major axis	153
5.16	A hot spot image from the KB-Framed diagnostic showing a 17% contour, an elliptical super-Gaussian fit and similar 17% contour level, and the difference between the data and fit	154
5.17	The 17% contour radius against angle from a KB-Framed hot spot, with the same radius contour from the semi-major axis of the elliptical super-Gaussian fit, and the fitted Legendre polynomial amplitude	155
5.18	A potential arrangement of two hot spot imagers with a hot spot that would produce the experimentally observed hot spots	156
5.19	KB-Framed hot spot images and their radii against time, plotted with the simulated and post-processed hot spot radii	157
5.20	The mounted target and time integrated image of the hot spot, as seen by the Gated Monochromatic X-ray Imager diagnostic	158
5.21	Representation of the asymmetric drive a misaligned capsule will receive	161
5.22	Comparison of the backscatter signal, laser power profile, two plasmon decay threshold parameter, and hot electron bremsstrahlung signal	163
5.23	Hot electron temperatures and energies from the Hard X-Ray Detector diagnostic	164
5.24	The previous and optimised time dependent Cross-Beam Energy Transfer multipliers	167
5.25	Inner edge shell radius against time with 3rd order polynomial fits from experimental data and simulations, both new and old, and their inferred implosion velocities	168
5.26	description.	170
B.1	Sydor framing camera data showing the effect of high frequency noise	179
B.2	Sydor Framing Camera data that has been cleaned by a custom noise removal routine	180
B.3	Sydor Framing Camera data that has been cleaned by a median pixel filter . .	180
B.4	Sydor Framing Camera data that has been cleaned by a Gaussian blur filter . .	181
B.5	Sydor Framing Camera data that has been cleaned by removing high frequency Fourier modes	181

B.6 The inner edge radius and inferred implosion velocity from raw cleaned Sydor
Framing Camera Data 182

Acknowledgments

First in my acknowledgements is my supervisor, Nigel Woolsey. I am a better scientist and more well rounded person from working with him. I owe him great thanks for pushing me to do the things that I felt I couldn't, and for knowing when I needed support for the things that I actually couldn't do. I hope that we can continue working together and that I receive your guidance for a little while longer.

Despite his constant attempts to the opposite, I did in fact manage to complete my thesis with Luca working next to me all this time. I have benefited so much from our rich conversations, both academic and otherwise, and always appreciated having a reminder of what is achievable when someone applies themselves. Inertial confinement fusion is forever worse off without you pushing it along.

Attentive readers will notice how much of the work presented in this thesis was planned, designed, performed, or generally aided by Robbie Scott, and they will have a good understanding of the thanks that he deserves from me. I owe much of my enthusiasm for inertial confinement fusion to him.

Many people have provided interesting conversations, helped me in my understanding, given me feedback on my work, or accompanied me on coffee breaks, all of which have been highly important. Those in YPI include Phil, Arun, Koki, and Emma, with special thanks to James who had to deal with more than he signed up for from me. Outside the YPI, thanks go to Kevin, Duncan, Reem, Nicola, SJ, and Alessandro.

Of course, the administrative staff here at York are the unsung heroes of all the work that is done. Thanks need to be given to Ruth, Katherine, Jenny, and Donna for all their help over the past six years.

Much of this work wouldn't have been possible without the patient and detailed assistance from various people at Rochester, in particular Wolfgang, Christian, and Manuel.

My friends Jav, Nick, Luke, and Will, given here in alphabetical order, have put up with me talking about laser on far too many occasions, and in situations where I should not have been talking about lasers in the first place. They have my lasting thanks for putting up with it for a fair bit longer.

To my Dad, I hope this lives up to your idea of me actually doing something, you'll never

know how much that comment meant to me. I am the person I am because of my Mum, and I could never find the words to fully express my gratitude, but I'll keep trying until I do. My sister might not know how much I have depended upon her guidance and inspiration over the years, but I will continue to depend upon it some more, and I hope to some day give back what you have given to me.

More than just thanks needs to be given to my fiancé Hannah, I'm so proud of what we have already achieved together, and I wouldn't have been able to do the things I have done without you. All the effort that we have poured into my PhD will hopefully be worth it, and that we can look back on this time with the fondness it deserves. I owe you my love and my gratitude.

Declaration

I declare that this thesis is a presentation of original work and I am the sole author. This work has not previously been presented for an award at this, or any other, University. All sources are acknowledged as References. All figures presented here are original and that I have produced, unless otherwise stated. This work was supported by the Engineering and Physical Sciences Research Council, grant numbers EP/L01663X/1 and EP/P026796/1.

Role Of The Author

This thesis presents work that was performed by a wide collaboration across multiple institutions. As such, much of the work was performed collectively, this section aims to highlight the work that was specifically performed by the author solely. Two experiments are reported on in Chapters 4 and 5 that had Robbie Scott and Nigel Woolsey as the principal investigators. The author played a significant role in the design, execution, and analysis of these experiments. Luca Antonelli and Kevin Glize played similarly large roles.

Chapters 1 and 2 presents simulated implosions that were designed by Robbie Scott. These were run by the author, who then performed the subsequent analysis.

Chapter 3 includes models for image plates, used extensively throughout this thesis, that were generated by the author. The response of the Zinc von Hamos (ZVH) diagnostic was originally presented by Leonard Jarrott and built upon by the author. The filter-detector analysis method was produced by the author.

The laser and target optimisations for the experiment presented in Chapter 4 were performed by Robbie Scott, as well as the h2d radiation-hydrodynamics simulations of the ablation plasma conditions. Christian Stoeckl supplied the raw and unfolded traces for the Hard X-Ray Detector (HXR) for both experiments present here. Kevin Glize processed the Full Aperture Backscatter (FABS) diagnostic data for both experiments, and calculated the predicted plasma temperature from the Two-Plasmon Decay (TPD) signature. The hot electron integrated radiation-hydrodynamics simulations presented at the end of the Chapter were performed by Duncan Barlow using the code Odin. The author produced all remaining material, including the subtraction of the reference shot, and analysis of the ZVH, Hard X-ray Image Plate (HXIP), and HXR data. This analysis involved Monte-Carlo simulations for all three diagnostics, and residual sum minimisation for the final two. The further analysis of the HXIP data for two temperature fitting and investigation of fitting hot electron distributions was also performed by the author.

In Chapter 5 the author performed all the data analysis from all the diagnostics that are reported; Sydor Framing Camera (SFC), X-Ray Pinhole Camera (XRPHC), TRXI, Kirkpatrick-Baez Framed microscope (KBF), Gated Monochromatic X-ray Imager (GMXI), and HXR. Prior to the experiment, the laser and target designs were again produced

by Robbie Scott, with input from the experimental team. These included the radiation-hydrodynamics simulations with HYADES, and fuel adiabat predictions. Wolfgang Theobald and Kristen Churnetski provided the hot spot images from the TRXI diagnostic, and Fred Marshall provided the KBF diagnostic hot spot images. Christian Stoeckl provided the neutronics data. Robbie Scott designed and improved the laser drive multiplier that is discussed in this Chapter, using measurements produced by the author.

Chapter 1

Introduction

A defining characteristic for the next century of human existence will be the balance between needing to provide an adequate standard of living to an increasing global population and the existential threat that climate change poses to humanity and the planet.

Almost all essential aspects of a high standard of living will require an affordable and plentiful source of electricity to fuel the development of necessary services and their expansion across populations. The current dominant methods of producing this electricity are having disastrous effects on the climate by emitting greenhouse gases on a scale not seen before in human history [1].

Fossil fuels such as coal and gas provided a means of progressing human industry and technology to the level that it is today, but alternatives are needed that do not have the same detrimental effect. Around the world, renewable electricity sources are being deployed such as solar and wind that aim to replace the contemporary fossil fuel burning methods. These often must be paired with some form of energy storage in order to match supply with the variable electricity demand throughout the day [2], where conventional storage methods have already been nearly saturated [3]. Nuclear fission is capable of producing the constant baseload power that can replace fossil fuel power plants but has its own history with environmental catastrophes [4,5]. Current reactor designs also produce long-lived radioactive waste that must be stored for millennia [6]. All of these methods for producing electricity without significant emission of greenhouse gasses must be pursued if climate change is to be limited, as no silver bullet exists that can solve this problem alone.

Nuclear fusion might provide a much-needed addition to these methods that can deliver the benefits of other renewables without succumbing to their shortfalls. It offers the possibil-

ity of reduced carbon emissions when compared with fossil fuels, but its energy supply would not suffer from the same intermittent output of solar and wind. Less long-lived radioactive waste would be produced than from fission, as well as having lower nuclear proliferation concerns, minimal damage from loss of confinement, and a more abundant fuel source.

Nuclear fusion occurs naturally in stars like the Sun that either directly or indirectly provides nearly all the energy used to produce electricity. The fusion reactions are initiated and contained by the immense gravitational forces present inside stars. Reaching and containing a burning fusion plasma are the key goals of nuclear fusion research. Recent breakthroughs in fusion experiments [7, 8] have brought new attention to the field and provided more confidence in the pursuit of nuclear fusion as a viable form of electricity production.

1.1 Laser Direct Drive

The laser direct drive is an approach to inertial confinement fusion which uses direct illumination of a spherical capsule containing fusion fuel to create an implosion that reaches the conditions where the fuel ignites and a burst of energy is released [9]. The capsule is a cryogenic hollow sphere that has a thin shell of solid fuel, with a gas-filled centre. Laser energy is deposited on a nanosecond timescale in the outer surface of the capsule, ionising the material and creating a plasma. The expansion of this ablation plasma outwards creates a reaction force on the remaining fuel, driving it inwards and compressing it. The fuel is accelerated to high velocities by the ablation of the shell material and acts like a piston on the gas core, raising its pressure. The rising pressure of the core pushes back on the shell, converting the shell's kinetic energy into internal energy of the core, raising its temperature. This central region of high pressure and rising temperature plasma forms a hot spot that is surrounded by a thick layer of highly compressed fuel. The hot spot is heated to the point that fusion reactions occur and reaches high enough areal densities to trap the fusion produced alpha particles within the plasma. The deposition of the alpha particle's kinetic energy further heats the hot spot and increases the fusion reaction rate. The alpha particles from this increased reaction rate will deposit their energy into the surrounding fuel, heating that to fusion temperatures. A thermal instability of fusion reactions occurs and a burn wave propagates out through the fuel. Energy gain can occur from the output of fusion reactions, the material quickly disassembles and the implosion is over. In-depth reviews of the inertial

fusion concept can be found in References [9–12].

1.2 Thesis Structure

This thesis is an investigation of the shock ignition variant [13] of direct drive inertial confinement fusion [9, 12, 14] (ICF). The two key stages of shock ignition, those of assembly and ignition of the fuel, are investigated with experiments on the Omega-60 laser facility [15]. The experiments looked into generation of hot electrons through laser-plasma instabilities and improving an empirical drive coupling model in reduced adiabat implosions that were compromised by the presence of low-mode asymmetries.

Chapter 1 gives an overview of laser direct drive inertial confinement fusion and the challenges that must be overcome. The alternate scheme of shock ignition and the laser-plasma interactions that produce high energy hot electrons are presented in Chapter 2. The instruments and analysis methods used for the experiments are described in Chapter 3. In Chapter 4 the results from a planar target experiment are presented that investigated laser-plasma interactions in a shock ignition relevant regime. Chapter 5 describes the study of reduced adiabat implosions to tune a drive coupling multiplier and the unintentional asymmetries that occurred. The main results and conclusions of this work are summarised in Chapter 6.

1.3 Fusion Reactions

1.3.1 Release of Energy

Energy is released from nuclear reactions due to the change in mass between the reactants and the products. Nuclear fusion occurs when two lighter nuclei are able to overcome the electrostatic repulsive forces between them to enable the strong nuclear force to reconfigure the nuclear binding arrangements between the nucleons and produce heavier elements. The reaction is exothermic when the total mass of the products is less than the mass of the reactants, with the loss in mass equating to the energy released, Q , with the following equation,

$$Q = \sum_i m_i c^2 - \sum_f m_f c^2 \quad (1.1)$$

where m_i and m_f are the masses of the reactants and the products respectively, and c is the speed of light. The energy that is released is imparted to the products of the fusion reaction in the form of their kinetic energy. It is this kinetic energy of the products that further heats the fuel, increasing the nuclear reaction rate and supports a fusion burn wave, and that can be extracted in order to produce electricity and breed more fusion fuel [16].

For a nucleus of nucleon number A and nuclear charge Z , the mass of the nucleus is given by the following equation,

$$m = Zm_p + (A - Z)m_n - \frac{B}{c^2} \quad (1.2)$$

where m_p is the mass of a proton, m_n is the mass of a neutron, and B is the binding energy of the nucleus. Large values of the binding energy imply a more stable nucleus. The binding energy per nucleon for the elements is given in Figure 1.1 as a function of the nucleon number. The vertical dashed line is given for ^{56}Fe which has one of the highest binding energy per nucleon and thus is among the most stable nuclei. Heavier elements to the right of this can undergo exothermic fission reactions to reduce in atomic number, while lighter elements to the left can exothermically fuse together up to this point. The nucleus of ^4He is of particular note because of its high binding energy. Fusion reactions that result in the production of this nucleus will typically have larger amounts of released energy.

The fusion reaction that is most commonly used in pursuit of energy production is that between two isotopes of hydrogen; deuterium (D) and tritium (T), having two and three nucleons respectively. It is given by the following reaction,



where an α particle is commonly used in place of a ^4He nucleus, and n is a neutron. The energy released for this reaction is $Q = 17.6$ MeV that is split between the α particle and the neutron according to the inverse of their masses, receiving 3.52 MeV and 14.06 MeV respectively [10]. Therefore, the total fusion energy released from the reaction of 0.2 mg equimolar DT that was used in the highest yield implosions to date would release 67.8 MJ, equivalent to the energy released from the explosion of ~ 16 kg of TNT. This highlights the need for a controlled release of fusion energy as a reactor vessel must be able to withstand the outburst.

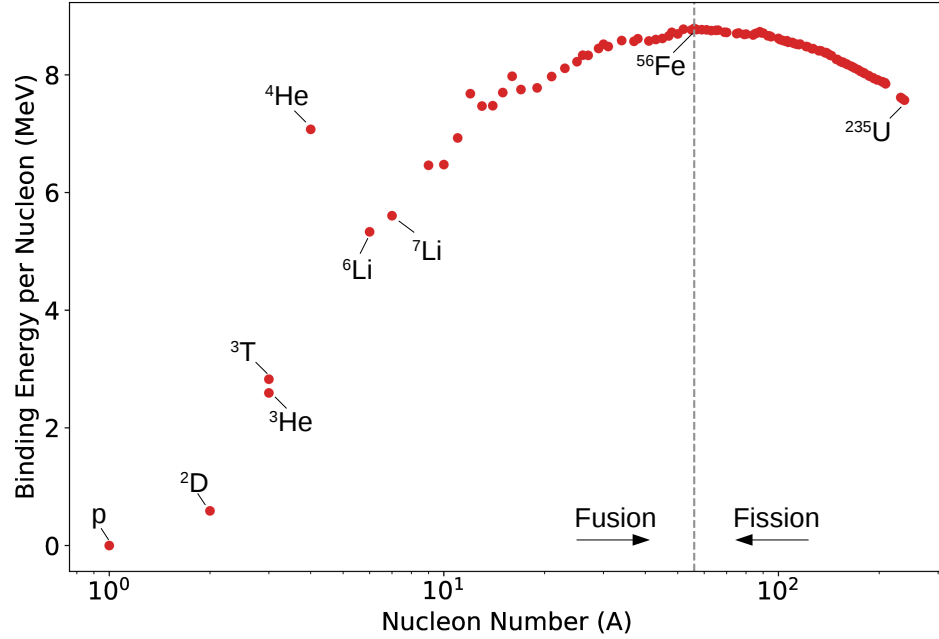


Figure 1.1: The binding energy per nucleon as a function of nucleon number [17]. The vertical dashed line represents the largest binding energy per nucleon which aligns with ^{56}Fe . Elements to the right can exothermically undergo fission, while those on the left can undergo fusion.

1.3.2 Fuel Reactivity

The choice of fusion fuel is largely dictated by the cross-section for reactions at plasma conditions that can be achieved on earth. In order for two nuclei to fuse, they must be brought close enough together and overcome the long distance repulsive Coulomb forces in order to reach the attractive strong nuclear force that acts over the shorter $\sim\text{fm}$ distance. Classical physics would dictate that only particles with energy greater than the Coulomb barrier would be able to overcome the repulsion, requiring particles to have $\sim\text{MeV}$ energies. This limitation however, is reduced by quantum tunnelling which allows particles to fuse at lower energies of $\sim\text{keV}$.

The overall cross-section for fusion includes contributions from the geometric cross-section of two particles colliding [10], the tunnelling or Gamow cross-section [18], and the cross-section for the nuclear processes [19]. The reactivity of a fusion plasma is the product of the fusion cross-section with the relative ion velocity averaged over the plasma ion velocity distribution function. Typically this ion velocity distribution function can be described by

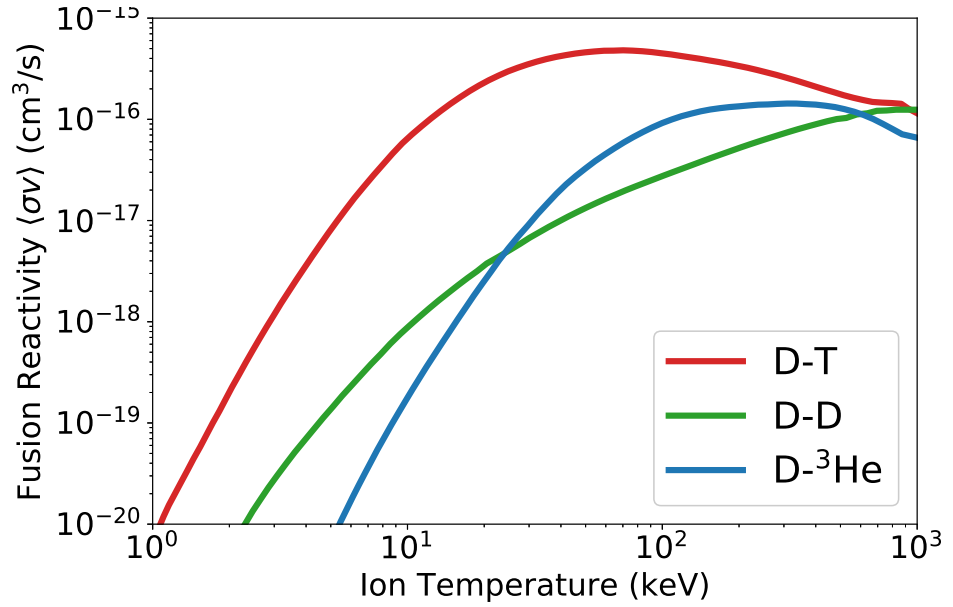


Figure 1.2: Reactivity of fusions reactions [20], averaged over a Maxwell-Boltzmann ion velocity distribution, for deuterium-tritium, deuterium-deuterium, and deuterium-helium-3. Reactivities peak for high plasma temperatures (keV-MeV), with the D-T reaction peaking at the lowest temperature of ~ 70 keV.

a Maxwell-Boltzmann distribution,

$$f(E, T) = 2\sqrt{\frac{E}{\pi k_B^3 T^3}} \exp(-E/k_B T) \quad (1.4)$$

where E is the ion energy and T is the ion temperature and k_B is the Boltzmann constant. It is typical that when quoting temperatures that they are given in units of eV or keV, and this will be done throughout this thesis when referring in particular to hot electron distributions and plasma temperatures. Equations though will include the Boltzmann constant for accuracy. Figure 1.2 shows the reactivity of three significant fusion reactions against ion temperature.

A large reactivity is needed to attain the number of fusion reactions necessary for energy production, achieved by heating a plasma to temperatures where the kinetic energy of the ions is sufficiently high, at which point it is said that thermonuclear fusion occurs. Temperatures of \sim keV are reachable in laboratories, with the D-T reaction having the highest reactivity in this range and hence why it is typically chosen. The reaction rate of a DT plasma with a

time dependent volume V is given by the following equation,

$$\begin{aligned}\frac{dN}{dt} &= n_D n_T \langle \sigma v \rangle V(t) \\ &= \frac{n^2}{4} \langle \sigma v \rangle V(t)\end{aligned}\tag{1.5}$$

where N is the number of fusion reactions, $\langle \sigma v \rangle$ is the reactivity, and $n_D = n_T = n/2$ are the deuterium, tritium and combined ion number densities respectively, where it is assumed that it is a constant equimolar mixture of D and T.

1.4 Implosion Metrics

1.4.1 Confinement Time

Containment of the fusion fuel in an ICF implosion is achieved during the brief period where inertia of the inflowing material confines the plasma long enough for a sufficient amount of fusion reactions to occur. Once the inflow of material has stopped, stagnation occurs and the high pressure built up in the centre will force the fuel back outwards where the plasma undergoes rapid expansion, cooling, and disassembly.

The central region of the implosion where fusion occurs can be considered to be a sphere of hot DT plasma. The imploding shell around the core will lose all of its inwards momentum as it is slowed by the back pressure. At the point where the shell's velocity is zero, the shell is said to have stagnated, the inflow of material has stopped, and the loss of confinement begins. A release wave will travel from the outer surface of this sphere inwards. The plasma will decompress as this wave propagates towards the centre, reducing the fusion reaction rate and lowering its temperature below that required for sustained reactions. The wave will continue to travel inwards at the local sound speed c_s until it reaches the centre and all the plasma has decompressed. The location of the wave with respect to time t is given by the following equation,

$$R(t) = R_0 - c_s t\tag{1.6}$$

where R_0 is the initial radius of the hot spot. Equation 1.5 can be used to find the fusion reaction rate inside this plasma sphere of volume $V(t) = \frac{4\pi}{3} R(t)^3$. Integrating from $t = 0$ when the disassembly begins to $t = R_0/c_s$ when the release wave reaches the centre yields

the total number of fusion reactions N_{fus} ,

$$\begin{aligned} N_{\text{fus}} &= \frac{n^2}{2} \langle \sigma v \rangle \int_0^{R_0/c_s} R(t)^3 .dt \\ &= \frac{n^2}{2} \langle \sigma v \rangle V_0 \frac{R_0}{4c_s} \end{aligned} \quad (1.7)$$

where V_0 is the initial volume of the hot spot plasma. The number of fusion reactions that would occur for a fixed volume of plasma with the same initial volume for a confinement time t_c is given by

$$N_{\text{fus}} = \frac{n^2}{2} \langle \sigma v \rangle V_0 t_c \quad (1.8)$$

Comparing equations 1.7 and 1.8 provides an approximation for the confinement time of an ICF implosion,

$$t_c = \frac{R_0}{4c_s} \quad (1.9)$$

The factor of 4 decrease in the confinement time is due to the spherical geometry of the hot spot. The large starting volume will produce a corresponding large rate of decrease in the volume of plasma where fusion can occur.

A typical ICF hot spot will have a radius of $\sim 100 \mu\text{m}$, a temperature of $\sim 10 \text{ keV}$ and a sound speed of $c_s \approx 1000 \text{ km/s} = 1 \mu\text{m/ns}$. This gives the confinement time of approximately 25 ps, occur at the final stage of the implosion and on a timescale far shorter than the $\sim \text{ns}$ laser driver that creates these conditions.

1.4.2 Fusion Triple Product

The minimum condition for a fusion relevant plasma to begin a self-sustaining burn is for the energy deposited back into the plasma from the fusion reactions to be greater than the energy required to heat it to that point. This can be expressed with the following inequality,

$$\frac{dE_{\text{fus}}}{dt} > \frac{E_{\text{Plasma}}}{t_c} \quad (1.10)$$

where E_{fus} is the fusion energy deposited in the plasma, E_{Plasma} is the internal energy of the plasma and t_c is the confinement time. The majority of fusion energy is imparted to the neutron and will escape the plasma. The high charge of the α particle will result in a much shorter mean free path and so all of its energy (E_α) will be captured by the plasma, raising

the plasma's temperature. The fusion energy deposition rate is thus given by the following equation,

$$\frac{dE_{\text{fus}}}{dt} = \frac{n^2}{4} \langle \sigma v \rangle E_\alpha V \quad (1.11)$$

The energy required to heat a plasma consisting of two species, electrons and ions, is given by the following equation [10],

$$E_{\text{Plasma}} = 3nk_BTV \quad (1.12)$$

Substituting equations 1.11 and 1.12 into 1.10 results in the fusion triple product [11, 21],

$$nTt_c > \frac{12 k_B T^2}{E_\alpha \langle \sigma v \rangle} \quad (1.13)$$

Noting that $\langle \sigma v \rangle$ has a T dependence, the right-hand side of this inequality has a minimum at ~ 15 keV [22]. Inserting this temperature provides an approximate value for the triple product that all energy producing DT fusion systems must aim for,

$$nTt_c \gtrsim 3.0 \times 10^{15} [\text{keV s cm}^{-3}] \quad (1.14)$$

This equation can be re-expressed using different parameters that are more relevant to an ICF implosion. The term areal density is the mass per unit area of a material and signifies the total amount of material that a particle must travel through to escape the target. For a particle created at the centre of the hot spot, the areal density of the fuel that it must travel through is given by $\rho R = \int_0^R \rho(r) dr$ where R is the capsule radius and ρ is the density of the fuel.

The plasma pressure of the hot spot can be estimated by the ideal gas equation, given by,

$$P = \frac{\rho k_B T}{\bar{m}} \quad (1.15)$$

where for a DT plasma the mean ion mass $\bar{m} = 2.5m_p$. The fusion triple product requirement of equation 1.14 can be re-expressed as a requirement on the areal density instead. This is achieved by using equation 1.15, replacing the confinement time with equation 1.9, and using the speed of sound in a plasma given by $c_s = \sqrt{2k_B T / \bar{m}}$. The resulting requirement

is given by the following relationship,

$$\begin{aligned}
 \rho R &> 3.0 \times 10^{15} \frac{4c_s \bar{m}}{T[\text{keV}]} \\
 &> 12\sqrt{2} \times 10^{15} \sqrt{\frac{\bar{m}e}{T[\text{eV}]}} \\
 &> 3.0 [\text{kg/m}^{-2}] = 0.3 [\text{g/cm}^{-2}]
 \end{aligned} \tag{1.16}$$

where $e = 1.6 \times 10^{-19}$ is the elementary charge, and the units of T needed are given in the square brackets. An ICF hot spot is therefore required to achieve a temperature of $T \sim 10$'s keV and an areal density of $\rho R \gtrsim 0.3 \text{ g/cm}^2$ in order to trap the created α particles and become an igniting plasma. Reaching these high temperatures and densities is a challenge for ICF and requires high efficiencies of energy coupling from the driver to the capsule. Any form of degradation or inefficiencies will act to raise these requirements further, increasing the difficulty of reaching ignition.

1.4.3 Burn-up Fraction

For an ignited hot spot and propagating burn wave, the burn efficiency of the fuel is given by the following equation [10, 11],

$$\Phi \simeq \frac{\rho R_{\text{tot}}}{H_B + \rho R_{\text{tot}}} \tag{1.17}$$

where H_B is the burn parameter, a slowly varying function of T that can be approximated by $H_B = 7 \text{ g/cm}^2$ over the range $20 < T < 100 \text{ keV}$ [10, 23]. The value of ρR_{tot} is the total areal density of the target, including the hot spot and compressed fuel. This equation implies that more efficient burn up of the fuel can be achieved when the areal density of the material surrounding the igniting hot spot is maximised. The burn wave can propagate more readily through compressed fuel since it is better able to trap the fusion α particles and locally capture their energy, resulting in more fuel being burned before disassembly. To reach a burn up fraction of 30% would require a total areal density of $\rho R_{\text{tot}} > 3 \text{ g/cm}^2$.

High levels of compression are needed for the DT fuel to reach these areal densities. A capsule containing 1 mg of cryogenic DT ice at solid density of $\rho_{DT} \simeq 0.2 \text{ g/cm}^3$ would have an initial radius of $\sim 1 \text{ mm}$ and a total areal density of $\rho R \simeq 0.02 \text{ g/cm}^2$. The areal density must therefore increase by a factor of over 100 for efficient fuel burn-up, which is only feasible

in the laboratory using spherical compression of the fuel. The mass of the fuel is given by the following equation,

$$\begin{aligned} M_{\text{fuel}} &= \frac{4\pi}{3} R_{\text{fuel}}^3 \rho_{\text{fuel}} \\ &= \frac{4\pi}{3} \frac{(R_{\text{fuel}} \rho_{\text{fuel}})^3}{\rho_{\text{fuel}}^2} \end{aligned} \quad (1.18)$$

Assuming no fuel mass is lost during the implosion then initial and final masses will be the same and the following relationship can be found between the initial ρ_i and final ρ_f densities

$$\frac{(\rho_f R_f)^3}{(\rho_i R_i)^3} = \frac{\rho_f^2}{\rho_i^2} \quad (1.19)$$

For an increase in areal density of $\times 150$, the density must increase by a factor on the order of ~ 1000 . Reaching these high densities while maintaining the symmetry of an implosion is incredibly complex and is one of the major challenges of ICF.

1.5 Energy Requirements

The most efficient method for reaching the high areal densities and temperatures required for ignition is to first compress cold fuel, and then to heat it. Less energy is required to compress fuel that is kept cold due to its higher compressibility, where the adiabat parameter is minimised. The adiabat of the material is the ratio of its pressure P to the Fermi degenerate pressure P_F , given by the following equation,

$$\alpha = \frac{P}{P_F} \quad (1.20)$$

The fuel is initially kept at cryogenic temperatures, ~ 18 K for the triple point of DT [24], which has an adiabat value of $\alpha \simeq 1$. During an implosion, the adiabat is increased by energy being deposited in the fuel either from radiation and high energy particles, or from a shock wave moving through the material. These increases in the adiabat can be intentional, to improve stability of the shell for example [25,26], but it will come at the cost of a decrease in the compression of the target. The energy required for compression can be found by

considering the PdV work done on the fuel as it implodes, given by the following equation,

$$\begin{aligned} E_{\text{Comp}} &= \int_{V_i}^{V_f} P dV \\ &= \mathcal{A}_{\text{deg}} \alpha M_{\text{fuel}} \int_{\rho_0}^{\rho_f} \rho^{-1/3} d\rho \end{aligned} \quad (1.21)$$

where V_i and V_f are the initial and final volumes respectively, and M_{fuel} is the mass of the fuel. The relationship of $P = \mathcal{A}_{\text{deg}} \alpha \rho^{5/3}$ has been used for equimolar DT [10], where $\mathcal{A}_{\text{deg}} = 2.17 \times 10^5 \text{ (J/cm}^3\text{)}/\text{(g/cm}^3\text{)}^{5/3}$. Integrating this and taking the initial density as approximately zero gives the energy required for compression as,

$$E_{\text{Comp}} \simeq 3.26 \alpha M_f \rho_f^{2/3} \quad (1.22)$$

For 1 mg of DT fuel and a final density of 800 g/cm^3 imploded on an adiabat of 2.5 gives an energy of $E_{\text{Comp}} \sim 120 \text{ kJ}$.

The energy required to heat the same mass of fuel to a given temperature T can be found by using equation 1.12.

$$E_{\text{Heat}} = 3 \frac{M_f}{2.5 m_p} k_B T \quad (1.23)$$

For a temperature of 15 keV for example, this equates to $E_{\text{Heat}} \sim 1.7 \text{ MJ}$. Igniting the entire volume of plasma uniformly by heating through mechanical work alone is an inefficient method for an implosion. The energy requirements on the driver would severely limit the gain that could be achieved. The solution is to produce a central hot spot that can initiate the fusion reactions in a fraction of the fuel, and to use the energy released to heat and burn the remaining compressed fuel. The central hot spot is achieved by compressing then heating the gaseous centre of the cryogenic capsule by imploding the fuel shell itself.

1.5.1 Shell Implosion Velocity

Heating of the hot spot is achieved through PdV work done by the shell on the hot spot, as the back pressure that is built up resists the imploding material. The required implosion velocity, v_{imp} , can be found by equating the needed hot spot energy to the shell kinetic

energy that supplies it, given the following equation,

$$\begin{aligned}
\frac{\theta}{2} M_{\text{sh}} v_{\text{imp}}^2 &= 3nk_B TV \\
&= 3 \frac{\rho}{\bar{m}} k_B TV \\
&= 3 \frac{M_{\text{hs}}}{\bar{m}} k_B T \\
\therefore v_{\text{imp}} &= \sqrt{\frac{6 M_{\text{hs}} k_B T}{\theta M_{\text{sh}} \bar{m}}}
\end{aligned} \tag{1.24}$$

where T_{hs} is the final hot spot temperature, M_{sh} and M_{hs} are the masses of the shell and hot spot respectively with $M_{\text{hs}}/M_{\text{sh}} \simeq 0.01$, v_{imp} is the implosion velocity, and θ is the conversion efficiency of shell kinetic energy into hot spot internal energy. Typical values of $\theta \simeq 0.5$ [9] are due to inefficiencies from asymmetries, instabilities, and the compressibility of the shell that result in imperfect coupling of shell kinetic energy to the hot spot. To reach a hot spot temperature of ~ 15 keV requires large implosion velocities of ~ 300 km/s and high accelerations to attain those velocities.

1.6 Hot Spot Ignition

The conditions required for the hot spot to ignite can be found by considering the power balance of energy gains and losses, necessitating an increasing internal energy U_{hs} . The change of internal energy with time for a hot spot is given by the following relationship [27,28],

$$\frac{dU_{\text{hs}}}{dt} = f_{\alpha} Q_{\alpha} - f_B Q_B - Q_e - P_{\text{hs}} \frac{dV_{\text{hs}}}{dt} - Q_{\text{other}} \tag{1.25}$$

where f_{α} is the fraction of alpha particles that are stopped and deposit their energy within the hot spot, Q_{α} is the alpha particle self-heating rate, Q_B is the bremsstrahlung x-ray loss rate, Q_e is the electron conduction loss rate, P_{hs} is the hot spot pressure, and V_{hs} is the idealised spherical hot spot volume.

The term Q_{other} that is shown in equation 1.25 is included to account for all other loss mechanisms that are not captured by the others. These may include low and high mode asymmetries of hot spot, or perforations of the shell from hydrodynamic instabilities. It is neglected for the remaining derivation, as an idealised case is assumed.

The first term on the right-hand side of equation 1.25 represents the energy that is

deposited back into the hot spot by the fusion α particles being stopped by the high areal densities. Using equation 1.5, the rate of deposited fusion energy is given by the following equation,

$$\begin{aligned} Q_\alpha &= \frac{P_{\text{fus}}}{5} \\ &= \frac{E_\alpha \rho^2}{20 \bar{m}^2} \langle \sigma v \rangle \end{aligned} \quad (1.26)$$

An approximation for the value of f_α is give by [29],

$$f_\alpha = 1 - \frac{1}{4 [(\rho_{\text{hs}} R)_{\text{hs}} / \rho_{\text{hs}} \lambda_\alpha]} + \frac{1}{160 [(\rho R)_{\text{hs}} / \rho_{\text{hs}} \lambda_\alpha]^3} \quad (1.27)$$

where ρ_{fuel} is in cold fuel density and λ_α is the mean free path length of an α particle. Increasing the areal density of the fuel will help trap the α particles and raise the energy deposition fraction. The value of $\rho \lambda_\alpha$ is the α stopping range where an analytic scaling has been found [30] using modern stopping power theory [31], given by the following equation,

$$\rho_{\text{hs}} \lambda_\alpha [g/cm^2] = \frac{0.01705 T_{\text{hs}}^{1.0804}}{1 + 0.007144 T_{\text{hs}}^{1.0804}} (1 + 1.7823 \rho_{100}^{0.2003}) \quad (1.28)$$

where ρ_{100} is the hot spot density in units of 100 g/cm².

Radiation losses are dominated by electron bremsstrahlung emission. The radiative loss rate loss for an optically thin hot spot, calculated from non-local thermodynamic opacity tables for DT using the Howard Scott DCA model [32], can be found from the following equation [10],

$$Q_{\text{rad}} = 4.24 \times 10^{14} \left(\frac{P_{\text{hs}}}{202.8} \right)^2 \left(\frac{R_{\text{hs}}}{0.004} \right)^3 T^{-1.3023} \text{ W} \quad (1.29)$$

where R_{hs} is the hot spot radius. Included in this model is reduction in radiative losses by approximately a factor of 2 because of the reabsorption of low energy < 2 keV x-rays by the high temperature and areal density plasmas that are typical in a hot spot [33]. Not included in this model is the mix of the high-Z ablator material with the hot spot that can increase bremsstrahlung loss rate and potentially quench ignition.

A temperature gradient will be present from the cold fuel up to the high temperature hot spot. Energy will be transported down the temperature gradient, carried mainly by the electrons. An approximation for the power density loss for thermal conduction can be

found [10] from the Spitzer model [34], given by the following equation,

$$\begin{aligned}
 P_{\text{cond}} &= -\frac{\chi_e \nabla T_e S_{\text{hs}}}{V_{\text{hs}}} \\
 &\simeq \frac{3A_e T^{7/2}}{\ln \Lambda R_{\text{hs}}^2}
 \end{aligned}
 \tag{1.30}$$

where S_{hs} , V_{hs} are the surface area and volume of the hot spot respectively, $\ln \Lambda$ is the α -electron Coulomb logarithm, χ_e is the electron conductivity, and $A_e \simeq 9.5 \times 10^{12} \text{ J s}^{-1} \text{ cm}^{-1} \text{ keV}^{-7/2}$ [10].

For an isobaric configuration where the pressure in the hot spot and compressed fuel are approximately equal, there is no mechanical work done on the system and the $-P_{\text{hs}} \frac{dV_{\text{hs}}}{dt}$ term can be ignored. Isochoric configurations have a pressure imbalance, where the pressure is higher in the hot spot than the cold fuel. Mechanical PdV work is then done on the fuel by the hot spot, increasing the ignition requirements because of the additional expended energy.

It should be noted that certain values, in particular f_α and f_B , evolve in time. A full treatment of the hot spot should include the changes in these terms with time. For this derivation, they can be well approximated as constant values over the short time period of confinement.

A hot spot of increasing energy density requires that $dU_{\text{hs}} > 0$. This produces a parameter space for the areal density and temperature that must be reached to produce a self heating hot spot, found by combing equations 1.26, 1.29 and 1.30 with 1.25. This requirement for isobaric ignition is plotted in Figure 1.3. The shaded region represents the areal density and temperature parameter space that meet the requirements for ignition. For temperatures below $\sim 3.5 \text{ keV}$ bremsstrahlung, radiation losses will dominate and no amount of areal density can compensate. The region in the top left of the graph ($\rho_{\text{hs}} R_{\text{hs}} \lesssim 0.3 \text{ g/cm}^2$) would fail to ignite due to conduction loss.

1.6.1 Central Hot Spot Approaches

Two main approaches to laser driven implosions have emerged; indirect drive and direct drive, shown schematically in Figure 1.4.

Indirect drive uses a high- Z material to convert the laser energy into high energy x-rays. The capsule sits in a hollow chamber called a hohlraum, typically a cylinder made of gold [12]. The lasers enter through holes in the ends of the hohlraum and are incident on

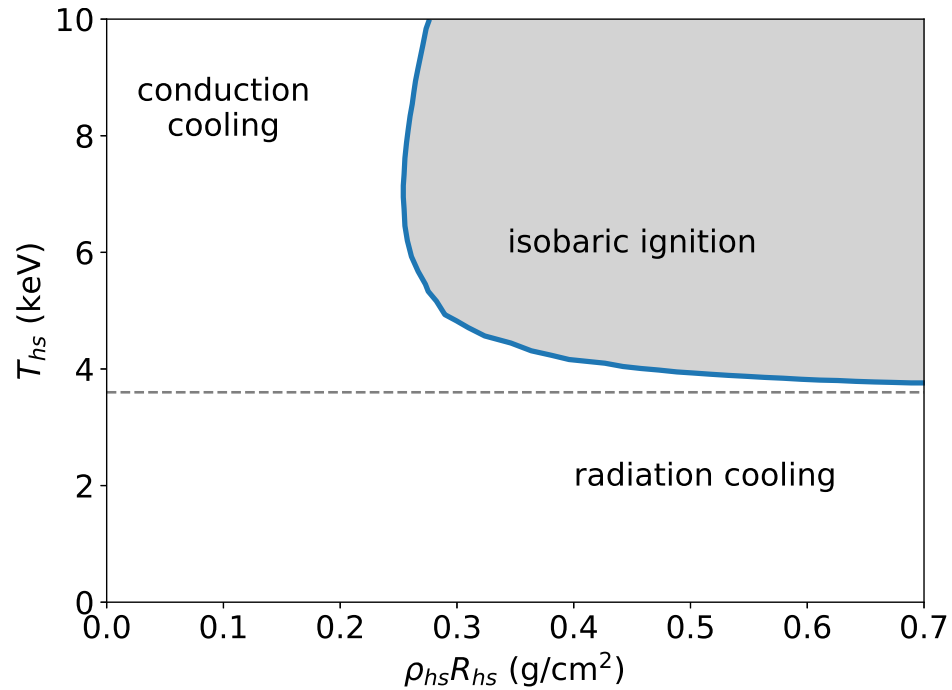


Figure 1.3: The conditions required for a self-heating plasma for an isobaric configuration of fuel. Regions outside of the grey shaded area will not achieve self-heating because of cooling due to conduction losses and radiation emission. Image reproduced with data taken from [35].

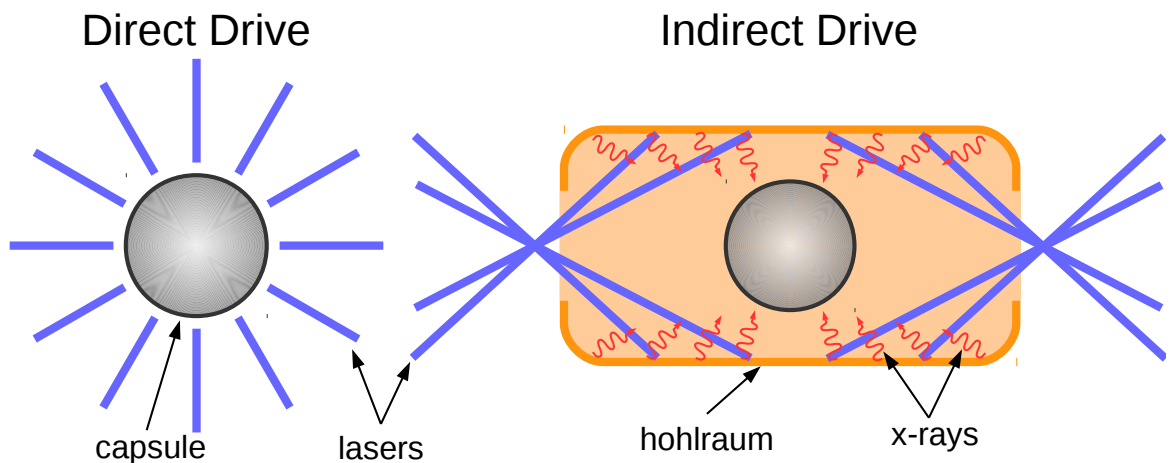


Figure 1.4: Direct Drive and Indirect Drive are two approaches to laser inertial fusion. Direct drive produces the ablation pressures needed by direct illumination of the capsule which allows for greater energy coupling. The lasers in indirect drive are incident on the inside of a hohlraum that contains the capsule which produces a more uniform x-ray radiation field.

the inner walls to heat them. The walls then re-radiate this energy, creating an x-ray bath for the capsule. While this technique greatly improves the symmetry of the radiation field by smoothing the incident laser profile, the x-ray conversion process reduces the energy that is coupled to the capsule.

The direct drive approach uses direct illumination of the capsule with lasers. Higher coupling efficiencies can be achieved with this technique as the laser energy impinges upon the capsule itself. A key problem for direct drive to overcome is its susceptibility to the small scale non-uniformities present in the capsule surface and the laser intensity profiles. These non-uniformities will degrade the implosion performance by reducing the symmetry and seeding instabilities. This worsens the coupling of shell kinetic energy to the hot spot and potentially mixes ablator material into the fuel. Laser smoothing techniques are employed to reduce the non-uniformities, and target compositions and laser pulses are designed to reduce the susceptibility to these asymmetries and instabilities.

Both techniques currently use Nd:Glass based lasers that are frequency tripled to a wavelength of 351 nm [36]. Increasing the photon frequency allows the light to reach higher electron densities where collisional absorption is more efficient, and it reduces the susceptibility to laser-plasma instabilities [37].

1.6.2 Direct Drive Implosion Design

Ignition and burn of ICF capsules are thought to be possible with \sim MJ scale laser drivers and \sim mm scale capsules. A design for a direct drive implosion is given in Figure 1.5 that uses 2.4 MJ of UV laser energy to implode a 1894 μ m outer diameter capsule. The target is a layered cryogenic capsule, containing a core of DT gas at a density of 0.62 mg/cm³, surrounded by a 176 μ m layer of DT ice at 0.25 g/cm³, and a 55 μ m CH plastic ablator on the outer surface. The laser pulse has a 4.2 TW foot and a slow ramp up to its peak power of 427 TW in order to maintain a low adiabat.

The implosion was simulated in spherical geometry using the 1 dimensional radiation hydrodynamics code HYADES [38]. The temporal evolution in the mass density of the imploding capsule is shown in Figure 1.6 where the laser pulse and fusion reaction rate are included for reference. The initial target structure can be seen at time $t=0$, with the low-density gaseous core surrounded by a layer of DT ice and CH ablator.

The small increase in laser power to the foot of the pulse will apply an ablation pressure on

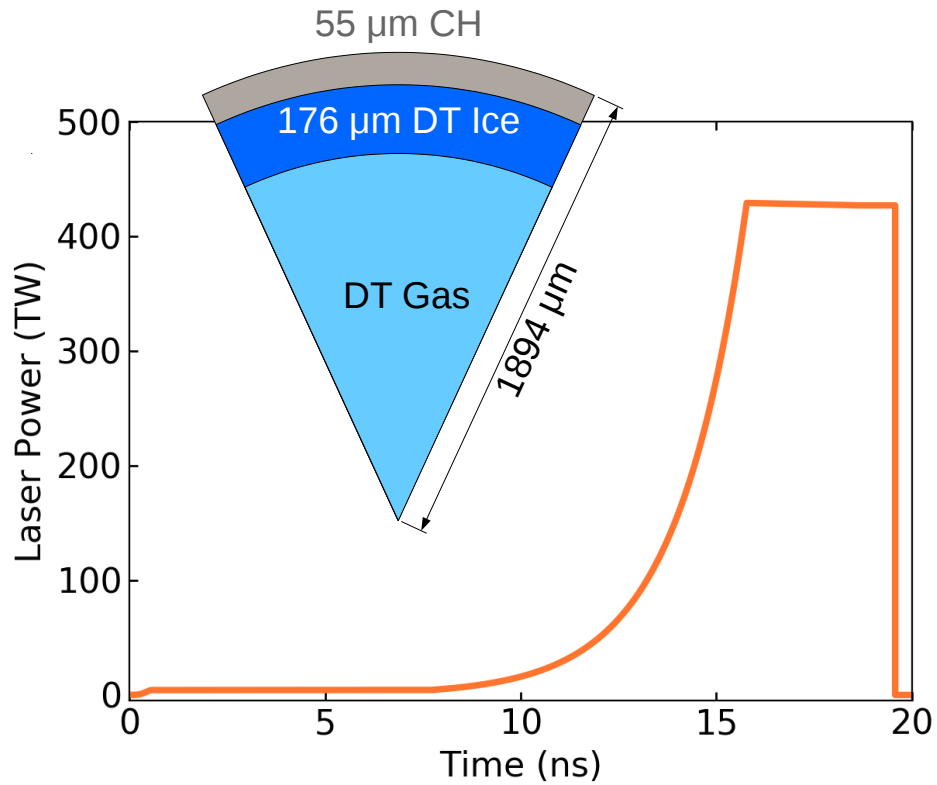


Figure 1.5: Target design and pulse shape for a 2.4 MJ laser energy direct drive implosion. Image inspired by [9].

the capsule that launches a shock into the target. This first shock is used to set the minimum adiabat of the material. By using a single weak shock, the increase in entropy during the implosion can be minimised, allowing the material to reach a higher final compression. As the shock moves through the shell, it compresses the material and increases its density. At ~ 11 ns the shock reaches the ice layer inner surface and the shell as a whole is in motion.

After a time of ~ 15 ns, the laser increases to its maximum power and launches the main shock. The shell is then accelerated to its maximum velocity of 360 km/s and is imparted with enough kinetic energy to reach ignition. The shocks merge in the gas core and rebound off the centre where the shocks meet the imploding shell, further compressing it and beginning its deceleration. The shell imparts its kinetic energy to the hot spot and convergence effects significantly increase its areal density.

A central hot spot has now formed, surrounded by compressed fuel. Figure 1.7 shows the radial profile of the ion temperature and the mass density at peak compression. The high temperature and low density hot spot occupies the central ~ 60 μm region, contained by the highly compressed cold fuel shell from 50 – 100 μm . The hot spot ignites and a burn

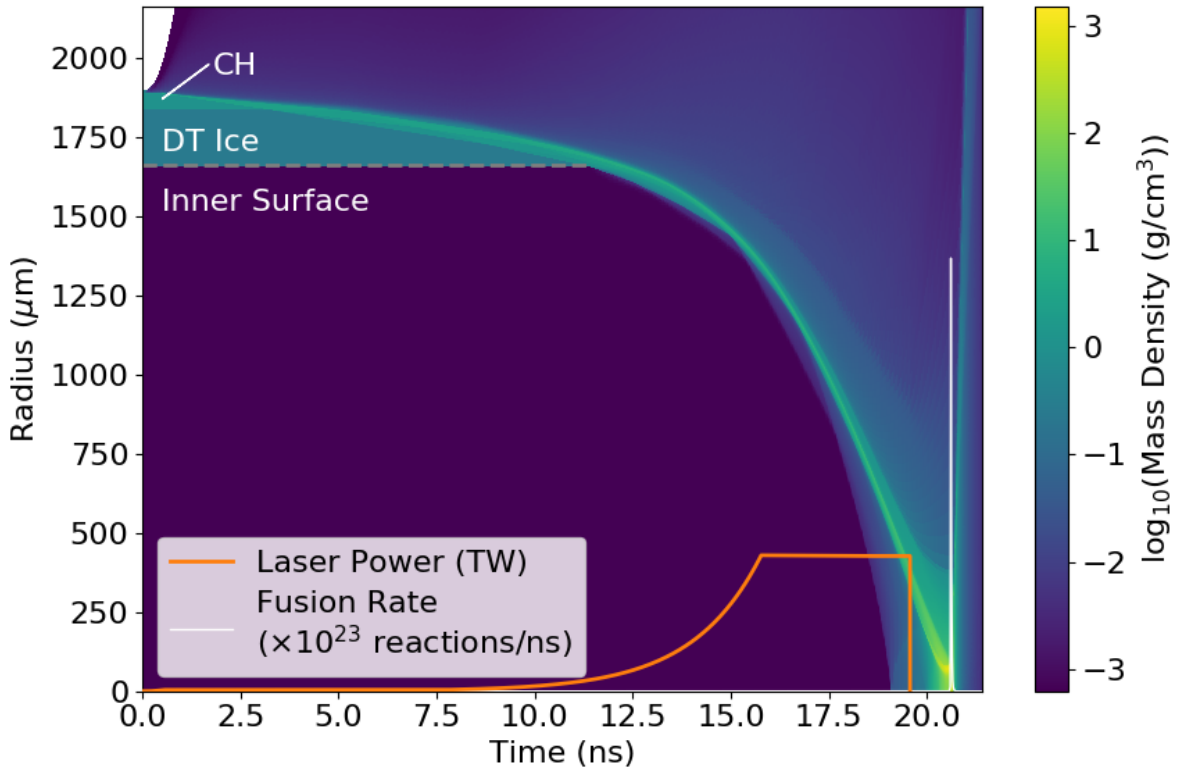


Figure 1.6: Radiation-hydrodynamics simulation of the implosion design shown in Figure 1.5. The logarithm of the mass density at each radius is given against time, with the laser pulse and the fusion rate overlaid.

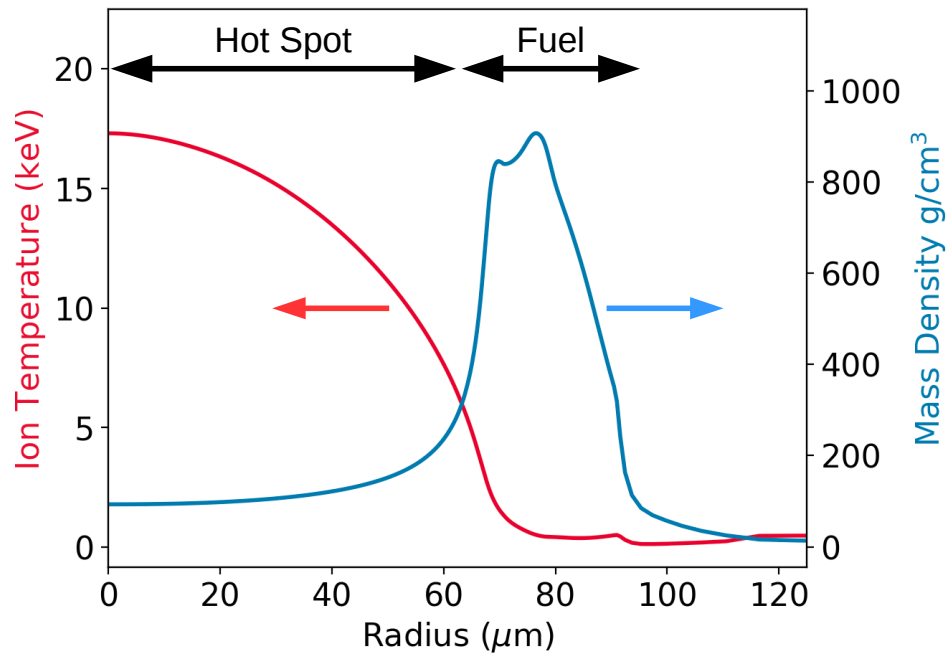


Figure 1.7: Ion temperature and mass density against radius from the simulation shown in Figure 1.6 at peak compression. The regions of the hot spot and fuel have been highlighted.

wave propagates through the fuel, producing 258 MJ of fusion energy. This idealistic case has not considered any degradation mechanisms that can worsen performance and increase the ignition threshold. The known degradation sources, which include imperfections associated with the target and laser, are currently inferred from experiment. Chapters 4 and 5 present results that aim to characterise some of these known degradation sources and their impact on implosion performance. Implementing these degradation sources into radiation-hydrodynamics codes and designing implosions that are robust to them is an essential step in ICF research.

1.7 Hydrodynamics

1.7.1 Shock Wave Physics

Compression of the fuel is most efficient when its temperature is kept low and is achieved in such a way to minimise the increase in the internal energy, in order to reach the high areal densities needed. Near isentropic compression can be achieved with specific laser pulses, the Kessler solution for drive pressure for example [39], or from compression with many laser induced shock waves. Shock waves are discontinuities in the pressure, density and temperature profiles, that raises the downstream values of these properties.

Lasers light that is incident on a target will deposit its energy into the material, forming an outwardly expanding plasma that exerts an ablation pressure on the remaining mass. This pressure acts like a piston on the capsule, sending a pressure wave through the material. For a large deposition of laser energy, the pressure wave will have an amplitude high enough that it will travel faster than the local speed of sound, and the pressure wave will develop into a shock, shown in Figure 1.8. The rear section of the pressure wave will be at a higher speed than the front section as it is travelling through higher pressure material. This is found by considering that the sound speed goes as $c_{\text{sound}} = \sqrt{\frac{\gamma P}{\rho}}$ where P is the pressure, ρ is the density, and γ is the adiabatic index or ratio of specific heats of the material. The spatial extent of the transition region in front of the pressure wave decreases until a near discontinuous jump in material properties exists. Viscosity will smear out this discontinuity such that it will have a finite width.

A shock will introduce a sudden increase in the internal energy of the shocked material, with stronger shocks increasing the internal energy by greater amounts. Such an increase

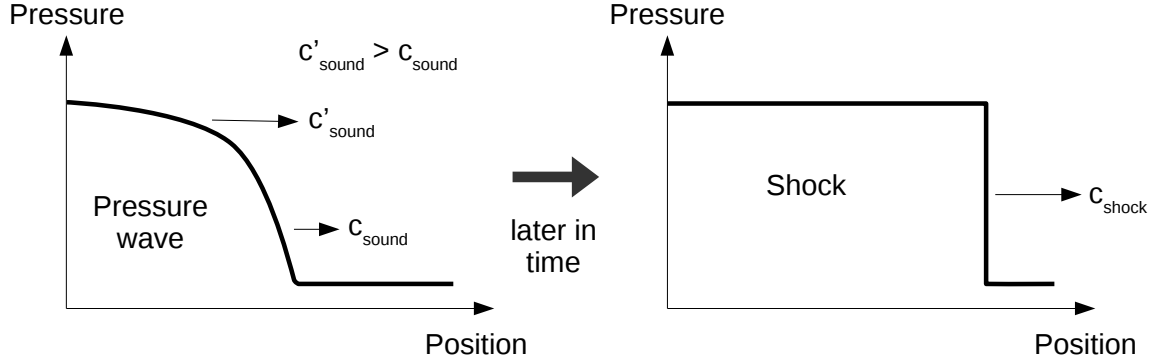


Figure 1.8: The development of a pressure wave into a shock because of the higher sound speed in shocked material.

can be beneficial for raising the hot spot temperature for ignition but is detrimental in the earlier stages of the implosion when the fuel temperature is to be kept low. Stronger shocks will produce a larger increase in internal energy of the shocked material, but a single shock can only reach a maximum compression ratio, regardless of its strength. A series of shocks can instead be used to minimise the increase in adiabat to the fuel but timed such that they merge into a single final shock that can provide the large increase in internal energy to the hot spot to aid ignition.

The conservation of mass, momentum, and energy of elements in a fluid in one dimension are expressed by the Rankine–Hugoniot conditions [40–42], given by the following equations,

$$\frac{\partial \rho}{\partial t} = -\frac{\partial(\rho u)}{\partial x} \quad (1.31)$$

$$\frac{\partial}{\partial t}(\rho u) = -\frac{\partial}{\partial x}(\rho u^2 + P) \quad (1.32)$$

$$\frac{\partial}{\partial t} \left(\rho \epsilon + \frac{\rho u^2}{2} \right) + \frac{\partial}{\partial x} \left(\rho u \left[\epsilon + \frac{u^2}{2} + \frac{P}{\rho} \right] \right) = 0 \quad (1.33)$$

This set of equations require an equation of state in order to close them, that links the pressure, temperature, and density of the material. A commonly used equation of state is the ideal gas equation $P = nk_B T$.

The relationship between the shocked and unshocked material can be found by consid-

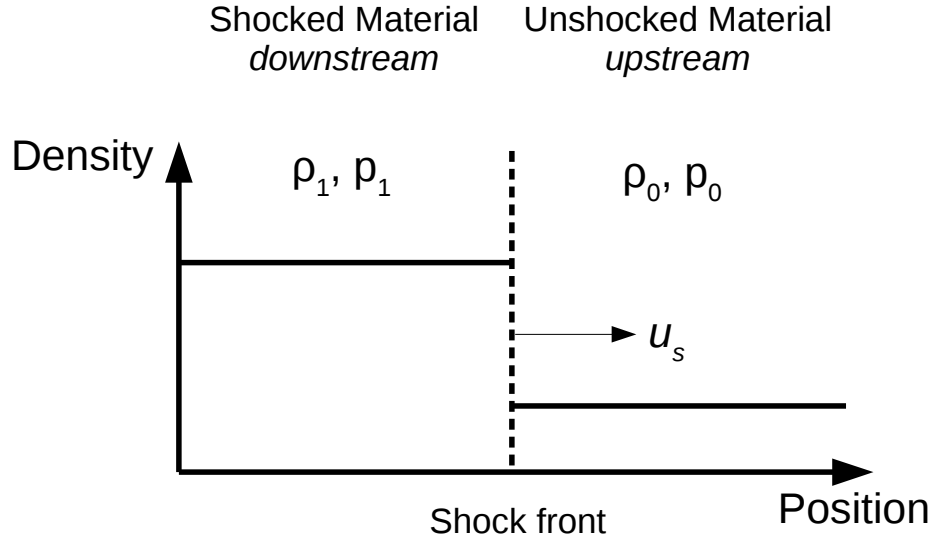


Figure 1.9: A shock wave will raise the density and pressure of the downstream material compared with the unperturbed upstream material. Image inspired by [43].

eriving equations 1.31-1.33 across the shock front seen in Figure 1.9,

$$\begin{aligned}
 \rho_1 u_1 &= \rho_0 u_0 \\
 \rho_1 u_1^2 + P_1 &= \rho_0 u_0^2 + P_0 \\
 \left[\rho_1 u_1 \left(e_1 + \frac{u_1^2}{2} \right) + P_1 u_1 \right] &= \left[\rho_0 u_0 \left(e_0 + \frac{u_0^2}{2} \right) + P_0 u_0 \right]
 \end{aligned} \tag{1.34}$$

where the subscripts 0 and 1 refer to the unshocked and shocked material respectively. These equations can be manipulated to give the following relationships between the densities,

$$\frac{\rho_1}{\rho_0} = \frac{P_1(\gamma + 1) + P_0(\gamma - 1)}{P_0(\gamma + 1) + P_1(\gamma - 1)} \tag{1.35}$$

In the limit of $P_1 \gg P_0$, the density ratio approaches,

$$\frac{\rho_1}{\rho_0} = \frac{(\gamma + 1)}{(\gamma - 1)} \tag{1.36}$$

which for a monatomic gas $\gamma = 5/3$ gives a compression ratio $\rho_1/\rho_0 = 4$. Higher compressions can be achieved with a series of shocks, each raising the density by up to a factor of 4.

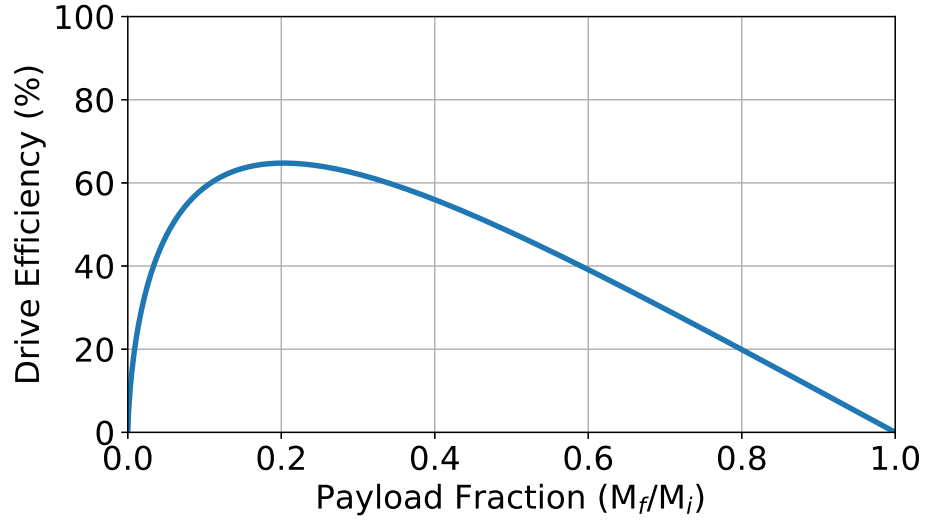


Figure 1.10: Drive efficiency of the rocket effect from ablation of the outer surface of the shell, defined as the ratio of the final shell kinetic energy to the exhaust kinetic energy. Given as a function of the payload fraction.

1.7.2 Hydrodynamic Efficiency

Implosion and compression of the capsule is achieved by ablative drive of the shell from laser illumination. Outward expansion of the ablated plasma applies a force on the remaining mass inwards from the conservation of momentum. The amount of kinetic energy that is transferred to the shell depends on the mass ablation rate and the velocity of the expelled mass u_{ex} , called the exhaust velocity.

The final implosion velocity v_{imp} that is reached when the ablation stops is approximated by the following equation,

$$v_{\text{imp}} = u_{\text{ex}} \ln \left(\frac{M_i}{M_f} \right) \quad (1.37)$$

where M_i and M_f are the initial and final (payload) masses respectively. The value M_f/M_i called the payload fraction, is the ratio of the mass remaining after the acceleration to the initial shell mass. The drive efficiency, η_{dr} , is defined as the ratio of the shell kinetic energy, E_{kin} , to the kinetic energy of the exhausted material, E_{ex} , as given by the following equation,

$$\eta_{\text{dr}} = \frac{E_{\text{kin}}}{E_{\text{ex}}} = \frac{M_f/M_i (\ln(M_f/M_i))^2}{1 - M_f/M_i} \quad (1.38)$$

This relationship is plotted in Figure 1.10 where the efficiency is peaked for a payload percentage of 20.3%, meaning that $\sim 80\%$ of the capsule mass must be ablated off before ignition.

The hydrodynamic efficiency is defined as the ratio of laser energy to shell kinetic energy. This simple model does not take into account other effects that go into the overall hydrodynamic efficiency of the implosion. Along with giving the exhaust plasma kinetic energy, laser energy must be used in the ionisation and heating of the plasma. Exhaust plasma temperatures of $\sim\text{keV}$ are produced, requiring large amounts of laser energy simply to heat the material to these temperatures.

Further inefficiencies arise from the imperfect absorption of the incident laser energy by the plasma. Reflection, refraction, backscatter, and other effects contribute to directing of laser energy away from absorption by the plasma. This energy is lost from the capsule and does not contribute to the ablative drive.

Simulations of ignition scale implosions [9] indicate hydrodynamic efficiencies of $<10\%$. The highest performing published indirect drive implosions on NIF [44–46] had a capsule absorbed energy of ~ 225 kJ and a shell kinetic energy of ~ 16 kJ, giving a hydrodynamic efficiency of $\sim 7.1\%$. The shell kinetic energy must then be converted into hot spot internal energy, presenting another opportunity for losses and inefficiencies. These losses result from malformed hot spots or residual kinetic energy at the point of ignition. For the NIF shot, a hot spot was formed with an inferred energy of ~ 17 kJ from 1.89 MJ of input laser energy (0.87%), highlighting the inefficiencies. High performing Omega shots [47] that are scaled to NIF energies and capsule sizes are predicted to have hot spot energies of ~ 30 kJ, implying a $<2\%$ conversion of laser energy to hot spot.

1.8 Inertial Fusion Energy Reactor Requirements

A crucial parameter for ICF in the context of energy production is the energy gain of the implosion. It is the ratio of the fusion energy released, E_{fus} , to the energy delivered to the target by the driver, E_{driver} , given by the following equation,

$$G = \frac{E_{\text{fus}}}{E_{\text{driver}}} \quad (1.39)$$

A gain of 1 would signify a breakeven fusion implosion, but this only accounts for the energy delivered to the target and ignores losses incurred between the wall plug and the laser energy output. Much higher gains are needed to overcome inefficiencies in the laser driver, to make energy production viable and economically competitive.

The portion of fusion energy released into the neutrons can be captured by a blanket surrounding the implosion chamber. This heats the blanket which is then converted into electricity via conventional thermal cycle with an efficiency $\eta_{\text{th}} \simeq 40\%$. Some of the electricity generated must be recirculated back to power the driver, which for future power plants might be diode-pumped solid state lasers. Current diode pumped systems can have efficiencies of up to 27.5% [48]. Further costs such as the power required to run the power plant and electricity transportation losses will only act to increase the gain requirements.

In order to achieve the power output of \sim GW in order to make the energy production economically viable, a 10 Hz shot rate will be required and gain of between 30-100 [10]. Demonstrating the ability to reach these high gains is crucial for ICF before it is to be pursued for future energy production.

1.9 Sources of Degradation

Implosions act as amplifiers [49], concentrating certain properties of the capsule. This effect is exploited to reach the high pressures and temperatures as these features are amplified through convergence. The same is true however for unintentional and detrimental effects that worsen the performance of an implosion, in particular non-uniformities and asymmetries.

These perturbations are typically characterised by Legendre polynomials that have associated amplitude and mode number, $\ell = 2\pi R/\lambda$ where R is the target radius and λ is the polynomial wavelength. Values of $\ell < 10$ have low polynomial frequencies and are considered low mode asymmetries, arising from macro scale perturbations. High mode number asymmetries, $\ell > 10$, are associated with high frequency perturbations and arise from small scale features much smaller than the capsule itself.

The presence of low mode asymmetries are typically the result of laser drive non-uniformity. These include beam imbalance [50] where perfectly spherical illumination is not achieved due to fluctuations in energy delivered by the individual beams. The positioning of the target [51] or the central focusing point of the beams [52] might not be well aligned to the target chamber centre. The laser-plasma instability of cross-beam energy transfer can cause the exchange of energy between beams leading to a drive asymmetry [53]. These mechanisms lower the spherical symmetry of the implosion that leads to a reduced conversion of shell kinetic energy into hot spot internal energy, increasing the residual kinetic energy.

High mode asymmetries are detrimental as they can seed hydrodynamic instabilities that grow during the acceleration and deceleration of the shell. They will lead to the decompression of the shell, mixing of ablator material with the fuel, and at worst the break-up of the shell. They can be seeded by an inhomogeneous laser intensity spatial pattern or speckling [54], roughness of the capsule surface and distortions to the overall shape [55,56], defects in the capsule composition [9], and radiation damage and ^3He contamination from the decay of tritium in the fuel [57]. This can lead to an increase in the hot spot surface area, raising the cooling rate through conduction and radiation which lowers the temperature. Higher atomic number ablator material can also become mixed with the fuel which increases the bremsstrahlung cooling rate [56].

It is crucial for the success of ICF to characterise these asymmetries with high resolution diagnostics. Only with these diagnostics can the size and effect of asymmetries be characterised, which is necessary to enable the judicious implementation of techniques for minimising them.

1.9.1 Rayleigh-Taylor Instability

The Rayleigh-Taylor instability [58–60] is a hydrodynamic instability that can amplify small scale perturbations. Perturbations in the interface between two materials are amplified if their density and pressure gradients have opposing signs. This arises from a low density fluid pushing on a more dense fluid. This can occur during the acceleration phase of an implosion where the low density ablation plasma acts as a piston on the denser shell, and during the deceleration of the shell when the low density hot spot is resisting the compressed fuel. The growth of these perturbations can lead to a reduction in the compression of the shell during flight [61,62], reducing the pressure in the hot spot. The resulting mixing of materials will introduce higher- Z elements into the core, such as carbon from the plastic ablator, cooling the hot spot by increasing radiation losses [63]. In extreme cases, the perturbations can grow large enough to disrupt the shell entirely, breaking up dense fuel and allowing hot spot plasma to be ejected [64]. During the deceleration phase, the growing perturbations act to increase the surface area of the hot spot. This leads to greater cooling from conduction and radiation loss, lowering the temperature and potentially preventing ignition.

An initial perturbation of amplitude h_0 that is accelerated at a rate g will at first grow

exponentially in time according to the Takabe equations [65],

$$h(t) = h_0 \exp(\gamma t) \quad (1.40)$$

$$\gamma = \sqrt{A_t k g} - \beta k v_{\text{abl}} \quad (1.41)$$

where $A_t = (\rho_1 - \rho_2) / (\rho_1 + \rho_2)$ is the Atwood number of two materials with densities ρ_1 and ρ_2 , k is the mode wavenumber of the perturbation, β is a material specific constant, and v_{abl} is the ablation velocity. The large accelerations needed to reach the high velocities of ICF implosions makes them very susceptible to the Rayleigh-Taylor instability which is why they are of such a large concern. This is particularly an issue for central hot spot ignition where the shell needs to reach velocities high enough to provide the kinetic energy for ignition itself. The second term in 1.41 provides ablative stabilisation to the system where high ablation velocities reduce the mode growth [66]. The amplitude of low- and mid-mode Rayleigh-Taylor perturbations further increases as a result of the convergence of shell through the Bell-Plesset effect [67,68].

The perturbations feedthrough through the denser shell and will have an amplitude at the inner surface given by the following equation [69],

$$h_{\text{inner}} = h_{\text{outer}} \exp(-k\Delta R) \quad (1.42)$$

where ΔR is the thickness of the shell. It has been shown [70] that equation 1.40 can be expressed as

$$h_{\text{outer}} \propto \exp\left(v_{\text{imp}} \sqrt{k\Delta R}\right) \quad (1.43)$$

Figure 1.11 provides a visualisation of the three scenarios of shell perturbation. For perturbations with $k\Delta R \gg 1$, it can be seen from equations 1.43 and 1.42 that the growth rate is high but it decays quickly in space so does not reach the inner surface. Conversely, perturbations with $k\Delta R \ll 1$ may reach the inner surface but typically do not grow fast enough to significantly affect the shell. It is the perturbations with $k\Delta R \sim 1$ that are the most detrimental and correspond with perturbations whose wavelength is approximately the same order of magnitude as the thickness of the shell.

Target susceptibility is not solely limited to high velocity implosions. Another key im-

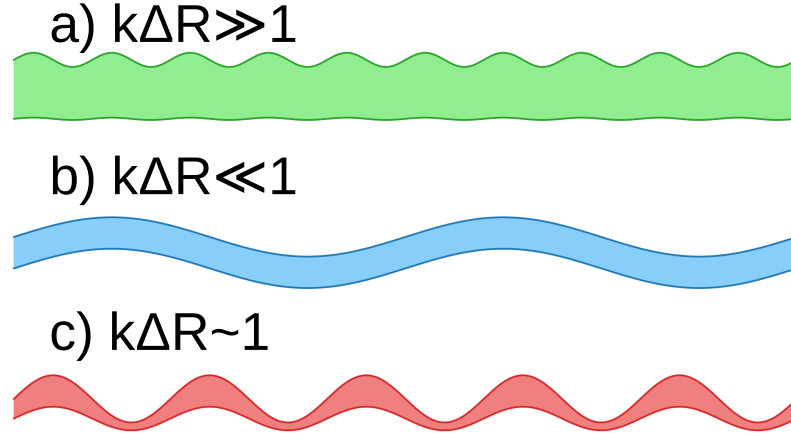


Figure 1.11: A visualisation of the Rayleigh-Taylor instability for linear shells. The instabilities are most detrimental when the product of the mode wave number and the shell thickness is approximately equal to unity. The perturbations are able to penetrate through and disrupt the inner surface. Image inspired by [73].

plosion parameter is the in-flight aspect ratio (IFAR) and is defined as the radius of the ablation front R_{abl} divided by the shell thickness ΔR , $\text{IFAR} = R_{\text{abl}}/\Delta R$, when the ablation front has reached a radius of $2/3$ of the initial radius of the inner shell [9]. Targets with thin shells and large diameters will have greater IFAR's than those with thicker shells and small diameters. Consider the first term in equation 1.41, $\gamma = \sqrt{A_t k g}$. For an exponential growth rate of the Rayleigh Taylor instability, $\exp(\gamma t)$, the number of e-foldings is given by $N_e = \gamma t$. Considering the most detrimental growth rate occurs for mode numbers $k \sim 2\pi/\Delta R$, and approximating a constant values for the acceleration of the shell $2R/3 = \frac{1}{2}g \left(\frac{t}{2}\right)^2$, then the overall growth rate will become $N_e = \sqrt{A_t \frac{32\pi}{3} \text{IFAR}}$. Other derivations of the growth rate produce the same exponent of the IFAR [71, 72]. This is consistent with equation 1.43 as the IFAR of an implosion scales with the implosion velocity squared [12].

1.10 Summary

Inertial confinement fusion provides a route to terrestrial fusion and potentially towards sustainable energy production but for this to be achieved the sources of degradation must be overcome. Energy gain is made possible through fusion reactions from the release of energy due to the change in mass between the reactants and the products. Contemporary fusion research is focused on the reaction of deuterium and tritium, as it has a high reactivity at

low and achievable plasma temperatures.

The aim with laser direct drive is to compress and heat a hollow capsule of this fusion fuel using direct illumination by lasers. The ablation of the outer surface drives the capsule inwards via the rocket effect, compressing the gas fill and forming a hot spot. Fusion reactions are then triggered in the hot spot and a burn wave propagates outwards through a layer of compressed fuel.

The burning of the fuel and subsequent release of energy is limited by the time that the fuel is confined by its own inertia. Ignition and sufficient gain must occur during this confinement time as the reaction is quickly quenched by the rapid expansion of the fuel outwards. Ignition is initiated by forming a hot spot with a high enough temperature that significant amount of alpha particles are produced through fusion reactions, and a large enough areal density to trap those alpha particles to further heat the hot spot. The following burning wave is made more efficient by surrounding the hot spot with a layer of highly compressed fuel.

Hydrodynamic instabilities and overall inefficiencies arise largely from the high implosion velocities that are needed to provide the hot spot energies. To overcome this, the adiabat of the implosion can be increased to provide greater stability but at the cost of gain, as the areal density that is built up is reduced. The goal is to create implosion designs that are capable of achieving ignition and high gain without succumbing to instabilities. Essential to the realisation of inertial confinement fusion is the identification and quantification of the degradation sources to implosions, found through accurately diagnosed experiments.

Chapter 2

Shock Ignition

Shock Ignition is an alternative scheme for ICF that decouples the assembly and the ignition of the fuel. It offers the potential for higher gain at lower laser energies and greater hydrodynamic stability of compression compared with central hot spot ignition. The fuel is first imploded with a low shell velocity that is more robust against hydrodynamic instabilities. The kinetic energy of the shell for such an assembly of fuel is not large enough to trigger ignition on its own and additional energy must be supplied to elevate the hot spot to ignition conditions. For shock ignition, this takes the form of a sudden increase in laser intensity late in the implosion that launches a strong shock into the fuel. This shock increases in strength as it spherically converges and its collision with the main compression rebound shock within the dense fuel will produce two new shocks travelling in opposite directions. The inbound shock will further compress the fuel and increase the pressure on the hot spot, triggering a non-isobaric ignition. The laser intensities needed to launch a shock of sufficient strength are $\sim 1 \times 10^{16}$ W/cm² and enters a regime where laser energy deposition is thought to be dominated by laser-plasma instabilities [13].

The laser-plasma instabilities direct energy away from the ablation that drives the implosion which depletes the laser before it can reach higher densities, lowering the applied pressure. The instabilities also produce high energy hot electrons with long mean free paths that can potentially aid shock generation or preheat the fuel and hinder ignition. Coupling laser energy into the shock without incurring the detrimental effect of laser-plasma instabilities is critical for success of shock ignition.

2.1 Motivation For Lowering Implosion Velocity

Reaching ignition conditions in the central hot spot scheme requires high implosion velocities for the shell as the heating of the hot spot is achieved largely from the conversion of shell kinetic energy into hot spot internal energy. Models for the predicted neutron yield, Y as it relates to key implosion metrics can be used to guide the design of implosions by highlighting which parameters have the most significant impact. One such model [27, 45] designed for indirect drive implosions on NIF is given by the following equation,

$$Y = P_{\text{abl}}^{16/25} \left(\frac{v_{\text{imp}}^{67/15}}{\alpha^{36/25}} \right) S^{14/3} (1 - \text{RKE})^{23/7} \eta \quad (2.1)$$

where P_{abl} is the ablation pressure, v_{imp} is the implosion velocity, α is the fuel adiabat, S is the the spatial scale factor [27], RKE is the residual kinetic energy of the shell that is not transferred to the hot spot, and η is the implosion efficiency that captures radiative loss and reduced compressed from hydrodynamic mixing. It can readily be seen from the large exponent on the v_{imp} term that moving to higher velocity implosions can significantly increase the neutron yield, as there shell has a greater kinetic energy that can be converted into internal energy within the hot spot. Previous models that were more general [74] or specifically focused on direct drive implosions [72] found that the laser energy required for a marginal ignition, E_L^{ign} , scaled with v_{imp} to powers of ~ 5.9 and ~ 6.6 respectively, again implying that, for a limited laser energy, reaching ignition requires large velocities.

Igniting a capsule indeed requires high shell implosion velocities but once ignition has been reached, the overall gain decreases with implosion velocity. The gain of an implosion is given by the following equation [72],

$$G \approx \frac{365}{I_{15}^{0.25}} \left(\frac{v_{\text{imp}}}{300 \text{ km/s}} \right)^{-1.25} \left(\frac{\rho R}{7 + \rho R} \right) \left(\frac{\lambda_L}{0.35 \text{ } \mu\text{m}} \right)^{-0.5} \quad (2.2)$$

where I_{15} is the laser intensity in units of 10^{15} W/cm^2 , v_{imp} is given in km/s, ρR is the shell areal density, and λ_L is the laser wavelength in microns. The inverse relationship of gain with implosion velocity is in part due to inefficiencies of the rocket effect for driving an implosion, worsening with higher velocities. A similar scaling was found for the peak energy gain [74] with a much larger amplitude of exponent of -3.3 , further demonstrating the inefficiency of high velocity implosions.

Reaching these velocities can only be achieved with large accelerations and requires the shell to be light and thin, creating capsules with large IFAR's. As discussed in Section 1.9.1, capsules with large IFAR values are more susceptible to the growth of hydrodynamic instabilities [69], in particular the Rayleigh-Taylor instability. The peak IFAR reached for an implosion is approximated by the following equation [75],

$$\text{IFAR} \approx 60 \left(\frac{v_{\text{imp}}}{300 \text{ km/s}} \right)^2 \left(\frac{P_{\text{abl}}}{100 \text{ Mbar}} \right)^{-2/5} \langle \alpha_{if} \rangle^{-3/5} \quad (2.3)$$

where $\langle \alpha_{if} \rangle$ refers to the spatially averaged in-flight adiabat of the fuel. The large accelerations increase the growth rate of the Rayleigh-Taylor instability where perturbations on the shell surface are amplified, and the large IFAR's allow these perturbations to penetrate through the shell. The penetration of these instabilities through the shell will degrade its integrity and disrupt the formation of the hot spot. Equation 2.3 implies that shell IFAR increases with velocity, and since large IFAR's have been shown experimentally to produce low stability implosions [76], this highlights further the instability of high shell velocities implosions. This has led current central hot spot designs to increase the adiabat of the implosion [77] in order to regain hydrodynamic stability at the cost of yield [78, 79].

Scaling laws such as these cannot accurately predict the outcomes of experiments. They can only provide an estimate for such values, and indicate which parameters need changing to improve the implosion performance. As such, different derivations can provide a range of values, depending on the approach taken and the input parameters chosen. Their inclusion is done to give the reader a basic sense for the dominant factors in an ICF implosion, and to highlight the motivation for exploring alternative concepts like shock ignition. They should not be taken as accurate methods for predicting implosion outcomes, and more detailed models or simulations must be used to complement them.

There is difficulty in balancing the high shell kinetic energies required for ignition with the necessity for low implosion velocities for stability and eventually high gain. This has pushed for the design of schemes that used a low implosion velocity and an external trigger of ignition. It has been suggested that this external trigger could come in the form of high energy particles in the form of fast ignition [80], or a well-timed strong shock wave as in the case of shock ignition. These alternatives are particularly appealing for electricity producing power plants as they offer larger gains as a greater mass of fuel can be assembled and burned

for the same laser energy.

2.2 Shock Ignition Principles

A shock ignition implosion consists of two steps, a sub-ignition implosion that allows for an assembly of the fuel that is less susceptible to hydrodynamic instability, and ignition from the launching of a strong shock as the shell is imploding. Beyond this, a wide parameter space exists where the implosion velocity and shock strength can be balanced as necessary to achieve ignition [81]. For the lowest implosion velocities, very strong shocks are needed that would require laser intensities where anomalous absorption by laser-plasma instabilities would likely dominate [82]. At the other extremity, high enough implosion velocities would self-ignite as in conventional central hot ignition and no shock would be needed but would suffer from higher degradation due to hydrodynamic instabilities. Shock ignition designs must balance between these two parameters that is both hydrodynamically robust in its implosion and that the shock strength needed can be feasibly launched without sabotaging the implosion [83].

Figure 2.1 depicts the design for shock ignition capsule and laser pulse. The design of the capsule is a scaled down version of that presented for a central hot spot design shown in Figure 1.5, for a total laser energy of 1.9 MJ down from 2.4 MJ [84]. The layers of the capsule are a 51 μm outer plastic (CH) layer, a 166 μm DT ice layer, and a central DT gas fill. Also plotted is an energy equivalent pulse that uses the conventional central hot spot approach, plotted as the dashed orange line. This is again a scaled down version of the pulse shown in Figure 1.5.

The compression of the capsule is performed during the first ~ 17.5 ns of the implosion. This is followed by a rapid rise in power at the end of the pulse to launch the ignitor shock. The laser pulse and capsule design were simulated using the 1D radiation-hydrodynamics code Hyades [38]. The results for the shock ignition design are presented in Figure 2.2.

The shock ignition pulse begins the implosion with a low 3.6 TW foot power to launch a weak shock to set the adiabat low at ~ 1 . The pulse then has a slow ramp up to peak power of 365 TW that compresses the fuel near isentropically, minimising the increase in adiabat of the fuel. The preliminary shock launched by the foot can be seen in Figure 2.2 to break out of the DT ice inner surface at ~ 10.5 ns and the shell as a whole begins to accelerate.

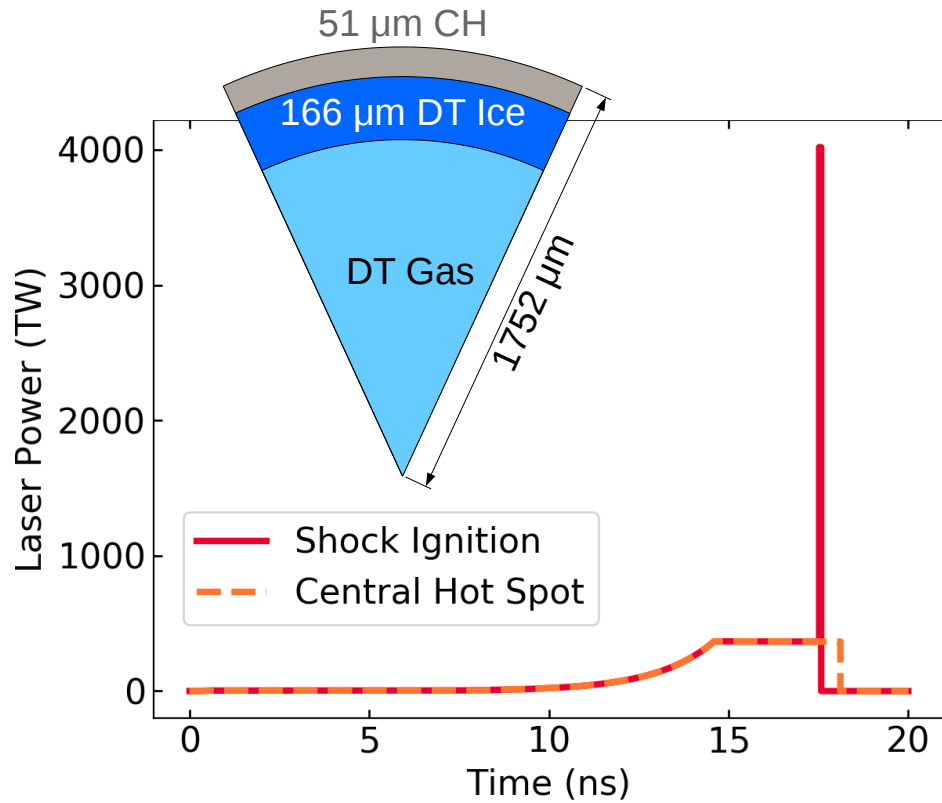


Figure 2.1: The laser power profile and capsule design for a shock ignition implosion. An energy equivalent central hot spot implosion is shown as the dashed line. Both pulses begin with a 3.6 TW foot and rise to a peak power of 365 TW. The shock ignition design spikes to 4020 TW to launch the ignitor shock, whereas the central hot spot design extends its peak power for another ~ 45 ps.

The shell is accelerated inwards by the main drive and reaches a peak velocity of ~ 315 km/s. The kinetic energy of the shell is converted into internal energy in the gas core, whose rising back pressure resists the inward motion of the shell. The initial shock rebounds off the centre and meets the imploding shell, beginning the deceleration phase.

At ~ 17.5 ns the shock ignition pulse has a sudden rise to high intensity. This results in a large increase in the ablation pressure which launches a strong shock into the imploding shell. The shock is launched late in the implosion when the capsule has converged to approximately one third of its original radius and the DT ice layer has been compressed to ~ 10 g/cm³. The ignitor shock travels through the compressed fuel and increases in strength as it converges inward. It then collides with the rebound shock near the inner surface of the shell and produces two new shocks, one travelling back out through the shell and another inwards towards the core. The inbound shock will further compress the shell, greatly raising its areal density. The increase in the piston action of the shell on the hot spot will further increase

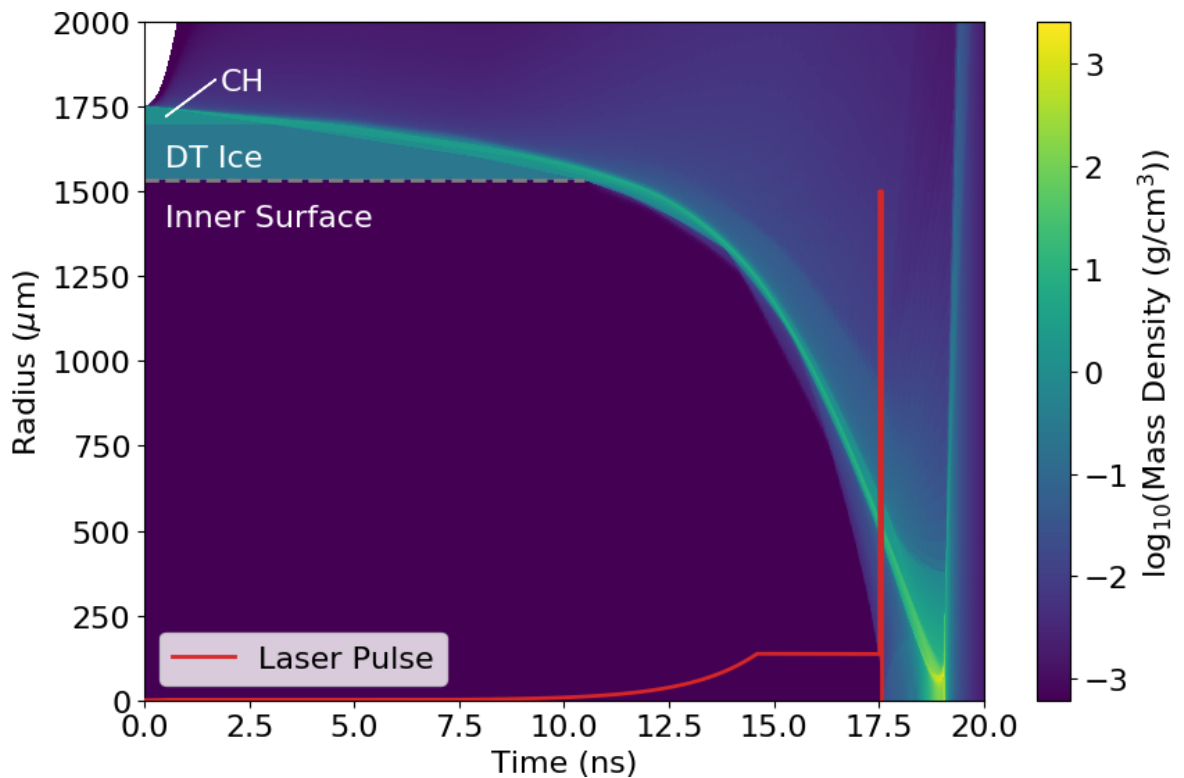


Figure 2.2: HYADES simulation of the shock ignition design given in Figure 2.1. The mass density of each Lagrangian element is plotted on a logarithmic scale with the laser power profile plotted over it. The capsule layers are highlighted at the start of the implosion.

the hot spot temperature. Once it breaks through the inner surface, it will continue to heat the core with multiple reflections off the centre and compressed fuel, triggering ignition at ~ 19 ns. A release wave quickly disassembles the compressed material and the majority of the fusion reaction occur over 200 ps after the point of ignition. A total of 195 MJ of fusion energy is released with a gain of ~ 100 .

In the central hot spot design, the energy of the spike has been redistributed to have a longer main drive and increase the kinetic energy of the shell. This increases the kinetic energy of the shell, needed as this approach relies solely on that energy to reach ignition. In the design present in Figure 2.1, the energy is too low and produces a core that was too cold to produce the necessary alpha particles to start the fuel burning. The capsule marginally fails to ignite, producing only 0.9 MJ of fusion energy. Higher implosion velocities would be needed to reach the threshold for ignition.

The difference in the hot spot and fuel configurations between the central hot spot and shock ignition designs are shown in Figure 2.3. The ion temperature and mass density are plotted for both designs, with the hot spot and fuel regions visible. The shock ignition design

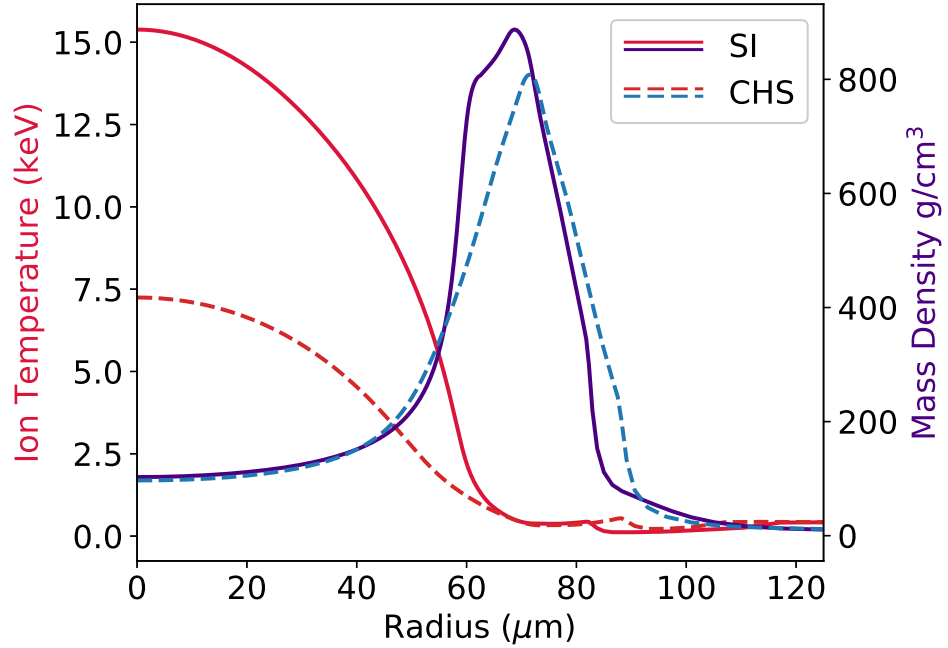


Figure 2.3: Temperature and density profiles for the hot spot and compressed fuel from shock ignition (solid lines) and central hot spot (dashed lines) approaches. The region of high temperature and low density ($\lesssim 60 \mu\text{m}$) is the central hot spot which is surrounded by the low temperature and high density fuel ($\sim 60\text{-}90 \mu\text{m}$).

produces a hot spot with approximately double the ion temperature than the central hot spot design and a fuel density that is $\sim 10\%$ higher. The higher temperature and density results in the shock ignition design igniting and burning more efficiently than the central hot spot. Equation 2.2 predicts that higher gains can be achieved for larger fuel areal densities.

In these 1D simulations, no degradation mechanisms have been included that might reduce the performance of the implosion. Hydrodynamic instabilities are one such degradation mechanism that is particularly detrimental to high velocity implosions. The central hot spot design had a peak implosion velocity of $\sim 345 \text{ km/s}$ resulting in higher susceptibility to instabilities. The benefit of the shock ignition implosion is not only that it is able to ignite at a lower laser energy but that it is imploded on a lower velocity of $\sim 315 \text{ km/s}$ where it is less susceptible to these instabilities.

The simulation of the shock launching by the radiation-hydrodynamics code does not include important physics effects that are known to impact the laser absorption and energy conduction. These include scattering from laser-plasma instabilities, hot electron generation and propagation, and non-local transport. It is nonetheless instructive to perform simulations of this kind to infer the strength of the shock needed to achieve ignition. Experiments must

then follow this to explore the coupling of the spike to capsule, and the shock strengths that can be produced.

2.3 Ignitor Shock Launching

The ignitor shock must meet two key criteria if it is to enable ignition of the fuel; it must be launched with a large enough ablation pressure, thought to be in the range 200-300 MBar [85], and it must be timed correctly with respect to the return shock from the main drive. The high pressure is necessary for the shock to be able to provide the hot spot with the internal energy increase needed to trigger ignition. A shock that is not of sufficient strength will not apply enough pressure on the hot spot and the implosion will fail no matter when it is launched. The shock can only aid in ignition though if it is timed correctly as both early and late shock launches will not provide the increase in internal energy at a time when it can push the hot spot above the threshold for ignition. This creates an ignition window over which the shock can be launched in order for collision and breakout to coincide with the timing of optimal hot spot conditions. A large simulated ignition window is beneficial for real world implosions as it provides a greater margin to account for unforeseen effects. Many features of the implosion will impact the timing and width of the ignition including the shell density profile, in-flight aspect ratio, laser-plasma instability generated hot electrons, laser absorption efficiency, and many more, all of which need to be accounted for within the implosion design.

Implosions where the shock is launched outside the ignition window will fail to ignite, placing importance on accurately determining where this window is and designing the implosion such that it is as wide as possible. This necessitates an understanding of the shock launching and transport physics, including the laser-plasma instabilities, and subsequent hot electron generation and propagation. Figure 2.4 shows the capsule gain against the shock timing for a shock ignition design [86] that was produced for the proposed HiPER facility [87]. The ignition window is defined as the time interval where the gain is above 80% of the theoretical maximum, shown between the vertical dashed black lines. The gain rapidly falls off outside this region.

The strong dependence that gain has on the shock timing is because of the importance of the location within the imploding shell where the spike launched shock collides with the

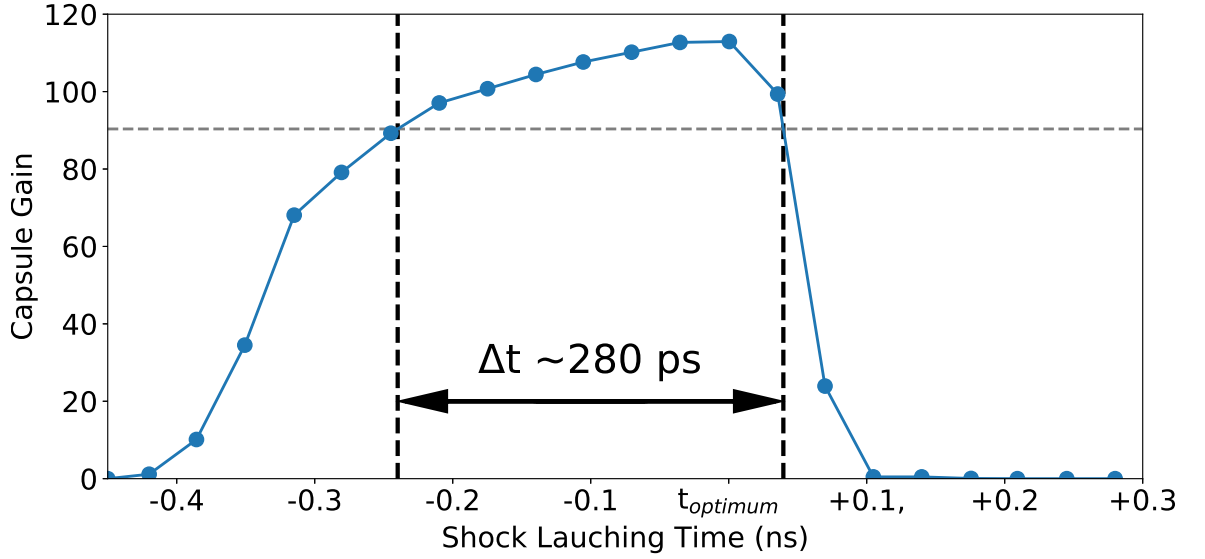


Figure 2.4: Ignition window for the HiPER baseline shock ignition design. The capsule energy gain against the time the ignitor shock is launched relative to the simulated optimum time, $t_{optimum}$. The horizontal dashed grey line is the gain for 80% of the theoretical maximum. The ignition window is defined by this threshold and is plotted with the two vertical dashed black lines, with a width of ~ 280 ps. Sharp ignition cliffs exist at the boundaries of this window where the capsule gain quickly falls to zero. Image reproduced with data from [86].

return shock. It is necessary that this collision occurs within the precompressed fuel and will result in two new counter-propagating shocks, one travelling inwards toward the core and another propagating outwards. The resulting shock travelling to the centre will increase in strength as it converges inward, raising the areal density of the fuel and applying pressure on the hot spot. This shock must have enough mass ahead of it to travel through and compress as it is this mass whose piston action is needed to maintain a high pressure on the hot spot. This then necessitates that the collision must occur sufficiently far from the inner surface of the fuel layer.

The shock collision however cannot occur arbitrarily far out as the effect of the outbound shock places an upper limit on the location. The break out of the outbound shock from the outer surface of the shell will initiate a release wave back through the fuel that decompresses it and begins the disassembly process. If ignition has not occurred before this disassembly then the fuel will not have a high enough areal density to sustain a burn wave and no gain can occur. There is a region for the shock collision close enough to the inner surface which will result in ignition before disassembly but far enough out that the required hot spot pressure is reached. This spatial restriction is then effectively a temporal restriction that results in

the ignition window.

The shock itself is launched by an increase in the ablation pressure P_{abl} over a short timescale t , given by a large $\Delta P_{\text{abl}}/\Delta t$. Laser ablation pressure arises from energy deposition occurring near the critical surface via inverse bremsstrahlung into the thermal electrons. These electrons then conduct the deposited energy to the ablation front. This increase of energy reaching the ablation surface raises the mass ablation rate and increases the applied pressure. The laser ablation pressure scales with $P_{\text{abl}} \sim (I_L/\lambda_L)^{2/3}$ [10] where I_L is the change in laser intensity and λ_L is the laser wavelength. Therefore, the shock launching requirement then becomes a large $\Delta I_L/\Delta t$ for a constant wavelength and demonstrates the necessity for the high intensity spike.

In order for the laser energy to reach the high densities near the critical surface where inverse bremsstrahlung is more efficient, the high intensity spike must travel through an extended ablation plasma corona created by the lasers driving the compression phase of the implosion. The plasma corona will have a high electron temperature of $T_e \sim 5$ keV and a long density scale length of $L_n \sim 500 \mu\text{m}$ [88], defined as $L_n = (\frac{1}{n} \frac{dn}{dx})^{-1}$. This combination of high laser intensities and plasma conditions enters a regime where it is believed there will be strong laser absorption and scattering by parametric instabilities [89].

2.3.1 Hot Electron Influence

Laser-plasma parametric instabilities can couple energy from the laser into electron plasma waves through the stimulated Raman scattering [90,91] (SRS) and two plasmon decay [92] (TPD) instabilities. The electron plasma waves have strong associated electric fields that can accelerate electron to supra-thermal energies, creating so-called hot electrons. These hot electrons have long mean free paths and can travel to the ablation front and beyond. This enables them to have a potentially beneficial effect of aiding in driving of the shock or impact the performance negatively by preheating the fuel which limits compression. At the point of shock launching, a considerable areal density of shell material will have been assembled that may have a strong stopping power for electrons. If they deposit their energy within this compressed material then it might increase the ablation rate as before and raising the pressure.

The penetration depth of electrons increases with their energy, where higher energy electrons can penetrate through larger areal densities. For an electron population with a

broadband energy spectrum this will result in energy deposition over a larger spatial region than for a spectrally narrow population, potentially resulting in a pressure wave that does not produce a shock, while also heating and limiting the compression of the fuel. To aid in shock generation, a population of hot electrons must be low enough in energy that their mean paths are small compared with the stopping power of the dense shell. This will prohibit them from penetrating through the dense material where they might preheat the colder fuel and limit the final compression. High levels of preheating can cause failure to ignite, typically caused by electron with energies $\gtrsim 100$ keV [93]. The broadband distribution and \sim keV temperatures of laser-plasma instability produced electrons means that there will inevitably be a finite number of electrons with energies above this value. High temperature distribution will have a higher fraction within this higher energy tail, leading to greater preheat.

2.3.2 Implosion Simulations Incorporating Hot Electrons

Laser-plasma instability driven hot electrons have the potential to aid in the launching of strong shocks but can also be detrimental to ignition overall by preheating the fuel. The influence of the hot electrons depends largely on their energy distribution and the areal density profile at the point of the shock launch. This impact on an implosion must be assessed with experiments backed by simulations that integrate hot electron production and propagation, in order to produce laser profiles and capsule designs that can either exploit their benefit or be robust against their detriment.

Radiation-hydrodynamics simulations are used to simulate the deposition of laser energy within the target, and the subsequent evolution of the implosion. Added to these simulations can be the conversion of laser energy into hot electrons during the high intensity spike, which can then go on to deposit energy within the capsule. Simulations performed by Fox *et al.* [94] suggested that large pressures could be achieved from hot electron driven ablation, provided they had low < 30 keV temperatures and high conversion efficiencies of $\sim 20\%$ of the laser energy into hot electrons. Similar results were seen by Shang *et al.* [95] that suggest high gains of ~ 100 might be reached for large conversion efficiencies of $> 20\%$. It was also seen that driving the ignitor shock with electrons would provide robustness against multimode hydrodynamic asymmetries. Colaïtis *et al.* [93] also saw increases in shock strength from hot electrons that was determined to be primarily from the low energy region of the electron distribution. However, the capsules failed to ignite due to preheating from the higher > 100

keV energy electrons.

Preheating of the cold fuel by high energy electrons before the fuel has reached peak compression can lead to reduced gains or failure to ignite. Design changes have been proposed to help mitigate the preheating, typically by increasing the areal density of the capsule at the point of the high intensity spike. Colaïtis *et al.* [93] proposed including a CH ablator layer that could limit the penetration of the hot electrons and shield the DT fuel. In shielding the fuel however, they found that any previous benefit the hot electrons gave to the shock strength was lost. Nicolaï *et al.* [96] determined that it was the >100 keV electron that caused the most detrimental preheat. They suggested that the capsule shell could contain a greater initial mass to increase the overall stopping power, or timing the shock later so that more areal density could be built up before the hot electrons are generated.

The hot electrons will have a great influence on a shock ignition implosion, with the magnitude of the benefit or detriment still undetermined. The need for a characterisation of the hot electrons is apparent, as the designing of ignition capable implosions cannot progress without an accurate knowledge of what electrons will be generated in the high intensity spike interaction.

2.4 Propagation of Waves in Plasmas

2.4.1 Fundamental Plasma Parameters

A plasma is a quasi-neutral collection of freely moving charged particles, ions and electrons, that can exhibit collective motion. Quasi-neutrality dictates that the collective charge of the plasma as a whole is balanced but that localised collections can emerge where the charge is imbalanced. A defining characteristic of plasma is its ability to sustain collective behaviour of particles over large distances. Perturbations in the densities of the constituent species will lead to waves that can flow through the plasma due to the long range inter-particle forces.

An initial perturbation in electron density will create a charge imbalance and an electric field that the electrons and ions will act to neutralise. The particles will respond to the force from this field and, if undamped, will collectively oscillate about the perturbation. This simple harmonic motion will have a frequency given by [37],

$$\omega_p = \sqrt{\frac{ne^2}{\epsilon_0 m}} \quad (2.4)$$

where n is the number density of the species and m is the particle rest mass. The terms ω_{pe} and ω_{pi} are used to denote the electron and ion plasma frequencies respectively. The $\sqrt{1/m}$ dependence of the plasma frequency reflects the different timescales ($\tau = 2\pi/\omega_p$) over which the electrons and ion react. The large inertia of the more massive ions resulting in less responsive motion and longer timescales, while the lighter electrons respond far quicker.

Thermal populations of electrons and ions can be characterised by a Maxwell-Boltzmann energy distribution and an associated temperature T , given by equation 1.4. The mean velocity of a particle of mass m in one direction, called the thermal velocity, is given by the following equation,

$$v_{th} = \sqrt{2k_B T/m} \quad (2.5)$$

For electrons and ion in thermal equilibrium such that $T_i = T_e$, the electron thermal velocity will be larger than that of the ions by a factor of $\sqrt{m_i/m_e} \simeq 68$ for a DT plasma. Electrons in an ablation plasma with a 4 keV temperature, inferred from simulations presented in Figure 2.2, will have a thermal velocity of $\sim 37,000$ km/s, while the deuterium and tritium ions of the same temperature will have thermal velocities of ~ 620 and ~ 505 km/s respectively. The simulations suggest that the ions have a lower temperature of 1.5 keV, reducing their thermal velocities by $\sim 40\%$.

The neutralisation of charge imbalance within a plasma by the free moving charged particles is imperfect due to their non-zero temperature. The scale length over which the plasma is able to screen or shield an electric potential is known as the Debye length and is given by the following equation,

$$\lambda_D = \sqrt{\frac{\epsilon_0 k_B T_e}{e^2 n_e}} \quad (2.6)$$

where T_e is the electron plasma temperature and n_e is the electron density. This equation assumes that the plasma fulfils the quasi-neutrality requirement and that the ion temperatures are small compared with the electron temperature. Interactions that occur on a smaller spatial extent than the Debye length are considered thermal collisions and longer interactions are considered to be collective. Again taking the ablation plasma conditions from the simulations shown in Figure 2.2, the Debye length would be ~ 15 nm.

2.4.2 Electromagnetic Waves

The dispersion equation for an electromagnetic wave (EMW), e.g. laser light, with angular frequency ω_{EMW} and wavenumber k_{EMW} is given by the following equation [37],

$$\omega_{\text{EMW}}^2 = \omega_{\text{pe}}^2 + c^2 k_{\text{EMW}}^2 \quad (2.7)$$

It can be seen from this equation that an EMW can only propagate in a plasma up to the point where its frequency is equal to the local electron plasma frequency, beyond which its wavenumber becomes imaginary, the oscillation is no longer sustained and the wave decays. This requirement on frequency can readily be expressed as a density restriction by rearranging equation 2.4, where the laser light can only reach a maximum critical density given by the following equation,

$$n_c = \frac{\epsilon_0 m_e \omega_L^2}{e^2} \quad (2.8)$$

$$\approx \frac{10^{21}}{\lambda_L^2 [\mu\text{m}]} [\text{cm}^{-3}] \quad (2.9)$$

where ω_L and λ_L are the angular frequency and wavelength of the laser light respectively. For obliquely incident light at an angle θ to the surface normal, reflection occurs at lower densities, given by $n_{\text{ref}} = n_c \cos^2 \theta$ due to the density dependent refractive index of the plasma.

2.4.3 Electron Plasma Waves

Electron plasma waves (EPW) are high frequency fluctuations of the electron density, where the large thermal speeds of the electrons results in waves effectively responding to a static ion background. The dispersion relation for electron plasma wave of frequency ω_{EPW} is

$$\omega_{\text{EPW}}^2 = \omega_{\text{pe}}^2 + 3k_{\text{EMW}}^2 v_{\text{Te}}^2 \quad (2.10)$$

where k_{EMW} is the wavenumber of the electron plasma wave. The final term in this equation is a correction due to the non-zero temperature of the electron. Since the phase velocity of an EPW scales with its frequency, $v_{\phi, \text{EPW}} = \omega_{\text{EPW}}/k_{\text{EPW}}$, it can be of a similar magnitude to the speeds of the thermal electrons, allowing them to efficiently exchange energy.

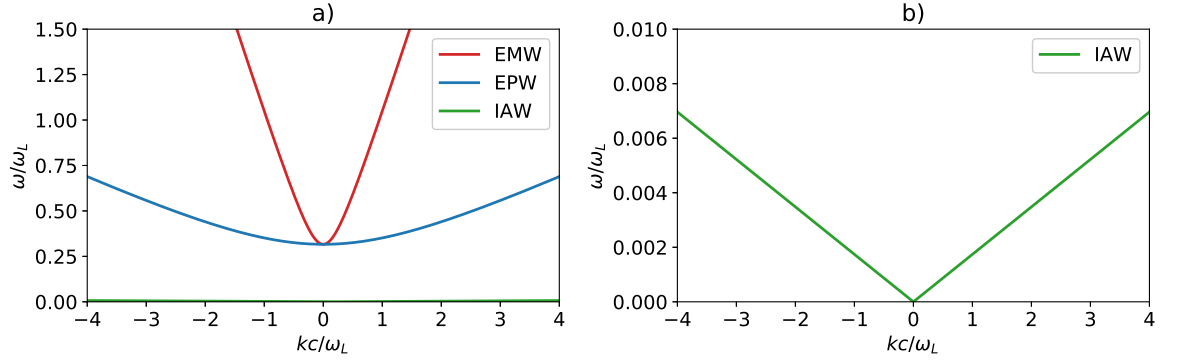


Figure 2.5: Dispersion relations for waves in plasmas, graph a) is rescaled in b) with a resolved y-axis. The red line shows electromagnetic waves (EMW), the blue line shows electron plasma waves (EPW), and green for ion acoustic waves (IAW). All relations have been normalised to the angular frequency of laser light (ω_L) of wavelength 351 nm in a vacuum. The plasma parameters are taken from the SI implosion give above at the time the of the laser power spike, described by $n_e = 0.1n_c$, $A=13/2$, $Z=7/2$, $T_e = 4.0$ keV, $T_i = 1.5$ keV.

2.4.4 Ion Acoustic Waves

In contrast to EPWs, ion acoustic waves (IAW) are low frequency perturbations in the ion density and are analogous to sound waves. The dispersion relation for IAW is given by the following equation [37],

$$\omega_{\text{IAW}} = c_s |k_{\text{IAW}}| \quad (2.11)$$

$$c_s = \sqrt{\frac{Zk_B T_e + 3k_B T_i}{m_i}} \quad (2.12)$$

where c_s is the IAW velocity (sound speed), T_i and T_e are the ion and electron temperatures respectively, and Z is the average nuclear charge. This equation assumes that $T_i \ll T_e$ which is typically satisfied for ICF ablation plasmas. Damping can occur due to collisions between the electrons and ions that suppressed IAW growth.

The dispersion relations for electromagnetic waves, electron plasma waves, and ion acoustic waves are plotted in Figure 2.5. The lines represent the characteristics of waves that could grow in the plasma if undamped. The low frequency IAW only appear at the very bottom of plot Figure 2.5a) and so the axis is rescaled to show their dispersion relation shown in Figure 2.5b).

2.4.5 Wave Damping

Wave damping mechanisms will limit the growth of plasma waves such that they cannot be amplified indefinitely. The first mechanism arises from collisions of the particles that are carrying the wave. For electron plasma waves this is the collision of an electron with a background ion which disrupts the coherent motion of the wave. The collisions themselves are stochastic and will result in an isotropic velocity distribution for the colliding particles. The wave carrying particles are then no longer moving collectively and the wave is damped. The collisional damping rate for an EPW is given by the following equation [97]

$$\gamma_{\text{coll}} = \frac{\pi n_e e^4 \ln \Lambda}{m_e^2 v_{\text{th},e}^3} \quad (2.13)$$

where $\ln \Lambda$ is the Coulomb logarithm and is dependent on the electron density and temperature. It can be seen from equation 2.13 that the damping rate increases with electron density and decreases with temperature, noting $v_{\text{th},e} \propto T^{1/2}$. This results in low damping rates for EPWs travelling in the plasma corona since the collisional frequency is low because of the high temperature and low density. Damping becomes much more prominent as the waves travel up the density gradient and towards lower temperature plasma where the growth of waves can be highly suppressed.

Landau damping is a form of collisionless wave damping that arises from the resonant transfer of energy from the plasma waves to a section of the thermal electron distribution [98]. Particles whose velocity is similar to the phase velocity of the wave will experience a quasi-constant electric field and are able to transfer energy either to or from the wave. Electrons with slightly greater velocity than the phase velocity will transfer energy to the wave, and those with slightly less will gain energy from it. For a flat velocity distribution function, this results in no net transfer of energy. However, thermal electron energies can typically be well described by a Maxwell-Boltzmann energy distribution where the number of electrons with progressively higher energies decreases. This results in more electrons having velocities slightly less than the phase velocity of the EPW than those with slightly more, allowing a greater amount of energy to be transferred from the wave to the electrons than from the electrons back, damping the waves as a whole. For an electron plasma wave of $\omega_{\text{EPW}} \simeq \omega_{\text{pe}}$

the damping rate normalised to the wave frequency is given by the following equation [37],

$$\frac{\gamma}{\omega} = \sqrt{\frac{\pi}{8}} \frac{v_{\varphi}^3}{v_{\text{th},e}^3} \exp\left(-\frac{v_{\varphi}^2}{2v_{\text{th},e}^2}\right) \quad (2.14)$$

For higher electron plasma temperatures and waves with lower phase velocities, the exponential term will dominate and there will be greater Landau damping. This is due to both of these features increasing the number of resonant electrons that the wave can exchange energy with, thereby increasing the damping. The damping rate will suppress the waves entirely for large values of $\frac{v_{\varphi}^2}{2v_{\text{th},e}^2} = \omega_{\text{EPW}}^2/2k^2v_{\text{th},e}^2$. This is commonly expressed as $\omega_{\text{EPW}}/k < 3v_{\text{th},e}$ or $k\lambda_D > 0.3$.

2.4.6 Wave Breaking

In a weak damping regime, the amplitude of electron plasma waves is able to grow and develop strong electric fields. Wave breaking is a non-linear damping mechanism that accelerates thermal electrons to high energy, producing hot electrons. The process is similar to Landau damping where there is resonant exchange of energy between the wave and the background electrons. For wave breaking however, the electrons that exchange energy are cold and not initially resonant. The strong electric fields of the waves are large enough that the oscillation speed of electrons in the field of the wave, $v_{\text{osc}} = eE/m_e\omega_{\text{EPW}}$, can become comparable with the phase velocity of the wave. Many of these electrons become trapped and a fast resonant transfer of energy from the wave to the electrons occurs, accelerating electrons to high velocities. The EPW will lose much of its energy and the wave is said to break. It is this mechanism through which electron plasma waves can produce hot electrons that are so significant to ICF implosions. The two key parametric instabilities that drive EPWs are discussed in the next sections.

2.5 Parametric Instabilities

Collective absorption of light can drive plasma waves that, through damping, will lead to high energy non-thermal populations of electrons. They also deplete the laser light through absorption and scattering such that less energy reaches the higher electron densities where inverse bremsstrahlung is more efficient. The threshold for collective absorption to occur is strongly linked to the intensity and wavelength of the laser, where greater values of $I_L\lambda_L^2$

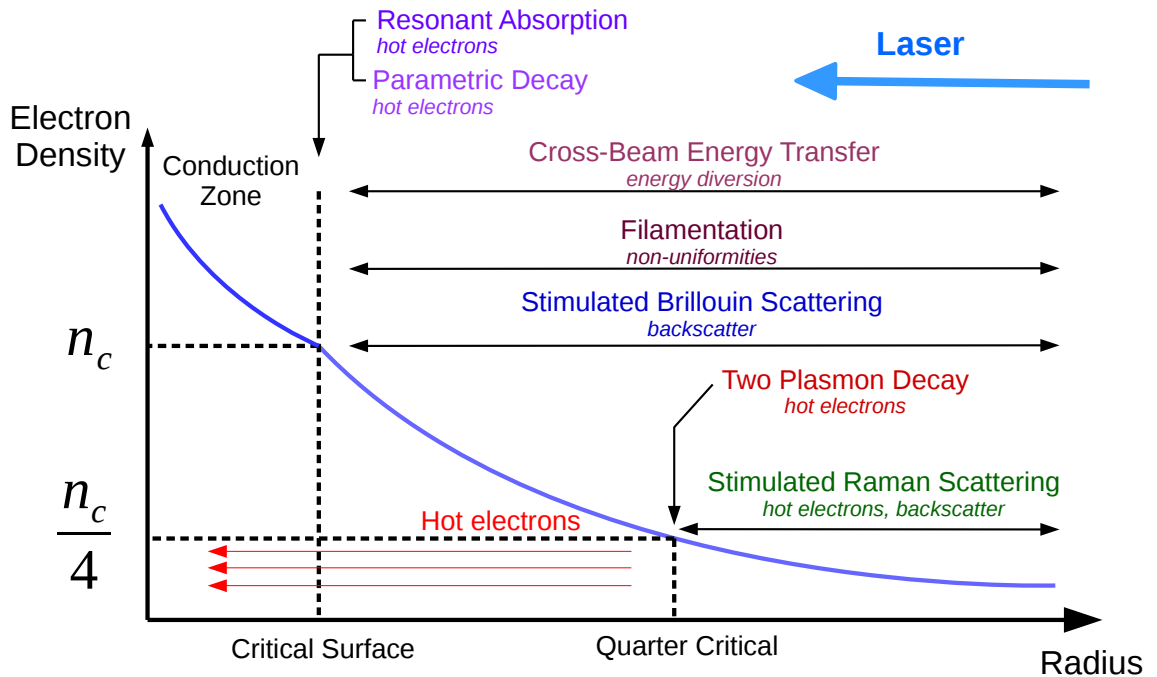


Figure 2.6: Laser-plasma parametric instabilities, the location they occur, and their main source of degradation. The key mechanisms for transporting energy to the ablation front are laser energy deposition via inverse bremsstrahlung, which can occur up to the critical surface, and conduction of that energy by thermal electrons, both of which are not depicted here. Image inspired by [99].

lead to a large prevalence of parametric instabilities [37]. This in part motivated moving to the shortest wavelength of light that is practical to drive the implosions, which meant using Nd:glass lasers and frequency tripling the light. Figure 2.6 depicts the main parametric instabilities that affect direct drive ICF, their locations of occurrence, and their main detriment to the implosion.

The two instabilities of stimulated Raman scattering (SRS) and two plasmon decay (TPD) are of particular importance as they drive electron plasma wave that are capable of generating high energy electrons through wave breaking. These electrons have large penetration depths and cause detrimental preheat, discussed in Section 2.3.1. Both mechanisms are three-wave instabilities where the incident laser light (electromagnetic wave) decays into two further waves. In the case of SRS this is an electron plasma wave and another EMW, while for TPD this is two EPWs. All decays must conserve both energy and momentum in three dimensions. This results in frequency and wavenumber matching conditions for each.

The remaining instabilities are explained briefly, further information can be found in

the references given. Resonant absorption [100, 101] occurs when obliquely incident light produces large electric fields at the critical density. Light that is p-polarised will have a component of its electric field in the same plane as the density gradient which, at the point of reflection, will lead to a resonant excitement of an EPW at the critical surface. Parametric decay [102] is the decay of an EMW into an EPW and an IAW. The energy and momentum balancing of this decay can only occur near the critical surface where most of the energy is transferred into the EPW. Filamentation [103–105] is the self-focusing of the laser seeded by the spatial inhomogeneity of the laser profile due to changes in the refractive index caused by the laser intensity profile. Stimulated Brillouin Scattering [106–108] is the coupling of an EMW to IAW and a backscattered EPW, similar to SRS discussed later.

2.5.1 Stimulated Raman Scattering

Stimulated Raman scattering (SRS) is the three wave decay of an incident electromagnetic wave into an electron plasma wave and a scattered electromagnetic wave. Laser light scatters off fluctuations in the electron density in the plasma and this scattered light then beats with the incident laser light. This beating of light drives a density modulation through the ponderomotive force. An instability can grow if this modulation is coherent with the initial fluctuation, leading to the amplification of the both density fluctuation and the scattered wave. This requires the satisfying of energy and momentum conservation, given by the following wave matching conditions [109],

$$\omega_L = \omega_{\text{EMW}} + \omega_{\text{EPW}} \quad (2.15)$$

$$\vec{k}_L = \vec{k}_{\text{EMW}} + \vec{k}_{\text{EPW}} \quad (2.16)$$

Neglecting thermal effects, the EPW will have a frequency equal to the electron plasma frequency. The scattered EMW will then have a frequency of $\omega_{\text{EMW}} \simeq \omega_L - \omega_{\text{pe}}$. This scattered wave can only propagate within the plasma if its frequency is greater than the local electron plasma frequency, that is to say that it is below its own critical density. Therefore, in order to satisfy both the wave matching condition and this EMW propagation restriction, the instability can only occur where $\omega_L > 2\omega_{\text{pe}}$ which corresponds to a density of $n_e < n_c/4$, known as the quarter critical density. Here n_c is the critical density of the incident laser light.

The amplitude of the instability can grow in space as the wave travels up the density gradient [110] referred to as convective SRS. As it approaches the quarter critical density, the wavenumber falls to zero and instability becomes stationary and growing only in time, called absolute SRS.

Threshold intensities exist [90,91] that must be exceeded by the laser intensity in order to stimulate SRS. For absolute SRS, this is given by the following equation,

$$I_{\text{abs, th}} = \frac{99.5}{L_{n_c/4}^{4/3} \lambda_L^{2/3}} \times 10^{15} \text{ W/cm}^2 \quad (2.17)$$

where $L_{n_c/4}$ is the density scale length at quarter critical density given in microns and λ_L is the wavelength of the laser also in microns.

The threshold intensity for backscattered convective SRS for a linear density profile with is given by the following equation [111],

$$I_{\text{conv, th}} = \frac{400}{L_{n_c/4} \lambda_L} \times 10^{15} \text{ W/cm}^2 \quad (2.18)$$

For a density length scale of 500 μm and a laser of wavelength 0.351 μm , the threshold intensities are 0.05 and $2.28 \times 10^{15} \text{ W/cm}^2$ for absolute and convective SRS respectively. These threshold equations imply that both absolute and convective SRS are more readily excited with longer density scale length plasmas and with lasers of larger wavelengths.

2.5.2 Two Plasmon Decay

Two plasmon decay (TPD) is another three wave mechanism where the incident laser EMW decays into two EPWs. The wave matching conditions are

$$\omega_L = \omega_{\text{EPW},1} + \omega_{\text{EPW},2} \quad (2.19)$$

$$\vec{k}_L = \vec{k}_{\text{EPW},1} + \vec{k}_{\text{EPW},2} \quad (2.20)$$

From this, a similar restriction can be found for the instability by noting that the decay plasma waves will have frequencies $\omega_{\text{EPW},1} \simeq \omega_{\text{EPW},2} \simeq \omega_L/2$. This will limit the TPD instability to the quarter critical density.

The wave matching conditions for SRS and TPD are visualised in Figure 2.7. Figure 2.7a) shows a pump wave in purple decaying via SRS into the two green waves, an EPW moving

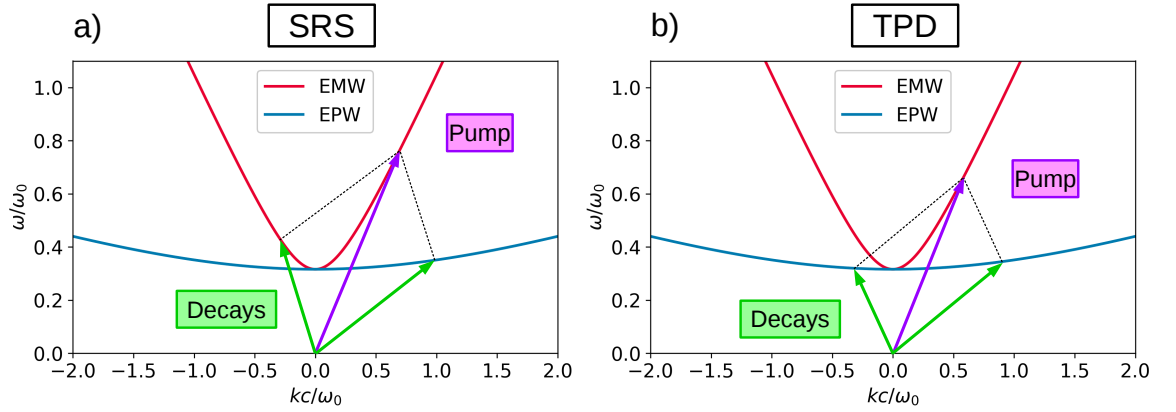


Figure 2.7: Decay of an incident pump electromagnetic wave into two further waves by a) SRS and b) TPD. The red and blue curves are the dispersion relations for electromagnetic waves and electron plasma waves respectively (see Figure 2.5). The connection of the waves by the dotted lines forms a parallelogram due to the energy and momentum matching conditions.

in the positive direction and a backscattered EMW. Figure 2.7b) shows TPD decay into forwardscattered and backscattered EPWs. The dotted lines are included to highlight the parallelograms that are formed from the matching conditions.

The TPD threshold intensity [92] is given by the following equations,

$$I_{\text{th}} = 8.19 \frac{T_{e,n_c/4}}{L_{n_c/4} \lambda_L} \times 10^{15} \text{ W/cm}^2 \quad (2.21)$$

where $T_{e,n_c/4}$ is the electron temperature at quarter critical density in keV. Similar to the SRS threshold, the TPD threshold is lower for longer density scale lengths but it also scales with the electron temperature.

The TPD threshold intensity is smaller than that for convective SRS by ~ 1 -2 orders of magnitude for most ablation plasmas, meaning that TPD is more readily stimulated than convective SRS. Increasing the density length scale to the point where the convective SRS intensity threshold is exceeded by the laser will result in the growth of that instability which pump depletes the laser and can reduce TPD.

The inclusion of the electron temperature and smaller dependence of the TPD threshold on density scale length compared with absolute SRS results in TPD dominating in Omega-like implosions and SRS dominating for those on NIF [88]. This is due to the smaller radius capsules on Omega producing colder ablation plasmas with shorter density length scales than the larger capsules used on NIF.

2.5.3 Cross-Beam Energy Transfer

Stimulated Brillouin scattering is another instability leading to the scattering of the incident laser energy. The wave matching conditions for SBS are similar to those for SRS where an ion-acoustic wave is driven in place of an electron plasma wave. As with SRS, it typically grows from thermal noise. Cross-beam energy transfer [112,113] (CBET) is a form of induced SBS where the instability grows from the beating of two laser beams crossing in a flowing plasma, of velocity v_{flow} . The interference pattern generates a beat wave which imprints a density fluctuation, becoming resonant if it verifies the IAW dispersion relation $|w_0 - w_1| = |k_0 - k_1|c_s + (k_0 - k_1)v_{\text{flow}}$ [111]. External to a flowing plasma, both beams share the same frequency so the coupling becomes resonant when the plasma expansion is flowing at the ion acoustic speed. The flow direction imposes the direction of the energy transfer.

In ICF experiments, laser light can be deflected away from the capsule and cross the path of an oncoming beam through either refraction, or from the capsule converging in size to smaller than the focal spot of the laser. In these conditions, the intersecting beams efficiently transfer energy from the inward travelling beam to the outward, and can exacerbate the drive asymmetry or reduce the laser energy that reaches the target. Chapter 5 describes an implosion experiment where the measured capsule trajectory is compared with simulation to tune a drive multiplier to account for laser power losses, primarily due to the CBET instability.

2.6 Simulating Laser-Plasma Instabilities

Particle-in-cell (PIC) codes [114] are used to investigate laser-plasma instabilities by simulating the motion of particles and the electron-magnetic fields present on an Eulerian grid. Two-dimensional PIC simulations of the plasma conditions from a shock ignition relevant experiment on Omega [115] were carried out and reported by Yan *et al.* [116]. These implosions had lower electron temperatures of $T_e = 1.6$ keV and shorter density length scales of $L_n = 170$ μm than what would be expected for an ignition scale shock ignition coronal plasma. The dominant parametric instability absorption was absolute SRS that generated 30 keV electrons, which the authors note were not accurately fitted with a 3D Maxwell-Boltzmann energy distribution function.

Plasma conditions relevant for NIF scale shock ignition were simulated in 2D without

collisions by Seaton and Arber [117]. Up to $\sim 90\%$ of the energy is either absorbed or scattered by laser-plasma instabilities, with 25% going to the TPD instability and 47% to SRS. Due to the lack of collisions, there is no inverse bremsstrahlung within these simulations. The time-integrated SRS spectrum was found to be mainly convective, with absorption occurring at density below the quarter critical. The absolute SRS instability is largely suppressed by the strong pump depletion of the laser before it reaches quarter critical. These LPI were not collisionally damped and so might represent an over-estimation of their prevalence. The hot electrons produced had a low temperature of 20-30 keV but may present a risk of preheat because of the high fraction of laser energy that was diverted to them.

2.7 Hot Electron Characterisation Experiments

A non-exhaustive overview of hot electron characterisation experiments that are relevant to shock ignition are presented. The main diagnostics used to find the hot electron temperature and energy are highlighted. These diagnostics will be the subject of discussion in Section 3.5.4 where the ability to directly compare the results is called into question due to their disagreement in parameter predictions for the same hot electron source.

A shock ignition like concept was tested on the Omega-60 laser facility by Theobald *et al.* [115]. Due to the limited total energy that can be delivered by each beam, the 40+20 scheme was devised where 40 beams would drive the compression of the capsule and the remaining 20 would be more tightly focused to launch an augmenting shock near the end of the compression. The strong shock launching beams had an intensity of 1.5×10^{15} W/cm² and were not equipped with smoothing by spectral dispersion or SSD, a beam smoothing technique thought to reduce laser-plasma instabilities [118] outlined in Section 3.2.2. Hot electrons were diagnosed with the Hard X-Ray Detector [119] (HXRD), outlined in Section 3.5.2, and were found to be ~ 40 keV. A backscatter diagnostic was used to identify the laser-plasma instabilities as arising from both SRS and TPD, with low signal intensities from both potentially indicating that the total energy of the hot electron population was low.

Spherical strong shock experiments were conducted again on Omega [120, 121], with peak intensities of up to 6×10^{15} W/cm². Hot electron temperatures were measured with the Hard X-ray Image Plate [122], outlined in Section 3.5.1, and Bremsstrahlung MeV X-ray Spectrometer [123] diagnostics. The average temperature between the two diagnostics was

~ 75 keV, with little dependence on intensity. However, the diagnostics reported inconsistent temperatures, differing by up to a factor of 2 which suggests large uncertainty in these results. The conversion efficiency when using SSD was $\sim 2.5\%$ which increased up to $\sim 8\%$ when it was switched off. The backscatter data showed both SRS and TPD signatures, with the intensity of the SRS feature increasing in emission by a factor of 5 when SSD was switched off.

Planar target experiments performed by Hohenberger *et al.* [124] on Omega found a strong dependence of hot electron temperatures on incident laser intensities, reaching 70 keV for a maximum intensity of 1.4×10^{15} W/cm². Conversion efficiencies of 1.8% were inferred from Molybdenum K_α measurements. The backscattered data indicated a TPD dominated system that the authors attributed to the multiple overlapping beams being able to drive common plasma waves.

A similar experiment to the spherical strong shock experiment was carried out by Theobald *et al.* [125] to investigate the effect of ablator material on hot electron production for intensities of 5×10^{15} W/cm². The plasma conditions at the point of the shock launch were found from radiation-hydrodynamics simulations to be an electron plasma temperature $T_e = 3.6$ keV and a density scale length at quarter critical $L_{nc/4} = 125$ μm . Hot electron temperatures of 60-80 keV were seen that were independent of both ablator material and the use of SSD. Conversely, the use of SSD strongly suppressed the SRS backscatter signal and decreased the conversion efficiency by up to a factor of 3, down to $\sim 3\%$.

Another set 40+20 configuration implosions were performed by Trela *et al.* [126] where the influence of the hot electrons on the implosion was controlled via the timing of the shock launch. Hot electron characterisation was performed with HXRD diagnostic that had been absolutely calibrated to provide total hot electron energy. Temperatures of ~ 38 keV were found, with conversion efficiencies of 1-2%. It was found that an early timed shock launch significantly degraded the areal density of the shell that was attributed to hot electron preheat. This degradation was minimised by timing the shock later as greater areal density had been built up with a greater hot electron stopping power.

A planar experiment was carried out by Zhang *et al.* [127] where the target was first illuminated by a set of low intensity beams to produce an ablation plasma and then a second set of high intensity beams to emulate the spike. Long density scale lengths of ~ 330 μm were achieved, with a plasma temperature of 1.8 keV, lower than is expected for SI. When

using a UV intensity of 10×10^{15} W/cm², modest electron temperatures of 27 ± 9 keV were observed with a $\sim 1\%$ conversion efficiency. A strong density perturbation was measured around the quarter critical location, indicating these electrons might have originated from TPD or absolute SRS.

The experiments to date have provided an indication of the hot electron characteristics produced in a shock ignition implosion but these results are inconclusive due to the limited ablation plasma conditions that have been achieved and the strong dependence of LPI on those conditions. The characterisation of hot electrons is currently experimentally led, with PIC simulations largely only providing support for them. The need to investigate high intensity laser interactions with plasmas that were hotter and had longer density scale lengths motivated the execution of the experiment presented in Chapter 4.

2.8 Summary

Shock ignition offers a route to achieving high gain from implosions using a more stable, low velocity fuel assembly, and ignition from the launching of a strong shock. An appeal of this scheme is that the spike intensities needed are achievable on current laser facilities where the concept can be demonstrated and the concerns about drive coupling can be addressed. The high implosion velocities needed for conventional central hot spot ignition renders the thin shells highly susceptible to detrimental hydrodynamic instabilities. By reducing the implosion velocities and igniting through an additional driver, in this case a shock wave, the implosion can have a greater robustness against these instabilities and the adiabat can be potentially lowered to increase the energy gain.

The key factor in determining the success of shock ignition is the interaction of the high intensity spike with the capsule, in terms of both the timing of the shock launch and the coupling of the laser energy into the target. The location where the ignitor shock collides with the outbound return shock is crucial for the resulting inbound shock to provide the energy increase needed to achieve ignition. The high intensity spike can drive parametric instabilities within the ablation plasma due to the high plasma temperature and long density scale length. These laser-plasma instabilities, in particular stimulated Raman scattering and two plasmon decay, will scatter laser light away from the capsule and generate suprathermal hot electrons.

The hot electrons can have a great impact on a shock ignition implosion, where the energy distribution characteristics will determine whether they can provide a beneficial increase in shock strength or detrimental preheating of the cold fuel. Previous work on characterising hot electrons relevant for shock ignition has been insufficient due to the limited plasma conditions that can be produced.

The short timescales and small spatial extents of the capsules require diagnostics with high resolutions. The next chapter outlines the instruments and methods used to carry out experiments on the Omega-60 laser facility. Further investigation into the two steps of compression and ignition are vital to show its viability as a concept and for the success of shock ignition. The final chapters present the results from two experiments; the first investigated laser-plasma interactions relevant for the shock launching spike, and the second used reduced adiabat implosions relevant for the compression of a shock ignition capsule to tune a drive coupling model.

Chapter 3

Instrumentation and Methods

3.1 The Omega Laser Facility

The Laboratory of Laser Energetics (LLE) at the University of Rochester houses the Omega laser facility and its two main target chambers; Omega-60 [15] and Omega-EP [128]. The former of these was used for a series of experiments that form the basis of this thesis. The Omega-60 laser system gets its name from the 60 beams that enter the spherical target chamber. The research conducted at this facility is focused on the direct drive approach to inertial confinement fusion (ICF) and so the beam arrangement and laser profile smoothing techniques are optimised for that purpose. The deliverable total energy of ~ 27 kJ enforces a limit on the maximum capsule size that can be imploded which are inherently sub-ignition. Ignition implosion designs are instead investigated in a sub-ignition regime and hydrodynamically scaled [84] to a system capable of providing \sim MJ of energy, such as the National Ignition Facility [129] (NIF) or Laser-Megajoule [130] (LMJ).

The 60 beams use a 1.8 m focal length final optic with an f-number of 6.7 [15]. They are arranged in spherical symmetry around a 3.3 m diameter target chamber in a truncated icosahedron pattern, often referred to as a football pattern, where each beam points to a vertex of such a pattern. In this design, each beam will have an opposing beam from the other side of the chamber.

3.1.1 Laser Overview

The laser begins with the master-oscillator and is fed into the pulse shaping system where the temporal power profile of the laser beam is constructed. Development of an integrated

front-end source [131] has greatly improved the pulse shaping capabilities by increasing the contrast of the picket and foot of up to 100:1 [132]. These high contrasts are needed for highly shaped ignition pulse designs. The pulse is then split into 3 legs where each undergoes a series of amplifications and further splitting up to the full 60 beams. Vacuum spatial filtering is used to improve the near field beam integrity by removing high-spatial-frequency noise in the beam and ensuring correct image relaying.

Each amplification stage uses neodymium doped glass amplifiers at a lasing wavelength of 1053 nm, starting with rods and moving to disks as the pulse intensity increases. The gain medium is pumped with xenon flash lamps and the shot rate of the system is limited by the cooling of the gain medium and the flash lamps to ~ 1 shot per hour.

Once amplified to full energy, the laser pulse is frequency tripled from the infrared (IR) (1ω) to the ultraviolet (UV) (3ω) with a set of two KDP crystals (potassium dihydrogen phosphate) [36]. The first being called the “doubler” where two IR photons produce an intermediate green photon, and the second being called the “tripler” where the final UV is produced from an IR and green photons. Conversion to the UV is a non-linear process and highly dependent on the input IR intensity which must be considered when designing pulses that need to be frequency tripled. The system works optimally for a 1 ns square pulse and can achieve conversion efficiencies of up to 70%, with highly shaped pulses typically achieving closer to 50% [133]. The 3ω light is directed to the final focusing optic with high reflectively UV mirrors to reduce the transport of any unconverted IR on to the target.

3.1.2 Target Alignment and Power Balance

Precision and uniformity are critical to the success of direct drive studies, as well as general laser experiments. The target alignment system uses 6 axis positioners to achieve a ± 5 μm alignment of the target to the target chamber centre (TCC) [134]. The entire laser system itself is isolated from the building as a whole as it is situated on top of its own optical table, in this case a large concrete box resting on a bed of gravel. This independence from the surrounding structure improves its resistance to macroscopic shifts that can affect alignment.

The variation between beams in terms of total delivered energy and instantaneous delivered power, referred to energy and power balance respectively, are minimised to a high degree in order to improve the uniformity of illumination. Each pulse shape is tested beforehand

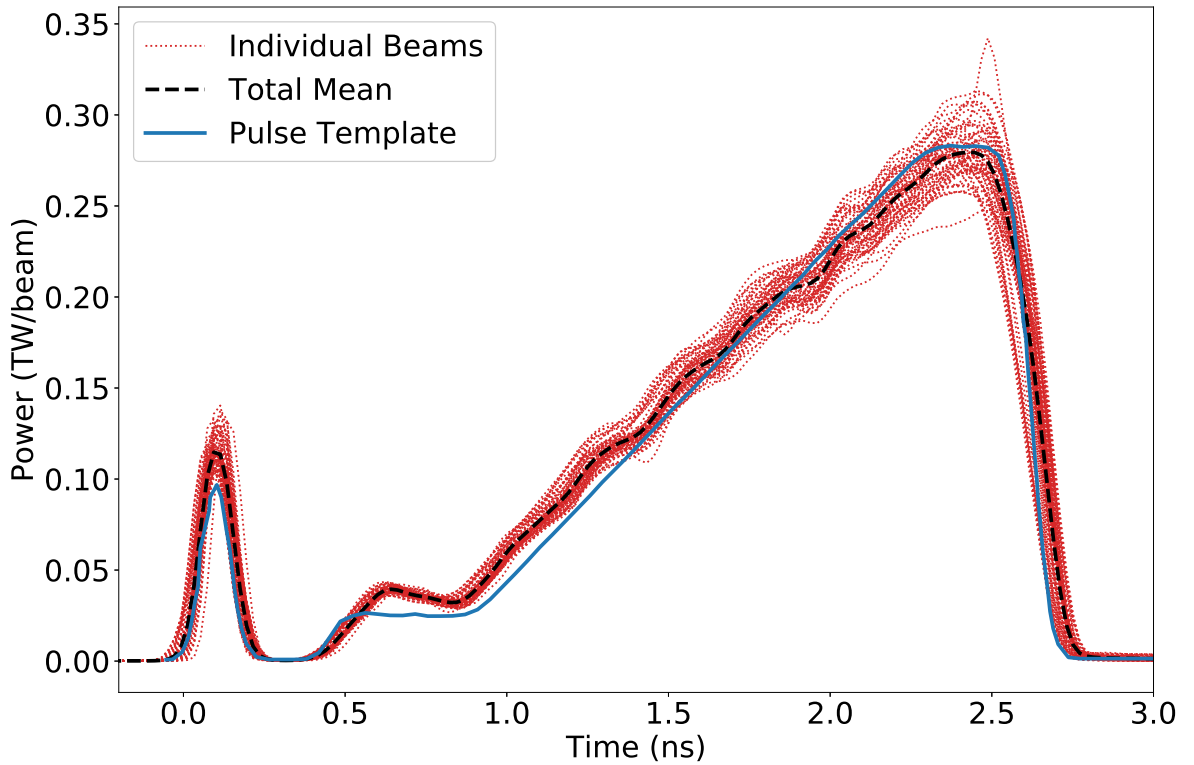


Figure 3.1: An example of the pulse delivery capabilities of Omega-60 from shot 93303. The solid blue line is the pre-shot template and the dashed red lines are the delivered pulses from each of the 60 beams, with their mean in solid black.

and a 4% pickoff of each shot is taken for analysis. The gain of the amplifiers at each step of the chain is tightly controlled to achieve a 0.6% energy variation between the IR beams at the point which they enter the KDP crystals. Variation in the individual beamline frequency conversions and transport optics result in an on target energy balance of 3-4% [133]. Overall power balance is maintained by using a single master oscillator seed, the controlling of the amplifier gain, and ensuring the same time of arrival at TCC.

Figure 3.1 shows a requested laser pulse shape with a solid blue line, the individual 60 beams in dotted red, and their mean in dashed black. The configuration of the 60 beams results in the incident power on any given point of a spherical target at TCC being delivered by many overlapping beams. For an energy of balance of 3-4%, this results in an improved radiation uniformity of 1-2% as beam-to-beam differences are reduced by the multiple overlapped beams [133]. The 60 beam that can be seen in Figure 3.1 therefore have a reduced drive imbalance than what would first be inferred from the apparent differences in delivered power from each beam.

3.1.3 Chamber Diagnostics

Several critical diagnostics are placed in fixed locations around the target chamber, including x-ray pinhole cameras and hard x-ray detectors. Additional to this are 6 available ports where user specified diagnostic TIMs (ten-inch-manipulators) can be inserted into the chamber to suit the needs of a specific experiment. The pre-shot alignment procedure requires all 6 TIMs to be used by pinhole cameras that check the reflection from a gold coated sphere. The weight of these insertable diagnostics (up to 45 kg) can be large enough that the chamber itself can deform and alter the alignment of the lasers. If other diagnostics are required for the experiment then they must be removed and replaced, meaning this warping of the target chamber is unavoidable, with any further changes in TIMs mid-experiment only increasing the effect. The drifting of alignment of the system is an ongoing issue at the Omega laser facility. The timescale of this drift is hoped to be larger than a day such that it does not significantly affect the target and laser alignment for a single shot day experiment. [135].

3.2 Beam Smoothing

For best coupling of laser energy to the target, the spatial intensity profile of the beam must be as smooth as possible. In reality, beam propagation through air, the amplifiers, and transport optics introduce amplitude modulations in the spatial intensity profiles. These modulations, when focused on to a capsule, are a major source of irradiation non-uniformities that can seed hydrodynamic instabilities and excite parametric instabilities. Several techniques are implemented to improve the spatial profile of the beam while maintaining large focal spot sizes.

3.2.1 Phase Plates

Phase plates [133, 136, 137] are an optical element placed in the near field of a laser in order to shape the far field intensity profile of the beam and to shift the non-uniformities in the intensity to higher spatial frequencies.

They consist of an array of smaller elements that induce a non-uniform phase shift in the beam as it pass through, each producing a beamlet. The phase elements are chosen to create a specific focal spot pattern, created by the interaction of many overlapping beamlets. A circular focal spot intensity profile is typically chosen for a spherical implosion, whose

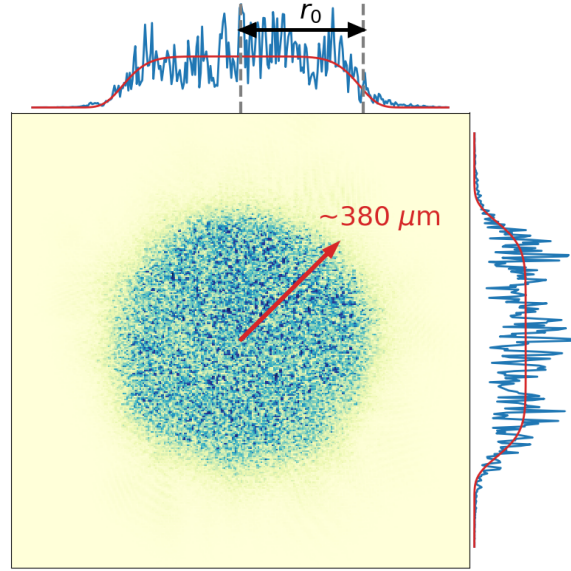


Figure 3.2: Far field intensity from a 380 SG5 phase plate [138], called so for the values of $n=5$ and $r_0=380 \mu\text{m}$ that describe the super-Gaussian envelope profile defined in the text.

spot size is similar to that of the capsule being illuminated. The intent is to produce a near circular focal spot with much of the energy contained within its radius to minimise energy loss and reduce the seeding of the CBET instability, described in Section 2.5.3. Phase plates also reduce the size of the high intensity non-uniformities producing many smaller speckles. These smaller intensity features are more readily smoothed by thermal conduction in the plasma or by smoothing by spectral dispersion (SSD), described in Section 3.2.2.

The far field intensity profile of a beam that used a phase plate is shown in Figure 3.2. The specific phase plate used is a so-called distributed phase plate that has a continuous relief profile, rather than discrete phase elements. The irradiation envelope profile is well described by a rotationally symmetric 2D super-Gaussian, as given by the equation $I(r) \propto \exp(-(r/r_0)^n)$ where r is the radius from the spot centre, r_0 is the specified spot size, and n is the order of the super-Gaussian which determines how much energy is contained within r_0 . Superimposed on this is a highly modulated speckle pattern created by the interference of all the beamlets.

3.2.2 Smoothing by Spectral Dispersion

The highly modulated speckle pattern produced by the phase plates can be smoothed further by temporally varying the spatial location of these speckles, significantly improving the time averaged intensity uniformity. This technique is known as Smoothing by Spectral Dispersion,

or SSD [139, 140].

Early in the generation of the laser pulse, an electro-optic modulator is used to create a temporally varying spectral profile. A bandwidth of 11 Å is in use for the SSD on Omega-60 [140]. A pair of gratings disperse the different spectral components of the beams such that their focused positions on the target are spatially separated. The varying focal position of speckles will change with the varying spectral components, shifting the position of the speckles on the target. When this high frequency spatial oscillation is averaged over the characteristic response time of the hydrodynamics of the target [139], the speckle pattern is smoothed out and its detrimental effects are reduced [118].

The rate of smoothing is determined by the spectral bandwidth imposed on the pulse, with large bandwidths offering higher smoothing rates. However, there is a trade-off between improved smoothing and total deliverable energy as any imposed bandwidth will reduce the efficiency of the frequency tripling process [133]. A second tripler crystal can be used to increase the bandwidth for efficient frequency conversion [141].

For one phase modulator and a single pair of gratings, the speckle pattern will oscillate in one spatial direction. Further smoothing can be achieved by providing oscillation in additional directions by using an additional electro-optic modulator with a different frequency and a second pair of gratings. This second pair will disperse the light in a direction perpendicular to that of the first, producing 2D SSD that is in use on Omega-60.

3.3 Sensors

Every diagnostic requires some way of amplifying or recording the desired experimental signal. The available detectors range widely in their response and capabilities. Several recording devices are presented here due to their use in instruments used in taking results presented in this thesis.

3.3.1 Image Plate

Image plate [142–150] is a reusable radiation detection medium widely used in laser-plasma experiments. It is capable of storing the spatial and intensity profile of a radiation dose that can be recovered later. Image plate is used in the Zinc von Hamos, Spherical Crystal Imager, and Hard X-ray Image Plate diagnostics, discussed in Sections 3.4.2, 3.4.3, and 3.5.1. It offers

Layer	Width (μm)	Density (g/cm^3)	Composition
Front Protective	9	1.4	$\text{C}_{10}\text{H}_8\text{O}_4$
Sensitive Phosphor	115	3.3	$\text{BaFBr}_{0.85}\text{I}_{0.15}:\text{Eu}$
Back	12	1.4	$\text{C}_{10}\text{H}_8\text{O}_4$
Base	190	1.4	$\text{C}_{10}\text{H}_8\text{O}_4$
Ferromagnetic	80	3.0	MnO , ZnO , Fe_2O_3 + plastic
Back Protective	25	1.4	$\text{C}_{10}\text{H}_8\text{O}_4$

Table 3.1: Composition of layers in the MS-type IP [149].

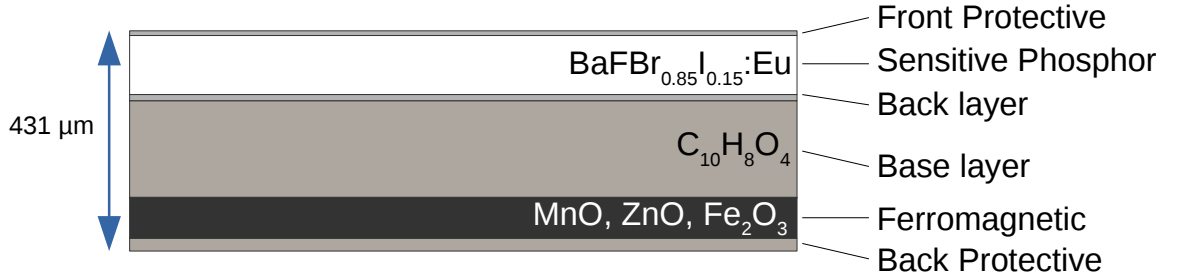


Figure 3.3: Schematic of the layers in the MS-type IP. Further details are given in Table 3.1.

a very high dynamic range of up to five orders of magnitude [145] and a linear response to dose [142]. They are immune to the harsh electromagnetic environments of typical laser-plasma interactions that would cause solid state electronic detectors to fail, and have a high durability to withstand debris. Unlike x-ray film [151], it requires no chemical development. Variations in the thicknesses of the active and inactive layers result in different types of image plate that are designed for different applications, offering super-resolution (type SR) or better sensitivity to electrons (TR). The multi-purpose standard (MS) will be described in detail but all types are based on the same underlying principles.

The layer structure of an MS-type IP is shown in Figure 3.3 and given in Table 3.1 with a detailed chemical composition of each layer. The sensitive layer on which the image is stored is composed of an alkali-halide crystal suspended in an organic resin in a ratio of 25:1 crystal to binder. The MS type has iodine included in this crystal due to its high absorption capabilities near its K-edge at 33.2 keV which greatly improves radiation detection above this energy.

Impinging radiation on the phosphor layer ionises the Eu^{2+} dopant ions and creates electron-hole pairs in the crystal forming Eu^{3+} ions. These photoelectrons enter the conduction band and can become trapped in the lattice defects called F- or trapping-centres,

resulting in a metastable configuration [149]. It has been proposed that the density of these trapping centres in the phosphor layer is proportional to the total energy deposited there by ionising radiation [152].

The original image can be recovered by stimulating the decay of this meta-stable state and recording the output intensity. The image plate is scanned with a 650 nm red laser that is absorbed by the Eu^{3+} ions which are then able to radiatively recombine with the trapped electrons, emitting ~ 400 nm blue light, in a process called photostimulated luminescence (PSL). Emitted PSL events are collected by a filtered photomultiplier tube internal to the scanner and digitised into a 2D image. The recorded 16 bit values (G) can be related to the number of PSL events with the following equation,

$$\text{PSL} = \left(\frac{G}{2^{16} - 1} \right)^2 \left(\frac{R_{\mu m}}{100} \right)^2 \left(\frac{4000}{S} \right) 10^{L/2} \quad (3.1)$$

Here, $R_{\mu m}$ is the scanner resolution in μm , and S and L are user specified values for sensitivity and latitude.

The meta-stable Eu^{3+} ions have a finite lifetime before naturally recombining due to thermal fluctuations. This decay has a lifetime on the order of \sim hour, resulting in a fading of the overall signal level. The rate of fading has been thoroughly characterised [144–147,153] and typically a double exponential decay is found to accurately describe this fading. The level of fading for a given signal is independent of the magnitude of that signal and can be calculated globally for the whole image plate. The fading factor decrease in signal for a time t between exposure and scanning is given by the following equation,

$$f(t) = A_1 \exp(-t/\tau_1) + A_2 \exp(-t/\tau_2) \quad (3.2)$$

where the A_i and τ_i coefficients are both temperature and IP-type dependent. The values chosen for analysis present in this thesis are taken from Rosenberg *et al.* [150] with the quick component having a decay time of 137 minutes and the slow component having a decay time of ~ 4.5 months. In these experiments, all exposed IP are held for 30 minutes before scanning to ensure consistency whilst minimising loss of signal from fading. The original signal level is found by calculating the fading factor and applying its reciprocal to the scanned signal.

The PMT internal to the scanner can become saturated if the PSL level is too high, saturating the image and requiring multiple scans. The unsaturated signal for the first scan

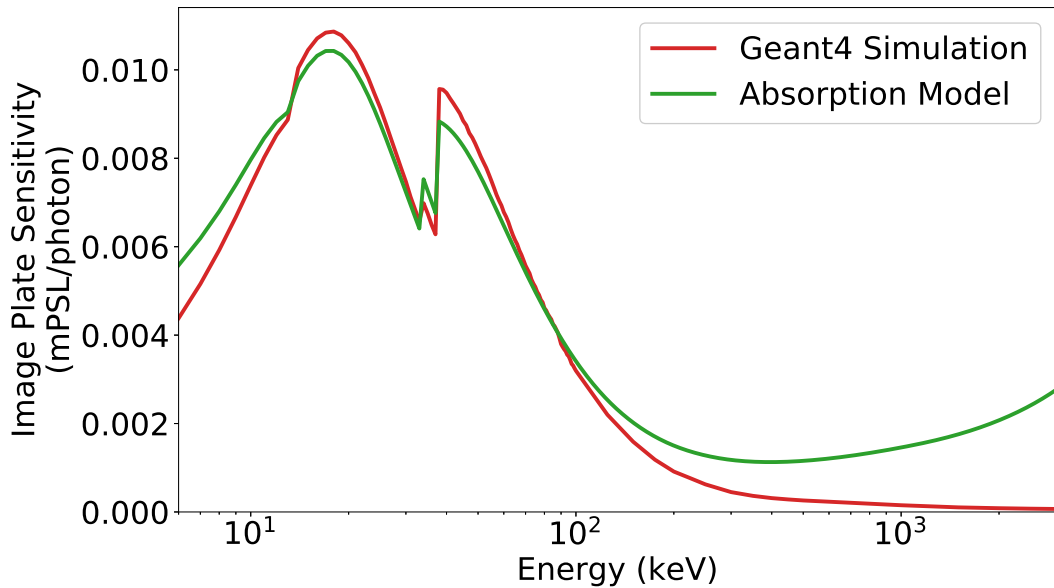


Figure 3.4: Two models of IP sensitivity, the first shown in green is based on an experimentally scaled absorption model and the second in red is found with Geant4 Monte-Carlo simulations.

can be found by inverting the signal fade from multiple scans. The fading level between scans is independent of the signal level, similar to the natural fading, and is found from the unsaturated regions.

Accurate knowledge of the sensitivity of the image plate is essential for correct analysis of its signal. Earlier models [144,145] used attenuation data to estimate the energy deposition in the active layer and scaled this to align with experimental data. These earlier models provide reliable values for the sensitivity for energies within the experimental range but are limited outside this region. These have been typically replaced with more detailed Monte-Carlo simulations which can provide modelling for a greater number of physical processes. These are primarily the recapture of scattered photons and secondary particle production, both of which are not included in earlier models. The two different techniques for modelling are shown in Figure 3.4, it can be seen that there is agreement in the range $10 < E < 100$ keV where experimental data is available but that the two diverge outside this.

3.3.2 Scintillators

Photon capturing media such as image plates described above provide excellent sensitivity to x-ray photons over a wide energy range but are inherently time integrated. They require long periods between shots where the exposed device needs to be removed, replaced, and

digitised. For current high energy facilities where shot rates are limited by laser cooling to $\sim 1/\text{hour}$, this does not restrict their use and several of the diagnostics described in this thesis readily use image plate for its many benefits. An effective complement to these low rep rate and time integrated devices are diagnostics that use scintillators in their detection. Since the response of a scintillator is proportional to the instantaneous dose, they can provide temporal resolution, and can be used at a high repetition rate.

The basic process of scintillation is the absorption of energy from incident ionising radiation to produce many electron-hole pairs which are then able to recombine and emit readily detectable near-monoenergetic optical photons [154]. The sensitivity of scintillator materials have been experimentally validated over a wide range of energies [155], and their light yield, the number of photons emitted per incident unit of energy, is typically well known [156].

The Hard X-Ray Detector [119, 157] (HXRD) discussed in Section 3.5.2 uses BaF_2 as the scintillator material, an unactivated inorganic crystal [158]. The high atomic number of Barium ($Z=56$) and the large solid density ($\rho = 4.88 \text{ g/cm}^3$) result in a strong radiation stopping power and a high detection efficiency.

Incident high energy photons with many times the ionisation energy of bound electrons will be absorbed by the material, typically via the photoelectric effect, and create multiple electron-hole pairs before losing its energy. These pairs are able to radiatively recombine via two processes in BaF_2 , the first being a recombination of electrons in the conduction band with a hole present in the valence band called self-trapped exciton (STE) emission, and a second much faster process of core-valence luminescence (CVL) that is more desirable for higher time resolution measurements. It is only present for crystals with a particular band gap structure that allows a valence band electron to recombine with a hole in the core band. It has a fast rise time producing a quick response to incident radiation and a short decay time, where the scintillation emission reduces quickly in time.

BaF_2 has one of the fastest CVL decay times and one of the highest light yields. Its CVL process emits a bright component at 220 nm with a decay time of 0.6 ns, and less dominant emissions at 195 and 175 nm [159]. The slower STE process produces photons with a wavelength of ~ 310 nm but with a far greater decay time of >600 ns. The slow component provides minimal signal over the $\sim \text{ns}$ timescales of typical laser-plasma experiments. The relative intensities of these emissions are shown in Figure 3.5. Despite the greater intensity of the ~ 310 nm component, the detected signal will be dominated by the other emissions

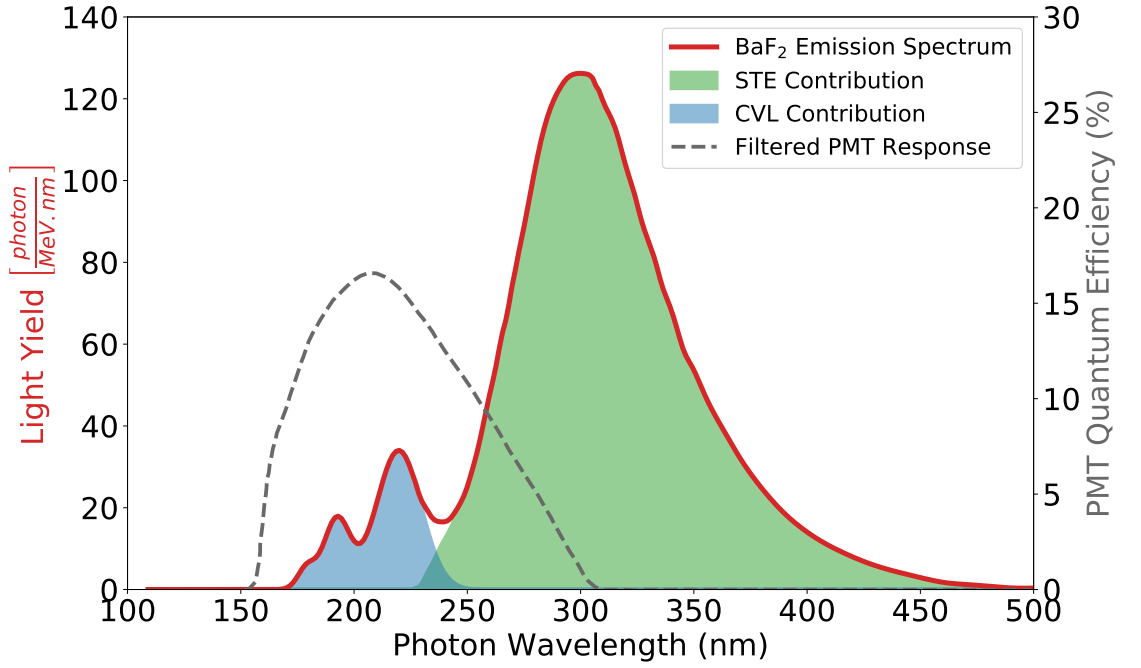


Figure 3.5: Emission spectrum from BaF_2 scintillator, including the contributions from the fast CVL and the slow STE processes. In dashed black is the quantum efficiency of a commonly used PMT. Image adapted from [160].

due to their quicker response and small integration time of the diagnostics. This scintillator is paired with a PMT that is filtered to remove the contribution of the slow component to the measured signal, also shown in Figure 3.5.

3.3.3 Charge Injection Devices

Charge Injection Devices (CIDs) [161] are a type of semiconductor imaging device, that performs a similar function to Charge Coupled Devices (CCDs) [158, 162, 163]. They offer large dynamic range and higher resistance to radiation damage than CCDs [164] which is advantageous for laser-plasma experiments. They provide inherent anti-blooming protection [165] which limits the effects of over saturation by stopping charge spilling over from saturated pixels to adjacent ones, effectively limiting over-saturation to the pixels where it occurs.

High energy photons incident on the CID surface eject electrons from their bound state, typically via the photoelectric effect and produce an electron-hole pair. This accumulated charge is transferred to a storage substrate layer via a voltage bias. They can remain in this layer until readout is required at which point the voltage bias is flipped and they are sent through a pre-amplifier and digitised.

The response of CIDs to x-rays was found via an empirical scaling of a phenomenological

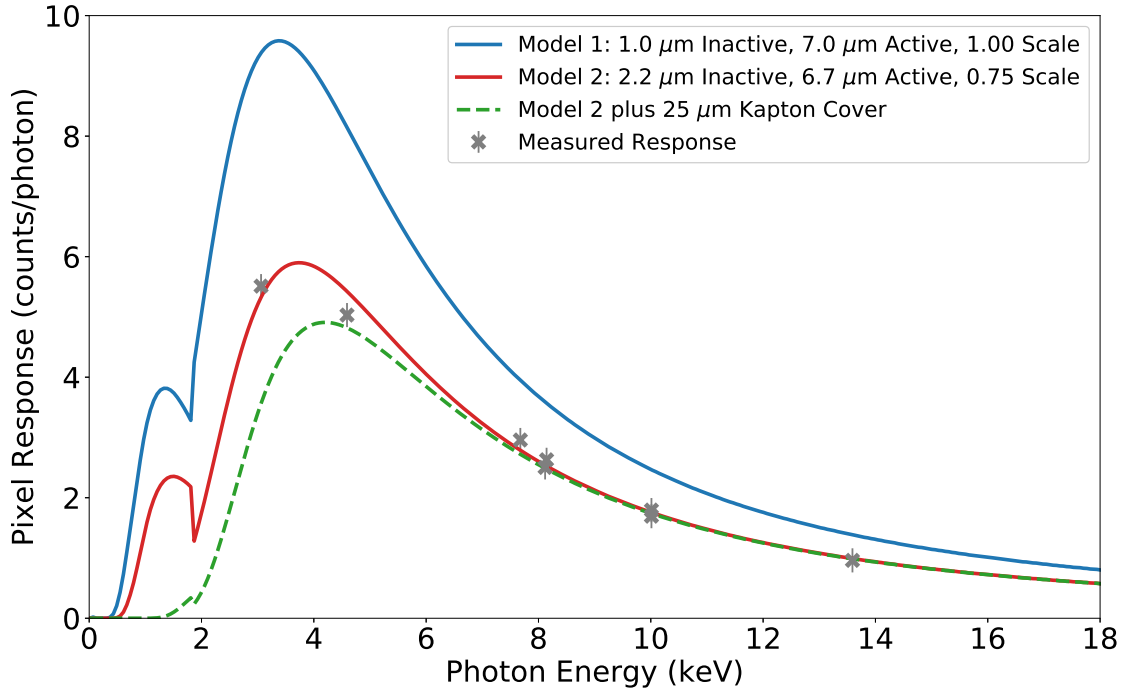


Figure 3.6: Experimentally measured response of a CID sensor with two models for the complete spectral response (solid blue and red) that use different values for the quantities in equations 3.3 and 3.4. The final response is plotted in dashed green once the attenuation from a Kapton cover is included. Image reproduced from [166]

model of x-ray absorption [166, 167]. The response $R(E)$ to a photon of energy E is given by the following equation,

$$R(E) = \text{QE}(E) \eta \kappa^{-1} \quad (3.3)$$

where QE is the quantum efficiency of detection, $\eta = E/3.66\text{eV}$ is the electron-hole pair yield, and κ is the gain of each pixel such that κ^{-1} is the number of counts recorded per electron-hole pair created. The quantum efficiency is proportional to the product of the transmission, $T(E)$, through the inactive “dead” layer and the absorption of the active layer which can be found using attenuation data from the NIST database [168], given by the following equation,

$$\text{QE} \propto T_{\text{inactive}}(E) \times (1 - T_{\text{active}}(E)) \quad (3.4)$$

The measured response of the CID is given by the crosses in Figure 3.6 along with two models described by equation 3.3. The first model uses the manufacturer specified values for the thicknesses of the inactive and active layers, while the second is found by adjusting these values within their errors to achieve better correlation with the data, as well as a global 0.75 scaling to account for errors associated with the gain [166]. The final CID response (dashed

green line) is found with the inclusion of the attenuation from a 25 μm Kapton cover.

3.3.4 Microchannel Plates

Microchannel plates (MCP) are a commonly used device in x-ray diagnostics, being utilised for fast-gated detection, photon to charge conversion, and high gain amplification of signal. A schematic of a gated MCP is shown in Figure 3.7. In this design, x-rays are incident on a front facing photocathode, typically a gold or other high Z microstrip. Primary photoelectrons are created through direct absorption, with many additional secondary electrons being produced through collisions. It has been shown that greater than 99% of the electrons that exit the photocathode are secondary electrons produced by these collisions [169] which exhibit a narrow energy spread of less than 10 eV. These electrons then enter an array of cylindrical microchannels with leaded-glass walls. A strong negative voltage accelerates the electrons down the channels. Collisions with the leaded walls creates additional electrons which themselves create further electrons. The original signal will have been amplified many times, depending on the voltage applied. After exiting, they can be collected directly by an anode or strike a phosphor to produce visible light for detection with a sensor.

Typical channel dimensions are a length of $\sim 400 \mu\text{m}$, a diameter of $\sim 10 \mu\text{m}$, and a centre-to-centre spacing of $\sim 12 \mu\text{m}$, with the channels themselves being slanted at 8-10°. The MCP response [170] to incident photons is plotted in Figure 3.8 with the filter transmission of Be blast shield and the final instrument response. It is found from the electron yield per photon, the gain in the system, and the geometry and material of the channels. Photon energies above 5 keV have large enough path lengths that the effects from crossing between multiple channels must be considered. The $\sim\text{keV}$ temperature plasmas that are imaged with an MCP as their amplifier means that the intensity of emission for energies higher than this limit is low enough that any discrepancies with the MCP response will have little impact on the final result.

The level of amplification or gain (G) is highly dependent on the applied voltage (V), with the relationship of $G \propto V^9$ being typically used [171] but exponents up to 25 have been reported under certain conditions [172]. This dependence on gain can be exploited to provide temporal gating to the MCP. The microchannels are instead held at a positive voltage which inhibits gain for the whole plate. A strong negative voltage pulse is propagated across the strip which enables signal amplification for the region of channels where the pulse is spatially

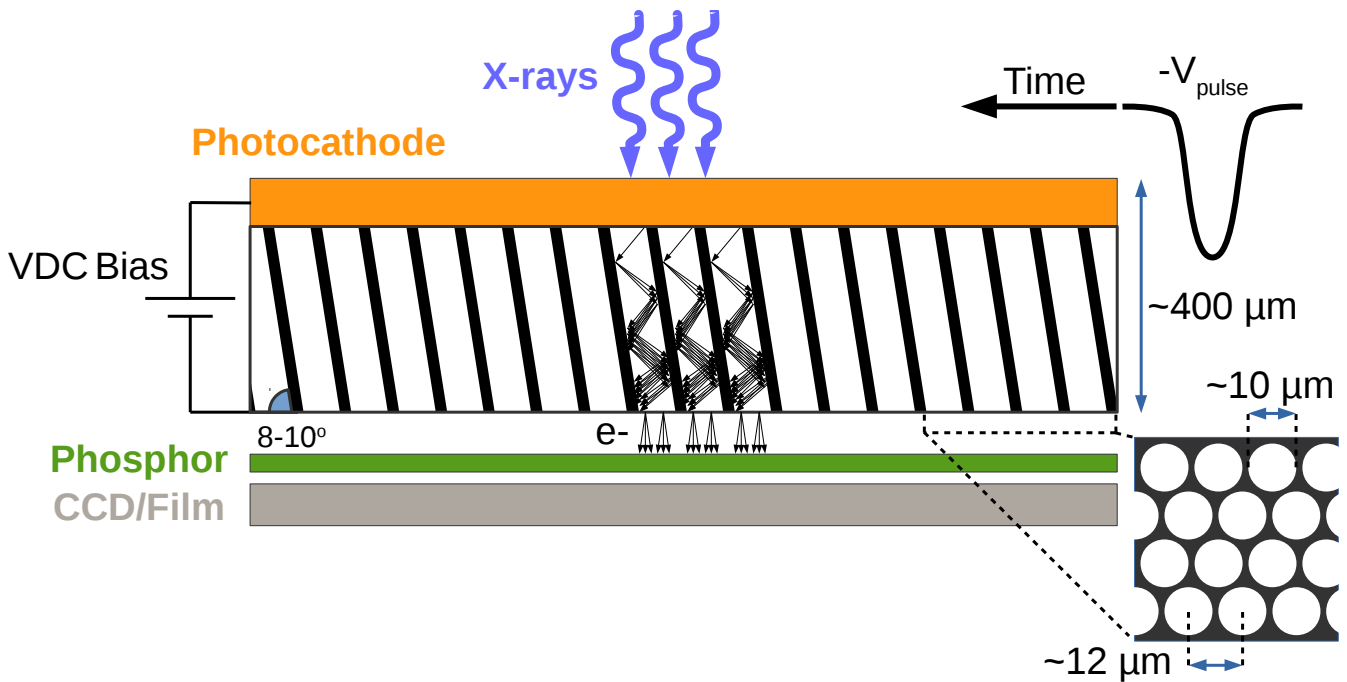


Figure 3.7: Schematic of an MCP design. The incident x-rays are incident on a photocathode producing free electrons down the MCP channels. The electron signal is amplified by collisions with the channel walls. They exit and strike a phosphor which is imaged with a CCD or film. A large negative bias is propagated across the strip to gate the channels. The spacing and size of the individual channels are shown in the bottom right.

located. This is used in the Sydor Framing Camera [173, 174] (SFC) and Kirkpatrick-Baez Framed [175] (KBF) diagnostics to produce fast gated images of imploding capsules.

A series of MCP's can be used in conjunction with each other to produce a compact and fast responding photomultiplier tube (PMT). This setup up is used in the HXR diagnostic to increase the signal before detection. The angle of the channels are reversed for consecutive MCPs in a chevron-like pattern to eliminate direct shine through of x-rays and reduce any positive ion feedback to the photocathode [176].

3.4 X-ray Diffraction Diagnostics

A diagnostic technique employed in many laser plasma experiments is place to a high Z layer or dopant as a tracer inside the target. Either through heating of these atoms or via bombardment by high energy hot electrons, they can emit characteristic line emission which reveals important information about the target material or hot electron source.

Figure 3.9 depicts the process by which the characteristic line emission is emitted. Inci-

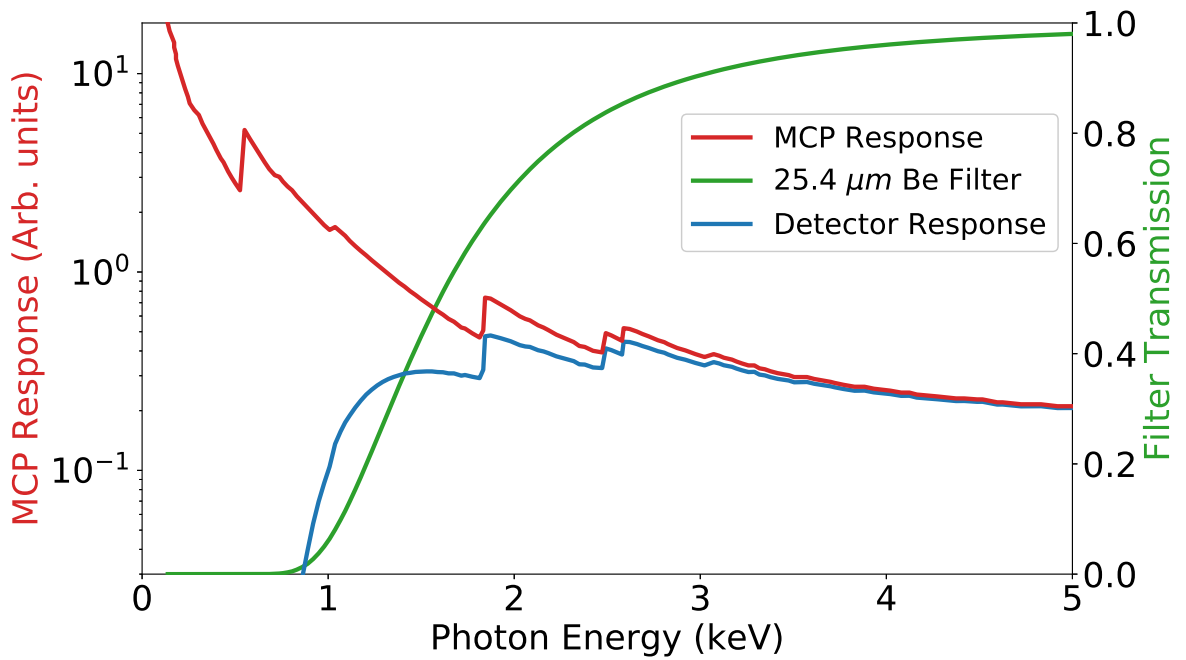


Figure 3.8: MCP response to incident x-rays taken from [170] in red. The MCP based diagnostics used in this thesis use a $25.4 \mu\text{m}$ Be filter to remove the low energy photons shown in green that results in the final response of the filter-MCP pair in blue.

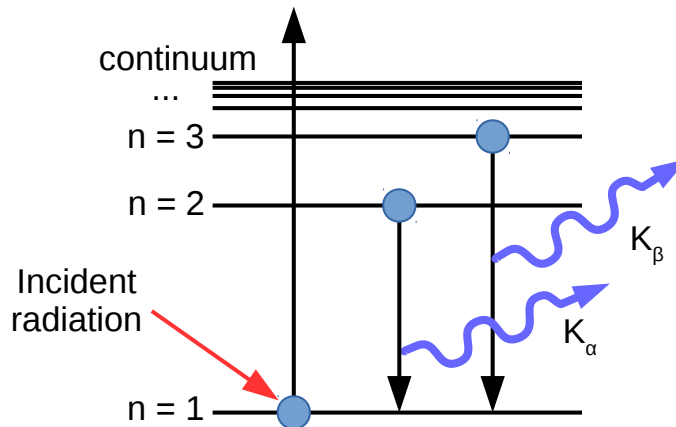


Figure 3.9: Diagram showing the ejection of an inner shell electron and the production of characteristic line emission in the form of K_α or K_β .

dent radiation, typically in the form of a photon or hot electron, collides with bound electrons in atoms or ions and eject them into the continuum. A remaining bound electron from a higher energy shell can relax down into the hole left by the ejected electron and a photon of characteristic energy is emitted. The ejection of an $n = 1$ inner shell electron can cause relaxation from electron in the $n = 2$ or $n = 3$ shells emitting photons which are given the names K_α and K_β respectively.

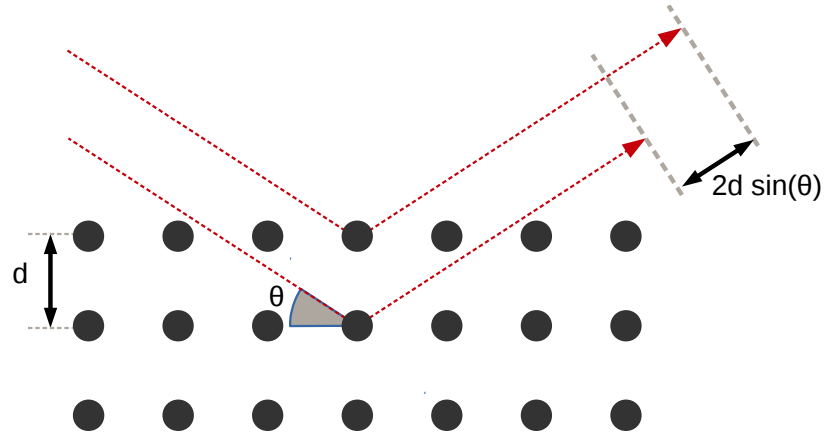


Figure 3.10: A geometric interpretation of Bragg's law of reflection, showing the reflection of incoming electromagnetic radiation from crystal lattice planes. For wavelengths that satisfy equation 3.5, the reflective waves will constructively interfere, isolating a narrow energy band.

The experiments presented in this thesis used a copper dopant and were measuring its emissions in the range of 7-10 keV, primarily the K_{α} at 8.05 keV. The diagnostics used for this rely on Bragg's law and x-ray diffractive crystals.

3.4.1 Bragg's Law

X-ray diffractive diagnostics rely on Bragg's law to disperse an incident spectrum using a crystal lattice. The layers of atoms in a crystal act as a grating that scatters the incoming x-rays. The superposition of the scattering from multiple atomic planes will lead to constructive and destructive interference.

A simple geometric representation of Bragg's law of diffraction is shown in Figure 3.10. In this image, the x-rays incident on the crystal are plane waves of electromagnetic radiation with a grazing angle θ measured from the crystal surface, where the radiation is then reflected off each atom in the crystal. For a lattice spacing d , light that has been reflected from the subsequent atomic plane will have an additional path length $2d \sin(\theta)$ compared with the previous. For these two waves to be in phase with one another, this additional path length must be an integer multiple of their wavelength, satisfying the condition outlined in the following equation,

$$n\lambda = 2d \sin(\theta) \quad (3.5)$$

where n is the order of the diffraction.

3.4.2 Zinc von Hamos

The Zinc von Hamos (ZVH) [177] diagnostic is a spectrometer in use at the Omega laser facility that relies on Bragg's law to disperse x-rays in the range of 7-10 keV. This range was initially chosen to be centred on the K_α emission from Zinc (8.64 keV) from which it gets its name but it is now primarily used for experiments involving emission from copper, with K_α and K_β emission at 8.05 and 8.9 keV respectively and He_α at 8.2 keV. Emission of He_α is the $n = 2 \rightarrow n = 1$ transition for helium-like Cu^{27+} ions that are produced through heating and sequential ionisation of the copper atoms.

Figure 3.11 shows a schematic of the ZVH diagnostic [177]. In the von Hamos geometry [178] the crystal is cylindrically bent around the dispersive axis, labelled in Figure 3.11 as the TIM axis, which focuses the light onto a central line on the detector. It uses a Highly Oriented Pyrolytic Graphite (HOPG) crystal; a high purity graphite crystal formed of many smaller crystallites with sizes on the order of 1-10 μm and an inter-atomic spacing of $2d = 0.67 \text{ nm}$ [177]. The mean orientation of these crystallites is zero compared with the crystal normal but there will be slight variation in each by up to a few degrees, referred to as mosaicity (γ), with a FWHM spread of $\gamma = 1.1^\circ \pm 0.2^\circ$ [177]. This increases the reflectivity of the crystal by offering more reflective planes but also results in a reduction of its spectral resolution. This makes it ideal for experiments with low signal, such as implosions with small concentrations of dopants or planar targets with thin tracer layers.

The diagnostic uses a BAS-MS type image plate which has a high sensitivity in the dispersive energy range and records a time integrated dose. The crystal and the detector are housed 25.4 mm tungsten shielding to reduce the background signal produced in typical high-powered laser experiments, and multiple internal layers to suppress fluorescence from the walls. A thin entrance slit and further shielding block the direct line of sight from x-rays and other high energy particles.

The alignment of the detector was determined by rearranging equation 3.5 and replacing the wavelength with $\lambda_0 = \frac{hc}{E_0}$, where $E_0 = 8.6 \text{ keV}$ is the desired central energy of the detector.

$$n \frac{hc}{E_0} = 2d \sin(\theta_0) \quad (3.6)$$

$$E_0 = \frac{nhc}{2d \sin(\theta_0)} \quad (3.7)$$

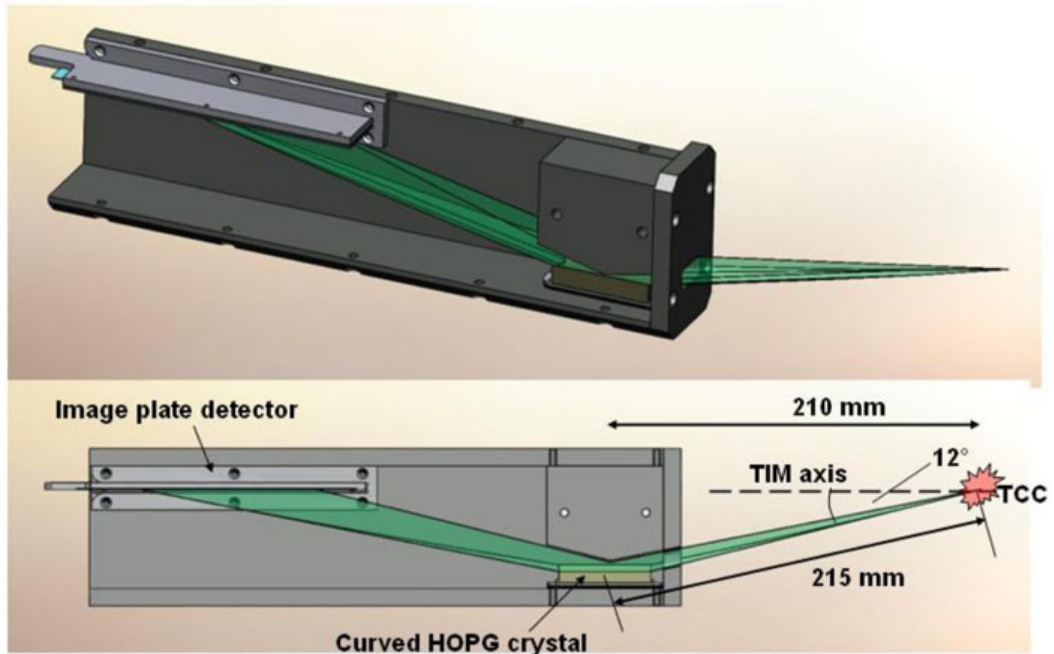


Figure 3.11: A schematic of the ZVH design [177], highlighting the source-crystal-detector orientation. The curve of the crystal can be seen in the upper image, it is in effect a segment of a total cylinder that would wrap around the TIM axis shown in the lower image. Reproduced from Jarrott *et al.*, *Rev. Sci. Instrum* 88, 043110 (2017), with the permission of AIP Publishing.

Using this, it is found that an angle of 12° is needed from the source, shown as TCC, and the crystal as shown in Figure 3.11. This angle is then repeated for the crystal to detector orientation since the detector and source share a common axis which is set by the axis of rotation for the cylindrical crystal.

Figure 3.12 shows a representation of the dispersion and focusing of a cylindrical Bragg crystal. The reflection off the concave surface will focus the emission from the source onto a line on the image plane. Only wavelengths of light that satisfy the Bragg condition are reflected and so the spectrum as a whole is also dispersed. The exact dispersion relation between energy and position along the detector is found by using the following geometric relationship,

$$x = 2R/\tan(\theta) \quad (3.8)$$

where x is the distance between the source and detection position for a given angle of incidence θ . The value of x is energy dependent and relies on the value of θ that satisfies

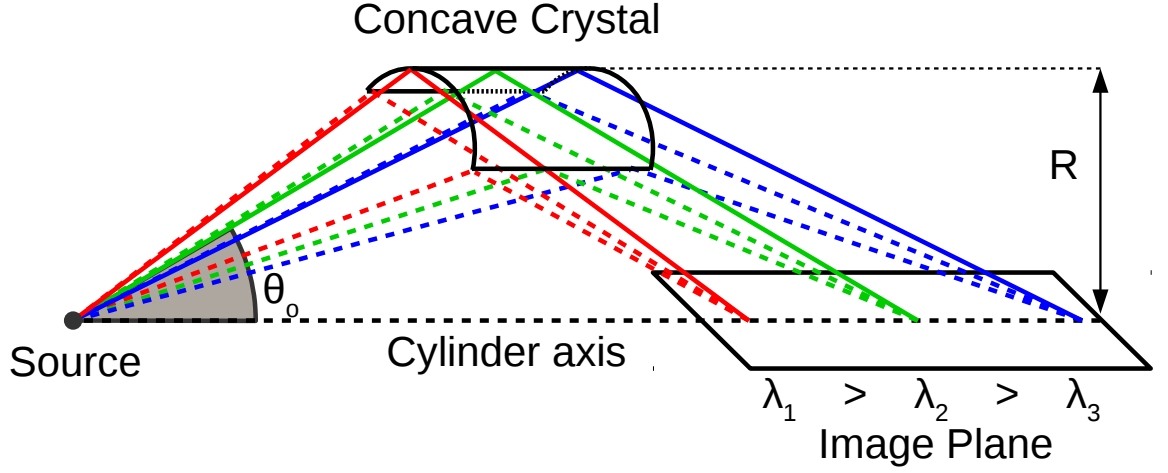


Figure 3.12: Dispersion and focusing of source emission by a concave cylindrically bent Bragg crystal on to an image plane. Longer wavelengths shown here in red satisfy the Bragg condition for larger angles compared with shorter wavelengths shown in blue. Image inspired by [179].

equation 3.7. The derivative of equations 3.7 and 3.8 are taken to find the following relations,

$$\frac{dx}{d\theta} = \frac{2R}{\sin^2(2\theta)} \quad (3.9)$$

$$\frac{dE}{d\theta} = E \cot(\theta) \quad (3.10)$$

Combining these two provides the dispersion relation along the detector axis.

$$\frac{dE}{dx} = \frac{E \sin(2\theta)}{4R} \quad (3.11)$$

The dispersion at the central energy of 8.6 keV is 20.1 eV/mm.

The ZVH diagnostic has been absolutely calibrated against a single photon camera for the Cu K_α and K_β lines generated from a short pulse laser incident on a planar copper target [177]. The calibration values were found to be 2.2×10^5 and 1.8×10^5 ph/(sr.PSL) for the K_α and K_β lines respectively, where a 20% experimental error is given for each. It is assumed that the calibration factor has a linear relationship with energy and is defined by these two points.

3.4.3 Spherical Crystal Imager

The Spherical Crystal Imager (SCI) diagnostic [180,181] uses a spherically curved crystal as both a diffracting element and mirror. This enables the system to produce a 2D image in a narrow band x-ray energy window, centred on the K_α line emission of copper. The crystal area improves x-ray collection efficiency whilst the narrow spectral bandwidth improves the signal to noise ratio, with values of up to 100:1 being possible [180].

The geometry of the SCI diagnostic is depicted in Figure 3.13. The spherical crystal defines and lies on a Rowland circle [182], where the diameter is equal to the radius of curvature of the crystal. The x-ray source lies off the axis of the crystal and the resulting aberrations [183] are inherent in the system, impacting the images created. To minimise this effect, the imaging system is designed to produce an incidence angle very close to normal and thus operating at a large Bragg angle. In order to achieve this for the copper K_α line centred on 8.05 keV, a quartz (21 $\bar{3}$ 1) crystal with $2d=3.08$ Å is used in the second order diffraction ($n = 2$ for equation 3.5), resulting in a Bragg angle of 88.7° .

For a geometry where the source, crystal, and detector all lie on the Rowland circle, a point-to-point focusing system at a specific photon energy will be produced. By moving the source inside the circle, the Bragg angle is matched for an extended object, enabling it to act as an imaging system. The SCI geometry allows a range of angles between 0.36° and 2.24° to the surface normal for which a bandwidth of ~ 6 eV [184] centred on the copper K_α line satisfies the Bragg condition, and is thus reflected off the crystal towards a detector. A magnified image will be recorded by placing the detector (typically an SR type image plate) outside of the Rowland circle. The SCI system uses a magnification of 14.7 [185].

In interpreting images from spherical imagers, it is important to account for any potential impact of the narrow bandwidth of the imaging system. For experiments that result in an increase in the temperature of the material producing the copper K_α emission, a shift in the K_α line centre to higher energy can be caused. This comes about when ionisation of the copper reduces the electronic shielding of the nucleus. This is compounded by Doppler broadening of the line emission, pushing the K_α signal across a broader bandwidth and potentially moving some of the signal outside the diffraction range of the imager.

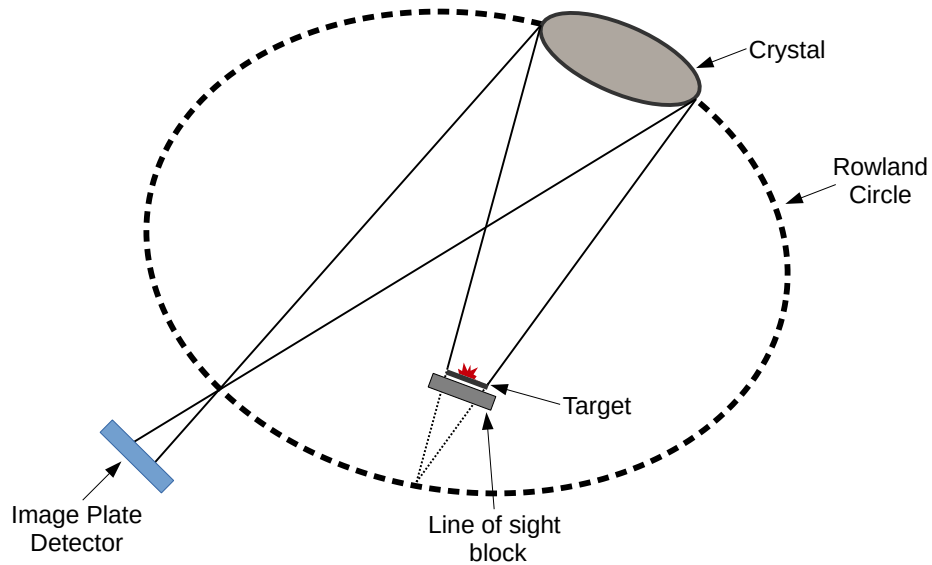


Figure 3.13: Alignment of the SCI diagnostic and opposing detector. The curvature of the spherical defines a Rowland circle, where the source (target) sits inside the circle. This produces a magnified image onto a detector placed outside the circle. The limited angles from source to crystal produce a narrow range of energies that can be reflected. A tungsten line of sight block is used to shield the detector from the target interaction.

3.5 Hard X-ray Spectrometers

Hot electrons generated from through parametric instabilities in high-powered laser experiments will produce bremsstrahlung radiation as they interact with the target. This bremsstrahlung emission spectrum can be collected and diagnosed by hard x-ray spectrometers in order to characterise the hot electron population that generated it. The hot electrons can be characterised by a Maxwell-Boltzmann energy distribution function with an associated temperature and total energy.

The hard x-ray spectrometers in use on Omega-60 use multiple filter-detector channels in order to sample the bremsstrahlung spectrum in separated photon energy regions. The temperature of the hot electrons can be found by considering the relative emission between the energy regions, and the absolute levels of emission can reveal the total energy in the hot electron population.

3.5.1 Hard X-ray Image Plate

The Hard X-ray Image Plate diagnostic in a multi-channel differentially filtered hard x-ray spectrometer [122, 186]. An array of 9 attenuating filters of increasing filtering strength are

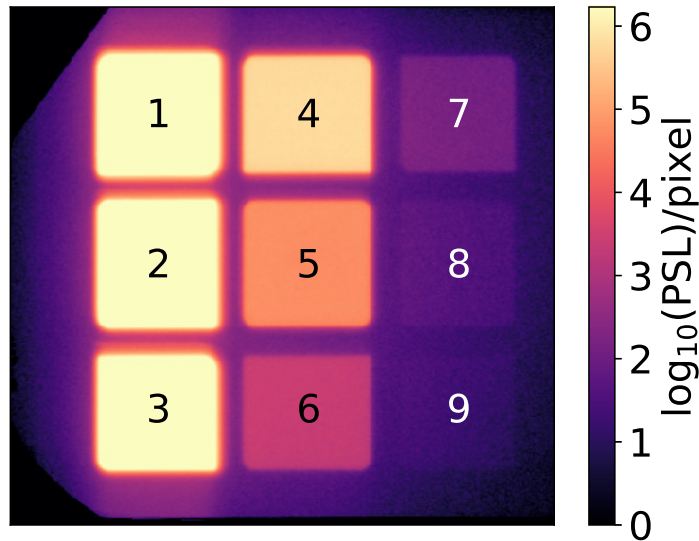


Figure 3.14: The PSL per pixel of an exposed image plate from the HXIP diagnostic. The transmission through the 9 channels are highlighted, in order of increasing attenuation strength and corresponding decreasing signal. The first three channels recorded a signal that has saturated the scanner and require multiple scans to fall below this saturation limit.

used to produce a different transformation of an incident x-ray spectrum. These transformed spectra are recorded by an image plate detector that integrates the signal in time. The material and thickness of these channels was specifically chosen to provide optimal spectral decomposition to radiation produced by hot electron of temperatures <100 keV.

The filter composition and thicknesses are given in Table 3.2. The increasing filter thicknesses will increase the attenuation strength, producing a minimum photon energy transmission and high-pass energy bands. The filters are placed midway between the target and the IP detector, with a total distance of 49 cm. A 1 mm tungsten aperture stop is used to separate the filters and provide moderate channel collimation.

Figure 3.14 shows a scan of an exposed image plate where the transmission through the 9 channels can be seen. The least attenuating filter is in the top left and the most attenuating filter is in the bottom right, with the decrease in PSL corresponding with stronger filtering. The non-zero background surrounding each exposed region highlights the effect of cross-talk between channels from imperfect collimation of the channels provided by the aperture stop and Compton scattering off the filters. There is also smearing of the signal in the direction of the scanner, vertically on the image shown. This smearing of signal is thought to be the result of internal reflections and scattering caused by the scanning process itself [149]. The diagnostic housing includes 1.9 cm thick lead shielding to isolate the IP from external

Channel Number	Al Thickness (mm)	Cu Thickness (mm)	Cut-Off Energy (keV)
1	0.97	-	12
2	1.92	-	16
3	2.89	-	19
4	9.63	-	31
5	19.31	-	42
6	19.31	1.14	54
7	19.31	3.43	71
8	19.31	6.85	94
9	19.31	9.14	121

Table 3.2: Filter composition and thickness for the 9-channel HXIP diagnostic, along with the approximate photon energy cut-offs [186].

radiation, as well as layers of copper, aluminium, and Mylar to suppress the fluorescence from the lead walls.

The response functions of the instrument were generated [186] from Monte-Carlo simulations of radiation incident on the detector using the code Geant4 [187] and are plotted in Figure 3.15 against photon energy. The 3 dimensional nature of the simulation is able to capture the internal scattering and channel cross-talk which is then incorporated into the response functions. These simulations showed that less than 0.1% of the signal detected by each channel was from energetic particles that escape the target, with the remaining signal being from bremsstrahlung radiation. The aluminium used is the alloy 6061 which includes smaller amount of other elements [188]. Including these in the contribution to the channel response functions can change the temperature predictions by up to 5% [186].

3.5.2 Hard X-Ray Detector

The Hard X-Ray Detector (HXRD) [119, 157] is a four channel time resolved high energy photon spectrometer. It uses a combination of aluminium and copper of increasing thicknesses to differentially filter the incident photon spectrum to create cut-off energies of >20, >40, >60 and >80 keV. After the filter for each channel is a fast scintillator connected to a quick rise time MCP-PMT, a photomultiplier tube based on the multiple MCP design outlined in Section 3.3.4. The accumulated charge from the MCP is passed through a 50 Ω resistor from which a time resolved voltage is found.

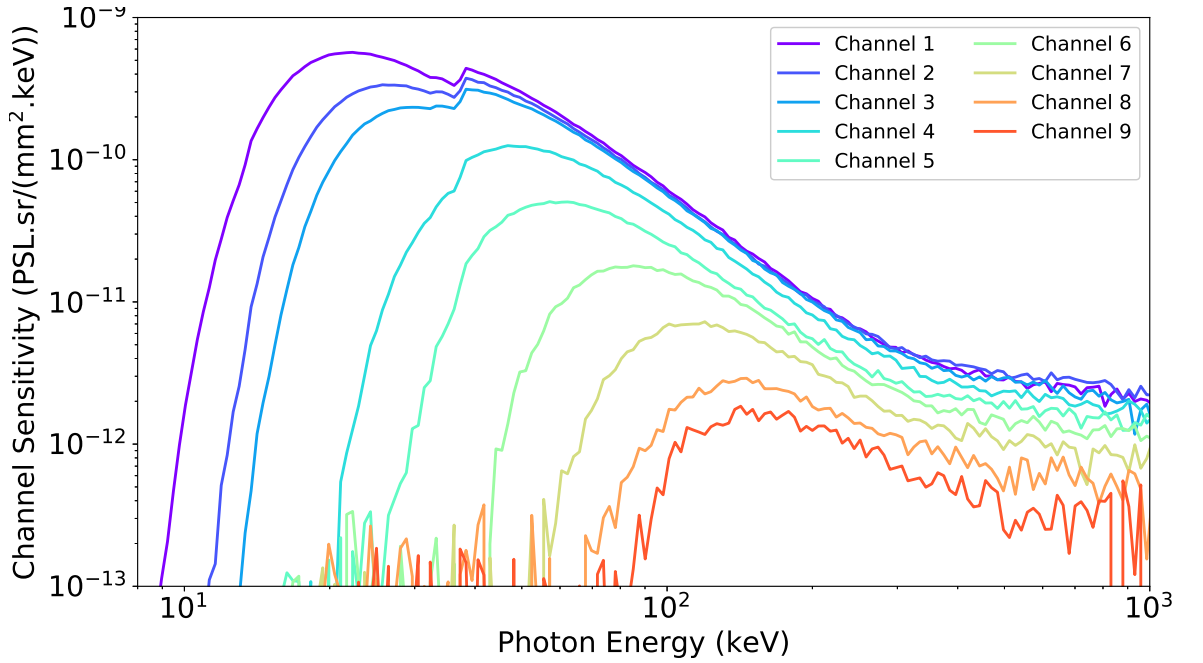


Figure 3.15: Response functions of the nine channels of the HXIP diagnostic [186]. The behaviours of response functions at low sensitivity and high photon energy is the result of statistical noise in the simulations.

Channel Number	Al Thickness (mm)	Cu Thickness (mm)	Cut-Off Energy (keV)	Scintillator Material
1	3	-	20	BC 422Q (1%)
2	20	-	40	BaF ₂
3	20	3.25	60	BaF ₂
4	20	6.3	80	BaF ₂

Table 3.3: HXR channel filter and scintillator compositions, with the approximate photon energy cut-offs for the filters [157, 186].

The filter and scintillators used in the four channels of HXR are shown in Table 3.3. An absolute calibration of channel 2 and a relative calibration of the remaining channels to channel 2 has been performed, [119]. The absolute calibration error for channel 2 is given as 20% and the accuracy in the timing is ~ 100 ps relative to the Omega timing fiducial. The uncertainty in the calibration of channel 1 was too large for this channel to provide reliable readings, likely due to its different scintillator material, and it is typically ignored from any further quantitative analysis [126]. For the three remaining channels, BaF₂ was used for the scintillator material due to its very quick 600 ps decay time for scintillation making it highly responsive, as outlined in Section 3.3.2.

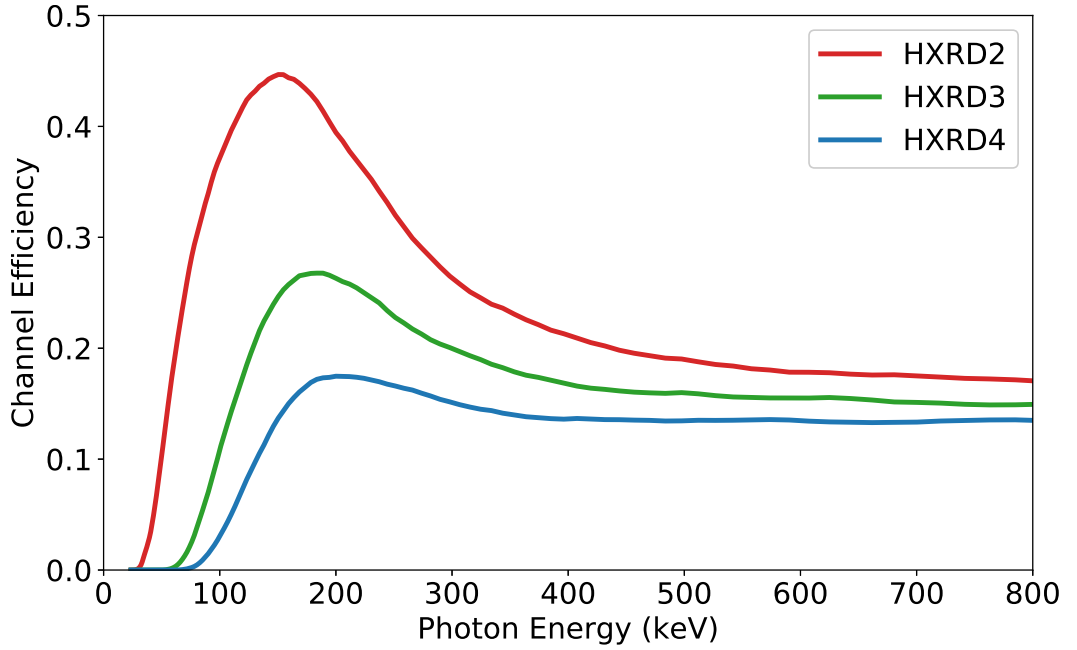


Figure 3.16: Response functions for the final 3 channels of HXRD found using the Monte-Carlo code Geant4. The curves shown here are the product of filter transmission and scintillator response, and require channel sensitivities given in [126].

To a first approximation the response of channel i is given by the following equation,

$$R_i(E) = \omega_i T_i(E) S_i(E) \quad (3.12)$$

where ω_i is the solid angle, $T_i(E)$ is the channel specific filter transmission fraction, and $S_i(E)$ is the scintillator absorption and response. The mass attenuation coefficients for the filter transmission and scintillator absorption can be found from databases such as CXRO [189] and NIST [190].

Equation 3.12 is a one dimensional approximation where only the radiation normal on the filter is considered and any scattered light is lost. An improved channel response was generated by Stoeckl and Solodov [186] where a more complete Monte-Carlo simulation was performed using the code Geant4. These simulations extended beyond the filter and scintillator materials to include the port cover, lead collimator and housing, in order to capture any contribution from scattering or fluorescence from these surrounding materials. The response curves found from these simulations are given in Figure 3.16, where it can be seen that each channel is sensitive to increasing energy ranges and thus a spectrum can be sampled at different points.

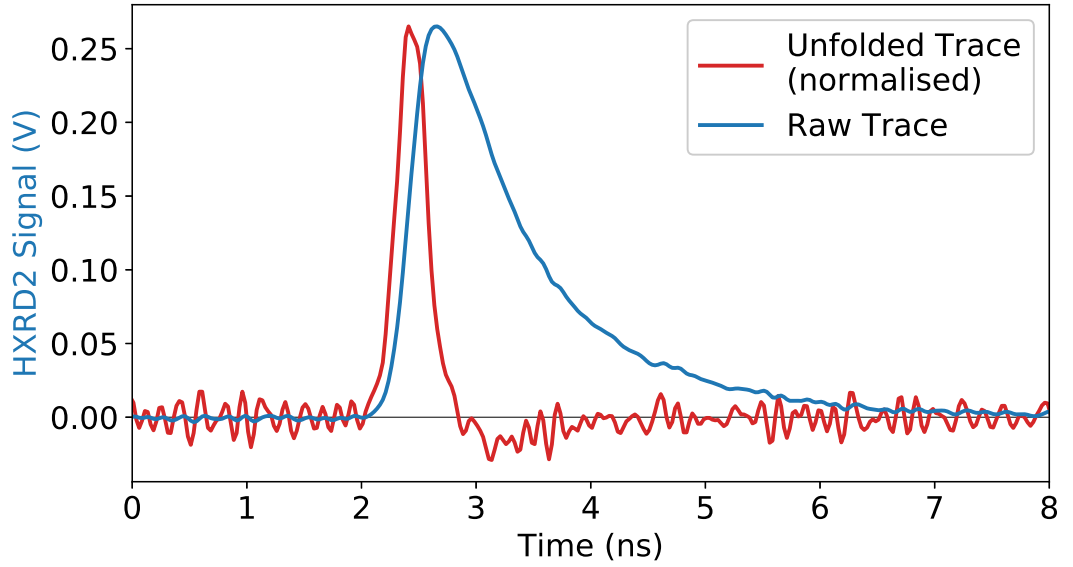


Figure 3.17: Signal from HXR2, showing the raw and unfolded traces.

Figure 3.17 shows the raw HXR2 trace from channel 2 along with the same trace that has been unfolded to remove the intrinsic scintillator response time and decay. This unfolding process is capable of recovering the temporal profile of the original bremsstrahlung source but it is susceptible to erroneously amplifying noise or over-correcting for weaker signals, hence why the signals fall below zero after the peak.

3.5.3 Filter-Detector Analysis Method

All filter-detector bremsstrahlung diagnostics operate on the same principle. This method compares the measured quantities Q_i with a set of expected quantities $S_i(T_\nu, E_\nu)$ and finds the set of parameters, (T_ν, E_ν) , that describes an emission spectrum denoted by ν where the collective difference between the two quantities is minimised. The measured quantities will be the detected radiation dose transmitted through the set of filters. It is necessary to make some assumption of the photon distribution f_ν that reaches the detector, or of the original hot electron distribution f_h that created the photon distribution. To a first approximation, the expected signal for channel i is given by the following relation,

$$S_i = \int f_\nu(\epsilon_\nu) R_i(\epsilon_\nu) d\epsilon_\nu \quad (3.13)$$

where R_i is the spectral response of channel i , and ϵ_ν is the photon energy. In many cases, this is further broken down into $R_i(\epsilon_\nu) = \alpha_i F_i(\epsilon_\nu)$ where F_i is the calculated detector efficiency

and α_i is an experimentally determined calibration factor. Approximations to the curves may be found by a phenomenological model using tabulated mass attenuation data or from detailed simulations of particle transport through matter.

The experimentally measured signal will include contributions from other sources such as fluorescence and scattering from external structures, imperfect shielding, particle bombardment, manufacturing imperfections in the filters and image plates, deterioration of physical image plate quality through repeated use, among other effects. For particle tracking simulations some of these will be included in the response curve, in particular scattering, while other effects might be small enough to be ignored, such as bombardment of electrons escaping the target [186].

The thick-target model for bremsstrahlung emission [191, 192] can be used when the hot electrons interact with a target that has a stopping power high enough that they lose all of their energy within the target and that a negligible amount escape. This is typically achieved by using thick targets with high- Z materials. The emitted bremsstrahlung spectrum under those conditions consists of a Boltzmann distribution given by the following equation [124],

$$I \left(\frac{\text{keV}}{\text{keV sr}} \right) = \frac{5 \times 10^{11}}{4\pi} \frac{Z^*}{79} E_{h,J} \exp \left(1 - \frac{\epsilon_\nu}{k_B T_h} \right) \quad (3.14)$$

where $Z^* = \langle Z^2 \rangle / Z$ is the average atomic number of the target, and $E_{h,J}$ is the total energy of the hot electrons in J . In using this model, it is assumed that the electron temperature is low enough that they are non-relativistic such that the bremsstrahlung emission is isotropic, and that the photon temperature is equal to the electron temperature, $T_h = T_\nu$. This second assumption improves in its accuracy when probing photon energies higher than the electron temperature [193].

The modelling of bremsstrahlung emission distribution can be improved by using particle simulation codes, such as the Monte-Carlo code Geant4, as described in Section 3.8.3. The experimental target design can be simulated, along with any arbitrary electron distribution. For a simulated experiment that satisfies the thick-target assumptions, the resulting bremsstrahlung spectrum recovers equation 3.14. A common energy distribution f_h to assume for the hot electrons of energy ϵ_h is a normalised 3D Maxwell-Boltzmann of the form,

$$f_h^{\text{MB}}(\epsilon_h, T_h) = 2 \sqrt{\frac{\epsilon_h}{\pi k_B^3 T_h^3}} \exp \left(\frac{-\epsilon_h}{T_h} \right) \quad (3.15)$$

This is then multiplied by the total number of hot electron N_h to give the full experimental distribution

$$f_h(\epsilon_h, T_h, E_h) = N_h \times f_h^{\text{MB}}(\epsilon_h, T_h) \quad (3.16)$$

$$= \frac{E_h}{1.5k_B T_h} \times 2 \sqrt{\frac{\epsilon_h}{\pi k_B^3 T_h^3}} \exp\left(\frac{-E}{k_B T_h}\right) \quad (3.17)$$

where the relationship $E_h = \int \epsilon_h f_h d\epsilon_h = 1.5N_h k_B T_h$ has been used to convert from electron number to total electron energy. Both of these methods for determining the photon source can be generalised with the following equation.

$$f_\nu(\epsilon_\nu, T_h, E_h) = \int I_{br}(\epsilon_h, \epsilon_\nu) f_h(\epsilon_h, T_h, E_h) d\epsilon_h \quad (3.18)$$

where $I_{br}(\epsilon_h, \epsilon_\nu)$ is the bremsstrahlung photon emission spectrum from a hot electron of energy ϵ_h .

The final generalised form of the expected signal for a Maxwell-Boltzmann electron distribution with temperature T_h and total energy E_h is given by

$$S_i(T_h, E_h) = \alpha_i \int F_i(\epsilon_\nu) \left[\int I_{br}(\epsilon_h, \epsilon_\nu) \times f_h(\epsilon_h, T_h, E_h) d\epsilon_h \right] d\epsilon_\nu \quad (3.19)$$

The experimentally measured signals, Q_i , can now be compared against a set of these synthetic expected signals to determine the parameters that most closely match the two. A χ^2 analysis is performed by scanning over the expected parameter ranges and minimising the value of the sum of the residuals. An associated quantity is the reduced value $\tilde{\chi}^2 = \chi^2/l =$ where l is the number of free parameters available to the fit, in this case $l = N - m$ where N is the number of measured signals and m is the number of fitting parameters. For an electron population determined by E_h and T_h the value of N only is 2. This enables comparison of $\tilde{\chi}^2$ values across different diagnostics and for proper uncertainty analysis.

The value that must be minimised is given by,

$$\tilde{\chi}^2 = \frac{\chi^2(T_h, E_h)}{l} = \frac{1}{N - m} \sum_{i=1}^N \frac{[S_i(T_h, E_h) - Q_i]^2}{\delta S_i^2 + \delta Q_i^2} \quad (3.20)$$

where δS_i and δQ_i are the uncertainties in S_i and Q_i respectively. The predicted values for E_h and T_h are those that give the minimum value, $\tilde{\chi}_{\text{min}}$. For a perfect model of the signals, a

value of $\tilde{\chi}_{\min}^2 = 1$ is expected rather than 0 due to the random uncertainties in the measured quantities. Values much larger than 1 indicate that the model is not physically accurate and that the measured results cannot be replicated well. Values much less than 1 suggest that an “over-fitting” of the data is being performed, likely due to an over-estimate of the signal uncertainties [194]. For situations where this occurs in the analysis presented in this thesis, the values of $\tilde{\chi}^2$ are normalised such that the minimum is equal to 1. An uncertainty can be placed on the best fitting set of parameters by considering the contour of parameters that lie above this minimum point. When fitting two parameters to the data, the 68% and 95% confidence intervals are given by $\tilde{\chi}(T_h, E_h) = \tilde{\chi}_{\min} + 2.3$ and $+4.6$ respectively [195].

3.5.4 Comparison of Diagnostics

An ideal characterisation of the hot electron population would be performed by a direct measurement of their spectrum. To overcome the inability to access the plasma directly, electrons are measured indirectly by either their secondary processes such as K_α or bremsstrahlung emission, or by measuring a subset of the population such as electrons that escape the target and are collected by an electron spectrometer [196].

Comparisons of hot electron characteristics found across experiments [117] must consider the diagnostic method implemented as well as the specific instrument that is used. Multiple experiments have demonstrated that HXIP and HXRD predict different hot electron temperatures when observing the same population [120–122, 186]. This is despite the response functions having been generated in the same way and using the same analysis technique [186]. The magnitude of this difference varies between experiments, with HXRD typically predicting higher temperatures by a factor of ~ 1.5 [122].

The uncertainty in the temperature predictions of any hard x-ray spectrometer is in part based on the spacing of the energy sensitivities for the channels. This is because it is the relative signal between the channels from which the spectrum is recreated and as such the sensitivities need to be well spaced to sample different energy regions. The sensitivity of the final two channels of HXRD, although having different absolute values, are relative close in energy and offer worse spectral decomposition capabilities than HXIP whose sensitivities cover a wider energy range. For this reason, HXIP is preferred for predicting the hot electron temperatures, whereas HXRD is best used for its time resolving capabilities.

Additional factors that must be considered when comparing experiments such as the

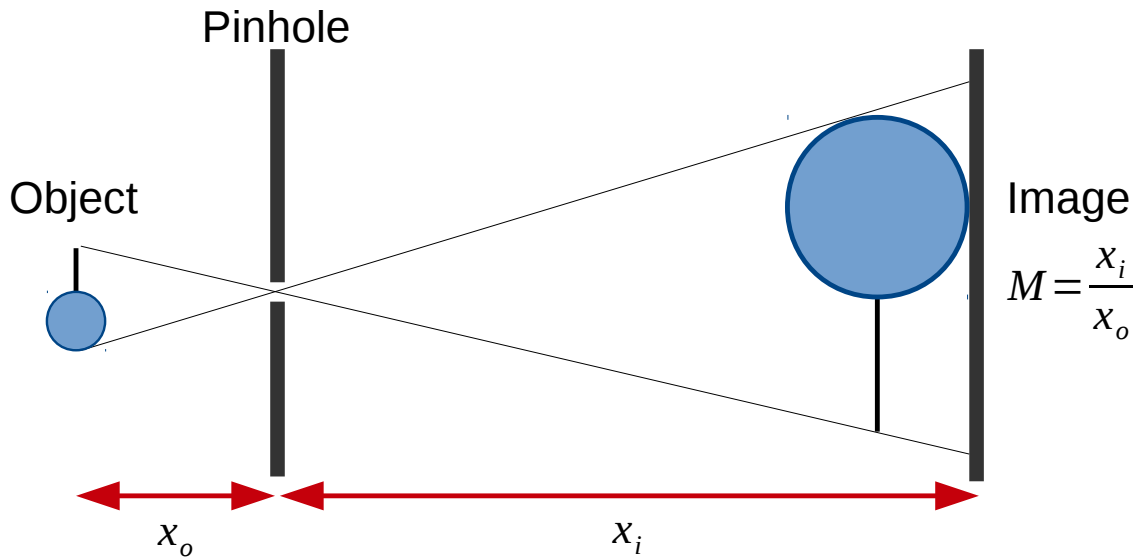


Figure 3.18: The basic geometry of a pinhole camera set up. A pinhole is placed between the object, in this case an ICF capsule and stalk, and the detector. The image that is produced is inverted and magnified, given by $M = x_i/x_o$.

choice of hot electron energy distribution function which is explored further in Section 4.7.1, where temperature predictions vary by up to $\sim 1/3$ when choosing a 1 dimensional Maxwellian compared with a 3 dimensional. It was demonstrated that refining the instrument response functions [186] led to changes in the predicted temperature, meaning that version of the response functions must also be considered.

3.6 Soft X-ray Imagers

3.6.1 X-Ray Pinhole Camera

X-ray pinhole cameras (XRPHC) are a widely used diagnostic [51, 197–199] for many laser-plasma experiments due to the useful information they provide, and their simple design and implementation. The principle of an XRPHC is that a small aperture is placed in between the source and a detector, such as a CID or IP, where an inverted image is formed. The basic geometry is shown in Figure 3.18. The magnification of the object is the ratio of the object to pinhole distance with the pinhole to image distance. Pinhole cameras are particularly useful for diagnosing total x-ray flux and assessing the spatial dimensions of the source.

The pinhole diameter must be smaller than the lateral extent of the source whereby light emitted from any point on the source would ideally only have a single path through to the

detector. In reality, the finite size of the pinhole will result in a small but non-zero range of paths each point of the source can take, reducing the spatial resolution.

The pinhole diameter is optimised to produce the smallest point-spread-function (PSF) with the highest resolution for the energy range of the emitter [200]. The XRPHCs that are in operation at Omega use a pinhole size of $10\ \mu\text{m}$ with a spatial resolution of $\sim 15\ \mu\text{m}$. The magnification of the system is chosen such that the pixilation that is inherent to the CID sensors that are used is less than the PSF of the pinhole such that each pixel images $< 10\ \mu\text{m}$. The setup used in this thesis had $x_i=648\ \text{mm}$ and $x_o=162.5\ \text{mm}$ for a magnification of 5. The precision of alignment of the diagnostic is to within $5\ \mu\text{m}$ so the magnification is known to a very high degree.

A $25.4\ \mu\text{m}$ Be filter is used to remove the low energy x-ray contribution, combined with a CID sensor whose response limits the detection of high energy photons. This produces a sensitivity range of $\sim 2\text{-}10\ \text{keV}$ can be seen in Figure 3.6.

The CID itself is run time integrated, producing a single image of the implosion as a whole. The diagnostic in effect encodes the time history of the implosion into space on the detector. An example XRPHC image is shown in Figure 3.19. The self-emission from the capsule whose energy is within the detector's sensitivity range is primarily from near the ablation front [201]. This creates an inward moving ring of emission while the capsule implodes that can be seen as the bright outer region of the figure. At the point the laser switches off, no more energy is deposited into the capsule and the self emission reduces. This can be seen as the inner region with lower intensity. A central bright region is seen from the glowing hot-spot that is formed late in time. The stalk and glue that holds the target in place can be seen on the bottom of the image, along with a channel inwards to the centre that is discussed in Section 5.4.

3.6.2 Self-Emission Shadography

The soft x-ray emission from the plasma corona can be imaged with a time resolved detector and related back to the temperature and density profile of an implosion. The Sydor Framing Camera [173, 174] (SFC) diagnostic uses a pinhole array and multiple gated MCP strips to produce a series 16 images of the implosion.

The intensity of emission from the corona will be a function of both the plasma temperature and density where the diagnostic integrates this self emission along its line of sight. A

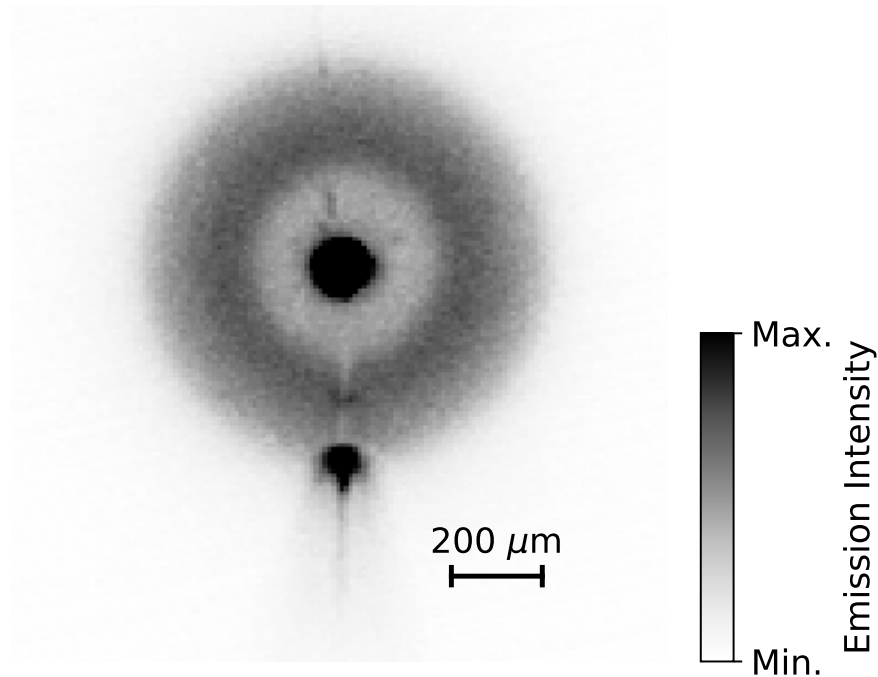


Figure 3.19: XRPHC time integrated image of a plastic shell implosion on Omega-60. The emission intensity of the outer ring corresponds with the amount of laser energy deposited in the capsule. The central bright emission is from the hot spot that forms late in time. The stalk and glue mounting can be seen at the bottom.

steep inner edge in the emission is observed due to the optically thick shell strongly absorbing the photons that are emitted from the rear side of the capsule. This absorption reduces the emission from behind the shell by up to a factor of 2, steepening the gradient [201]. A $25.4 \mu\text{m}$ Be filter is used to act as a high pass filter that optimises for high contrast imaging of the steep gradient [174]. The diagnostic is performing a shadography measurement of the shell where the backlighter is being provided by the self-emission from the plasma itself, leading to the naming of this technique as self-emission shadography.

A 4×4 array of $15 \mu\text{m}$ pinholes are projected on to 4 independently timed MCP strips, producing 16 two-dimensional images, depicted in Figure 3.20. Across a strip, each image will be separated by ~ 50 ps, with a relative inter-strip timing accuracy of ~ 2.5 ps and an absolute timing accuracy with respect to the laser of ~ 10 ps [52]. The high voltage pulse used to gate the MCP strips has a square shape and an integration time of ~ 40 ps which is small compared with the implosion velocity of the target and avoids significant blurring of the image. The spatial resolution of $15 \mu\text{m}$ is determined by the PSF of the pinholes and the effective binning from the discrete pinholes [52].

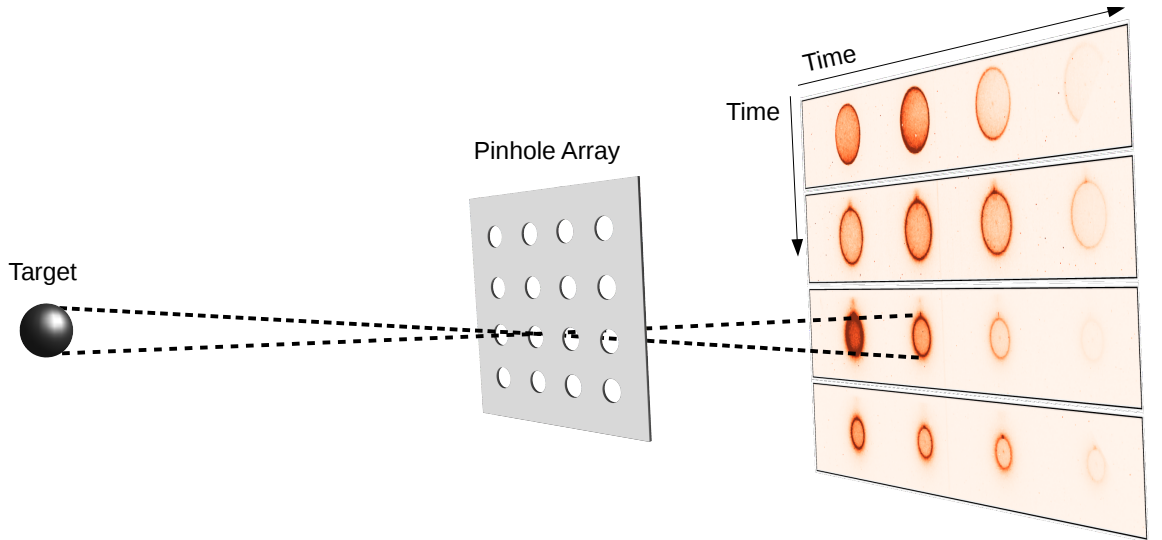


Figure 3.20: SFC diagnostic concept, depicting the pinhole array imaging the target with the use of 4 independently timed MCP strips. Image inspired by [202].

Each 2D image has azimuthal slices taken from its centre that are averaged to produce radial intensity profiles. The location of the steep inner gradient is commonly defined [203] by a 65% rise in the intensity from the centre of the capsule (I_{min}) to the peak in the radial profile (I_{max}), give by $I_{65\%} = 0.65 \times (I_{max} - I_{min}) - I_{min}$. Radiation-hydrodynamic simulations are performed using the same design information and the output is post-processed to find the spectral emission. The same analysis procedure can then be applied to these synthetic images to relate the radius between the experiment and simulation.

3.6.3 Time Resolved X-ray Imager

Imaging the x-ray emission of hot-spots in ICF implosion can provide valuable information about its shape, size, and morphology. This can help assess the performance of the implosion as a whole and inform future designs. To this aim, two high spatio-temporal resolution and time resolved 2D x-ray imagers are used on Omega, orientated at near-orthogonal angles to each other. The first of these is the Time Resolved X-ray Imager [204, 205] (TRXI) that achieves high spatial and temporal resolution with the novel combination of a signal dilation tube and fast gated framing cameras.

High time resolution is achieved in part with the use of an electron pulse-dilation tube [206], a method that stretches out the input signal by up to two orders of magnitude. A schematic of the process is shown in Figure 3.21. X-ray emission is first converted to an

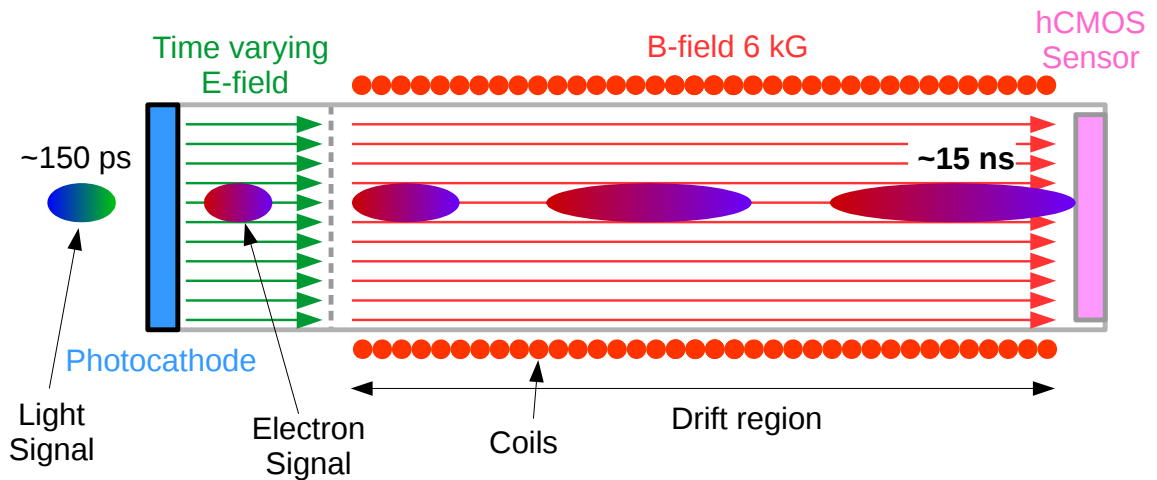


Figure 3.21: Pulse dilation tube for TRXI. The photon signal from the hot spot will have a ~ 150 ps duration that is converted to an electron signal by a photocathode. A time varying electric field accelerates the electrons before they enter a drift tube. The electron signal dilates in time and is detected by a hCMOS sensor.

electron signal via a CsI photocathode, where the electron bunch will have the same spatial and temporal properties as the x-rays that generated them. These electrons are then accelerated by a time dependent electric field that begins with a high accelerating voltage which decreases over the course of the signal. This results in electrons that are generated at earlier times having a greater speed than those generated later. The electrons then enter a drift tube, confined to gyro-orbits down a strong axial 0.6 T B-field in order to maintain the original x-ray image. The travel down this drift tube allows the electron signal to dilate, as those created earlier with greater speeds will pull away from the slower electrons that were generated later.

The second fundamental aspect of TRXI's high resolution is the choice of a hybrid-CMOS sensor (Complementary Metal Oxide Semiconductor) [207]. This implements additional architecture to standard CMOS chips and allows these hybrid sensors to store an additional frame before being read out. This provides two gated images in a so called burst-mode. Further to this, the sensor itself is split into 2 sections, called hemispheres A & B, that can be independently gated which provides a total of 4 hot spot images. Each image is gated over 2 ns for a total of 8 ns of detection which equates to 120 ps of hot-spot emission when the pulse dilation is considered. A temporal resolution of ~ 40 ps is achieved [204].

An array of $10 \mu\text{m}$ pinholes are used to project multiple images on the sensor. Each time resolved image is formed from an average of these images in order to improve the signal to

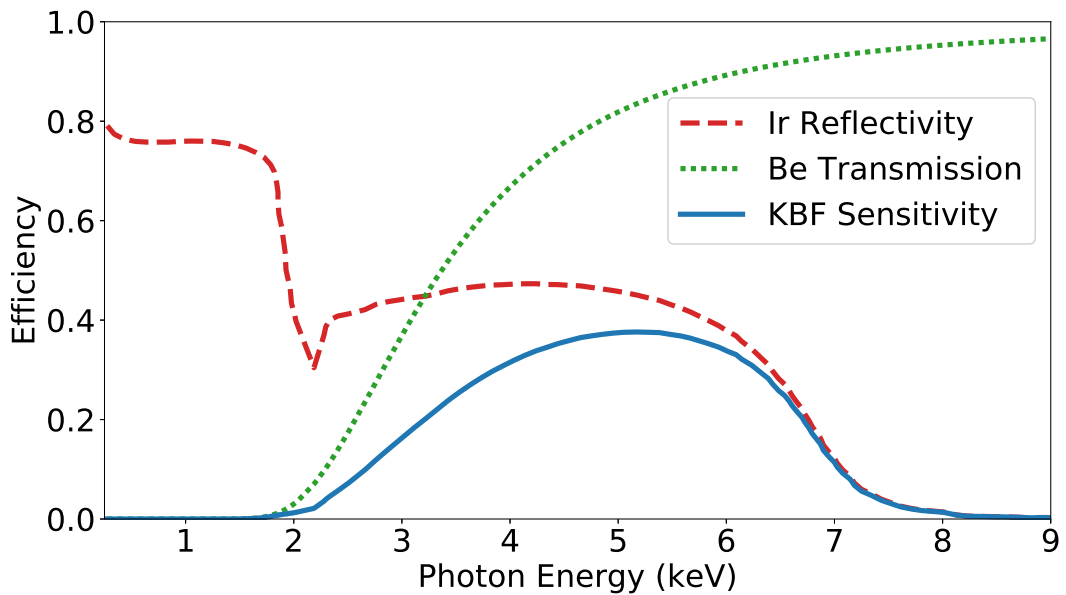


Figure 3.22: Reflectivity of Ir coated mirrors at a 0.7° grazing angle, Be filter transmission and KBF sensitivity.

noise level and enhance the spatial fidelity. A total of $508 \mu\text{m}$ of Beryllium is used between the source and the photocathode to act as a blast shield, vacuum filter and a low energy photon filter. This thickness of filter was chosen in order to detect emission in the range 4-8 keV as the compressed shell is optically thick for energies less than this [204]. This results in a spatial resolution of better than $10 \mu\text{m}$ [204].

3.6.4 Kirkpatrick–Baez Framed Microscope

The second hot-spot diagnostic combines a set of Kirkpatrick-Baez mirrors [208] with a high speed framing camera to provide a series of time resolved high spatial resolution image, aptly named KB-Framed or KBF [209, 210].

The Kirkpatrick-Baez configuration uses a pair of concave grazing angle of incidence surfaces whose surface normals are perpendicular to each other in order to focus the light in both the vertical and horizontal directions.

A total of 16 pairs of mirrors are used to produce an equivalent number of images. The mirrors themselves use a fused silica base and are coated in 500 \AA of Iridium that have been super polished for a roughness of $\pm 4 \text{ \AA}$. The grazing reflectivity of the Ir coated mirrors is shown by the red line in Figure 3.22. The final sensitivity of 2-8 keV shown in blue is found when combined with a $140 \mu\text{m}$ Be filter that is shown in green.

A novel compact design and mirror repointing outlined by Marshall [175] allows this set of

16 mirrors pairs to be combined with a fast four strip MCP based framing camera, similar to that used by the SFC diagnostic described in Section 3.6.2. Each strip can be independently timed with a relative accuracy of ~ 2 ps and an absolute timing accuracy of ~ 50 ps [209]. A resolution of $< 5 \mu\text{m}$ can be achieved when the framing camera is replaced with film, largely due to spherical aberrations and diffraction effects from the focusing mirrors. When operating in time resolved mode, blurring from the non-zero integration time provide a practical resolution of about $\sim 6 \mu\text{m}$.

3.7 Full Aperture Backscatter Diagnostic

Laser-plasma instabilities can backscatter light from the plasma back in to the laser optics. This backscattered light can be collected and analysed to provide information about the laser-plasma instability, such as the electron density of plasma where it was stimulated and its temporal profile. The full aperture backscatter diagnostic [211] (FABS) collects the light that is backscattered in the full aperture of the laser beam. This light is spectrally dispersed and temporally streaked. It has a spectral range of 400-750 nm, a 5 nm spectral resolution, and a 0.4 ns temporal resolution.

3.8 Simulation Codes

3.8.1 Radiation-Hydrodynamics Codes

Radiation-hydrodynamics codes aim to simulate the interaction of laser energy with matter, and the resulting temperature and density profiles as they evolve in time. HYADES [38] is a one dimensional radiation-hydrodynamics code. It uses a three temperature system for electrons, ions, and radiation. The electrons and ions are treated as separate fluids, and a multi-group transport model is used for the radiation. It is capable of simulating planar, cylindrical and spherical geometries for symmetric targets.

HYADES implements a Lagrangian co-ordinate system where a user-defined mesh is filled with specific mass elements and it is the mesh itself that is allowed to move freely. The Spitzer-Harm model [212] of thermal transport is used, with flux limited diffusion to restrict the heat flow to a user specified fraction of the free streaming limit when large temperature gradients are present.

At half integer time steps, the velocities are calculated from the momentum conservation equation, using pressures and viscosities of the mass elements. An equation of state is required to close the system and relate these quantities to each other. This can be a simple ideal gas equation or tabulated values such as the SEASAME library [213] maintained by the Los Alamos National laboratory. Each integer time step, the positions are updated from these velocities and the cycle continues.

HYADES has been extended to two dimensions with the code h2d. It simulated cylindrical geometry with an r, z co-ordinate system and uses many of the same physics packages as HYADES.

3.8.2 Spect3d Post-Processor

SPECT3D [214] is a multi-dimensional collisional-radiative spectral synthesis code that is capable of post-processing the outputs from various radiation-hydrodynamics simulations. Many experimental diagnostics rely on the emission of light from the target in various forms and as such the output of radiation-hydrodynamics simulations require this extra post-processing step for them to be directly comparable.

It is capable of modelling the emission of light from the target, including broadband self-emission and characteristic line emission, as well as the transport and absorption of this light as it is directed towards a simulated detector. These are all calculated using tabulated values for emissivities and opacities. Instrument specific features can be recreated such as inbuilt filters, time gating and integration, and line broadening.

3.8.3 Geant4 Monte-Carlo Code

Geant4 [187] is a single particle Monte-Carlo code that is able to simulate a rich variety of physical processes over a wide range of energies and a diversity of particles. It is used to model the physical geometry of the system and the component materials, potentially extending beyond simply the target and detector to include and shielding, housing or target chamber structure that might influence the measurement. It simulates particle production and propagation through matter, tracking its interactions with the materials and any potential creation of secondary particles.

At the beginning of each event in Geant4, a single primary particle is created with a unique random number combination which sets its creation point, energy, and momentum.

Interaction between particles and materials are calculated using cross-sections from large databases. The event is finished once the energy of the system, that is the primary particle and any further created particles, reaches zero. At this point, a new particle is again generated with a different random number.

Geant4 is then best suited for recreating stochastic processes where many particles can be sampled with across energy distributions. An example of this would be for simulating the bremsstrahlung emission from hot electrons propagating through a target. It is also well suited to simulating the response of detectors to incident radiation. For the simulations presented in this thesis, typical simulated particle numbers are on the order of 10^9 .

3.9 Summary

Omega-60 is capable of high accuracy target and beam alignment, and is currently the largest laser facility designed for direct drive inertial confinement fusion implosions. The facility is capable of implementing multiple forms of beam smoothing techniques in order to produce repeatable and uniform intensity profiles. Illuminating targets with these focal spots increases the amount of energy that reaches the target and reduces the susceptibility to laser-plasma instabilities.

A wide array of instruments is implemented that are capable of diagnosing multiple aspects of an experiment. These include hot electron diagnostics that record the characteristic line emission from embedded high-Z materials, and hard x-ray bremsstrahlung radiation. High accuracy soft x-ray imagers are used to infer the size and shape of a capsule during its implosion and of the hot spot that forms late in time. These diagnostics are supported and interpreted through simulation codes. These codes aid in the design, execution, and planning of experiments.

Chapter 4

Laser-Plasma Interactions in Shock Ignition Relevant Conditions

4.1 Introduction

This chapter describes results from an experiment performed on the Omega-60 laser facility designed to excite hot electron populations from laser-plasma instabilities in plasma conditions and laser intensities relevant for MJ-scale shock ignition implosions. This involved replicating the plasma corona conditions that are expected for a shock ignition implosion, and illuminating this plasma with a high intensity pulse to emulate the ignitor spike. Previous work on characterising hot electrons for shock ignition purposes have been unable to reach the relevant plasma conditions, in particular the temperature and density scale lengths, primarily due to the inability to couple enough energy into the target. A novel target and beam pointing set-up was established for this experiment in order to access the required regime using a sub-ignition laser. Several hard x-ray and backscatter diagnostics were used to establish the temperature, energy, and accelerating mechanism of these electrons. The novel laser-target scheme and certain results presented here have been published in *Physical Review Letters* [215]. The chapter concludes with an outlook on how these hot electrons might impact shock ignition by considering the results from radiation-hydrodynamics simulations that integrate a hot electron population with the experimentally found parameters.

4.2 Experiment Overview

The potential success of the shock ignition approach is largely dependent on the ability to launch a shock of sufficient strength without detrimentally affecting the fuel assembly process. This means in particular knowing how the energy from the high intensity part of the laser pulse couples to the plasma corona, and how this energy is then transported to the ablation front and beyond. In order to reach the higher densities where inverse bremsstrahlung absorption is most efficient, the high intensity spike ($I \sim 10^{16}$ W/cm²) must travel through the under-dense plasma where the high electron temperatures ($T_e \sim 5$ keV) and long density scale lengths at quarter critical ($L_{nc/4} \sim 500\mu\text{m}$) make it particularly susceptible to laser-plasma instabilities (LPI). These instabilities have the potential to be highly detrimental as they scatter laser light away from the target and generate plasma waves far from the ablation front which accelerate electrons to suprathermal temperatures, as discussed in Section 2.5. The stimulation of LPI and the competition between individual processes is dependent on the specific laser-plasma conditions from which they are stimulated. Changes in temperature and density scale length can affect which mechanism dominates over the others, and by extension the properties of the hot electron distribution that is generated. Assessing what effect these instabilities will have on a full-scale shock ignition implosion will require accessing the relevant regime and recreating shock ignition conditions as close as possible.

Spherical implosions [115,120,126] on Omega-60, currently the largest direct drive facility, replicated a shock ignition like laser drive that produced Gbar pressure at peak convergence, and showed an enhancement in neutron production from a well-timed shock launch. These experiments successfully demonstrated the shock launching abilities of such a scheme but were limited in their hot electron characterisation because of the limited laser energy and therefore limited capsule size of Omega implosions. These smaller capsules suffer from flow divergence [216] that results in a shorter density scale length for the plasma corona of only $\sim 125\mu\text{m}$, outside the shock ignition regime.

A novel platform was thus established for creating the laser-plasma conditions exceeding those that can be created with spherical or conventional planar targets on Omega. This offers the opportunity to explore a laser-plasma parameter space previously unexplored and removing the restriction that this can only be performed on the largest laser facilities, allowing the study of ignition scale direct-drive implosions to be achieved with sub-ignition

drivers. This platform is based on an open conical target and laser beam repointing to significantly improve the coupling of energy to the target, generating longer and hotter plasmas. An experiment was designed around this new concept that used one set of beams to create a shock ignition-like ablation plasma and a second set of higher intensity beams to simulate the shock ignition spike. Convective stimulated Raman scattering was identified as the dominant LPI mechanism, producing hot electrons with modest temperatures (~ 40 keV) and conversion efficiencies ($\sim 2\%$).

4.3 Experimental Set-Up

A basic schematic of the experiment is shown in Figure 4.1, showing the two sets of beams in images a) and b), the conical target discussed in Section 4.3.1 and a second target labelled as the exploding pusher. The target was first illuminated by a set of 10 beams at an intensity of $I \sim 6 \times 10^{14}$ W/cm² to produce a shock ignition-like ablation plasma, that will be referred to as “low beams” in this chapter. A total of 4.8 kJ (480 J/beam) frequency tripled to 3ω (351 nm) was delivered across all beams in a 0.5 ns flat top pulse with a 0.5 ns rise and fall time. These beams were fitted with the SG5 phase plates discussed in Section 3.2.1. A second set of 10 beams (again at 3ω) were more tightly focused using E-IDI phase plates with a smaller spot size to replicate the high intensity spike and will be referred to as the “high beams”. High beams of increasing on-target intensities were used for different shots, controlled by the energy in these beams. It was inferred from radiation-hydrodynamic simulations that when these beams delivered the full 4.8 kJ of energy, an intensity of $I = 8 \times 10^{15}$ W/cm² reached the $n_c/4$ surface. The high beam pulse shape was the same as for the low beams, with the relative timing of the two pulses enabling some control over the plasma conditions at the time the high beams are delivered.

An exploding pusher was deployed to provide a proton backlighter for radiography of the shock wave, and can be seen in the bottom left of each image in Figure 4.1. This capsule was imploded by the remaining laser beams not used for the main target interaction, and contained D-He₃ whose fusion reactions would create MeV protons [218]. In addition to the protons, the exploding pusher produced a second source of x-rays that impacted the measurements of all x-ray diagnostics. This source was separated in both space and time which meant that its contribution could be estimated and removed from certain diagnostics

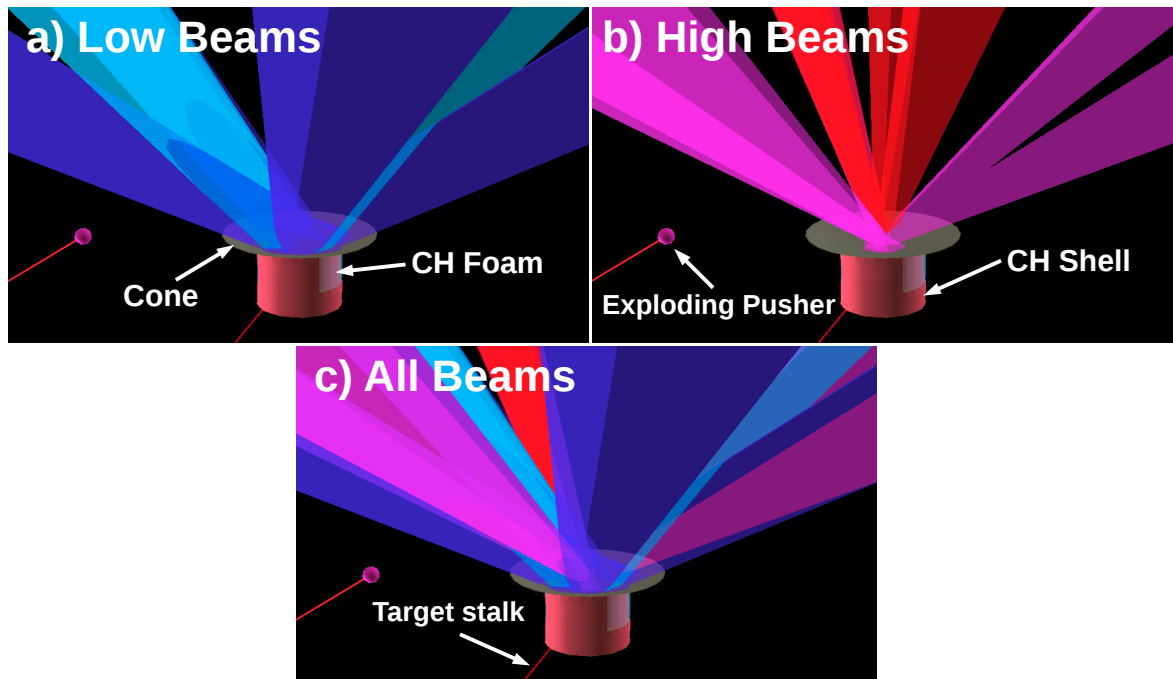


Figure 4.1: VisRad-generated [217] images of the target illumination. In each, the cone target can be seen and is held in place by a stalk. Attached to the back of each cone is a CH cylindrical shell containing a low density foam that was intended to allow the high beam driven shock wave to propagate through and could be radiographed, discussed further in Section 4.3.1. An exploding pusher capsule can be seen in the bottom left that acted as a proton backlighter through a window cut in the CH cylindrical shell. Image a) shows the low beams with the light blue cone angled at 48° to the target normal and the purple cone at 62° . In image b) the red and pink cones are the high beams angled at 23° and 62° to the normal respectively. Image c) shows all the target beams.

but with an increase in the uncertainty of the inferred results.

4.3.1 Target Designs

The different target designs used are illustrated in Figure 4.2, where the relative thicknesses and dimensions are given. Three types (A, B, and C) were conical with a wide half cone angle of 76° . Each target had a front facing layer CH, typically $40 \mu\text{m}$ thick, to mimic the ablator layer of a direct drive ICF capsule. This was followed by a thin tracer layer of copper that was varied in thickness, typically $5 \mu\text{m}$. This layer was added as a means of diagnosing the hot electrons produced in the ablation layer as they travel through the target. Characteristic K_α line emission will be produced from collisions between the hot electrons and the copper atoms, whose total yield can be diagnosed to provide the hot electron population energy. Further to this, the copper layer will be more efficient at producing bremsstrahlung from the

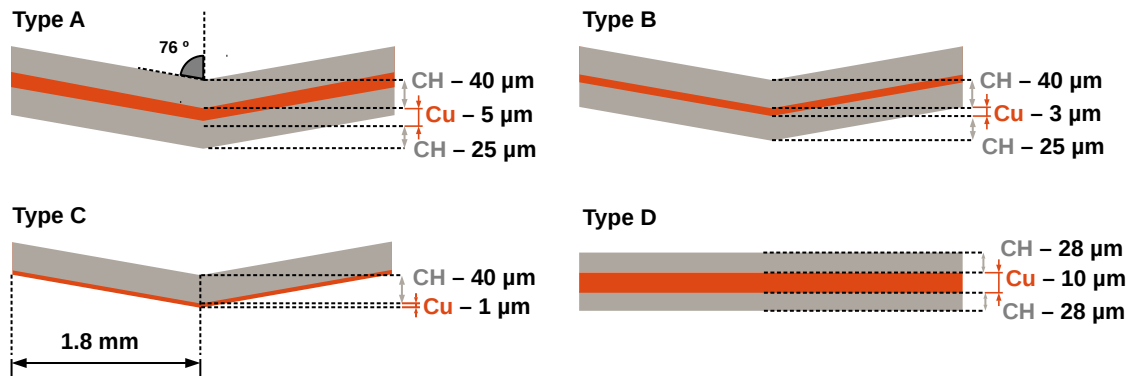


Figure 4.2: Four multilayered target types used throughout the experiment. Types A, B, and C were conical targets with a half cone angle of 76° consisting of a preliminary CH ablator layer followed by a thin Cu fluorescor layer and a CH backing that was omitted for type C. A flat planar target was used in order to produce a shorter density length scale plasma which had a similar target composition to the conical ones, with changes made to account for different laser absorption.

hot electrons due to its higher atomic number [219], increasing signal for diagnostics that rely on bremsstrahlung measurements.

A tamping layer was added to the rear of most of the targets to reduce the number of electrons that are able to recirculate back into the copper layer, called refluxing, and to limit the decompression of the copper layer before the high beams are turned on. This back layer was omitted from type C targets to allow this refluxing of electrons back into the copper layer. A flat planar target, type D, was also used in order to enable the study of shorter density scale lengths, with a thinner ablator layer due to the weaker energy coupling and thus lower ablation rate. The different copper thicknesses were to account for the changing photon yields which ensured that a detectable and statistically significant measurement was achieved for each shot whilst not impacting the physics being investigated.

Not shown in Figure 4.2 was the addition of cylinder 2 mm in diameter that was attached to the rear side of each target. This cylinder had a $30\ \mu\text{m}$ CH wall to act as a support and was filled with a low density CH foam. The illumination of the target with the high beams drives a shock wave that would travel through this foam filling. The aim of adding this cylinder was to produce radiography image of the travelling shock wave using protons produced by the exploding pusher, seen in Figure 4.1, in order to determine properties like shock strength and speed. These protons would pass through a window cut out of the plastic wall and act as a backlighter. A Nickel grid with $19\ \mu\text{m}$ wires and a $125\ \mu\text{m}$ spacing was attached to

the main target to act as a fiducial. However, no quantitative analysis could be performed on the radiography data, potentially due to charging of the grid, and the results will not be included in this thesis. A second Cu fluorescor layer was also added to the rear of the cylinder.

Hot electron characterisation was performed with the Hard X-ray Image Plate (HXIP) diagnostic, a nine channel and time integrated hard x-ray spectrometer, and the three channel time resolved Hard X-ray Detector (HXRD), both discussed in Section 3.5. The line emission from the Cu tracer layer was measured by two Bragg crystal based diagnostics; the Zinc von Hamos (ZVH) spectrometer and the Spherical Crystal Imager (SCI), both discussed in Section 3.4. ZVH was used to provide the total hot electron population energy and SCI gave a qualitative measure of the divergence of the hot electrons. Backscattered laser light was collected by the Full Aperture Backscatter (FABS) diagnostic on the 23° cone of high beams, providing temporal and spectral information of the LPI present.

4.3.2 Ablation Plasma Conditions

The plasma conditions produced by the low beams were determined by detailed simulations of their target illumination. The radiation-hydrodynamics code *h2d* [220] was used for these simulations (see Section 3.8.1). A 2D and cylindrically symmetric target was simulated, with 3D ray tracing for the lasers and the SESAME [213] database was used for the equation of state.

Optimisation of the target and beam configuration was needed to improve the coupling of the laser energy to the target. Due to the spherical arrangement of the Omega beams, all illumination of the target would be off normal for a conventional planar target. The polar angles of the clusters to normal were 23° , 48° and 62° , where large angles of incidence have greater levels of refraction and are thus unable to reach higher densities where energy deposition is increased. A conical target was used instead to reduce this refraction by decreasing the angle of incidence and thereby coupling more energy to the target. The beams were repointed to beyond the axis of symmetry such that they were incident on the surface of the target facing them, further reducing the angle of incidence. The density scale length is also increased by the restriction of the plasma flow divergence from the conical target. The cone remains wide enough such that simulations show there is minimal flow convergence on axis and no resulting plasma jet. With these improvements, the coupling of the laser energy

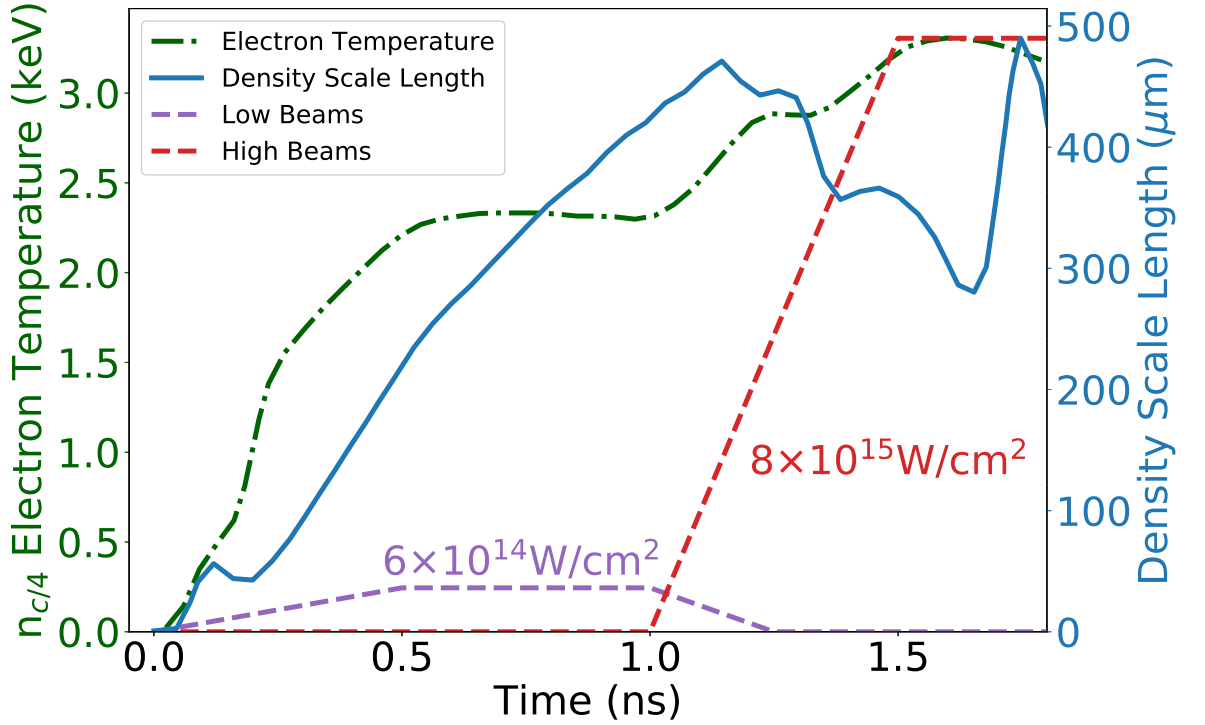


Figure 4.3: Evolution of the ablation plasma conditions at the quarter critical density created by the low beams as simulated by h2d. The electron plasma temperature is plotted as the green dot-dashed line whose axis is on the left and the density scale length is the solid blue line with its axis on the right. The intensities of the low and high beams are given as the purple and red dashed lines respectively.

was increased from 60% to 90% [215], and longer density scale length plasma with higher temperatures can be produced.

The temporal evolution of plasma conditions at the quarter critical density are shown in Figure 4.3. The illumination of the low beams in the first \sim ns produces an ablation plasma with shock ignition like characteristics before the high beams are switched on. The decrease in the density scale length from 1-1.5 ns is due to the increase in ablation from the ablation front from the high intensity beams that compresses the under dense plasma at the quarter critical. This behaviour is expected to be similar to that of an actual shock ignition implosion. It can be seen that the additional energy from the high beams will augment the ablation plasma, heating it further. It can be inferred from the graph that at the point which the high beams interact with the target, the approximate conditions were a plasma temperature of $T_e \sim 3$ keV and a density scale length of up to $L_{n_c/4} \sim 450 \mu\text{m}$.

4.3.3 Reference Shot Subtraction

The illumination of the target by the low beams will itself have its own laser-plasma interactions and produce a population of hot electrons, in addition to the primary population produced from the later timed high beams. This additional population will also interact with the target, producing bremsstrahlung and K_α emissions. For time integrated diagnostics, such as those that use image plate, these two populations will be indistinguishable and appear as one single combined set of signals on the detector. In order to account for this, a reference shot was taken that used the low beams only, so that this additional population could be characterised, and its contribution to the total signal could be found.

The characteristics of low beam generated hot electrons, and the hard x-rays they emit, will be determined by the laser parameters and target type used. It was assumed that the temperature of the hot electrons generated by the low beams remained constant for each shot, and that only the total radiation yield changed. This assumption is based on the consistent low beam laser intensity and subsequent ablation plasma conditions, both of which determine the hot electron population temperatures. An estimate for the changing radiation yield was found from the time resolved HXRD diagnostic, where the low beam population produced a distinct signal from the high beam population. Differences in the low beam yield arises from changes to the set up that include the use of SSD on certain shots, the inherent variance in the delivered energy, discussed in Section 3.1.2, and the target type, primarily from the changing Cu thickness.

The left-hand image of Figure 4.4 shows the low beam bremsstrahlung emission profile from the reference shot as recorded by HXRD. The peak in signal and decay is the result of the scintillator detector, and the apparent displacement of the low beams reaching peak intensity and the recorded signal reaching its maximum being due to the delay in response time of the scintillator, as discussed in Section 3.5.2. The signal amplitude decreasing for increasing channel numbers is a result of their increasing filtering. The image on the right shows the bremsstrahlung emission profile for a shot that used both the low and high beams. There are two clearly visible peaks in the emission that begin at ~ 0.5 ns and 1.5 ns which correspond with the low beams and high beam reaching their peak intensities respectively, the timing of which is indicated by the vertical dashed lines. The dotted coloured line within each of these profiles is the same reference shot profile shown on the left, where each has been scaled by the same factor, $g_{\text{HXRD}}=0.56$ for this shot.

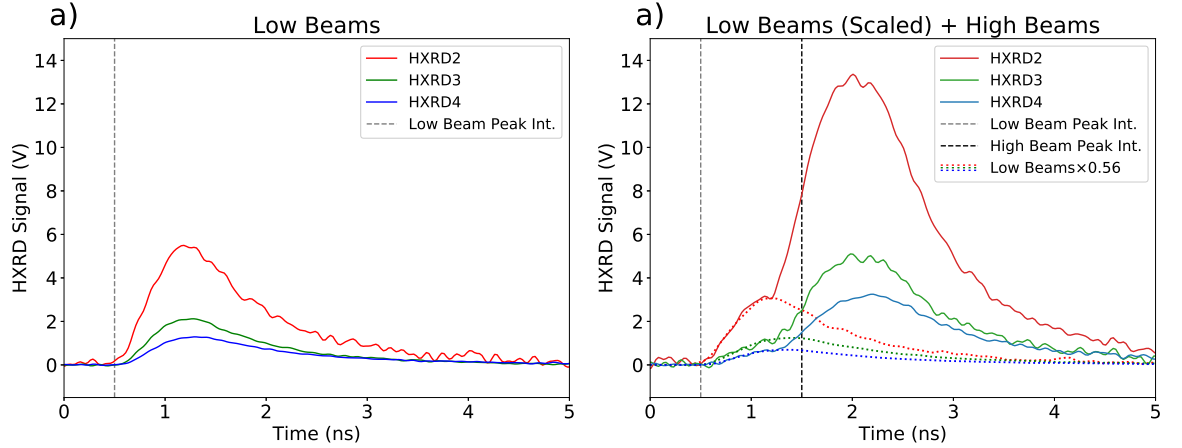


Figure 4.4: a) The bremsstrahlung hard x-ray signal from the hot electrons generated by the low beams only as measured by the HXR diagnostic for the reference shot. The vertical dashed line shows when the low beams reach their peak intensity and the signal can be seen to peak shortly after that. b) The signal from a shot with maximum high beam intensity, where each profile has two clear peaks that follow the low and high beams reaching peak intensity. The profiles on the left have been scaled to match the low beam signals on the right and are plotted as the coloured dotted lines.

The scaling factor was found by fitting scaled versions of the reference shot profiles to the high beam profiles for each channel in HXR independently, and taking the mean. The standard deviation of the scaling factors predicted by all the channels was low, justifying the assumption of a consistent low beam hot electron temperature. Fitting errors of $\sim 5\%$ were found from the procedure. For each of the diagnostics discussed here, the relevant measured quantity had the scaled low beam contribution removed before analysis. A decrease in the low beam scaling factor is seen when using target A which had a thinner copper layer and would thus produce less bremsstrahlung. Another decrease of $\sim 15\%$ is seen when using SSD for the low beams which corresponds with a similar percentage decrease in the energy delivered, suggested that it is not suppressing the LPI but that less laser energy is available to stimulate them.

4.3.4 Shot Summary

A total of 12 shots were taken, 11 with increasing high beam laser energy and intensity, and the reference shot that used the low beams only. Table 4.1 gives a summary of shot specifications, including information about the laser parameters, the target set-up, and inferred low beam scalings.

The error on the energy per beam is the standard deviation across all the beams used.

Shot Number	Low Beam (J/beam)	High Beam (J/beam)	No. High Beams	$n_c/4$ Intensity ($10^{15}W/cm^2$)	SSD	Exploding Pusher	Target Type	$g_{\text{HXR D}}$
88976	433±138*	473±12	10	7.77	No	No	A	0.56
88978	476±9	0.0	10	0.60	No	Yes	B	1.00
88980	481±9	247±34	5	2.74	No	Yes	B	0.86
88981	442±7	221±46	5	1.84	Yes	Yes	B	0.66
88982	482±9	23°: 249±3 62°: 488±6	10	5.68	No	Yes	B	0.87
88984	486±9	479±18	5	5.30	No	Yes	B	0.78
88985	439±8	429±16	5	3.24	Yes	Yes	B	0.67
88986	493±9	493±14	10	8.39	No	Yes	B	1.04
88987	435±6	434±14	10	5.58	Yes	Yes	A	0.71
88988	490±8	492±13	10	8.36	No	Yes	C	N/A
88990	482±8	486±12	10	8.24	No	Yes	C	N/A
88991	489±12	492±10	10	8.35	No	Yes	D	N/A

Table 4.1: Shot parameters including the low and high beam energies, total number of high beams used, the calculated high beam intensity at the quarter critical density, the use of SSD or the exploding pusher backlighter, and the low beam scaling factor. Shot 88976 has an elevated low beam variance due to a single misfiring beam (see text). The $n_c/4$ intensity for the reference shot (88978) is the low beam intensity. Shot 88982 used different energies for the sets of high beam cones (see text). No scaling factor could be found for the final three shots due to overlapping signals on HXR D.

Shot 88976 has an elevated low beam variance due to one of the beams misfiring and delivering a tenth of the requested energy. Were this beam not included, then the delivered energy per beam would have been 477 ± 9 J. Shot 88982 aimed for an intermediate intensity on target and therefore used two different energies for the two cones of beams; the 23° cone delivered ~ 250 J/beam and the 62° cone delivered ~ 490 J/beam. For the remaining shots, all beams used the same energy. The final column gives the low beam scalings as derived from HXR D. The final three values could not be obtained due to the exploding pusher illumination being moved to coincide with the target illumination.

4.4 Laser-Plasma Instability Identification

The Full Aperture Backscatter diagnostic (FABS), discussed in Section 3.7, collects light backscattered by laser-plasma interactions, spectrally disperses it and streaks it in time. Each LPI will have an associated spectral feature that can be used to identify the presence and timing of that instability in the experiment. The spectral range of FABS can

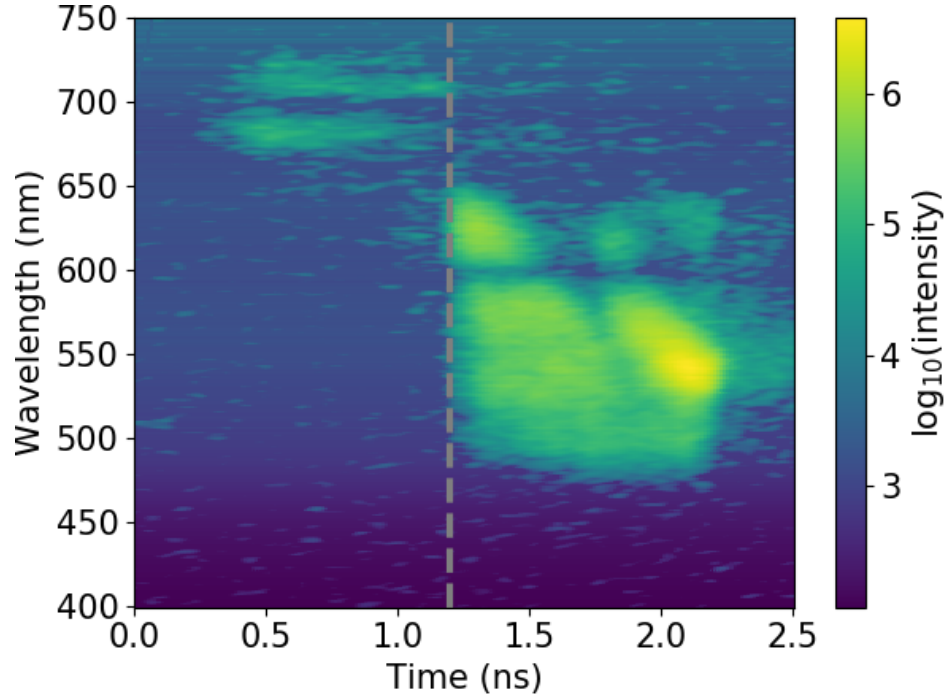


Figure 4.5: Backscattered light collected by the FABS diagnostic that gives both temporal and spectral resolution. The vertical dashed line represents the low beams turning off and the high beams tuning on. The doublet feature in the top left centred on ~ 702 nm is attributed to the TPD instability from the low beams, while the broad feature on the right is consistent with convective SRS from the high beams. The low emission feature at ~ 600 nm is artificial and the result of damage on the FABS sensor.

detect backscatter signatures from both convective and absolute stimulated Raman scattering (SRS), and two plasmon decay (TPD) instabilities, which are discussed in Section 2.5.

An example FABS backscatter data is given in Figure 4.5 where the vertical axis is the wavelength of the backscattered light and the horizontal axis is time. The colour bar gives the intensity of the backscattered signal and is plotted on a logarithmic scale. The vertical dashed line indicates when the low beams are switched off and the high beams are turned on.

The doublet feature present in the first nanosecond centred on ~ 702 nm (top left-hand corner) is characteristic to the TPD instability [221,222]. This is identified as an odd-integer multiple of $n\omega_L/2$ where ω_L is the frequency of the laser, in this case $n = 1$. The timing of this signal corresponds with the low intensity beams only, with no significant signal once these beams turn off and the high beams turn on. The broad feature at 450-600 nm which is present from approximately 1-2 ns is indicative of convective SRS [223]. The broadband

emission is a result of this radiation being scattered at varying electron densities as the pulse travels up the density gradient. Backscatter at the wavelengths shown are from electron densities ranging from 0.04-0.16 n_{crit} , well below densities 0.22-0.25 n_{crit} where TPD and absolute SRS can occur. The SRS threshold parameters given in Equations 2.18 and 2.17 are exceeded for the peak intensity of the high beam pulse.

The absence of the features for absolute SRS and TPD from Figure 4.5 does not definitively eliminate their presence in the experiment. It is possible that these LPI were in fact stimulated within the plasma but that their backscattered signals did not reach the FABS diagnostic. The backscattered light will undergo inverse bremsstrahlung absorption as it exits the plasma and can also be refracted away from a direct line back to the diagnostic by the density gradients in the plasma. Absorptions of up to 98% have been reported [224] for absolute SRS backscattered light in similar planar experiments. In those experiments, a significant reduction in the backscatter signal from the quarter critical is seen when increasing the angle of incidence of the backscatter diagnostic. Features that were clearly visible at normal incidence were not seen at 50° from the target normal. For the experiment presented here FABS was only used on beams at 23° which presents the possibility that absolute SRS was stimulated but that it was not detected.

The intensity of backscatter was seen to increase when the intensity of a single set of high beams were increased in energy and intensity. When a second set of high intensity beams are used though, no further increase in backscatter signal is observed despite the collective intensity of overlapping beams increasing. This suggests that the observed convective SRS is the result of single beam interactions, and not multibeam.

The competition between the instabilities can be explained by the changing laser and plasma conditions. In early time, the low beams are creating and interacting with a steep density gradient, initially the solid target and later an expanding plasma. This short density scale length inhibits convective SRS growth and enables TPD to dominate. Once the long and hot plasma has been generated, convective SRS is able to grow and deplete the laser which suppresses TPD and absolute SRS by limiting the energy that reaches the densities at which they occur.

It should be noted that the intensity of the TPD signal cannot be directly compared with the intensity of the SRS signal. This is because the SRS backscatter is the result of a primary process, whereas the TPD signal is inherently secondary. For TPD to be observed, an EPW

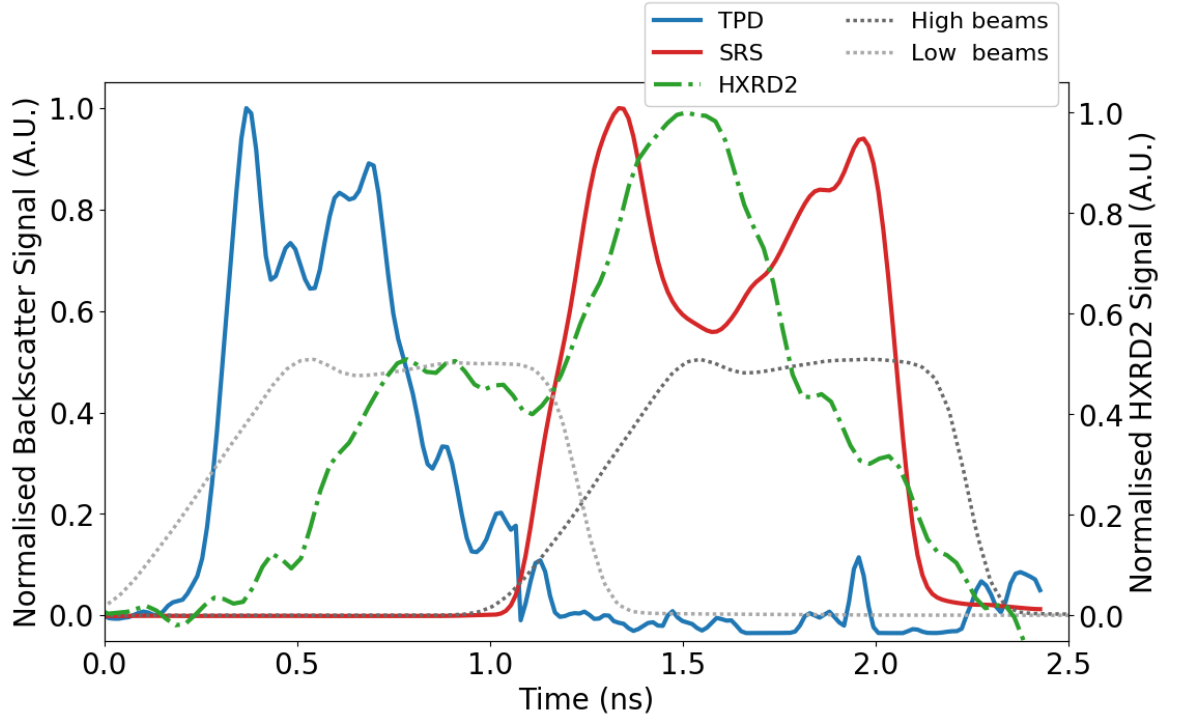


Figure 4.6: A graph showing a comparison between the backscattered signals, the hot electron bremsstrahlung, and the laser beams. The solid blue and red profiles are the spectrally averaged and individually normalised TPD and SRS features from FABS data. The low and high beam power profiles are the grey dotted lines. The dot-dashed green line is the unfolded HXR D2 hard x-ray trace where the two peaks from the two sets of beams can be seen.

must go on to produce a backscattered photon. There are many processes that might be responsible for the TPD emission as discussed by Seka *et al.* [222], with each providing some spectral shift, either red or blue about $\omega_L/2$. The red-shifted component, most likely caused by hybrid Raman-TPD, can give information about the thermal electron temperature where the instability occurred [221]. Once corrected for the Doppler and Dewandre shifts [225], this gives electron temperature $\sim 2\text{-}3$ keV, in line with that calculated from simulations.

The HXR D diagnostic presented later provides the temporal profile of the bremsstrahlung emission from the LPI generated hot electrons. Figure 4.6 shows the unfolded profile of the second channel of HXR D (HXR D2) that is sensitive to photons with energies $\gtrsim 40$ keV. The unfolding process removes the scintillator decay and is discussed in Section 3.5.2. This profile is plotted with the laser energies and the two distinct backscatter features from TPD and SRS. These features have been spectrally averaged in a range that encompasses their feature only, and have been individually normalised in order for them to be plotted on the same scale.

It can be seen that the TPD signal is peaked to the early part of the low beams while the hot electron signal is delayed by comparison. Conversely, the high beam hot electron signal is strongly peaked early in the high beam pulse and decreases for the remainder of the pulse. The SRS backscatter on the other hand remains high throughout the high beam pulse. It is at present unclear why the SRS signal and hot electrons are not better correlated, though it should be noted that both the hot electrons and LPI are measured indirectly and so a direct comparison of timing is difficult.

Improved laser smoothing with SSD has been seen [120, 121, 125] to reduce hot electron energy and temperature. The efficacy of SSD to suppress LPI and hot electrons was investigated by repeating certain shots with SSD on and off. As discussed in Section 3.2.2, using SSD incurs an $\sim 10\%$ energy reduction, changing the delivered intensity between shots. When SSD was turned on, a lower backscattered signal was detected, with an approximate order of magnitude decrease of SRS. No corresponding decrease in either total energy or temperature was seen for the hot electrons. It is unclear why the significant decrease in backscatter does not correlate with a decrease in hot electrons, and could be a subject of further investigation.

4.5 Hot Electron Characterisation

The hot electron population was characterised by measuring their x-ray emission from target interactions, both bremsstrahlung radiation and collision induced characteristic line emission. This characterisation was performed by two filter-detector bremsstrahlung diagnostics, HXIP and HXRD, and a K_α spectrometer, ZVH. The method for analysis of the bremsstrahlung diagnostics was outlined in Section 3.5.3, with the K_α spectrometer being discussed later in Section 4.5.4. Results from these diagnostics are used to infer the temperature and total energy of the hot electron population.

The material and thickness of the channel filters for HXIP were chosen to provide spectral decomposition for bremsstrahlung produced by <100 keV electrons. It's nine channels provide ample coverage over the relevant photon energy range, and electron temperature fitting is well achieved with the spacing of their energy sensitivities. The HXIP diagnostic was the primary diagnostic used to infer the temperature of the hot electron population and its prediction quoted as the final result, with HXRD's predicted temperatures given

for comparison. A comparison of HXR D's and HXIP's capabilities are presented in section 3.5.4.

The ZVH diagnostic was designed specifically for high efficiency detection of K_α sources and has been absolutely calibrated against a single photon camera. HXIP however, has only been cross-calibrated for its total yield and was not designed for determining the total electron energy. For these reasons, only the ZVH predicted energies are given later. The HXIP predicted total electron energies followed the same trend in total electron energy as ZVH but consistently saw larger values.

4.5.1 Monte-Carlo Simulations of Electron-Target Interactions

The spectral emission of the target as a response to incident hot electrons was modelled with the Geant4 code, see Section 3.8.3 for details. The 3D geometry of each target structure was replicated within the simulation environment and hot electrons were projected on it. The resulting bremsstrahlung and K_α radiation was collected by detectors placed at their respective locations, as used in the experiment. Figure 4.7 depicts the target, detectors and injected hot electron paths. The electrons were injected from a disk at a height of $200 \mu\text{m}$ above the target, in line with the expected quarter critical density location. The disk had a radius of $100 \mu\text{m}$ which was based on the overlapped laser focal spot size, and a half cone angle of 45° was chosen, estimated from SCI data. The Livermore physics package [226] was used for its improved low energy modelling of electrons and photons.

To establish the bremsstrahlung emission from the target, a series of 30 many-particle (up to 2×10^9 particles) simulations were performed. Each consisted of a narrow energy bin of electrons that were logarithmically spaced from 10 keV to 1 MeV, encompassing the expected range of electron energies. By recording the target response to mono-energetic electrons, the bremsstrahlung emission for any arbitrary electron distribution can be recreated, reducing simulation time and allowing the testing of different distribution functions.

The spectral emission was recorded by an annulus detector, created by rotating the actual HXIP detector position around the axis of symmetry of the system. This improves the collection statistics while maintaining the correct target-detector orientation. The electrons interacted with a static target at solid density. This does not include the real-world effects of heating, expansion, and compression. The buried copper layer provides the majority of the target's electron stopping power due to it being a much higher-Z material than the CH. The

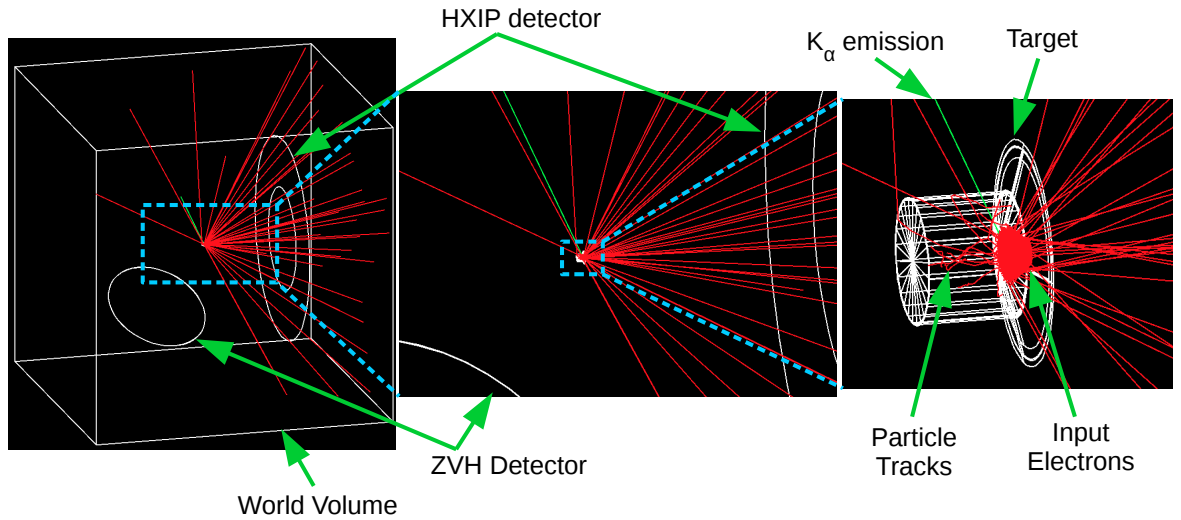


Figure 4.7: Geant4 simulations of hot electrons interacting with the target. The red paths are the electron tracks where their collisions within the target can be seen. The green line represents radiation emission. The electron source details are given in the text. The HXIP annulus and ZVH detector are highlighted, along with the world volume within which they all sit.

radiation-hydrodynamics simulations for the laser target interaction have suggested that this layer remains low in ionisation and maintains its inner shell electrons, and therefore the penetration depth of the hot electrons will remain unaffected. This results in very similar photon distributions, both in terms of bremsstrahlung spectra and K_{α} yield. Similar conclusions were found by Tentori *et al.* [227].

These bremsstrahlung emission simulations were used to find the hot electron temperature. With a temperature established, additional simulations were performed with a single preconfigured distribution of electrons at this temperature and at high resolution, that focused on finding the copper K_{α} emission alone. The set-up of these simulations was identical to those for the bremsstrahlung calculations.

4.5.2 Hot Electron Bremsstrahlung Detection

The HXIP diagnostic was fielded to primarily determine the hot electron temperature. It provides a time integrated dose of the x-ray emission as transmitted through 9 filter channels, where temperature is calculated from the relative transmission through the channels and the total energy can be determined from the absolute dose. The material and thickness of these channels was specifically chosen to provide optimum sensitivity to radiation produced by hot electron of temperatures <100 keV. These temperatures are expected from the SRS and

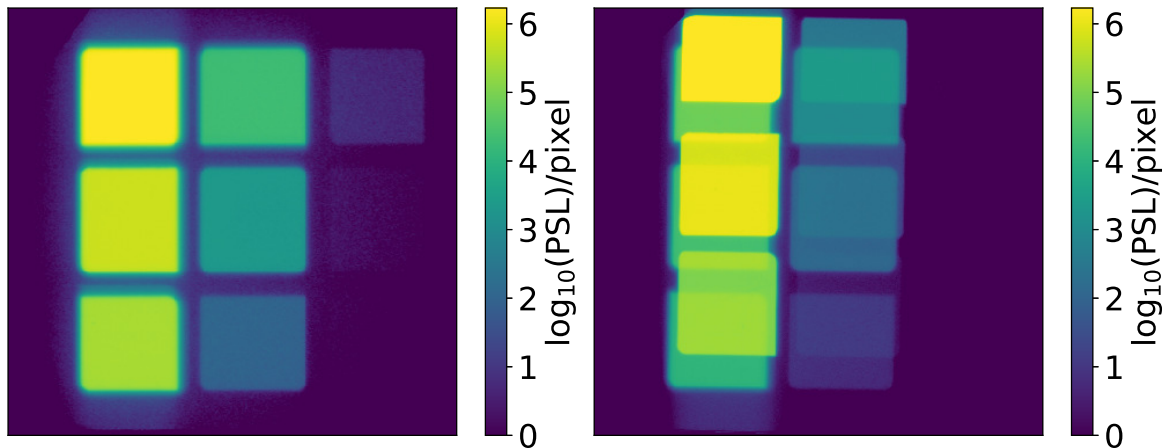


Figure 4.8: Scanned PSL per pixel from the HXIP image plate for shot 88976 on the left that did not use the exploding pusher and shot 88986 on the right that did. The nine exposed regions correspond to the 9 filter channels. Channel 1 with the least attenuating filters is in the upper left, with channels 2 and 3 below it. The remaining channels descend from there with increasing attenuation strength. This image is the fourth scan of the same image plate where the preceding scans had the first three channels saturated, channel 1 can be seen to still be saturating the scanner. The apparent glow around each channel is from scattering within the diagnostic from the filters and the inter-channel shielding.

TPD laser-plasma instabilities.

Two example image plate scans are shown in Figure 4.8 for the only shot that did not use the exploding pusher (left) and a shot that did (right). The overlapping of the signal from the exploding pusher with that from the main target can be clearly seen. The lack of collimation between the channels results in cross-talk of the signal that arises from scattering off the filters and other internal components. This is readily captured in simulations of the detector for a single photon source but increases the complexity of the signal extraction for more than one source.

The smearing of the signal from the scanner, discussed in Section 3.5.1, can be seen as the greater background in the vertical direction than the horizontal. It is typically accounted for by subtracting the mean signal in the regions above and below each channel from its total signal. These background regions were compromised by the signal from the exploding pusher which overlapped with them entirely. The background values had to be estimated by comparing regions exposed by different combinations of emission. This led to increased uncertainty in the channel signals and the first and last channels being unusable for certain shots.

The signal levels recorded for the least filtered channels are typically above the saturation

level for the scanner, and required multiple scans to reach non-saturated levels. The scanning process will decrease the signal on each pixel by a uniform fraction across the entire IP. This fraction was determined by comparing regions between scans that were neither saturated nor at the background level. Repeating this process from the first scan to the last scan and applying the reciprocal of the total decrease in signal provides the unsaturated signal level on the first scan. Further to this, the natural fading of the signal from the time of exposure to the time of the first scan can be calculated from the hold time of the exposed image plate, and reversed to provide the signal level produced in the experiment.

The two fitting parameters, T_{hot} and E_{hot} , are from a $\tilde{\chi}^2$ reduction, the method was outlined in Section 3.5.3. This technique involves scanning over the relevant parameter space and evaluating the $\tilde{\chi}^2$ value at each point, as given by equation 3.20. The measured quantity S_i needed for this equation is the background subtracted signal for each channel. The uncertainty δS_i on these was an estimation of the noise level on the IP. Simply taking the standard deviation of the exposed region can lead to elevated uncertainty due to imperfections in the image plate such as scratches, and the inhomogeneous signal level across the region due to scattering and smearing. Instead, a 5×5 median pixel filter is used to create a smoothed version of the data. The difference between the original data and this smoothed version is assumed to be the result of noise. The uncertainty on each measurement is the standard deviation of this noise for the exposed regions. The value δQ_i of the diagnostic response is estimated by Stoeckl and Solodov [149] where the uncertainties in a cross-calibration with HXRD and image plate calibrations are combined to give $\delta Q_i/Q_i \sim 0.3$.

Up to $N = 9$ data points are available for the reduction procedure where $m = 2$ parameters are fitted T_{hot} and E_{hot} , however in practice the first 2 and last channels are typically not included in the fit so N would be 5. This results in $l = N - m = 3$.

The output of the $\tilde{\chi}^2$ reduction for shot 88976 is shown in Figure 4.9, with lower values of $\tilde{\chi}^2$ indicating a closer fit. The minimum value, and therefore the best fit, is shown by the white cross near the centre. The graphs to the left and below are the projected $\tilde{\chi}^2$ minimum values for each individual parameter and are used to find their associated errors. The three contours plotted are for 25%, 68% (1σ), and 95% (2σ) above the minimum, with the 68% confidence interval taken as the errors on each parameter. The well-defined minimum and closely bunched contours indicate the synthetic population is able to match the data well.

The fitted electron temperatures for all the shots are given in Figure 4.10. The data

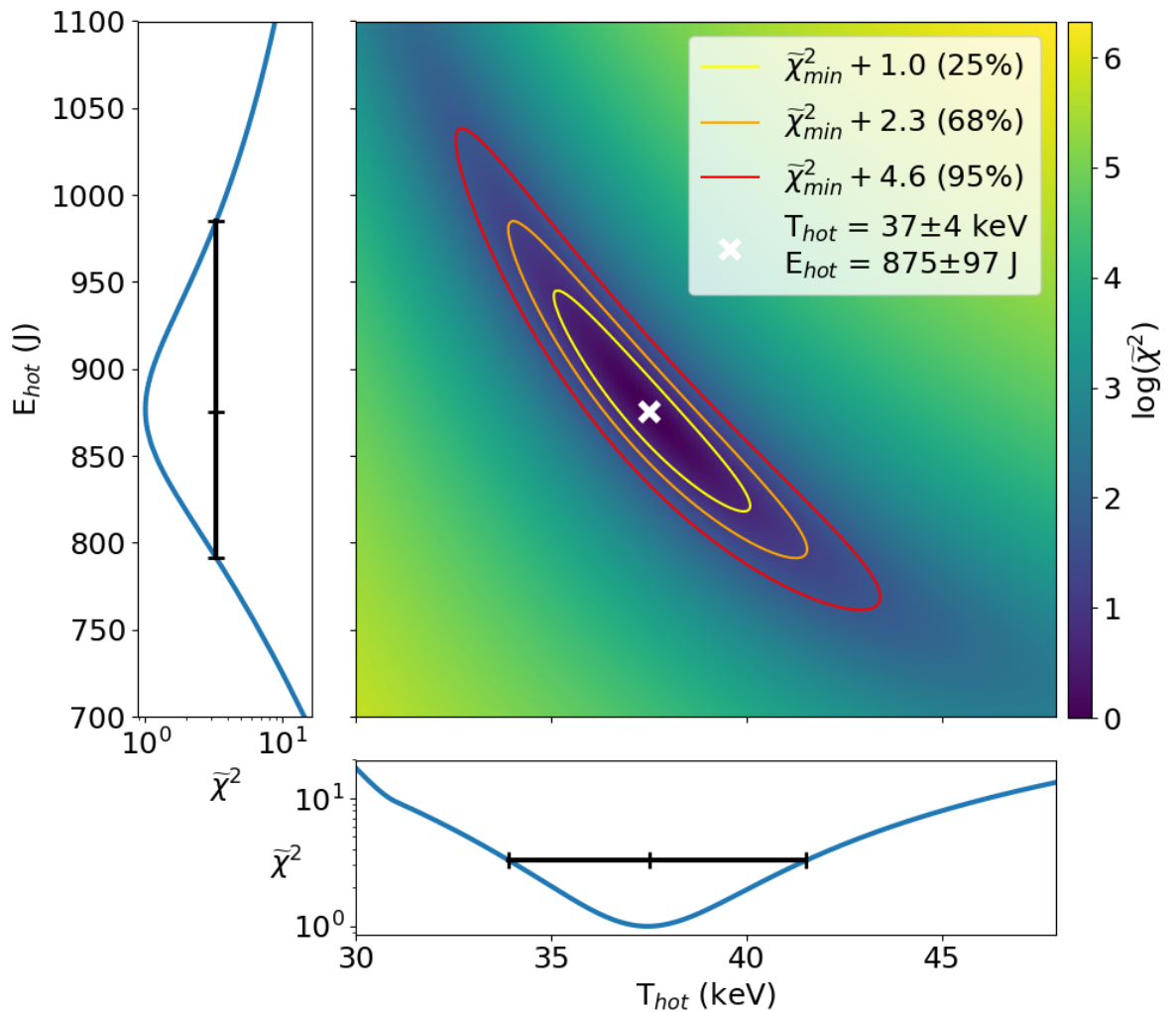


Figure 4.9: The central image is a parameter scan for the $\tilde{\chi}^2$ reduction fitting procedure for the hot electron temperature (T_{hot} x-axis) and total energy (E_{hot} y-axis). The colour bar on the right gives the value of $\tilde{\chi}^2$ for each combination of those two parameters with lower values representing better fit. The minimum value is shown by the white cross and is surrounded by contours of particular values above this minimum (see legend). The graphs to the left and below are projections of the lowest $\tilde{\chi}^2$ values for each of tested E_{hot} and T_{hot} respectively. The minima of these graphs correspond with the best fitting parameters and their errors are for the 68% confidence interval.

point with a green marker at the lowest intensity was the reference shot that used the low beams only, and so is plotted with the low beam intensity. It is interesting to note that the reference shot temperature is similar with the remaining shots that used the high beams in addition to the low beams. The square blue markers are highlighted to distinguish them as having used the unbacked targets that were designed to allow refluxing. Finally, the circular red marker used the flat planar target.

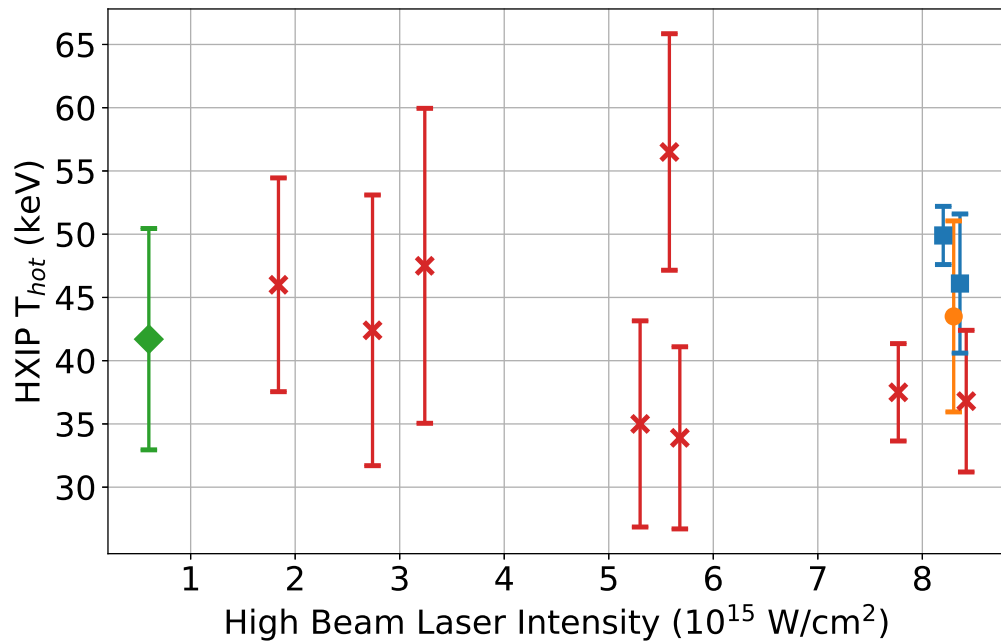


Figure 4.10: Hot electron temperature predicted by HXIP against high beam intensity at the quarter critical density. The green diamond at low intensity is the low beam only reference shot. At high intensities, the blue square markers show the unbacked targets (type C) and the orange circle is the flat planar target (type D).

4.5.3 Time Resolved Hard X-ray Signal

The HXRD diagnostic is a 3-channel hard x-ray spectrometer similar to HXIP described above that uses a scintillator and MCP-PMT to provide a time resolved dose of radiation. A full description of the design and absolute calibration is given in Section 3.5.2. With the available time resolution, the emission from both hot electron populations, those from the low beams and the high beams individually, can be analysed separately as they were displaced in time on the detector. The illumination of the exploding pusher occurred well after the low and high beams for the first nine shots, meaning that its signal did not interfere with the experiment.

Figure 4.11 depicts the hard x-ray signals as seen by HXRD. The graph on the left shows the raw traces from the detector while the image on the right are the same traces unfolded to remove the scintillator decay. The grey and black dotted lines show the calculated low and high beam intensities at the $n_c/4$ surface. The timing of the two hot electron populations with respect to the beams can be seen very clearly with the unfolded traces, where the high beam population in particular aligning almost exactly with the beams.

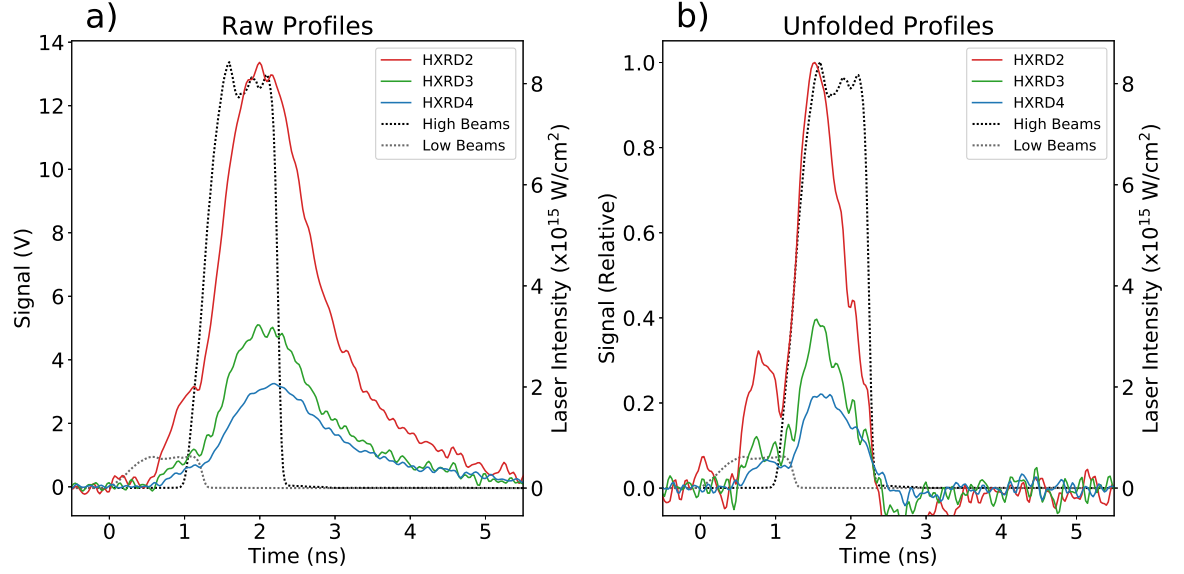


Figure 4.11: The time resolved bremsstrahlung hard x-ray signals detected by HXR. The solid profiles in a) shows the raw scintillator traces with the dotted lines showing the laser intensity of the low and high beams. The same profiles are plotted in b) that have been unfolded to remove the scintillator response time and decay. It is clearly visible for the unfolded traces that the two peaks in emission correspond with the two laser pulses.

Equation 3.19 is again used to determine the optimum fitting parameters. The detector response needed for this are found from Geant4 simulations and the thick-target model for bremsstrahlung given by equation 3.14 was used. The measured quantity used in equation 3.20 is the total accumulated charge from the MCP-PMT, found by passing the voltage shown in Figure 4.11 through a 50Ω resistor and integrating the current in time. The errors in the expected signals are dominated by the 20% uncertainty [119] in the calibration of channel 2, such that $\delta S_i/S_i = 0.2$. The number of available data points is 3 and again the 2 parameters T_h and E_h are being fitted, therefore $N = 3$, $m = 2$ and $l = 1$. The thick-target model for bremsstrahlung was used for the HXR analysis.

A parameter scan and $\tilde{\chi}^2$ reduction was performed for HXR that follows the procedure outlined for HXIP. Figure 4.12 shows the temperature predictions from HXR in orange against the high beam intensity. Again, the green marker is the temperature from the reference shot plotted with the low beam intensity. As discussed in Section 3.5.4, it has been experimentally observed that HXR predicts temperatures higher than HXIP for the same hot electron population by a factor of 1.6 [122], the reason for which remains unclear. The grey markers under each point represent a reduction in temperature by this amount which brings the two bremsstrahlung diagnostics in a far better agreement, with HXIP predicting

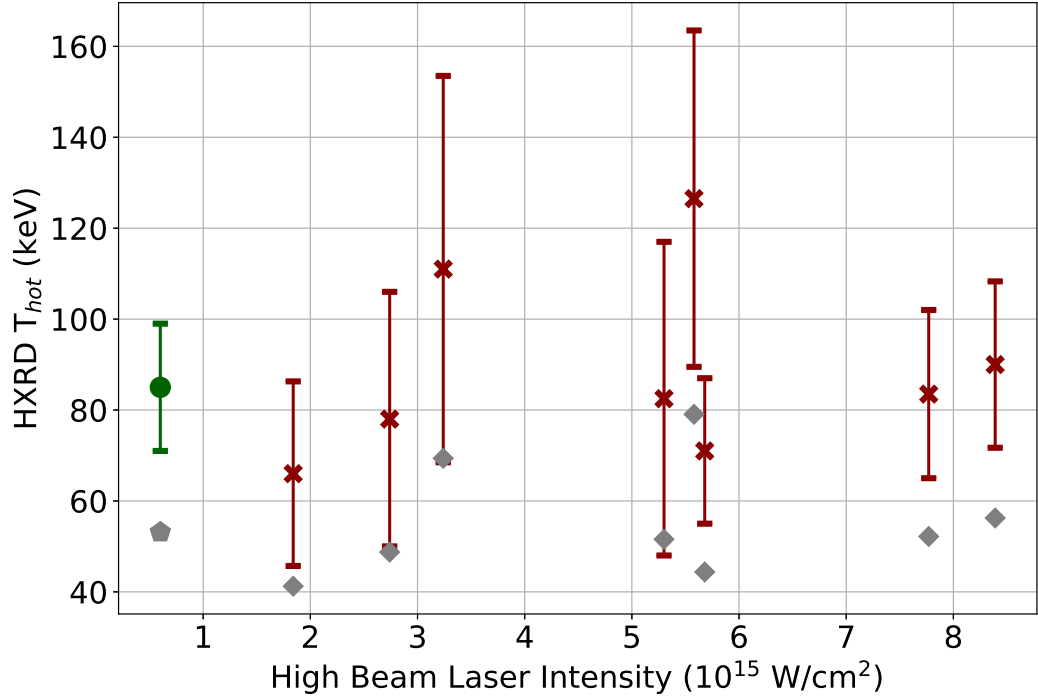


Figure 4.12: The brown crosses show the HXR D predicted high beam hot electron temperature and their errors against the high beam intensity at the quarter critical density. The dark green circle on the left gives the low beam only hot electron temperature. HXR D is known to predicted higher temperatures than HXIP for the same hot electron population. The grey diamonds represent each temperature scaled by a factor of 1.6, as given in [122]. With this scaling, the temperatures are much more in agreement with those from HXIP, see Figure 4.10. Unbacked and flat planar target shots could not be analysed due to overlapping exploding pusher signals.

temperatures of ~ 40 keV. The mean scaling factor between HXR D and HXIP was 2.1 with a standard deviation of 0.3, slightly higher than those reported in [122] but close to those reported in [186].

4.5.4 Hot Electron Induced Cu K_{α} Emission

The Zinc von Hamos spectrometer (ZVH) was used to determine the total energy of the hot electron population. The device itself is designed for high efficiency collection of K_{α} photon sources, such as those from the thin buried copper layer. It has been absolutely calibrated against a single photon counting camera. The experimental yield will be dependent on the number of hot electrons impinging on the copper layer as well as their temperature, since the cross-section for inner shell ionisation is energy dependent [228].

Hot electrons produced in the ablator travel through the target and collide with copper

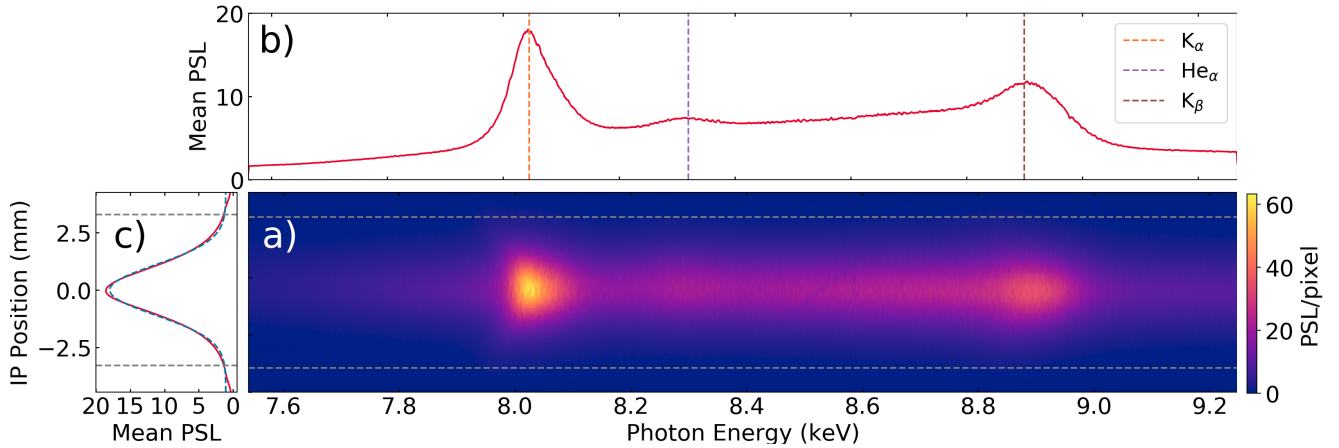


Figure 4.13: a) Scan of an image plate from the ZVH diagnostic. The spectrum is dispersed by a HOPG crystal, with photon energy on the x-axis. The vertical spatial axis is averaged to produce the profile in b), the Cu K_α , He_α and K_β energies are plotted. The spectral axis is averaged to give the red profile in c), where a Gaussian has been fitted to this. The dashed horizontal lines are three standard deviations away from the mean and the IP is cropped to these limits for further analysis.

atoms, liberating an inner shell electron, which in turn results in characteristic line emission through the relaxation of an upper bound electron. This line emission along with underlying continuum radiation is spectrally dispersed by the diagnostic and recorded with an image plate that integrates the signal in time. This again combines the contributions of the low and high beam hot electrons.

Figure 4.13 shows the PSL signal of the scanned image plate for shot 88976 where the high beam intensity at quarter critical was calculated to be $7.8 \times 10^{15} \text{ W/cm}^2$. The profiles above and to the left are the mean signals along the spatial and spectral axes respectively. In the figure above three peaks can be seen at 8.05, 8.35, and 8.90 keV that correspond with the Cu K_α , He_α and K_β respectively [229,230]. These peaks sit on top of a bremsstrahlung background that extends across from left to right in the centre portion of the image plate. For analysis, the image is spatially cropped along the dashed grey lines of the main figure to remove extra background contribution, including the exploding pusher that was not used for this shot. The exploding pusher signal was spatially separated on the IP and was entirely broadband over the range of the detector meaning that its contribution in signal could be readily incorporated into the fitted background. These cropping values were chosen by fitting a Gaussian function to the spectrally averaged profile, that is plotted in blue on the left image, and were three standard deviations from its centre.

To extract the total K_α yield, several effects must first be accounted for. The spectral axis is found by using the dispersion relation of equation 3.11 and aligning to the known position of the bright K_α peak. The filter attenuation must be removed, where the orientation with respect to incoming radiation is taken into account as this results in an increase in apparent thickness of approximately 5 times its nominal thickness. The calibration factors given by Jarrott [177] are interpolated and applied to the full spectrum. A correction due to the IP fading is made, given by equation 3.2. The signal is integrated along the spatial axis and is further cropped to a region around the K_α line that also includes the He_α . This is shown as the upper grey line in the top graph of Figure 4.14. The K_α and He_α lines are then masked off to isolate the background, to which a low order polynomial is fitted (dashed purple line) and subtracted to provide the line emissions only (solid blue line).

The K_α and He_α emissions are close enough in energy that the broadening present in the lines will cause overlap between the two signals. This overlap must be found and removed to avoid an overestimation of the K_α signal. The fits to the data are shown as dashed lines in the lower graph of Figure 4.14. The He_α is fitted with a single Gaussian function whose energy is fixed at 8.347 keV, the cold emission energy. The K_α peak is fitted with a Voigt profile, again fixed to its cold emission energy of 8.045 keV. A third Gaussian function is fitted to be an approximation for the satellites' emissions from increasing ionisation states of copper. It is constrained to within 100 eV of the K_α line. In reality, a series of profiles would need to be fitted, one for each of the increasing ionisation states. The fitting for the K_α line and satellites is done only to improve the fit for the He_α . The final value for the total K_α photons is found by subtracting the fitted He_α signal and integrating the remaining profile.

It has been assumed that the only contribution to the K_α signal was from hot electrons. Photons from the ablation plasma also have the potential to excite a copper inner shell electron and produce K_α emission. Simulations have suggested that this photo-excitation did not contribute a significant level of emission and it was assumed that the signal measured was from hot electron induced K_α only.

The hot electron propagation and resulting K_α emission was simulated using Geant4. These provided the K_α yield per unit energy of hot electrons for each given target type. As with the HXIP analysis, the contribution to the total signal from the hot electrons produced by the low beams was removed. This was done using the signal from the reference shot and the relative scalings found from the HXRD diagnostic. The final hot electron energy is then

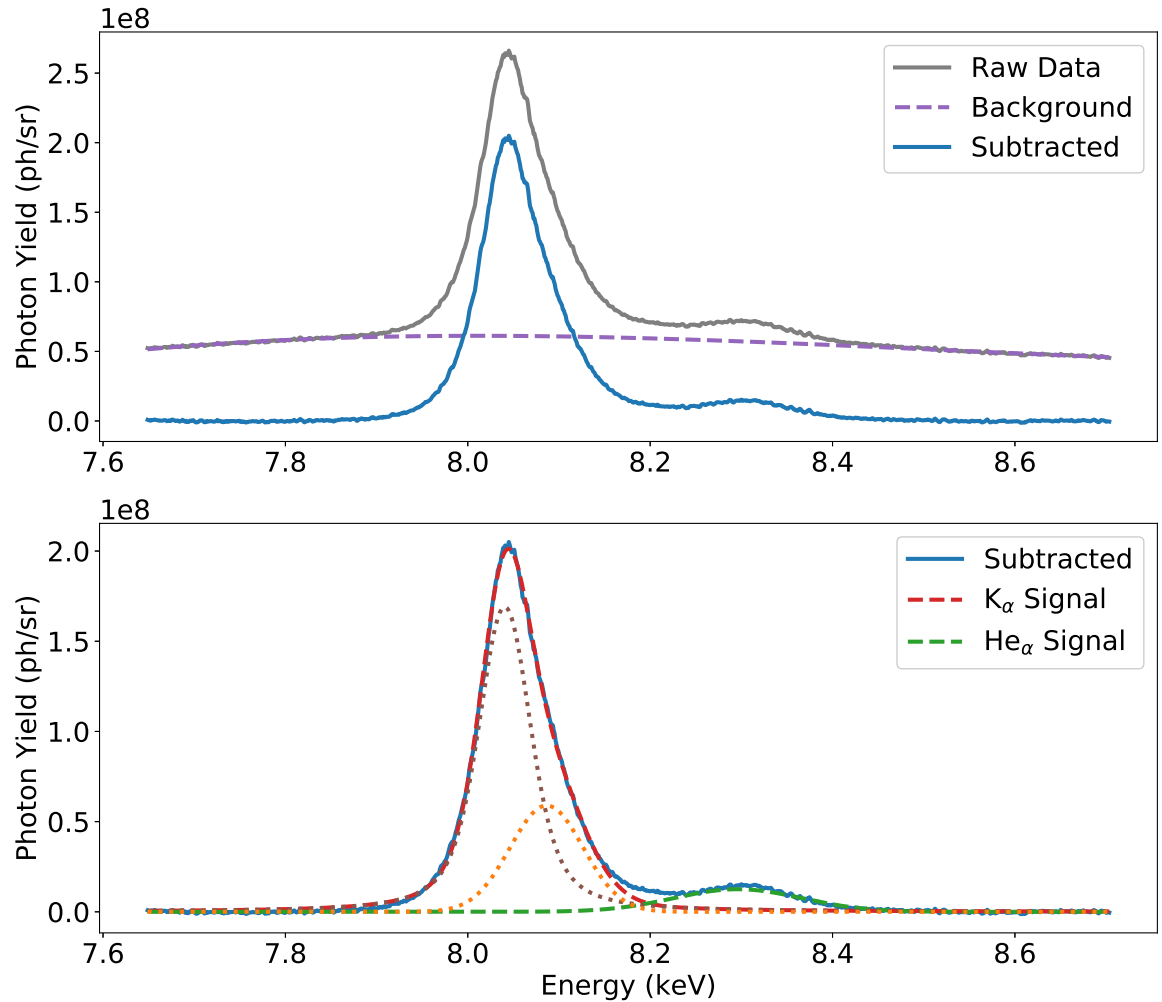


Figure 4.14: The ZVH detected spectrum and analysis procedure. The upper graph shows the raw signal integrated along the spatial axis in grey, to which a background is fitted in the form of a low order polynomial shown as the dashed purple line. This is then subtracted to give the solid blue line in both graphs. The low graph shows the fitted K_α (red dashed) and He_α (green dashed) signals. The K_α signal is fitted with a Voigt function (dotted brown) that has its centre constrained close to 8.045 keV and a Gaussian function (dotted orange) for higher ionisation state emissions. These functions are only used to improve the fit for the He_α removal and not to determine the K_α signal level, see text for details.

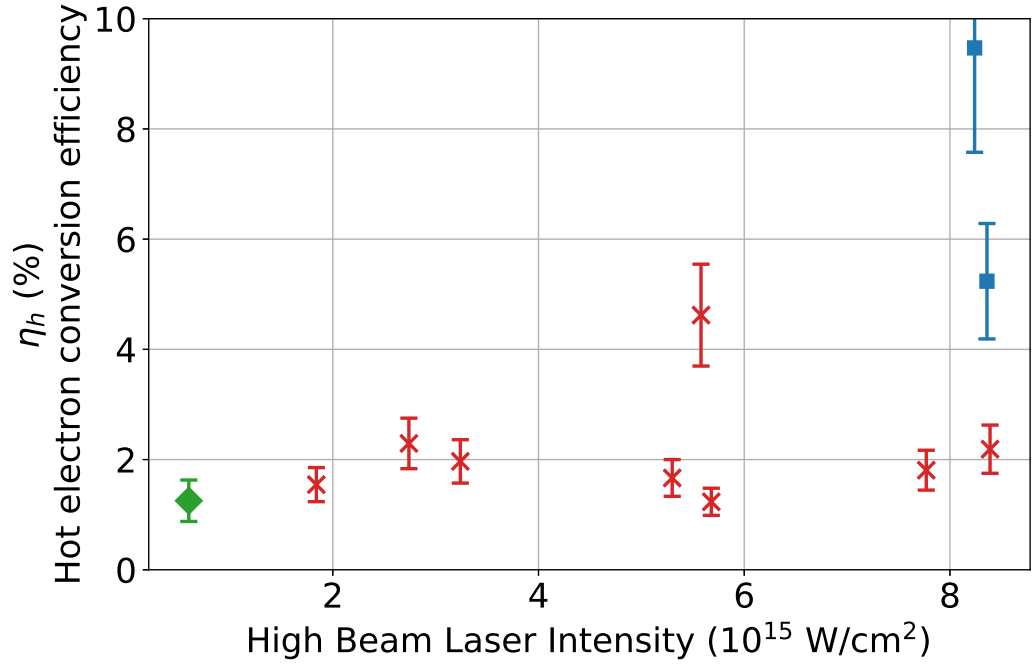


Figure 4.15: Conversion efficiency for high beam laser energy into hot electrons against the high beam intensity at $n_c/4$. The values for the hot electron energies were found with ZVH and the laser energies can be found from Table 4.1. The green diamond is for the low beam only reference shot and is plotted with the low beam intensity. The square blue markers are the unbacked targets which likely have elevated predictions due to refluxing electrons.

found using the following expression,

$$E_{hot} [J] = \frac{N_{K_{\alpha,i}} - g_{\text{hxr}} N_{K_{\alpha,88978}}}{N_{K_{\alpha,\text{sim}}} [1J]} \quad (4.1)$$

Where $N_{K_{\alpha,i}} = \int f_{\nu}(E) - f_{\text{He}\alpha}(E) dE$, and g_{hxr} is the low beam signal scaling factor. A useful metric for modelling implosions is the conversion efficiency of laser energy into hot electron energy, given by $\eta_h = E_h/E_L$ where E_L is the energy of the laser.

Figure 4.15 shows the hot electron signal against the high beam laser intensity. The errors on the measurement arise from several sources, including a 20% calibration error [177] a 5% alignment error [231], uncertainty in simulated yields as discussed by Tentori [227], and the uncertainty in the low beam scaling factor. The conversion efficiency of the laser into hot electrons is relatively constant with the laser intensity, with the exception of the unbacked targets. It also remained relative low at $1.8 \pm 0.3\%$ and is similar to previous estimates. The conversion of the reference was approximately half this value at $1.0 \pm 0.2\%$.

The importance of refluxing is highlighted by the points shown as blue squares. These

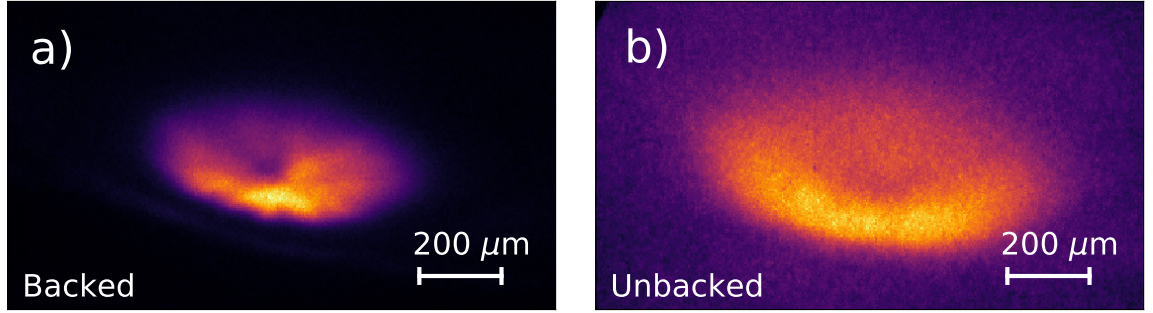


Figure 4.16: Images from the Spherical Crystal Imager diagnostic showing 2D emission of hot electron induced Cu K_{α} from the read side of the target. Image a) show a target type B which had a $40 \mu\text{m}$ CH backing layer that limited refluxing of electrons by adding extra areal density, while image b) shows a target type C that did not have a backing layer. The K_{α} emission is far more dispersed, likely due to electrons refluxing to wider areas of the target.

targets lacked the plastic backing that was present for the other shots resulting in the refluxing of electron back into the copper layer and passing through multiple times, potentially stimulating K_{α} emission with each pass and elevating the total yield. This effect is not modelled in the Geant4 simulations and so the Monte-Carlo simulations are likely underpredicting the K_{α} yield for a given total energy of electrons. The inferred conversion efficiencies for these shots should then be interpreted with this feature in mind as they are most likely elevated.

The effect of refluxing can be clearly seen when comparing the SCI images of the plastic backed targets with the unbacked ones, shown in Figure 4.16. This diagnostic produced a 2D image of the K_{α} emission from the rear side of the target. The bright parts correspond to this emission and thus also to the location of the hot electrons. The wider and more dispersed emission from the unbacked targets is likely from the hot electrons refluxing and reaching further out from the centre.

4.6 Two Temperature Fit

The plasma formed by the low intensity beams produced thermal radiation that likely contributed a measurable portion of the signal to the lowest energy channels of HXIP. The fitting routine outlined previously for HXIP would typically ignore the first two channels and a single temperature fit would reproduce the remaining signals. Including the first two channels requires the addition of a secondary population to model the thermal plasma emission. The

emissivity of a plasma is given by the following equation [10],

$$\eta_{ff} = \frac{16\pi}{3\sqrt{6\pi}} \frac{e^6}{m_e^2 c^3} \frac{Z_i n_e}{\sqrt{k_B T_e / m_e} A m_p} \exp\left(-\frac{\epsilon_\nu}{k_B T_e}\right) \quad (4.2)$$

where ϵ_ν is the emitted photon energy, Z_i is the ion charge, and n_e and T_e (electron density and temperature) both have a space and time dependence. The signal detected by HXIP is given by the integral of equation 4.2 over the plasma volume and time, and for each line of sight from the plasma to the channels. This is simplified for the fitting procedure by assuming that the emission can be described by a single exponential function with a constant slope temperature, as given by

$$f_\nu(\epsilon_\nu, T_{cold}, A_{cold}) = \frac{A_{cold}}{\epsilon_\nu k_B T_{cold}} \exp\left(-\frac{\epsilon_\nu}{k_B T_e}\right) \quad (4.3)$$

A two temperature fitting routine was written to find a secondary set of parameters produced by a population of this nature. It performs a broad parameter scan over the 4 controlling parameters T_{hot} and E_{hot} for the dominant hot electron population seen in the single temperature fits, and A_{cold} and T_{cold} for the ablation plasma population.

Figure 4.17 depicts the $\tilde{\chi}^2$ values for each combination of temperatures, T_{cold} and T_{hot} . Each pixel represents another parameter scan made over the two amplitudes, A_{cold} and E_{hot} , with the temperatures being held constant. The resulting value shown is the minimum $\tilde{\chi}^2$ from that sub-parameter scan. The routine then iteratively repeats over every combination of the two temperatures, performing an amplitudes scan for each. As can be seen from the figure, the secondary population is not well constrained, with temperatures in the range 1-4 keV producing reasonable fits. This is likely due to the secondary population being very low in temperature, thereby contributing only a small fraction of the total signal and to only the first three channels. This contribution is also significantly smaller than the errors on the channels. This parameter scan could only be performed for the shot that did not use the exploding pusher due to its emission overlapping with the target emission.

The parameter space for the second population was also moved to scan for a higher temperature population that has been seen previously [231, 232]. This found no significant higher temperature population for similar reasons as the lower temperature scan shown above. Those being that a single temperature population was able to reproduce the highest energy channels well on its own and that those high energy channels had significant uncer-

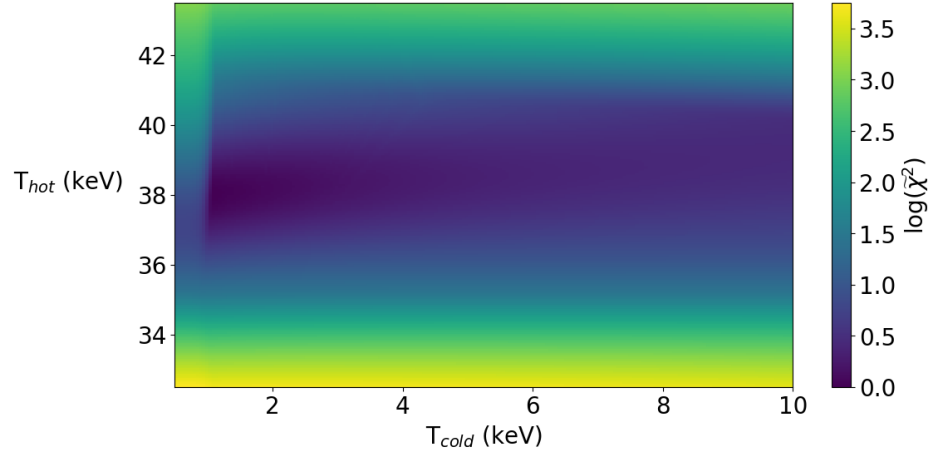


Figure 4.17: Two temperature fitting to HXIP data, parameter scanning over energy and temperature for a cold population (A_{cold} , T_{cold}) and a hot electron population (E_{hot} , T_{hot}). The $\tilde{\chi}^2$ value is shown for each combination of temperatures. Every point is itself the result of a scan over a range of the energies and the resulting minimum of each of those scans are shown here. T_{hot} reproduces a similar temperature to the single population fit.

tainties for their total signals. This does not outright confirm that no higher temperature population exists, but only that it has a low enough total energy to not be detected by this diagnostic.

The ability to detect additional populations is limited by using a single diagnostic. The sensitivity range of the HXIP filters are not well suited for the low <5 keV thermal plasma temperatures or a potentially high \sim MeV population. The weakest filtering channel has an energy cut-off of ~ 12 , higher than the thermal plasma temperature. A greater number of channels with lower cut-off energies could rectify this but would significantly worsen the internal scattering within the device due to the increased signal that would pass through the filters, potentially jeopardising the remaining measurements. Additional diagnostics would be best to supplement these measurements, for example x-ray spectrometers that are sensitive to the range 1-10 keV [233]. Detection of a higher temperature population might be achieved using diagnostics with a greater sensitivity to high energy photons, such as the Bremsstrahlung MeV X-ray Spectrometer [123]. High energy electrons are also more likely to overcome the sheath field that trap lower energy electron to within the target so could be collected and diagnosed by external electron spectrometers [196].

4.7 Further Discussions

Trela *et al.* [126] provides empirical scalings for the expected SRS and TPD hot electron temperature and conversion efficiency, based on simulations and experiments. For SRS these scalings are

$$T_{hot} = 34.3 + 1.5T_{e,n_c/4} \text{ keV} \quad (4.4)$$

$$\eta_{hot} = 12.5 \left[1 - \exp \left(- \left(I_{n_c/4} / I_{th} \right)^{1/3} - 1 \right) \right] \quad (4.5)$$

where the $n_c/4$ subscript refers to the quarter critical density, T_e is the electron plasma temperature as calculated from radiation-hydrodynamics simulations, I is the laser intensity, and I_{th} is the SRS threshold intensity given by equation 2.17. For the laser plasma conditions in the experiment presented here $T_e \sim 3.0$ keV, $L_{n_c/4} \sim 500$ μm , resulting in a threshold intensity of $I_{th} = 6 \times 10^{13}$ W/cm² which is exceeded by all the high beam intensities tested.

Using these scalings, a temperature of ~ 38 keV and a conversion efficiency of $\sim 12\%$ are predicted. The temperature measured in the experiment differ by $\sim 10\%$ compared with this scaling which is well within the inferred uncertainty. Another feature of this scaling is that it is solely dependent on the electron temperature. The consistent temperatures seen for all laser intensities here would then be in agreement with this dependency. The conversion efficiency prediction is far larger by an order of magnitude. This scaling predicts a conversion efficiency of $\sim 8\%$ for intensities well below the threshold and $\sim 12.5\%$ for those well above. This scaling therefore cannot predict the inferred conversion efficiencies seen in this experiment. It does however predict that intensities that far exceed the threshold to have minimal variation in conversion efficiency which is seen here, but that the overall level is very different.

For TPD, the temperature and conversion efficiency scalings are given by the following equations [126],

$$T_{hot} [\text{keV}] = 15.5 + 17.7 \frac{I_{n_c/4}}{I_{th}} \quad (4.6)$$

$$\eta_{hot} = 2.6 \left[1 - \exp \left(- \sqrt{\frac{I_{n_c/4}}{I_{th}}} - 1 \right) \right] \quad (4.7)$$

where the threshold intensity is given by equation 2.21.

The TPD scaling is most relevant for the reference shot. The plasma conditions were taken from the radiation-hydrodynamics simulations presented in Figure 4.3, $T_e \sim 2.5$ keV, $L_{nc/4} \sim 300$ μm . The threshold intensity in this case is then 2×10^{14} W/cm² that is exceeded by the low beams. The scaling however predicts temperatures of ~ 750 keV, far beyond the modest ~ 40 keV seen for the low beams. The conversion efficiency predictions were closer at only 2.6%, still twice the value seen here though. This indicates that these TPD scalings are inappropriate for the TPD conditions obtained in this experiment.

When the flat planar target was used, shorter density scale lengths (~ 200 μm) and lower temperatures (~ 2 keV) were calculated. TPD was observed throughout the high beam interaction on the FABS backscatter data and SRS was suppressed, being observed with much lower intensity. Despite being more heavily TPD dominated, no corresponding increase in hot electron temperature was seen. It is apparent then that when moving between the different regimes, those of shorter density scale lengths and lower temperatures like those seen in the flat planar target, to the longer and hotter plasmas of the strongly absorbing conical targets, that there is a transition from TPD domination to SRS.

4.7.1 Choice of Electron Energy Distribution Function

The choice of electron distribution of function for the hot electrons, either as input for simulations or as the basis for an analytic model, will have a significant effect on the bremsstrahlung photon distributions that are ultimately fitted to the channel signals for HXIP and HXR. A wide variety of distributions have been used in previous work including 2D [93, 227, 234] and 3D [88, 122, 126, 235–237] Maxwell-Boltzmanns, 1D [231] and 3D [238] Maxwell-Jüttner [239] distributions, and unspecified “Maxwellians” [95, 120, 121, 125, 240–242], typically assumed to be 3D Maxwell-Boltzmann.

The dimensionality of the electrons cannot be discerned from this diagnostic alone. The first three dimensions of Maxwell-Boltzmann were fitted to the data, and all produced synthetic signals that reproduced the experimental channel signals to a high degree, indicated by low $\tilde{\chi}^2$ values. The individual distribution functions are presented in Appendix A. The resulting best fitted electron distributions along with their parameters are shown in Figure 4.18 for shot 88976. It is clear that they all agree with the distribution shape in the electron energy range of 100-300 keV because the HXIP effectively measures electrons in this range. The diagnostic itself is most sensitive to photons within the range 20-100 keV which are

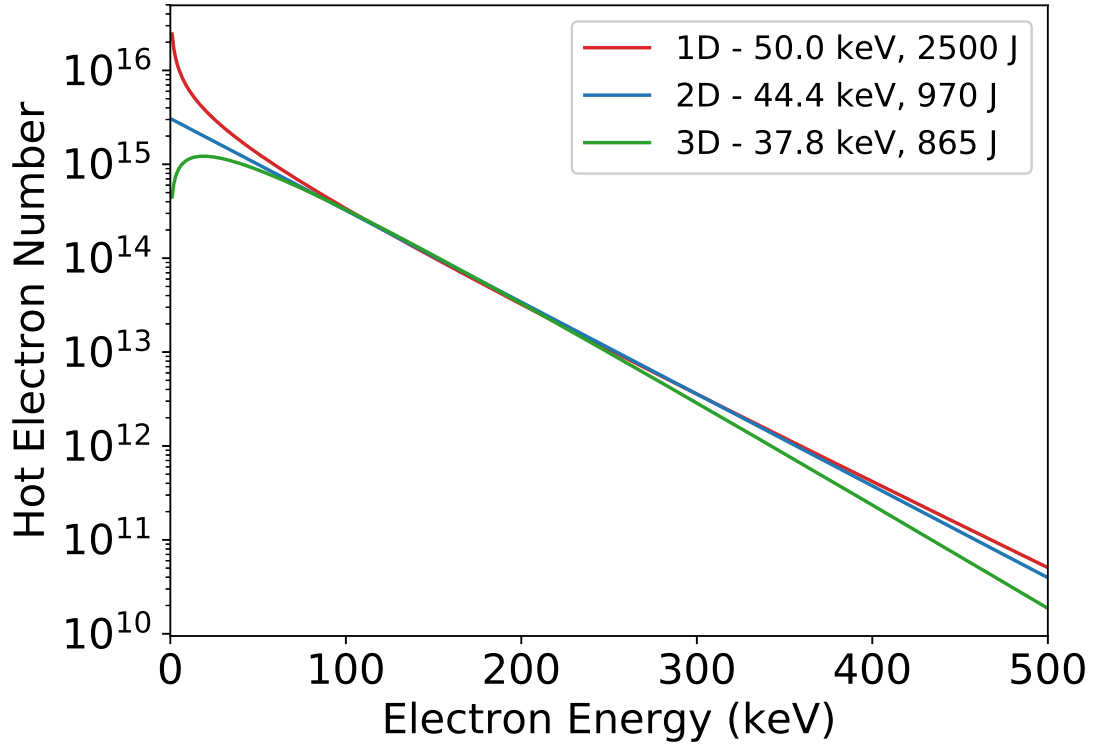


Figure 4.18: Electron energy distribution functions against electron energy. Each emits a bremsstrahlung sources that produces good fits to the HXIP data. The three different functions are 1D, 2D, and 3D Maxwell-Boltzmanns whose fitted parameters are given in the legend.

emitted most by electrons in the range 100-300 keV. This is because the bremsstrahlung spectrum from a single electron of a given energy is dominated by photons at lower energies. This can readily be seen from the following equation which gives the spectral intensity of emission I from an electron of energy ϵ_h [193],

$$I = CZ (\epsilon_h - \epsilon_\nu)^\alpha \text{ (energy/keV)}, \text{ for } \epsilon_\nu < \epsilon_h \quad (4.8)$$

where Z is the atomic number of the material, C is a constant equal to $2.2 \times 10^{-6} \text{ keV}^{-1}$, and $\alpha \approx 1$. This is highlighted to note that although any bremsstrahlung detector is sensitive to a particular photon energy range, it is in effect measuring electrons of a higher energy. This needs to be considered when designing and simulating the target interaction for example, to ensure that electrons of a high enough energy are considered.

The HXIP diagnostic cannot discriminate between the distribution function due to the limited number of channels and the limited energy sensitivity range. From Figure 4.18 it

can be seen that the most pronounced differences are in the low and high electron energies. HXIP is limited in its low energy detection by the additional signal from the plasma emission, and in the high energy by the low sensitivity to high energy photons. Integrating additional measurements from different diagnostics would be needed in order to differentiate between the distributions. Particle-in-cell simulations for laser plasma interactions for ICF relevant conditions have predicted both 2D [243,244] and 3D [116,117,245,246] Maxwell-Boltzmann hot electron populations, showing that there is not a conclusive agreement about what distribution is to be expected.

The importance of the distribution function for the hot electrons is that their effect on a shock ignition implosion, with potential benefit being gained from aiding the shock or degrading performance by preheating the fuel, is largely determined by their spectrum. For an accurate simulation of a shock ignition implosion, the hot electrons must also be modelled accurately, necessitating the determination of their distribution function. Moving forward, it is important that published work be clear and explicit about what distribution is being used in this analysis to ensure that effective comparisons can be made across experiments.

4.7.2 Thick-Target Model Validity

The hot electron temperature and energy were inferred from the HXIP measurements, where both the Geant4 simulated spectrum and the thick-target bremsstrahlung model being tested. The temperature predicted by the thick-target model differed from the simulated spectrum by $\sim 20\%$, within the uncertainty of the diagnostic. The effect on energy was more pronounced, with the Geant4 simulations predicting twice the total energy than the thick-target model. These two models effectively represent the two extremes of energy deposition within the target, and therefore provide reasonable bounds on the temperature and energy estimations. This uncertainty in the total energy is inline with previous published work [247,248] and the uncertainty given for the thick-target model [191,192]. The key difference in the physics assumptions between the two, that being the thick-target assumes no escaping electrons whereas Geant4 does not, could be the reason for this discrepancy in energy predictions, suggesting that this effect and that of refluxing electrons could be present within this experiment.

It has been previously argued [248] that the thick target emission model can be used for thin targets, justified with use of a refluxing model [249]. Such models predict a refluxing

efficiency of nearly 100%, where the hot electrons fulfil the thick-target criteria of depositing all their energy within the target. However, a significant return current can be supplied to the target over the \sim nanosecond timescales involved, reducing the target potential and lowering the refluxing efficiency, conceivably invalidating this assumption.

4.7.3 Improvements for Future Experiments

Improvements could be made to the set-up of this experiment that would improve the data analysis and the confidence level in the results. Thicker copper layers would increase the stopping power to hot electrons, increasing the amount of bremsstrahlung radiation emitted and lowering the effect of electron refluxing. The layer should not be too thick though, such that it begins to significantly attenuate the bremsstrahlung and K_α that is produced within the layer. This could be combined with a thicker backing layer to further suppress refluxing. The thickness of the high-Z layer in previous experiments has been between 10-30 μm [124, 250, 251], and have included an additional thicker backing layer of aluminium [231, 252].

More backscatter measurements would have been able to provide more conclusive results about the dominant laser-plasma instabilities. The FABS diagnostic was available on only one set of beams and at one angle. Further experiments should aim to record data on as many sets of beams as possible, in order to confirm the presence of additional backscattered light.

It was known before the experiment that the addition of the exploding pusher backlighter and the resulting secondary hard x-ray source would impact several detectors, in particular HXIP and ZVH. Future experiments that include a backlighter of any kind should take data on many more shots where the backlighter is not used in order to produce a baseline of measurements. Additionally, shielding of the diagnostics from the backlighter could be implemented however, this was unavailable on Omega for the experiment presented here.

The time resolution of the HXRD diagnostic provided valuable information on the timing of the signals and the yield of the low beam produced hot electron population. It was however, limited by the small number of channels, the close spacing of the energy sensitivities, and consequentially unreliable temperature predictions. Diagnostics based on the same design principles, such as the Fitter-Fluorescer X-ray diagnostic [253] in use at NIF, have a great number of better spaced channels that enables probing over a wider range of photon energies

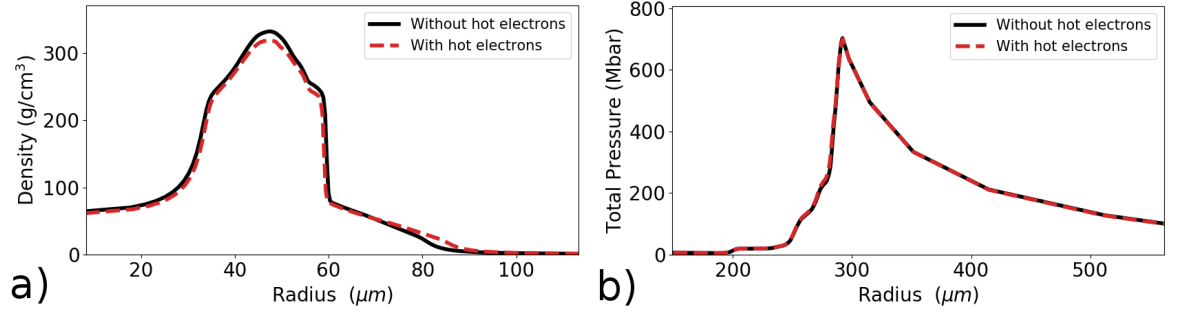


Figure 4.19: Simulations of a shock ignition implosion with and without hot electrons, showing a) the density at peak compression, and b) the pressure generated during the spike. A minimal decrease in density is observed when hot electrons with the characteristics seen in this experiment are included in the simulation. Reproduced with permission from Scott *et al.*, Phys. Rev. Lett. 127, 065001 (2021) Copyright ©2011 by American Physical Society.

and provides the required temporal resolution. This diagnostic would be able to characterise the hot electrons with less uncertainty, it would overcome the impact of the additional signal from backlighters that compromised time integrated diagnostics, and potentially would enable the detection of secondary populations.

4.8 Hot Electron Integrated Radiation-Hydrodynamic Simulations

The potential effect that the hot electrons measured in this experiment might have on a shock ignition implosion was investigated with radiation-hydrodynamics simulations that included laser to hot electron conversion. A 500 kJ implosion set-up [254] was simulated using the 2D arbitrary Lagrangian-Eulerian code Odin [43, 255]. Once the laser had reached the quarter critical surface ($n_c/4$), 2.5% of the energy is converted into hot electrons with a temperature of 40 keV. The hot electron transport, including energy deposition and scattering, is modelled with a Monte-Carlo approach that has been benchmarked against MCNP [256].

The density at peak compression and the pressure generated during the high intensity laser spike for an implosion with and without hot electrons are shown in Figure 4.19. The profile shown in a) shows minimal reduction in the fuel density at peak compression from the inclusion of the hot electrons, indicating that minimal preheating was occurring. The total pressure shown in b) is almost unchanged by the influence of the hot electrons, suggesting that they are neither aiding nor degrading the ignitor shock. The small influence of the hot electrons is thought to be primarily due to the low total energy of the hot electrons.

4.9 Conclusion

The ablation plasma conditions relevant for MJ-scale direct drive shock ignition were achieved on a sub-ignition facility with the use of a novel target and beam repointing scheme. Long density scale lengths ($\sim 450 \mu\text{m}$) and high electron plasma temperatures ($\sim 3 \text{ keV}$) were produced from an energy limited laser, representing a unique platform for studying laser-plasma instabilities relevant direct drive, that remain a significant unknown. With these conditions achieved, the laser-plasma interactions for the shock launching spike of shock ignition were emulated and the hot electrons that they produced were studied.

Time and frequency resolved backscatter measurements allowed the identification of individual laser-plasma instabilities by distinct wavelength features present during the interactions of the two sets of beams. The dominant LPI observed was convective SRS that produced hot electrons of moderate $\sim 45 \text{ keV}$ temperatures, and conversion efficiencies of $\sim 2\%$, found through comparison between multiple hard x-ray detectors. A significant decrease in the amount of backscattered light was seen when using SSD but there was no corresponding significant change in hot electron parameters.

The hot electron characteristics found were used as an input for radiation-hydrodynamics simulations of shock ignition implosions that included a generated hot electron population. The inclusion of hot electrons did not have a significant detrimental effect on the implosion, with pressure and density remaining largely unchanged from the case without them.

The results shown here are an indication that shock ignition might be a viable route to igniting an ICF implosion, and that continued research is justified and necessary. Future experiments are required to characterise LPI and hot electrons using higher energy facilities where the expected ignition scale shock ignition conditions are fully met. Beyond this, MJ-scale shock ignition implosions should be performed at available facilities to further evaluate the concept [257].

Chapter 5

Drive Coupling and Low Mode Asymmetries in Reduced Adiabatic Implosions

This chapter presents results from an implosion experiment performed on the Omega-60 laser facility. Laser pulse designs that keep the imploding fuel on a reduced adiabat, where the increase in internal energy is minimised, have the potential for greater energy gain through the higher areal densities than can be reached. This is beneficial for both conventional hot spot ignition and as the fuel assembly stage of the shock ignition concept where there is greater hydrodynamic robustness due to the lower implosion velocity.

Maintaining a low adiabat offers the potential for larger fuel areal densities and with this, higher gains. There are risks as highly compressible low adiabat implosions are more prone to hydrodynamic instabilities seeded by imbalances in the drive, and capsule and drive imperfections. The shock ignition approach to inertial confinement fusion proposes to use a low adiabat assembly of fuel, achieved through the improvement in robustness from lowering the implosion velocity. This type of implosion must be tested, to evaluate its performance, and to improve the ability to accurately model them.

Contemporary implosion modelling approaches employ empirical laser absorption multipliers to apply a heuristic correction for processes not included in the models, in particular cross-beam energy transfer (CBET) as well as other laser-plasma instabilities. Improvements were made to one such existing multiplier by using data taken in the experiment presented

in this chapter. Time resolved self-emission imaging of the imploding capsule was used to track its trajectory and stability, and these results were compared with post-processed radiation-hydrodynamics simulations. Gated and time-integrated x-ray imagers revealed low mode-asymmetries in the imploding capsules as well as in the final hot spots. Performance of the implosion was additionally assessed by the neutron yield, and through comparison with the simulated yield.

The improved drive multiplier enabled the reproduction of the results from a cryogenic-DT implosion based on this reduced adiabat concept that did not achieve the level of performance that was previously expected from simulation. The areal density, and neutron yield matched closely between experiment and simulation once the improvements to the multiplier were implemented. The pulse shape was reconfigured using the new laser drive and they await further testing.

5.1 Introduction

A series of 12 implosions were tested on the Omega-60 laser facility with novel laser pulse shapes that maintained a reduced fuel adiabat. The targets were warm 860 μm plastic shell capsules with 27 μm thick walls, filled with D_2 gas at 15 atmospheres of pressure. The laser drive used in this experiment included variable power picket and foot powers to control the adiabat of the fuel. A cryogenic-DT version of this design is predicted to be capable of reaching high neutron yields of $>10^{14}$ neutrons, similar to that of the highest performing shots on Omega to date [258].

The radiation-hydrodynamics code HYADES, discussed in Section 3.8.1, is commonly used to simulate ICF implosions, both to validate experimental results and as a step in developing new implosion designs or improving existing ones. It is able to predict the neutron yields well for a wide range of implosion velocities, as can be seen in Figure 5.1 where it is compared with another code Lilac [259]. HYADES is seen to reproduce the experimental results well for yields of $<10^{14}$ but can over-predict for the highest performing shots. Neutron yield is only one measure of performance, and the accuracy of a code's ability to model an implosion cannot be judged from this alone.

The longer term aim is to develop a predictive code that is able to successfully simulate experiments with the minimum number of tuning parameters. An example where a tuning

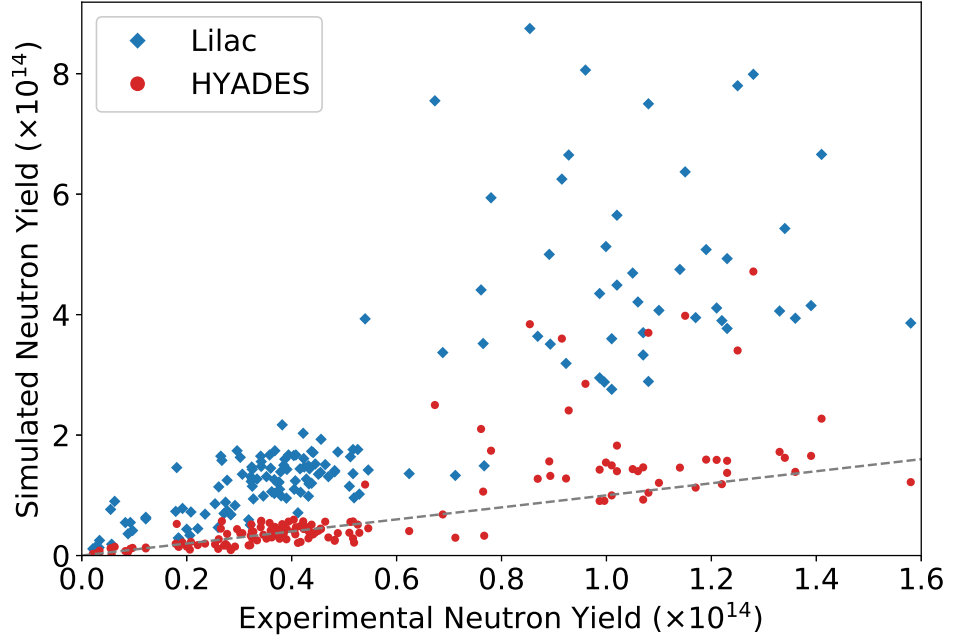


Figure 5.1: Simulated neutron yield against experimental neutron yield for an ensemble of cryogenic-DT direct drive implosions on Omega as simulated by two radiation-hydrodynamics codes, Lilac and HYADES. The grey dashed line indicates a matching of simulated and experimental yield.

parameter is needed is a data driven time dependent multiplier that is used to incorporate the effect that the CBET instability has on the laser intensity that reaches the target. Significant amounts of energy are directed away from the target due to opposing beams overlapping in an underdense expanding plasma corona that can lead to drive asymmetries and, if not properly corrected for, an overestimation in the laser drive on the capsule. One such multiplier, designed by Robbie Scott, uses the analysis presented here to refine, or tune, a CBET multiplier to improve the matching of simulated implosions with an ensemble of previous experiments.

Implosions using this reduced adiabat concept were predicted to have high performances on their own, without the need of a shock ignition-like spike. A cryogenic-DT implosion was performed on Omega-60 to test this concept whose laser design was based on the highest performing pulses of the experiment presented in this chapter. The implosion under-performed compared with predictions based on simulations that used the previous un-optimised CBET multiplier. These metrics and the simulation performance as a whole however, were well reproduced with the tuned multiplier. The pulse has been redesigned to account for the improved laser drive modelling and is intended for further testing on cryogenic-DT implosions.

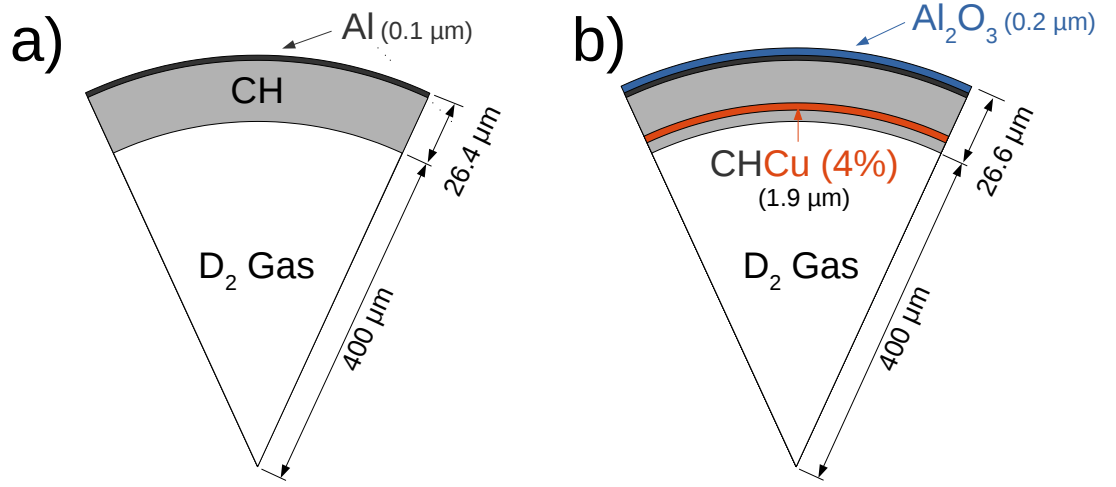


Figure 5.2: Capsule target designs for the warm implosions, a) Plastic shelled D₂ gas filled with an Al shine through barrier, b) Similar plastic shell and D₂ gas filled with a thin Cu doped tracer layer and an extra Al₂O₃ coating resulting in a slightly larger total wall thickness.

5.2 Experimental Set-Up

The warm-DD experiment was conducted using the standard configuration for a spherical implosion on Omega-60. The two target designs that were used are shown in Figure 5.2 and illustrate the size of capsules and the thicknesses of the layers. All the capsules had an outer diameter of $\sim 860 \mu\text{m}$ that included a $\sim 26 \mu\text{m}$ thick CH shell and D₂ gas fill at ~ 15 atm of pressure. A thin $0.1 \mu\text{m}$ aluminium layer was coated on to each target that acted as a shine-through barrier to stop laser light immediately penetrating through the shell. Several targets included a buried $\sim 2 \mu\text{m}$ dopant layer that consisted of CH doped with 4.6% copper and located $1.5 \mu\text{m}$ from the inner surface of the shell. This was intended for diagnosing the hot electron number and divergence. This is not discussed in this thesis due to lack of data, likely a result of low hot electron fluxes.

The addition of the doped layer affected the surface roughness of the capsule during the manufacturing process, resulting in the need for an additional thin $0.2 \mu\text{m}$ coating of Al₂O₃ to help retain the gas fill. The atomic-layer-deposition coating method for this required the capsule to be held in place with a small adhesive that was not coated. This area was approximately circular with an $80 \mu\text{m}$ diameter. The tracer layer, subsequent surface roughness, and additional coating hole can all lead to worsened performance due to seeding of hydrodynamic-instabilities.

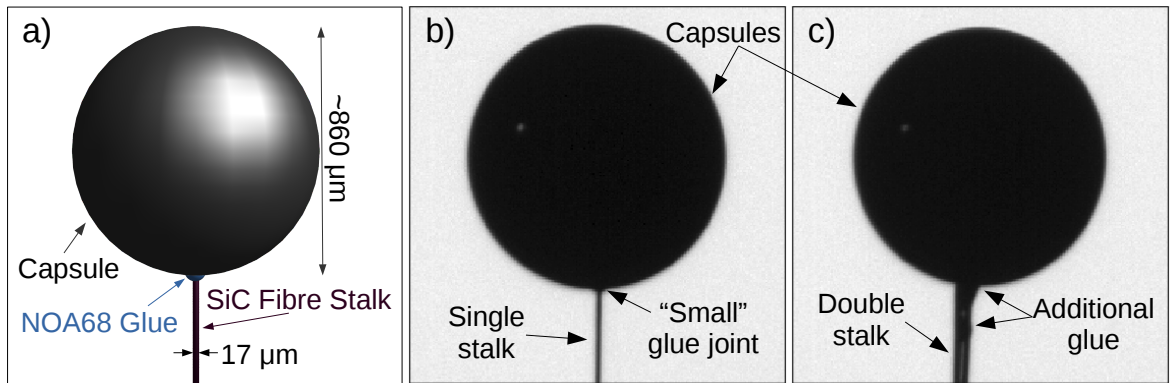


Figure 5.3: a) A schematic and description of the capsule, stalk, and glue. The stalk is to scale with the size of the capsule in the image. b) The standard stalk thickness and glue joint size. c) An additional stalk and extra glue was added to ensure that the capsule remained in place for later shots.

The capsules were held in place using a $17\ \mu\text{m}$ diameter SiC stalk [50, 260, 261] and NOA68 glue [262]. During the experiment, many targets were lost when attempting to align them, the cause of which was attributed to vibrations of the stalk that were too severe for the glue to keep the capsule attached. To ensure stability for the remaining shots, a second stalk was attached with additional glue being applied. A comparison between a regular capsule and one with an additional stalk is shown in Figure 5.3. These images are obscuration photographs of the targets taken by the target viewing system just prior to being shot. The increase in the glue size and the additional thickness of the second stalk are clearly visible, and far larger than in the single stalk case. This resulted in no more targets being lost but it increased the likelihood of seeding perturbations and non-uniformities from the stalk and glue.

The capsule was illuminated with a shaped laser pulse shown in Figure 5.4, delivering 22.8 kJ of 351 nm UV (frequency tripled, 3ω) energy. Each beam was smoothed with 2-dimensional 1-THz bandwidth smoothing by spectral dispersion (SSD), super-Gaussian-5 (SG5) distributed phase plates, and polarisation smoothing that are discussed in Section 3.2. The pre-pulse picket that precedes the main drive is Gaussian shaped with an 110 ps FWHM and variable peak power. The tested peak picket powers of 1.5, 3, and 7 TW total are shown, achieved by varying the energy contained within the pulse, using 162, 372, and 744 J respectively. The purpose of this picket is to launch a weak shock into the capsule in order to set the adiabat profile within the shell. Following the picket at approximately 1 ns is a variable delay to the foot where the foot power rose to 2 TW and was held constant for

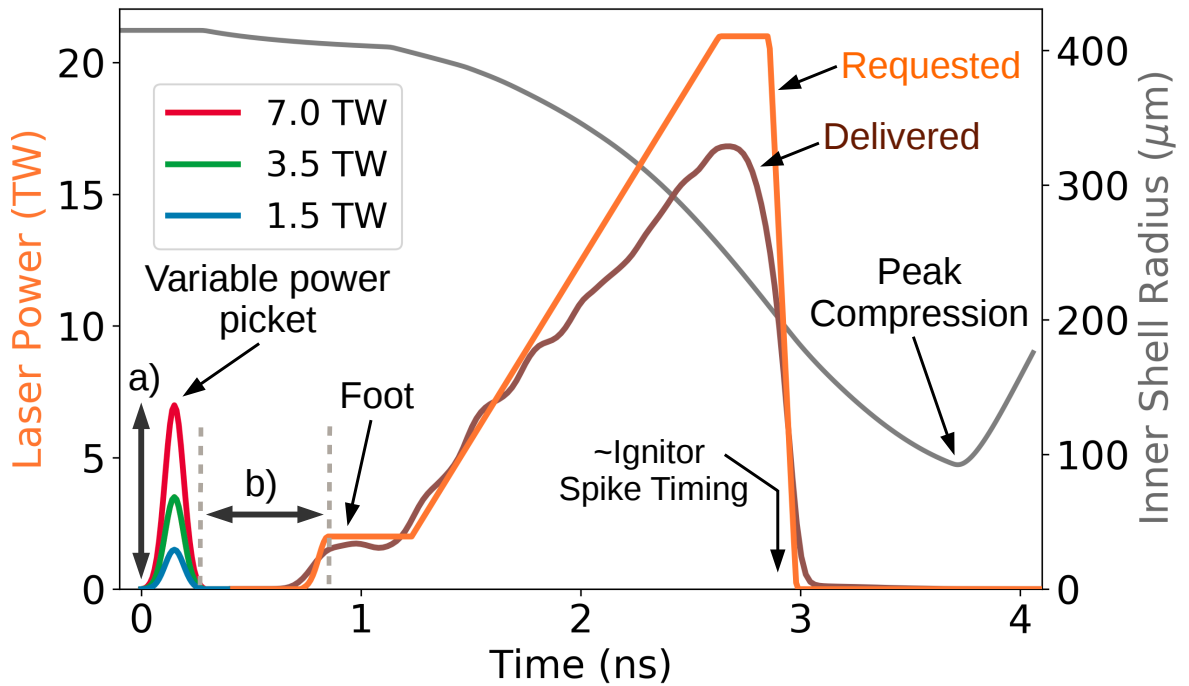


Figure 5.4: Laser pulse template for variable adiabat implosions. The picket power a) and foot delay b) were varied across the shot day to achieve different shell adiabats. The orange profile is the requested laser power, and the delivered laser power is shown in brown. Plotted in grey on the right y-axis is the location of the inner edge of the shell as simulated by HYADES. The capsule will reach peak compression just before 4 ns before expanding back out again. An approximate timing for a potential ignitor spike is shown.

all shots. The timing of the foot, and thus the timing of the shock it also launches, were tested at delays of 25, 40, and 70 ps with respect to the picket. Following the foot, the pulse has a slow and constant rise to its peak power of 23 TW over 1.4 ns. This slow rise in power results in a weaker shock being launched than compared with that of a fast rise, maintaining a low fuel adiabat during the implosion.

Table 5.1 summarises the key parameters for the implosions. The values for the minimum adiabat and the adiabat of the entire shell averaged by its mass were found from HYADES simulations. The correlation between the picket power and minimum adiabat can clearly be seen, with the higher power 7 TW pickets producing higher adiabats of 3-4, with the low 1.5 TW pickets producing minimum adiabat in the CH of ~ 2 . Due to the higher density of CH compared with DT ice, the adiabat for a cryogenic implosion based on this concept would be higher, with a minimum of 3.5.

The fielded diagnostics included self-emission imagers, neutron and proton detectors, a hard x-ray hot electron diagnostic, and laser diagnostics. In-flight trajectory and veloc-

Shot Number	Picket Power (TW)	Foot Delay (ns)	Minimum Adiabats	Mass-Averaged Adiabats	Cu Dopant & Al ₂ O ₃ Coating	Additional Stalk & Glue
93300	7	0.4	3.94	7.43	Yes	No
93303	7	0.4	2.76	5.27	No	No
93305	7	0.2	3.18	6.08	Yes	No
93306	1.5	0.2	2.05	3.96	Yes	No
93307	1.5	0.7	2.20	4.90	Yes	No
93309	3.5	0.7	2.39	4.65	No	Yes
93312	3.5	0.4	2.09	4.09	Yes	Yes

Table 5.1: The key design features of the laser pulse and targets. The picket power and foot delay are shown schematically in Figure 5.4. The values of the adiabats are calculated in-flight from HYADES simulations. A Cu dopant was added to certain shots that necessitated an additional coating of Al₂O₃. The final shots required an additional stalk and glue in order for them to be held in the target chamber.

ity were recorded by the time resolved Sydor Framing Camera (SFC) that images the self emission of the capsule during the implosion with 16 pinholes. Time resolved hot spot images were recorded with the near-orthogonally placed KB-Framed (KBF) and Time Resolved X-ray Imager (TRXI) diagnostics which revealed the shape and evolution of the hot spot. The Gated Monochromatic X-ray Imager (GMXI) is a third hot spot diagnostic that records time integrated emission. The X-Ray Pinhole Camera (XRPHC) diagnostic provides a time integrated overview of the self-emission from the implosion where the spatial extent of the images captures the capsule as a whole and integrates the signal for the entirety of the implosion. Neutron emission and total yield were measured with the neutron temporal diagnostic (NTD) [263] and neutron time-of-flight (nTOF) detectors [264]. Finally, the laser-plasma interactions and the hot electrons they generated were diagnosed by the Full Aperture Backscatter (FABS) diagnostic and the Hard X-Ray Detector (HXRD), respectively.

5.3 Implosion Trajectory

A full description of SFC is given in Section 3.6.2, with the key features repeated here. A 4×4 array of 15 μm pinholes project 16 images of the self-emission on to 4 micro-channel plate (MCP) strips, each independently timed with a relative accuracy of ~2 ps and an absolute accuracy of up to ~50 ps [209]. The images across a strip are spaced by ~60 ps, each with an integrated time of ~40 ps. The filtering of the detector and absorption of

the MCP provide a sensitivity to photons in the range of 2-8 keV [209], resulting in the approximate imaging of the ablation front where the combination of plasma temperature and density are maximised [201]. Simulations of the implosions are post-processed using the code Spect3D [214] where the self-emission and detector features are modelled.

Figure 5.2 shows an example of the images taken with SFC, where the 16 images across the four strips can be seen, with time moving from left to right, and top to bottom. The independent start time of each of the strips is given in relation to the first. The time of each individual image is given relative to that strip's start time. The timing of the strips was changed throughout the shot day in order to capture images from different stages in the implosion.

The four images at the top of Figure 5.2 are from the first MCP strip and are timed to coincide with the picket of the laser pulse. The emission that is seen is largely from the picket interacting with the aluminium in the thin coatings of the target. Analysis suggests that the variable emission around the capsule is caused by variation in the thickness of the Al layer that was estimated to differ by up to 40% [265]. The expansion outwards of the emission that can be seen across this strip is from the coatings ablating off, and not the shell as a whole moving outwards.

The emission at the centre of the third image on this strip has been attributed to shine through of the bright hot spot that forms long after the images are exposed. The gating of the images will have some finite contrast such that emission from bright enough sources, the late formed hot spots for example, can bypass the gate and be picked up by the detector [266]. The final image is cropped due to the edges of the MCP. The remaining analysis of SFC data typically ignores this first strip and uses the remaining 12 images.

The capsule can clearly be seen to start imploding from the second strip onward, with the emission ring getting smaller with each progressive image. The vertical line at the bottom of the capsule is the emission from the stalk and glue that held the target in place. It is unclear why the stalk is not visible in the first images but it is perhaps due to the lack of plasma expansion from the capsule. The final strip sees the shell beginning to slow in its implosion and reaching the point of stagnation. At the same time a bright central hot spot is forming.

The MCP is triggered by a high voltage pulse sent across the strip. This pulse experiences gain droop across the strip where its amplification of signal diminishes for each successive image [267]. This can be seen by the decrease in signal to noise ratio across each of the strips,

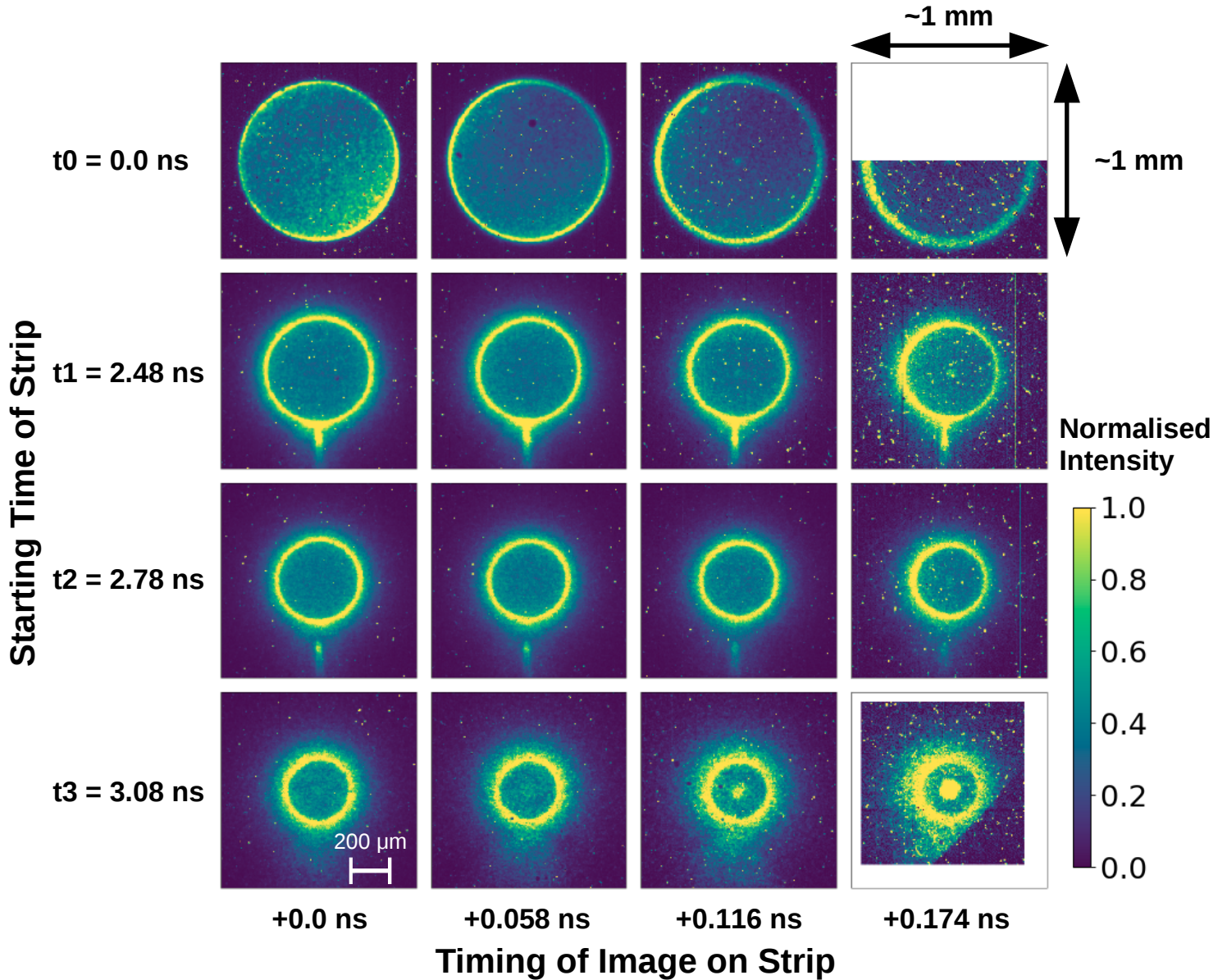


Table 5.2: Capsule self-emission images captured by SFC at 16 different times during an implosion. Each of the four horizontal strips has an independent start time given on the left of the figure. The strips have four images on each, with their times relative to the first image given at the bottom of the figure. All images are normalised for their own emission intensity with the colour bar given in the lower right. The brightly glowing ring is the ablation front moving in as the capsule implodes. Also visible is the glowing stalk and glue, and a hot spot forming late in time. The clipping of the images in the top and bottom right are due to the edges of the MCP strips.

and especially in the final images where the left-hand side of the capsule emission is visibly brighter than the right-hand side. This is simply the pulse losing the ability to produce as much gain, and the signal not being amplified as much.

The amplified MCP signal was recorded by a CCD sensor, making it more susceptible to signal bleed from high energy photon noise than the CIDs used in the XRPHC diagnostic for example. This noise produced saturated pixels that bled over to the surrounding ones. For further analysis, a custom routine was written to identify and remove both the saturated pixels and the effected surrounding pixels, while preserving the sections of the data that arise from the self-emission in its entirety. Alternative smoothing techniques like median pixel filters or removal of high frequency Fourier modes do not achieve the same level of data preservation. A comparison of smoothing techniques is presented in Appendix B.

An initial estimate for the hot spot position relative to the outer shell, referred to as hot spot offset, was found from these final images. The images on the edge of the MCP strip however are far more susceptible to gain droop and had low signal to noise ratios, where the fitting procedure implemented produced poor results. Offsets of $\lesssim 10 \mu\text{m}$ were found but the parallax of the diagnostic must be considered when interpreting these results. It was found from the XRPHC diagnostic discussed later that a hot spot offset was seen in the approximate direction of the stalk. The viewing angle of SFC relative to stalk of $\sim 45^\circ$ will reduce the perceived distance in that direction by $\sim 30\%$.

5.3.1 Radius and Velocity Determination

The images seen in Figure 5.2 have thin rings of self-emission, with steep inner gradients in the intensity profiles. This is the result of the bright ablation plasma acting as a backlighter that images the optically thick and dense fuel [174]. This technique of self-emission shadography is discussed in Section 3.6.2. A high precision in the determination of the radius is achieved by taking many measurements around the capsule. The approximate centre of each image is first found by fitting an idealised rotationally symmetric emission profile to the data. This consisted of a centred broad high order super-Gaussian for the background emission of the capsule and a thin Gaussian ring for the shell, with the total function given by the following

equation,

$$I(x, y) = A_{\text{cap}} \exp \left[- \left(\frac{r'^2}{2\sigma_{\text{cap}}^2} \right)^{n_{\text{cap}}/2} \right] + A_{\text{shell}} \exp \left[- \left(\frac{(r' - r_{\text{shell}})^2}{2\sigma_{\text{shell}}^2} \right)^{n_{\text{shell}}/2} \right] \quad (5.1)$$

where $r' = \sqrt{(x - x_0)^2 + (y - y_0)^2}$ is the radial distance from the fitted centre (x_0, y_0) , r_{shell} is the radius of the centre of the shell emission, and $A_{\text{cap/shell}}$, $\sigma_{\text{cap/shell}}$ and $n_{\text{cap/shell}}$ are the amplitude, standard deviation and super-Gaussian order of the capsule or shell emission respectively.

The data is then interpolated around this centre point onto a polar coordinate system, defined by (r, θ) . Slices are then taken around this point, where the data is azimuthally average over 5° in order to match the size of the emission area with the PSF of the detector. The arc length of the emission for a wedge at radius R and angle $\Delta\theta$ is give by $l = R\Delta\theta$, therefore to match the detector resolution of $\sim 15 \mu\text{m}$ for an emission radius of $\sim 250 \mu\text{m}$ yields a wedge angle of $\Delta\theta = l/R \approx 5^\circ$. The data is purposely over-sampled with a step size of 1° . The radius of each slice is determined as the 65% intensity contour from the minimum intensity, typically at the centre, to the peak intensity. The radii extracted from each angle are used to define a circle and the data is moved to align with its centre. The process is then repeated until the centre does not change by more than $1 \mu\text{m}$ between iterations, typically only requiring <3 iterations to complete.

Each implosion was simulated with HYADES using the experimentally delivered laser pulses and targets. The output of these simulations were then post-processed using Spect3D to find the x-ray emission profiles. Within this post-processor is the capability to recreate the specific properties of the detector such as integration time, spatial resolution and response function. Synthetic images were then made with this post-processor, timed to the experimental image, and the same radius determination procedure was applied to them.

The experimental self-emission image, along with the idealised fit, and synthetic image are given in Figure 5.5. Below is a comparison of the lineouts taken through each image. The HYADES and Spect3D simulation appears to overpredict the peak emission intensity for the capsule. This does not significantly impact the extracted radius though, as the intensity gradient is so steep that the location of the radius only weakly depends on the contour value chosen, for contours between ~ 45 - 85% .

The extracted radius from the experimental and simulated images are plotted in Figure

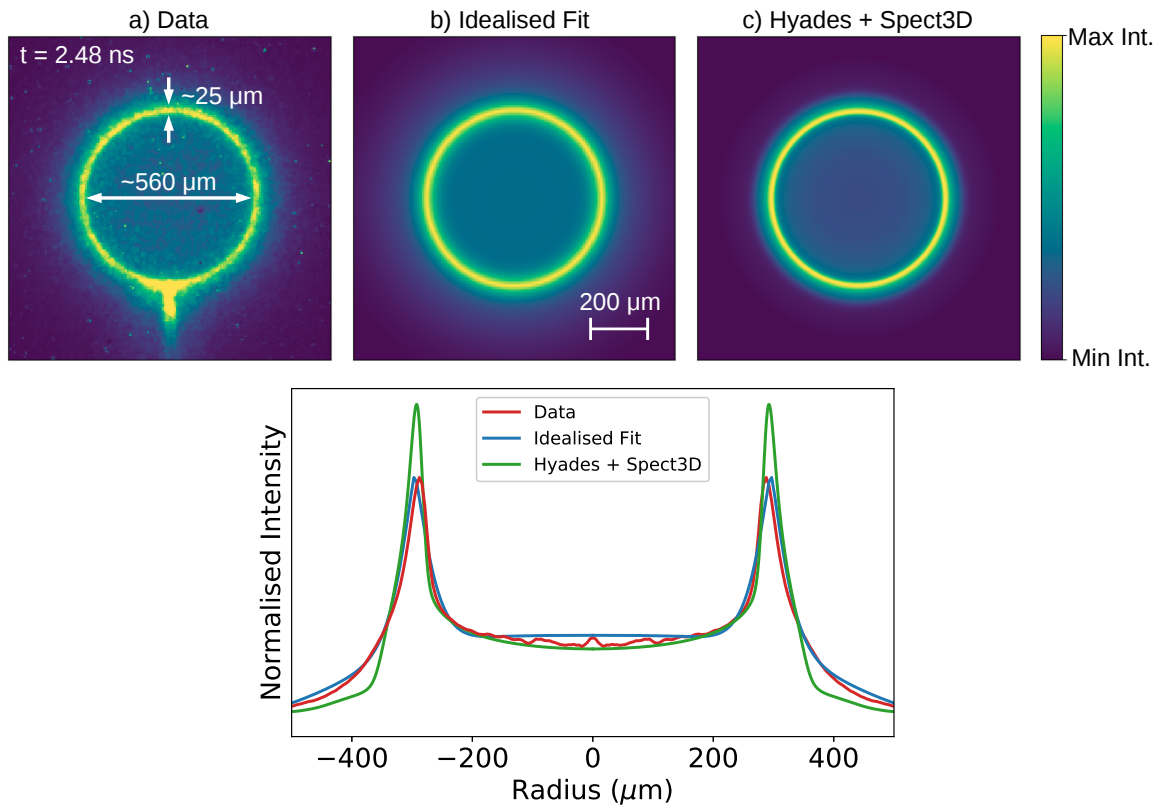


Figure 5.5: Each SFC image a) is analysed starting with an idealised fit given by equation 5.1 b), and a HYADES simulation post-processed with Spect3D c). The plot below shows a lineout through the centre of each image that gives a comparison of the data (red), the idealised fit (blue) and the simulation (green).

5.6 along with the laser pulse. Each set of radii has been fitted with a 3rd order polynomial in order to determine the implosion velocity for data smoothing purposes [268]. The simulated radii are in close agreement with the experimental values, that are well within the errors associated with the radius determination of $\sim 3\%$. The normalised simulated and experimental neutron emissions are also plotted, highlighting the timing accuracy of peak emission.

Figure 5.7 shows the radius and velocity measurements from a shot where SFC was timed to coincide with the peak implosion velocity. Inferring the velocity requires the additional steps of fitting a polynomial to the radius trajectory and taking the derivative of that polynomial introduces additional discrepancies between the two sets of data. The difference in the timing of the peak velocities of ~ 65 ps is thus not a significant indication of inaccurate modelling. The close agreement between the peak velocity magnitudes of 210 km/s and 207 km/s for the experimental and simulated data respectively further highlights the accuracy

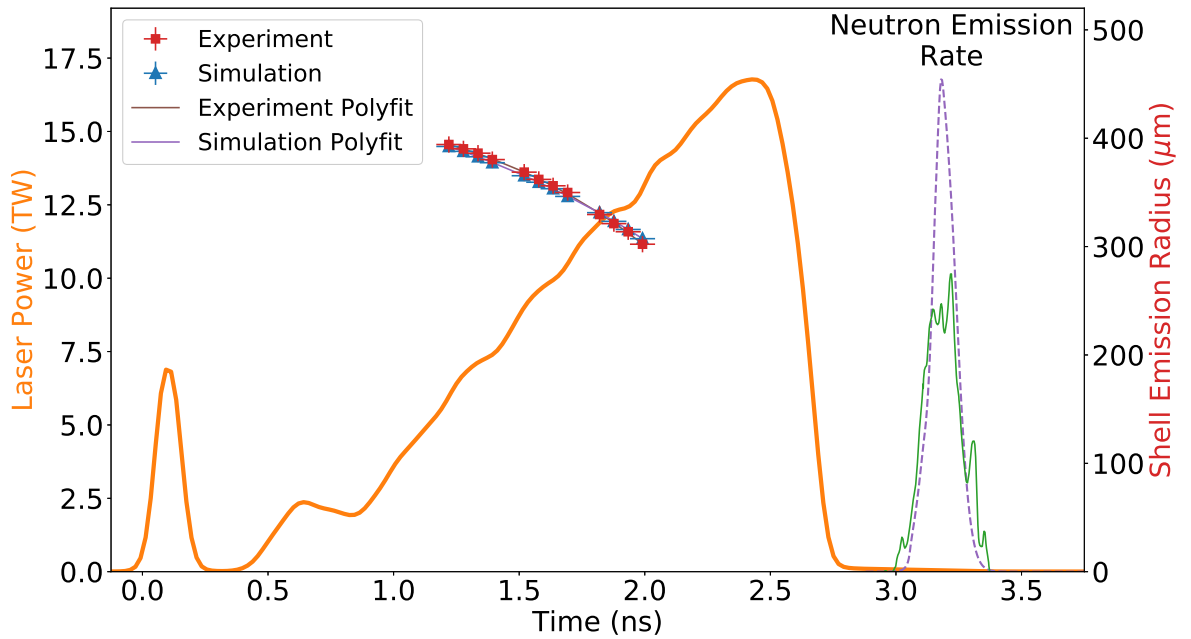


Figure 5.6: The inner radius of implosion as found by SFC (red squares) and for post-processed HYADES simulations (blue triangles) against time, plotted with the laser power. A 3rd order polynomial is fitted to radius points. The solid green line is the normalised experimental neutron emission rate and the dashed green line show the normalised simulated neutron emission rate.

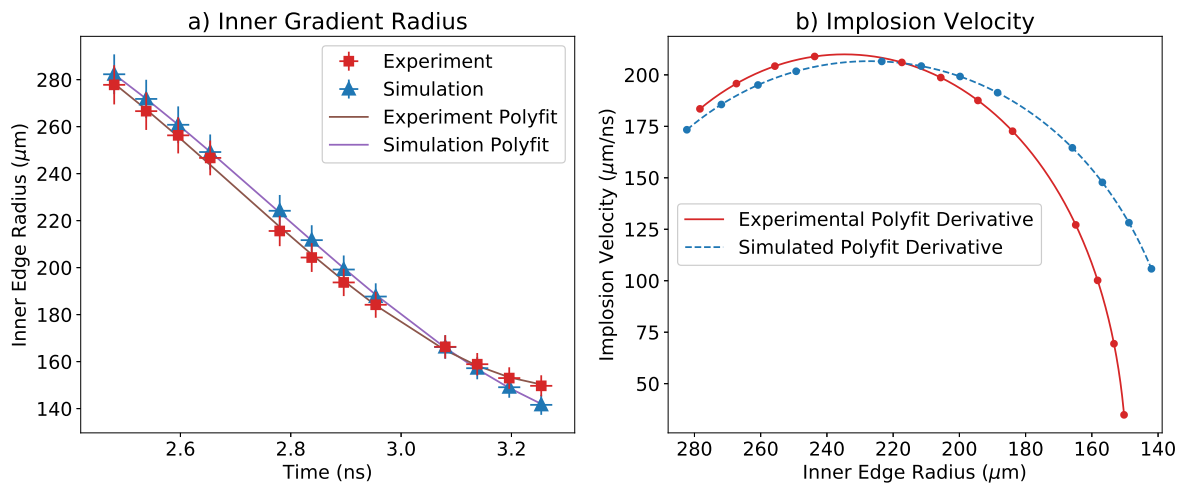


Figure 5.7: a) Inner gradient shell radius against time with 3rd order polynomial fits from experimental data in red and simulations in blue. b) Implosion velocities from experiment and simulation found by differentiating the fitted polynomials with respect to time.

of the simulation.

5.3.2 Low Mode Implosion Asymmetries

The radius determination technique averages the inner edge location for each azimuthal slice, ignoring any asymmetries or non-uniformities in the capsule shape. Unfolding the azimuthal radius as a function of angle can reveal low mode asymmetries of the capsule for each image, and their evolution over time during the implosion. Figure 5.8 shows the percentage variation in the radius from the mean against angle shown as the red line for one SFC image, shown in the inset. The area shaded out represents the section where the emission was dominated by the stalk and glue. This bright emission disrupted the inner edge determination and lead to an elevated radius estimate that can be seen from the graph, as such it was not included in subsequent fitting procedures.

The deviation away from circular is highlighted on this graph by the sinusoidal-like nature of the percentage radius deviation. The dominance of a mode 2 is clearly visible, indicating that the shell was elliptical during the implosion. To demonstrate this, a single mode 2 cosine was fitted with the form $A_2 \times \cos(2\theta + \phi)$ where A_2 is the amplitude and ϕ is the phase. This is shown as the dotted brown line and tracks the overall shape of the data.

The data was further characterised by both a Fourier transform and Legendre polynomial analysis. The Fourier modes 0-6 are plotted as the dot-dashed green line in Figure 5.8 a), and the amplitudes of these modes are given in b). Large amplitudes for the Fourier mode indicates a greater prevalence of that mode component in describing the radius profile. Each mode >1 represents a deviation away from a circularly spherical implosion. The large mode 2 amplitude indicates an ellipticity of the capsule. Modes 0 and 1 can give information about the mean radius of the capsule and its offset from centre respectively, both of their amplitude were identically zero as the modes were fitted to the fractional radius deviation that has a mean of zero, and the capsule was aligned to its centre before the fit was performed. Without a reference point outside of the capsule, no mode 1 offset information can be determined. The low values for the remaining modes suggest that they are not present in the data or that they are too low in amplitude to be detected above the noise.

Following this, the data was rotated such that the $\theta = 0$ line is pointing in the same direction as the phase of the mode 2. The rotated fractional radius deviation is then decomposed into the Legendre polynomial series. Each mode in the polynomial series is given

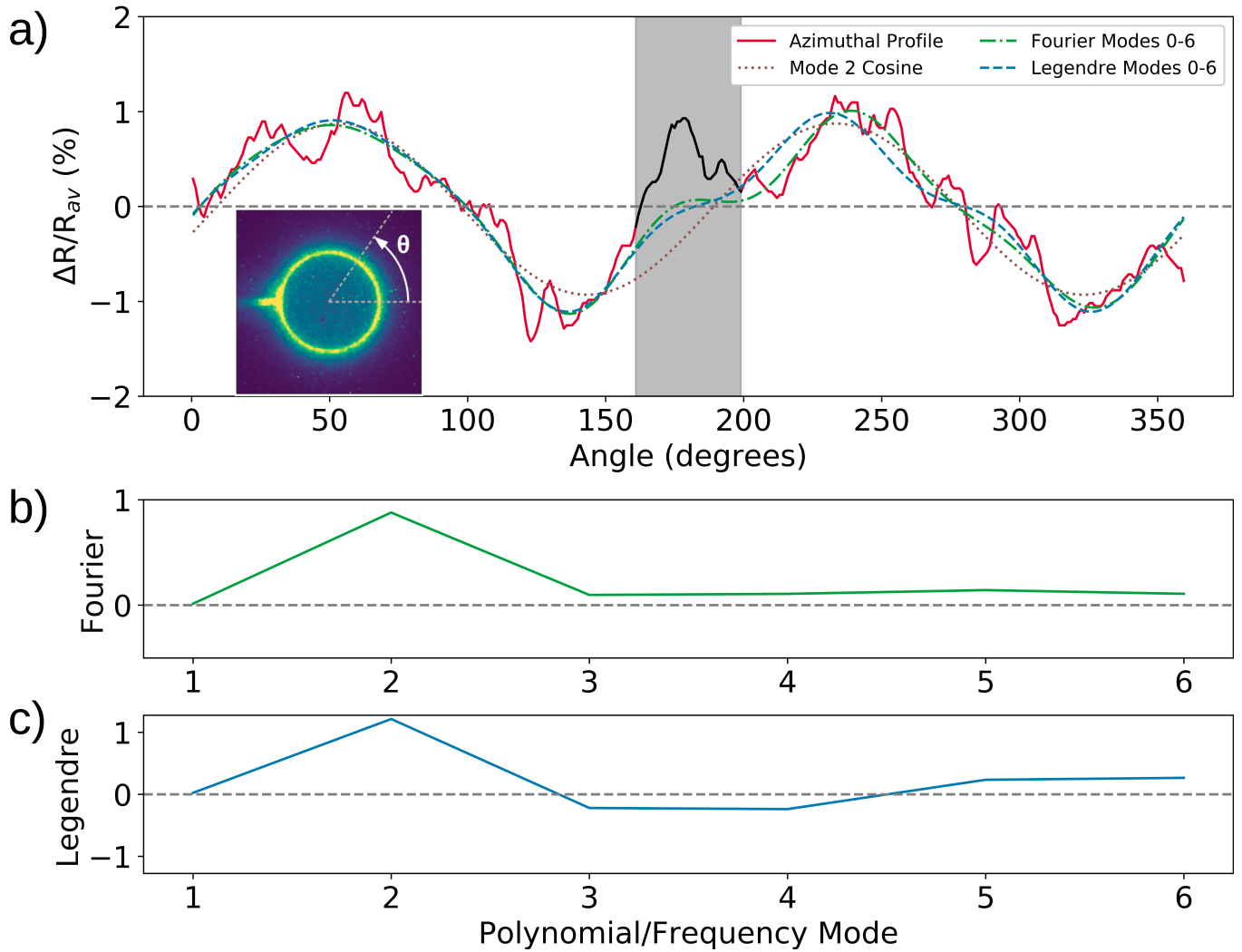


Figure 5.8: a) The red line shows the percentage deviation of the inner shell radius from the mean radius as a function of angle of the SFC image shown in the lower left of the graph. The area in grey represents the region where the emission from the stalk affected the ability to determine the inner radius, and was not included in any fitting procedure. The fitted profiles for modes 0-6 of Fourier and Legendre Polynomial analyses are shown in green and blue respectively. A simple $\cos(2\theta)$ is plotted in dashed orange. b) and c) give the mode amplitudes for the fitted Fourier modes and Legendre polynomials respectively.

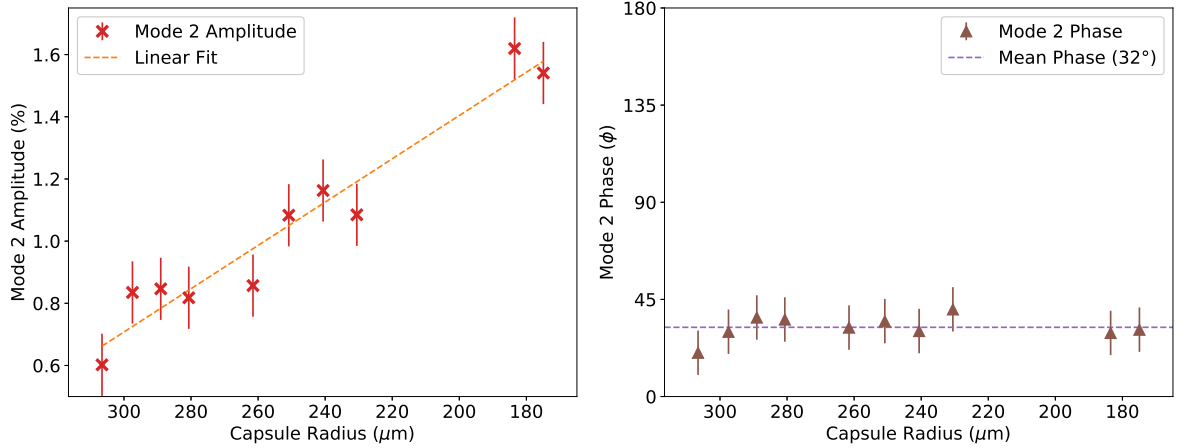


Figure 5.9: The mode-2 amplitude growth and phase angle consistency against capsule radius. Note the decreasing radius such that time moves from left to right. The dashed lines represent a linear fit for the growth of the amplitude and the mean phase angle. The mode-2 is not aligned with the stalk which is located at an angle of 0° .

by

$$r(\theta) = \sum_l A_l P_l(\cos \theta) \quad (5.2)$$

where θ is the polar angle from the x-axis, P_l is the polynomial for mode l , and A_l is its associated amplitude. Negative values for the amplitude represent the phase of the polynomial component and it is the magnitude that is used to determine the relative presence of the polynomial. The 0-6 polynomials are plotted in Figure 5.8 a) as the dashed blue line, and the amplitudes are given in Figure 5.8 c). There is another clear dominance of the mode 2, with the remaining modes being much less prevalent.

Figure 5.9 shows the mode 2 amplitude as a percentage of the radius and the phase of that mode against the average radius of the capsule during the implosion between 2.5 and 3.1 ns. The amplitude of the mode 2 can be seen to grow linearly with the decrease in radius, highlighted by the linear fit. The phase remained largely constant during the implosion with a value of $\sim 32^\circ$. For reference, the stalk axis was at $0^\circ/180^\circ$ as seen in the inset of the upper graph in Figure 5.8.

5.4 Hot Spot Offset

The XRPHC diagnostic is a time integrated x-ray sensitive camera that images the entire capsule with the use of an $10 \mu\text{m}$ pinhole and CID sensor. A CAD view of the target as viewed by XRPHC produced by VisRad [217] and an image of the implosion recorded by the

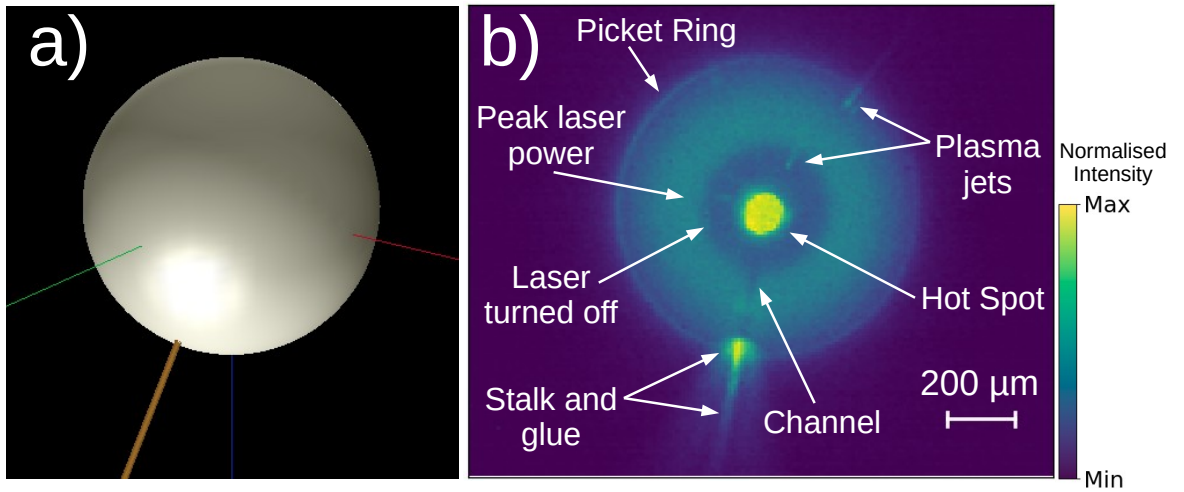


Figure 5.10: a) The view of the target as seen by the detector, showing the orientation of the stalk to the target, and the target to the chamber. b) The time integrated image from XRPIC for shot 93305. The outer ring and increasing emission intensity tracks the laser intensity, as the capsule ablation front radius decreases. The bright central region is the hot spot that forms late in the implosion. The stalk and glue produces a similarly large emission intensity can be seen in the lower centre of the image.

detector are given in Figure 5.10, with the key features highlighted on the data. The stalk is shown as the thick yellow line to the bottom left, the three remaining coloured lines represent the three orthogonal axes of the target chamber which are shown for better comparison of the lines of sight between detectors. The diagnostic effectively encodes the time history of the implosion onto space in the detector plane.

Important features of the implosion can be gathered from the image, beginning with the outer edge of the emission and moving inwards, tracking with both the time of the implosion and the decrease in radius of the capsule. The bright ring at large radius defining the outer edge is the result of the picket interacting with the coatings containing higher atomic number materials than the shell and is particularly visible with the capsules that received the additional Al_2O_3 coating.

The emission increases in intensity as the capsule decreases in radius which corresponds with the rising laser energy that is being deposited into the material. The emission intensity sharply drops as the laser turns off, at which point the capsule is coasting inwards. A bright hot spot forms at the centre of the image, corresponding with the final stages of the implosion.

The stalk and the glue glow brightly during the implosions and a channel of low intensity emission can be seen directed towards the centre. This effect is explained as the difference in

shock speed through the glue and the plastic creating a conical shock that produces a cold and dense column directed towards the centre [50]. This does not produce as high of a level of self emission as the surrounding material but it may produce a high velocity jet that can disrupt the hot spot [50]. The bright streaks that can be seen at various points are likely contaminants or dust on the capsule that produce these plasma plumes and potentially seed instabilities. Because the XRPHC diagnostic integrates in time and one spatial dimension along its line of sight, the source location of the streak cannot be established.

The hot spot itself is visibly asymmetric, possibly elliptical, where the asymmetry is approximately oriented towards the stalk. It is also slightly offset from the centre of the capsule and again approximately towards the stalk. To characterise the ellipticity, a region around the centre of the image was isolated that included the hot spot, the low intensity region, and the emission from the peak laser power and the data was cropped to this. Two independent 2D elliptical super-Gaussians and a constant background were fitted to this data. These included a positive amplitude super-Gaussian for the hot spot and a negative amplitude one for the low intensity region. Each was defined by the following equation,

$$I(x, y) = I_0 \exp \left(- \left[a(x - x_0)^2 + 2b(x - x_0)(y - y_0) + c(y - y_0)^2 \right]^{n/2} \right) \quad (5.3)$$

where x_0 and y_0 are the x and y coordinates of the centre of the ellipse, n is the order of the super-Gaussian, I_0 is the peak intensity, and a , b , and c are given by

$$a = \frac{\cos^2 \theta}{2\sigma_X^2} + \frac{\sin^2 \theta}{2\sigma_Y^2} \quad (5.4)$$

$$b = -\frac{\sin 2\theta}{4\sigma_X^2} + \frac{\sin 2\theta}{4\sigma_Y^2} \quad (5.5)$$

$$c = \frac{\sin^2 \theta}{2\sigma_X^2} + \frac{\cos^2 \theta}{2\sigma_Y^2} \quad (5.6)$$

where θ is the angle of the semi-major axis to the x-axis. The values σ_X and σ_Y are the standard deviations of the semi-major and semi-minor axes respectively.

Figure 5.11 shows an example of the cropped data and the fit, and a lineout through the centre of each demonstrating the effectiveness of the fit. The centres of the two super-Gaussians are shown on the data image, highlighting their offset from one another. This analysis procedure was performed for the remaining shots and it was found that the centre of the fitted hot spot ellipse is typically between 15 and 30 μm offset from the centre of the

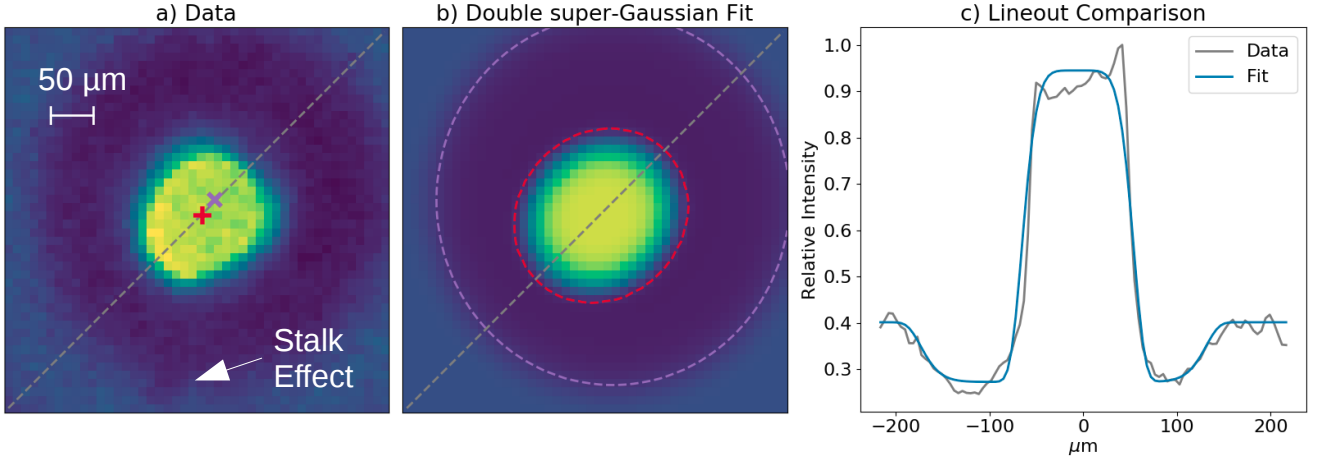


Figure 5.11: Central region of the XRPHC image for shot 93306 for a) the data, b) an optimised fit to the data, and c) the same lineout drawn through each (dashed grey) as a comparison. A dark region can be seen at the bottom of a) that is the result of the stalk (explained in the text). The fit uses a homogeneous background and two elliptical super-Gaussians, one with a negative amplitude for the decrease in intensity for the coast time, and the other with a positive amplitude for the hot spot. The centres of the two super-Gaussians are shown in a), highlighting their displacement from each other, with their respective contours shown in b).

fitted negative ellipse. Errors of approximately $8 \mu\text{m}$ are attributed to the hot spot offset measurements due to the pixellation of the data from the CID. The phase angle of the hot spot ellipse is typically between 230° and 250° which is similar to the stalk angle of 255° .

The hot spot offset estimation requires a centre of the implosion to compare the hot spot centre against. The centre of the implosion must be determined from some other feature from the XRPHC image itself, and can be defined in multiple ways. These include the centres defined by the outer picket ring, and the ring of emission greater corresponding with the peak laser intensity, both of which are the result of emission occurring at earlier stages of the implosion than that shown in the analysis above. The outer edge bright ring around the implosions was found from the steepest gradient using a Sobel filter [269]. The ring of the greater emission corresponding to the peak laser intensity is found by using the same polar interpolation and radial slices as with the SFC data and as outlined in Section 5.3.1. The radial points were found by placing a mask over the regions outside this emission peak and fitting a single Gaussian to the remaining profile. The centre of this Gaussian was taken to be the location of the peak intensity.

The centres of the outer edge, the peak intensity ring, and the negative cavity ellipse were all within $\sim 10 \mu\text{m}$ of each other for all the shots, this is close to the uncertainty of the fits,

while the hot spot remained consistently offset. This indicates that the capsule remained largely aligned during the implosion but that the final hot spot was formed off centre. The perceived size of a hot spot detected by XRPHC can be larger than the actual hot spot due to the time integration of the signal. The recorded image of a moving hot spot will be smeared out, increasing its apparent size.

5.5 Hot Spot Imaging

Characterisation of the hot spot is performed with images taken by three diagnostics; TRXI, KBF, and GMXI. Each hot spot image was fitting with a 2D elliptical super-Gaussian function convolved with a Gaussian point spread function $\text{PSF}(x, y)$ whose standard deviation was given by the detector resolution. The fitted hot spot intensity distribution had the following equation,

$$I'(x, y) = \text{PSF}(x, y) \otimes I(x, y) \quad (5.7)$$

where $I(x, y)$ is given by (5.3). This fitting provides a measure of the hot spot ellipticity, the rotation angle and mean radius. The size of the hot spot is found from the average radius around a given contour value A , which by convention is either the 17% or $1/e$ of the peak intensity [270, 271]. For the elliptical fits used here this is given by,

$$r_A = r_0(-\ln 1/A)^{1/\eta} \quad (5.8)$$

where r_0 is the geometric mean of the semi-major and semi-minor radii of the fitted ellipse, given by $r_0 = \sqrt{\sigma_X \sigma_Y}$ and η is the order of the super-Gaussian [209].

The data is realigned to the centre of the fitted ellipse and rotated such that the semi-major axis is aligned with the x-axis. The capsule is split into two hemispheres down the semi-major axis of the elliptical fit. A Legendre polynomial decomposition is then performed on the radius profile extracted from each hemisphere. The Legendre polynomials represent the azimuthally symmetric spherical harmonics along the hot spot imager line of sight, Y_{l0} , a subset of the full 3D spherical harmonics Y_{lm} that describe the hot spot as a whole. Figure 5.12 shows an example of these operations for hot spot imaged by TRXI, with the two hemispheres labelled as left-hand side (LHS) and right-hand side (RHS). The mode amplitudes for the hot spot along a line of sight are given by the mean of those from either

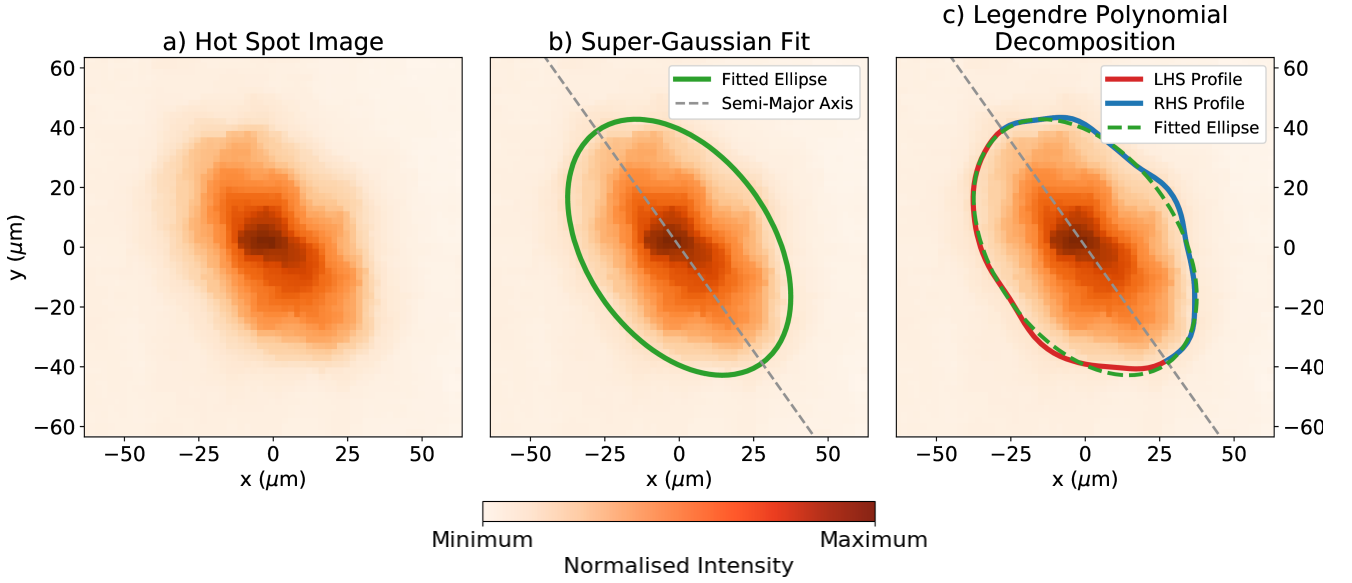


Figure 5.12: a) An image of a hot spot seen by the TRXI diagnostic, b) a 2D elliptical super-Gaussian is fitted to the hot spot image in order to determine the radius and orientation of the semi-major axis, a 17% contour is plotted in green. c) the contour azimuthal profile is split between the two hemispheres determined by the fitted semi-major axis from b), and a Legendre polynomial analysis is performed on each half. The data is from the TRXI diagnostic, discussed in Section 5.5.1.

side, and the errors given by their differences.

5.5.1 Time Resolved X-ray Imager

The time resolved x-ray imager (TRXI) diagnostic provides 4 snapshots of the hot spot emission timed to coincide with peak compression. Figure 5.13 shows the view that TRXI has of the target and the stalk, along side which is a similarly constructed view for KBF for comparison.

Figure 5.14 shows an image of the hot spot along with the fitted 2D elliptical super-Gaussian, and the normalised difference between the two. It can be observed from the difference that the fitting function can accurately replicate the overall size and shape of the hot spot, with only high frequency differences due to small scale structure and diagnostic noise. The high ellipticity seen in Figure 5.14 was observed in all the TRXI images.

Figure 5.15 shows the radius of the contours presented in Figure 5.14 against their angle from the semi-major axis. The contours for the data are separated into the left and right components, and each has the 0-10 Legendre polynomials fitted to it. The same contour from the super-Gaussian fit is also presented, highlighting the dominance of the ellipticity.

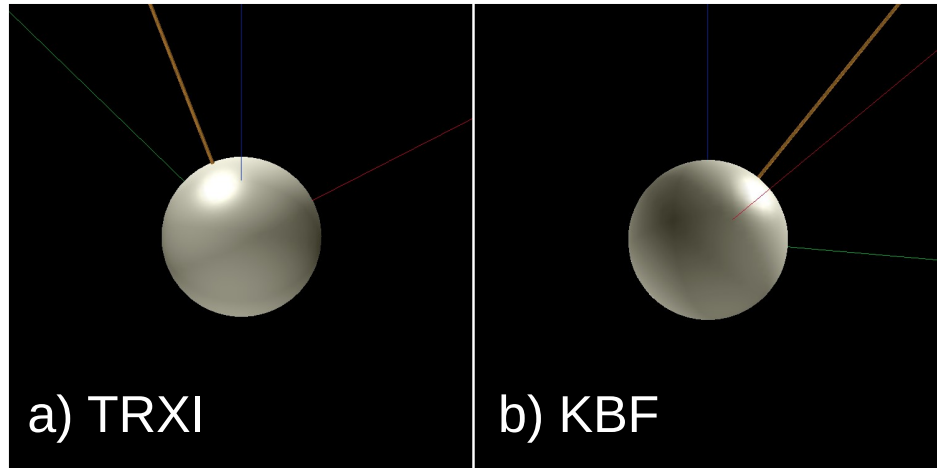


Figure 5.13: a) A representation of TRXI’s view of the target and stalk generated with VisRad, depicting the stalk in yellow, and the three orientation axes of the target chamber in red, green, and blue. b) A similar representation for KBF.

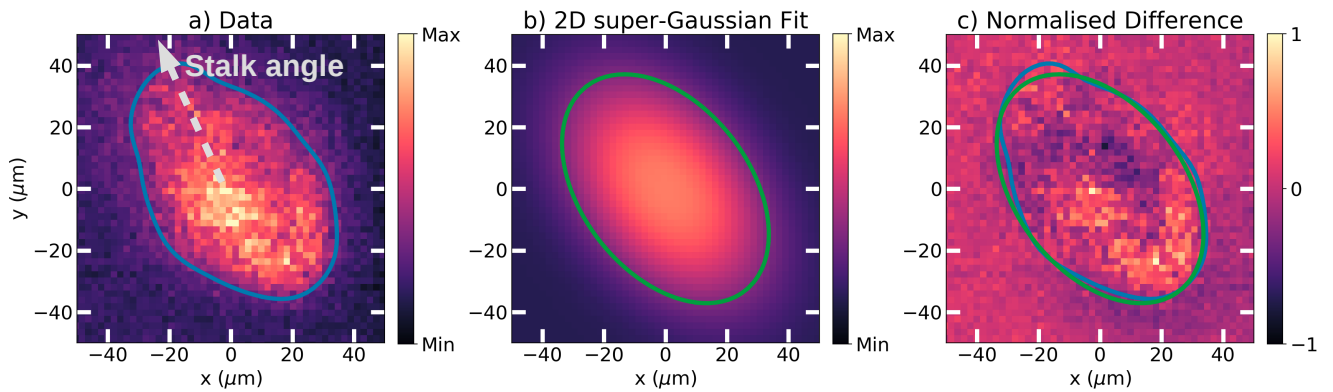


Figure 5.14: Hot spot analysis of images from the TRXI diagnostic showing a) the hot spot emission data and stalk angle, b) an elliptical 2D super-Gaussian fit, and c) the difference between the two. The 17% contour lines are shown individually for a) and b), and combined in c). The hot spot shown here is highly elliptical, with a semi-major axis aligned closely with the direction of the stalk. The fit is able to reproduce the overall shape of the hot spot, with the main difference being the off centred peak of the hot spot emission.

Given below are the amplitudes of the fitted modes. The mode 0 and mode 1 relate to the mean radius and centre offset respectively. Since this analysis is performed with a hot spot that is centred specifically for the fit then without a reference to the location of the implosion centre, no mode 1 can be found.

As expected there is a large mode 2 but beyond this, the dominating even modes are consistent with the modes amplitudes expected of an ellipse, justifying the choice of the 2D super-Gaussian fit. Reasonable cylindrical symmetry of the hot spot is inferred from the agreement between the hemispheres on the amplitude of the polynomials, seen by the errors largely not crossing the x-axis, and the relatively small errors on those amplitudes. The remaining odd modes are far lower in their amplitudes which indicates that there is also symmetry across the semi-minor axis. The higher order modes ($\gtrsim 6$) are much less significant and likely fits to noise, being less than 5% of the mode 0 amplitude and changing in sign between the two sides.

Table 5.3 summarises the properties of the hot spots seen by TRXI for all the shots where data was available. These include mean radius, eccentricity ($\epsilon = \sqrt{1 - \frac{r_{\text{minor}}}{r_{\text{major}}}}$), angle of the semi-major axis from the x-axis, and $P2/P0$, a common measure of the relative deviation from spherical that is the ratio of the mode 2 and mode 0 amplitudes. The relatively stable eccentricity and phase angle for all shots suggests that these elliptical hot spots are systematic. This is highlighted with the inclusion of shot 93316 which used a different implosion pulse shape and target, meaning that the asymmetry seen is not likely to be the result of the reduced adiabat implosion design.

Shot 93307 appears to be somewhat of an outlier compared with the other shots but is in fact consistent with the observations made here. It produced a hot spot with a smaller mean radius but that value had overlapping error bars with other shots. Similarly for the phase angle, although being slightly higher, was within the errors of others. It had lower eccentricity but it was still large enough to be considered elliptical like the others. The cause of these differences is currently not known but its parameters are close enough to those of the other shots to suggest it was affected by the same systematic issues.

It is possible that the ellipticity of the hot spots seen in TRXI is the result of an unknown instrument artefact [272]. A comparison has been made between the time resolved images produced by the drift tube and hCMOS chip in TRXI, discussed in Section 3.6.3, with a time integrated image plate placed at the detector entrance. A less elliptical hot spot is

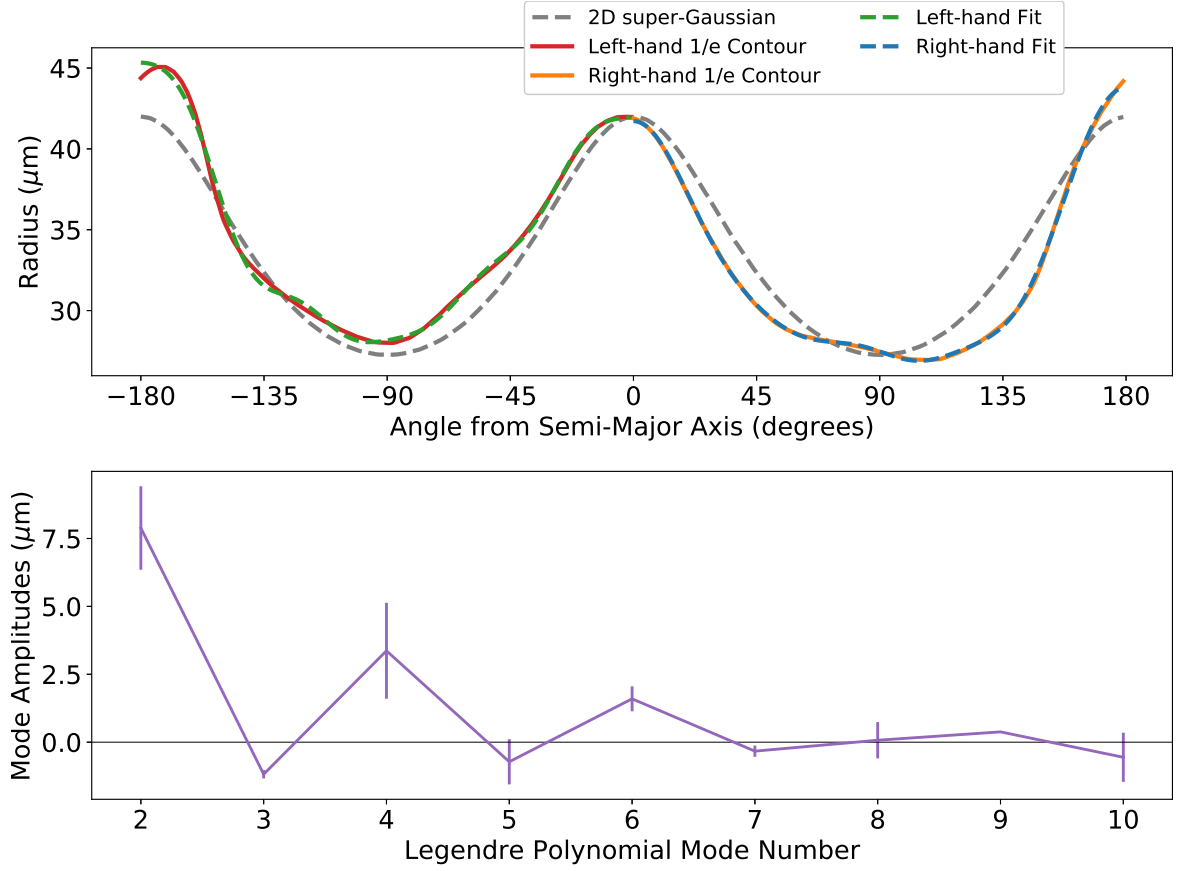


Figure 5.15: The radius of the 1/e contour of a TRXI hot spot image and fitted elliptical super-Gaussian (dashed grey) as a function of angle from the semi-major axis. This contour is split into left- and right-hand sides (red and orange solid lines respectively) to which the first 10 Legendre polynomials are fitted (green and blue dashed lines respectively). The mean of the two sets of amplitudes of the fitted coefficients are given below with the errors given by the difference between the sets.

Shot Number	Mean Radius (μm)	Eccentricity	Phase Angle ($^\circ$)	$P2/P0$
93305	24.8 +/- 8.0	0.63 +/- 0.08	37 +/- 5	0.26 +/- 0.05
93306	33.4 +/- 2.6	0.61 +/- 0.03	38 +/- 2	0.28 +/- 0.03
93307	19.8 +/- 5.4	0.35 +/- 0.09	46 +/- 5	0.14 +/- 0.08
93309	28.1 +/- 3.1	0.58 +/- 0.04	35 +/- 3	0.32 +/- 0.02
93316	23.7 +/- 2.2	0.59 +/- 0.04	37 +/- 3	0.31 +/- 0.11

Table 5.3: A table of the key parameters for the shots where TRXI data was available, including the geometric mean of the ellipse radius, its eccentricity defined in the text, phase angle, and ratio of the modes 2 and 0 ($P2/P0$). Shot 93316 was taken on the same shot day and is included as a comparison, it used an entirely different implosion concept in terms of target and pulse shapes from the reduced adiabat designs presented here but still reproduced the same asymmetries.

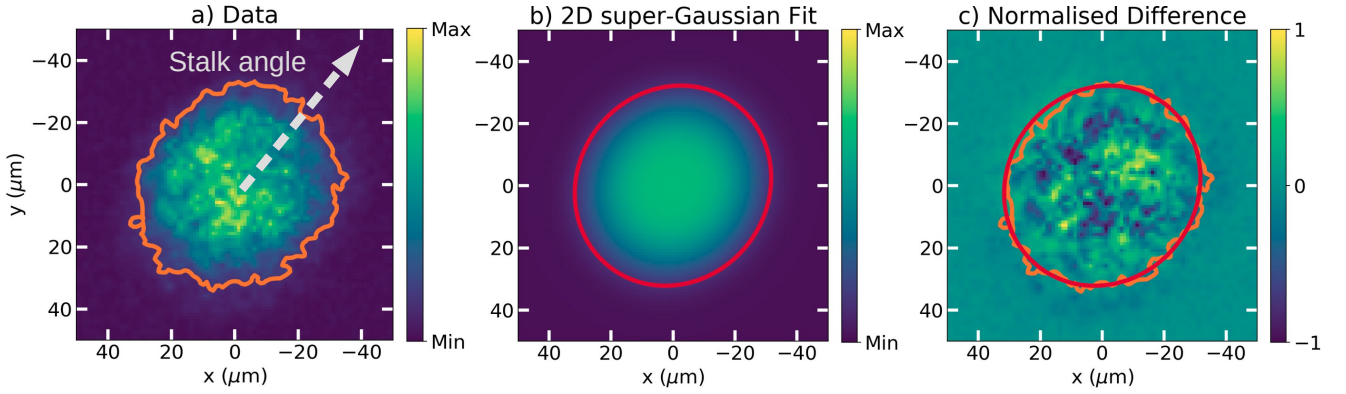


Figure 5.16: a) KBF hot spot image and 17% contour, b) elliptical super-Gaussian fit and similar 17% contour level, and c) the difference between the data and fit, dominated by the high frequency emission of the hot spot, with both of their contours.

seen for the time integrated image, suggesting that the ellipticity might be an artefact of the instrument or that the hot spot shape is evolving in time. This is the subject of ongoing investigation at the Omega facility.

5.5.2 KB-Framed

KB-Framed (KBF) is a second time resolved hot spot imager and is positioned at a near orthogonal angle to TRXI. It is capable of recording up to 16 images with a spatial resolution of $6 \mu\text{m}$ and is sensitive to x-rays in the range of 2-8 keV [209]. The absolute timing accuracy can be as large as 50 ps, with an inter-strip accuracy of 2 ps [209]. A single image taken with KBF is shown in Figure 5.16 along with the fitted 2D elliptical super-Gaussian, and the difference of the fit with the data. It is apparent that the hot spot shown here is much closer to circular than those seen with TRXI.

The Legendre polynomial analysis outline in Section 5.5.1 was applied to the contours shown in Figure 5.16. The results of this are presented in Figure 5.17. There still remained a dominant mode 2 but with a much reduced amplitude as compared with TRXI. The high order modes were far lower in magnitude and many of them changing signs across each hemisphere, suggesting that these are fits dominated by noise.

KBF observed hot spots that had lower eccentricity than TRXI and GMXI, the data for which is shown later. It is possible that the asymmetry observed using TRXI is real, and that it was aligned near orthogonally to that asymmetry. KBF however, would view the same elliptical hot spot down the semi-major axis, resulting in an apparent reduction in the

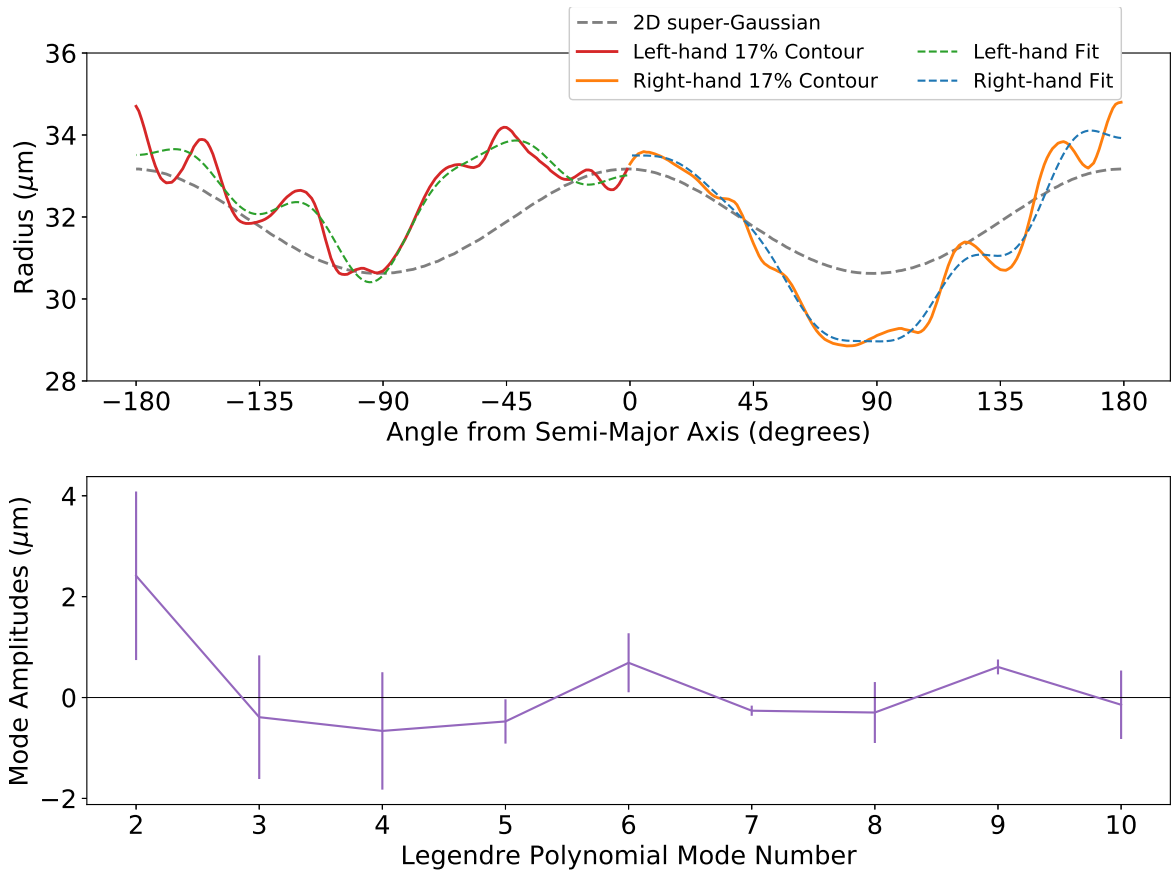


Figure 5.17: KBF hot spot 17% contour radius against angle from the semi-major axis of the elliptical super-Gaussian fit (dashed grey line). The contour is split into two hemispheres of the fitted ellipse (left- and right-hand sides) defined by the semi-major axis, plotted as the red and orange solid lines. To each hemisphere, the 0-10 Legendre polynomials are fitted, plotted as the green and blue dashed lines. The lower graph plots the mean of the amplitudes for these Legendre polynomials, where the errors are given by the difference between each hemisphere. The first Legendre mode amplitude is not shown in order to better view the remaining modes.

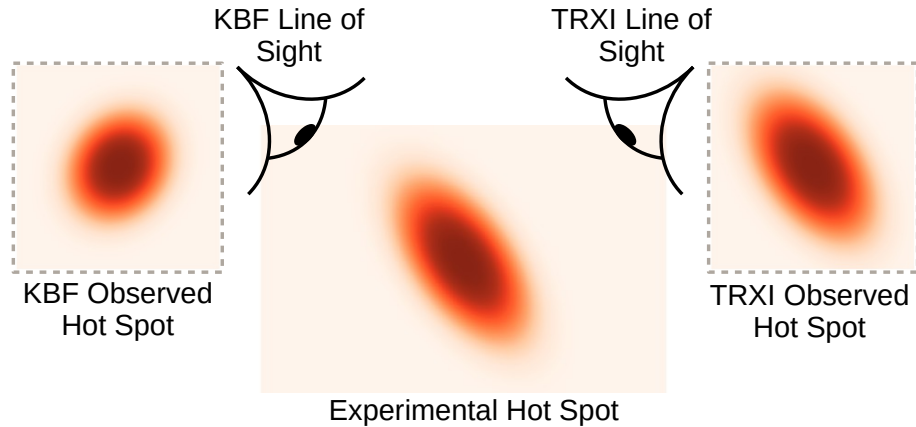


Figure 5.18: A potential arrangement of two hot spot imagers, KBF and TRXI, with a hot spot that would produce the observed hot spots found in this experiment. In this schematic, TRXI is approximately orthogonal to the hot spot asymmetry and so observes an elliptical hot spot. KBF is approximately looking down the semi-major axis of the hot spot and so observes a near circular image.

observed ellipticity. This effect is visualised in Figure 5.18 where the proposed approximate orientation of the two diagnostics with an experimental hot spot is depicted, along with the shape of the hot spot they would observe. This phenomenon has been seen before for cryogenic-DT shots on Omega where hot spot imagers at different viewing angles produce different hot spot eccentricities, where the asymmetry is aligned with KBF's viewing angle [273]. The mean radius for of the hot spots measured by KBF are largely in agreement with semi-minor radius of the TRXI images, reinforcing this interpretation.

With the increased time window of KBF, the evolution of the hot spot radius can be seen for certain shots. The evolution of the size of the hot spot is dictated by the exchange of energy between it and the shell. Initially the shell is imploding inwards, compressing the hot spot and decreasing its size. Once the shell has lost all of its kinetic energy, the hot spot reaches its peak convergence before expanding out again and increasing its radius.

The compression of the hot spot is clearly visible for shot 93309 as shown in Figure 5.19. The images show the decreasing hot spot size with time. Also plotted is the same contour radius for a post-processed HYADES simulation. The simulated compression agrees with the experimental data at peak convergence but the signal of the expanding hot spot was too low to be seen by the detector. The shallow convergence of the experimental hot spot compared with the simulated trajectory is currently not well understood. It is perhaps an effect of the lower signal produced by the forming hot spot or the result of the 3D nature

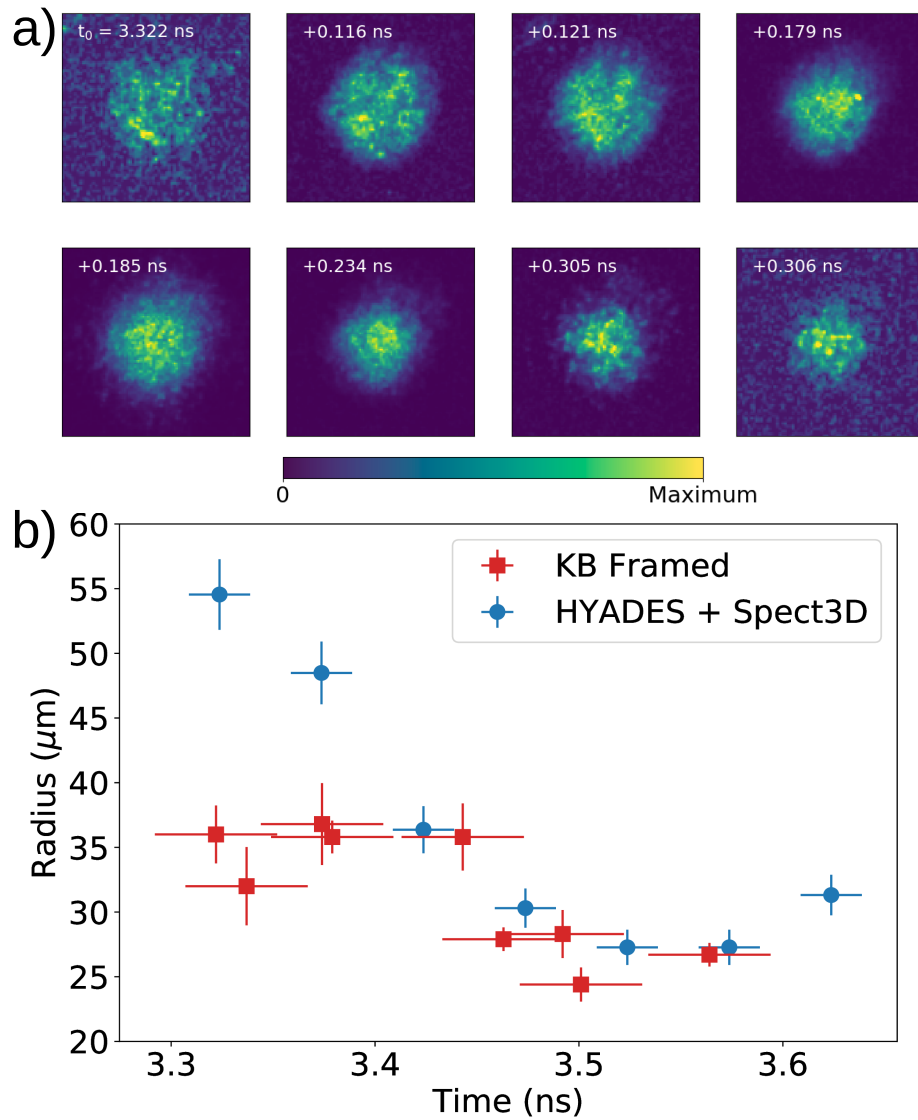


Figure 5.19: a) The hot spot images from the KBF diagnostic at different implosion times for shot 93309. Each image represents a $100 \mu\text{m} \times 100 \mu\text{m}$ region and the intensity of each has been normalised. Image b) shows the radius of the hot spot against time for the 8 images shown above, along with the simulated hot spot radius calculated with the same contour value.

of the hot spot and the single line of sight that the diagnostic has. The hot spot evolution of a shallow convergence and the lack of data for the expansion has been reported before by Shang *et al.* [271].

5.5.3 Gated Monochromatic X-ray Imager

The function of the Gated Monochromatic X-ray Imager (GMXI) has changed since its initial naming, as it is now run neither gated nor monochromatic. It is a time integrated

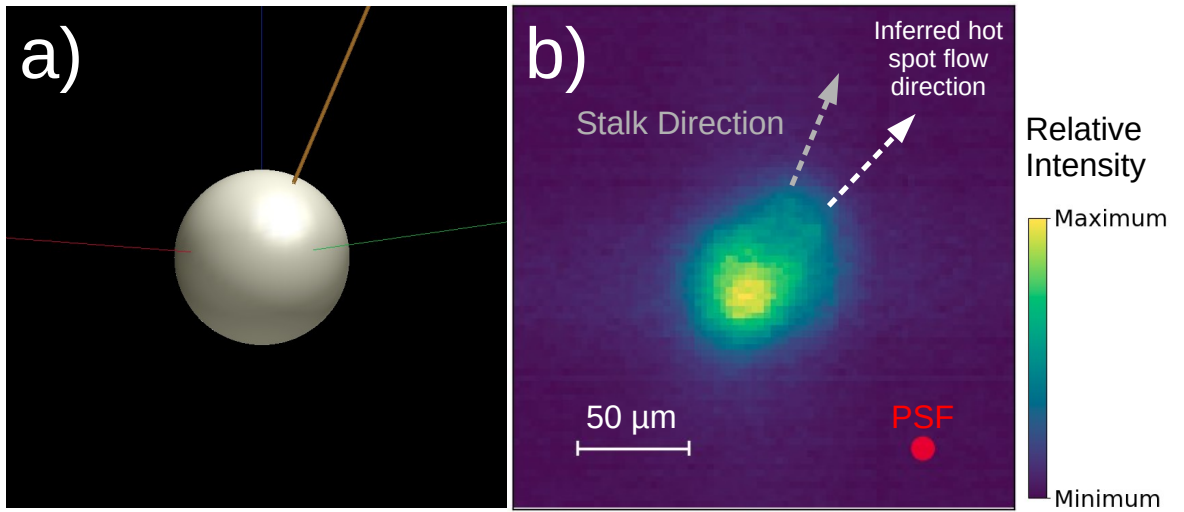


Figure 5.20: a) The view of target and stalk from the diagnostic, showing the three orientation axes of the target chamber. b) A time integrated image of the hot spot, as seen by GMXI. The hot spot emission is visibly peaked in one direction. The hot spot flow direction is inferred as opposite to the peak, and is approximately in the direction of the stalk. The diagnostic PSF of $5 \mu\text{m}$ is shown in red in the lower right corner.

hot spot diagnostic sensitive to x-ray energies in the range $\sim 2\text{-}8 \text{ keV}$ [274]. The result of the diagnostic integrating in time is that the emission from a moving hot spot is smeared across the detector, this results in images that are elongated along the line of apparent motion.

Figure 5.20 shows the VisRad view of the target and stalk prior to implosion, and the final hot spot as imaged by GMXI for shot 93305. There is a strong ellipticity to the hot spot shape and a clear inhomogeneous emission profile across it. The hot spot emission is peaked on one side of the elliptical shape, in the opposite direction to the stalk. These features indicate that the hot spot does not remain on the centre of the implosion and suggests that it has some relative velocity to the remaining fuel which is characterised by a mode 1 asymmetry.

Asymmetries in the capsule drive that produce aspherical hot spot formations are thought to be able to produce jets within the hot spots and bulk flow of the plasma [275,276]. These jets are susceptible to instabilities (in particular the Kelvin-Helmholtz instability [277,278]) that can mix cold fuel with the hot spot, and limit the potential confinement of the hot spot as a whole [279]. Any movement of the plasma within the hot spot represents wasted energy that is not used to compress or heat the fuel and will degrade the performance of the implosion and lower the fusion yield [64].

A quantitative analysis of the hot spot flow requires measurements of the Doppler shift

in the neutron spectra [264] and can only be performed with the high neutron fluxes that are typical for DT shots. Previously performed experiments [260, 279] inferred the hot spot velocity from neutron time-of-flight diagnostics and correlated them with the asymmetric features observed with GMXI. These correlations can then be used to infer qualitative hot spot flows for warm-DD filled implosions using GMXI data alone, where the neutron fluxes were too low for such a detailed neutron spectral analysis.

It was observed in these previous experiments that the high intensity feature at one end of the elliptical emission corresponded with a hot spot flow velocity direction opposite to the enhancement feature. Gatu Johnson *et al.* [260] in particular investigated the effect of mode 1 asymmetries by imposing a purposeful target offset from target chamber centre (TCC) and found that the maximum hot spot flow was observed when the offset was in the direction of the stalk. Smaller and even no flows however, were observed when the offset was in other directions. They also observed no significant hot spot flow for targets that were well aligned to TCC and had no imposed offset. This suggests that the stalk alone is not the cause of the observed hot spot offset but that it does increase the magnitude of an offset if one is present to begin with. These observations applied to the experiment reported on in this chapter indicate that the asymmetries seen here are not likely to be the result of the stalk alone.

5.6 Target Performance

Table 5.4 provides the key implosion metrics for all the shots, including experimental and simulated results. It provides calculated minimum fuel adiabat, the neutron yields for each implosion, the HYADES simulated yields, the yield-over-clean, the P2/P0 asymmetry value as measured by TRXI, and hot spot offset distance as measured by XRPHC. The yield-over-clean (YOC) is the ratio of the experimental performance to the simulated “clean” implosion performance. The shots that used targets containing the Cu dopant layer are signified by the asterisk next to the shot number, and the cross signifies those that required an additional stalk and glue to be held in place.

Two distinct categories for the implosion performance are present; those that contained the Cu dopant layer, subsequent capsule roughness and additional coating, and those that did not. The uncoated capsules when imploded were able to reach $\sim 90\%$ of the simulated yield while those with the dopant layer significantly under-performed.

Shot Number	Minimum Adiatat	Neutron Yield ($\times 10^{10}$)	Simulated Yield ($\times 10^{10}$)	YOC	$P2/P0$	Hot Spot Offset (μm)
93300	3.94	1.20	2.11	0.57	-	27
93303*	2.76	2.70	3.05	0.89	-	11
93305	3.18	1.85	3.82	0.48	0.14 +/- 0.08	20
93306	2.05	0.98	3.79	0.26	0.32 +/- 0.02	22
93307	2.20	1.14	4.00	0.29	0.26 +/- 0.05	18
93309* [†]	2.39	2.64	3.04	0.87	0.28 +/- 0.03	16
93312 [†]	2.09	1.13	3.31	0.34	-	23

Table 5.4: Key metrics for the implosions, including the minimum value of the calculated fuel adiabat, the experimental neutron yield, the simulated neutron yield, the yield-over-clean (YOC) or the experimental yield divided by the simulated yield, ratio of modes 2 and 0 amplitudes ($P2/P0$), and the hot spot offset from centre. Shots that used no Cu dopant layer and Al_2O_3 coating are indicated with an *. Shots that had an additional stalk and extra glue are indicated by a [†]. The uncertainty on the experimental yield was $\sim 5\%$, and the uncertainty on the hot spot offset was $\sim 8 \mu\text{m}$.

The extra stalk and glue do not appear to have degraded the implosion performance more than the single stalk and glue. Comparing similar shots, such as 93303 with 93309[†] and 93307 with 93312[†], shows a very similar performance and YOC with or without these additions. It has been predicted [280] that larger glue spots should lead to greater degradation, but no such decrease is seen on experiments with either more glue [280] or thicker stalks [50]. This is consistent with the observations found here.

The limited data set that is available and the many interconnected factors that affect performance make it difficult to assess the magnitude that any one single factor has on performance. Any substantial inference of the relationship between the shell adiabat and the experimental yield would thus be inappropriate, as the other factors highlighted would play a significant role in affecting that yield. Further implosions would be required that aimed to reduce the other effects through removal of the dopant layer and improved target mounting. This would remove the uncertainty around which factors, adiabat or otherwise, are dominant in determining the yield.

5.6.1 Influence of the Stalk Mount on Implosions

It is widely believed that the stalk and glue will be a source for degradation of implosion performance for all implosions that implement them as a target mount [50, 56, 260, 261, 280–

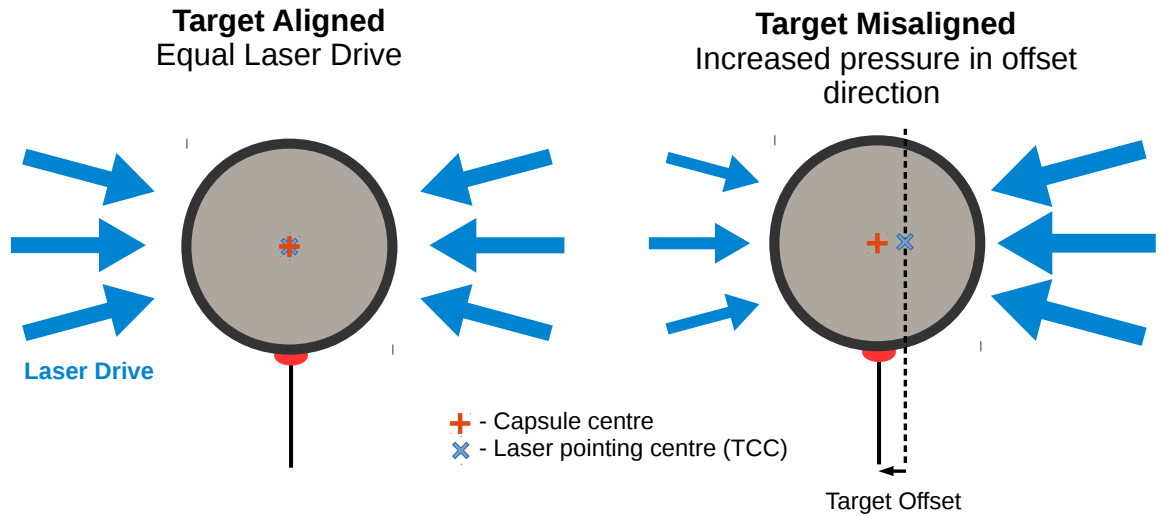


Figure 5.21: A visual representation of the effect a target offset will have on the laser drive pressure. Both aligned and misaligned targets receive spherical illumination from the lasers, where not all the beams are shown here for clarity. A target capsule that is aligned to TCC will have a symmetric and spherical drive pressure from the incident lasers, if they are also aligned to TCC. The misaligned target has a higher laser energy density on one side resulting in a larger drive pressure in the direction of its offset from TCC, pushing it further in that direction. The offset has been exaggerated for illustrative purposes and depicts a misalignment of $100\ \mu\text{m}$, 20 times larger than the target alignment accuracy that can be achieved on Omega.

283]. The effect that they have on implosions has been studied previously where it has been acknowledged that it is detrimental to performance, but the reason behind this and the magnitude of the degradation remains unclear. Further to this, if a mode 1 offset exists during the implosion then the magnitude of this degradation can vary because of the strong interplay between this offset, the stalk, and their relative orientation to each other [260].

An offset of a capsule from TCC will result in a drive asymmetry, shown in Figure 5.21. Here, an increased pressure from the laser drive is seen in the direction of the offset, pushing it further from TCC [260]. For an offset in the opposite direction of the stalk, the shadowing of the laser by the glue and stalk may compensate for the increased drive on this side of the capsule which reduces the driving of the mode 1. However, for an offset in the same direction of the stalk, potentially like those observed in this experiment, the capsule is in fact driven into the stalk which increases any detrimental effects that could occur.

5.6.2 Hot Electron Adiabatic Increase

Preheating of the fuel by hot electrons can act as a significant source of performance degradation for ICF implosions [284]. The pulse shapes here were designed to limit the excitation of LPs and hot electrons. Nevertheless, some level of LPs are expected. The deposition of the hot electron energy in the cold fuel increases the adiabat where higher values have a more detrimental effect on certain key metric. These include hot spot pressure and shell areal density, both decreasing with adiabat α scaling as $P_{\text{hs}} \sim \alpha^{-0.90}$ and $\rho R_{\text{shell}} \sim \alpha^{-0.54}$ [72].

Figure 5.22 shows the characterisation of the laser-plasma interactions and hot electron production. The upper image shows the backscatter signal that has been spectrally dispersed and temporally streaked by the full-aperture backscatter diagnostic, displayed on a logarithmic colour bar. The feature that is present at ~ 2.5 ns is characteristic of the two plasmon decay instability, identified by the centre of the signal at ~ 702 nm and the split features, which are discussed in Section 4.4. The periodic features at the top are from a timing fiducial. No other distinct features are seen on the backscatter diagnostic, suggesting that two plasmon decay is the dominant laser-plasma instability. This instability is typical for interactions with shorter density length scales plasma, such as the ablation plasma seen in Omega-60 implosions [88].

The lower plot provides the delivered laser power profile once the drive multipliers have been applied, the two plasmon decay (TPD) threshold parameter, the unfolded hot electron induced bremsstrahlung emission as recorded by HXR2, and the spectrally integrated TPD signature from the upper plot. The threshold parameter was calculated with equation 2.21 using values for the electron temperature and density scale length at quarter critical from HYADES simulations. The jagged nature of the threshold parameter is due to the finite grid size of the implosion simulation and therefore should not be taken to be a precise value but instead an estimation. The region where the threshold parameter is exceeded ($\eta > 1$) is highlighted in yellow. The unfolded bremsstrahlung signal created by the hot electrons is recorded by the second channel on HXR2 (HXR2) that is sensitive to x-rays of energies $\gtrsim 40$ keV.

There is clear correlation between the time over which the threshold parameter is exceeded and the presence of the TPD feature. The hot electron bremsstrahlung signal peaks near the maximum laser intensity and correlates very closely with the timing of the TPD signal.

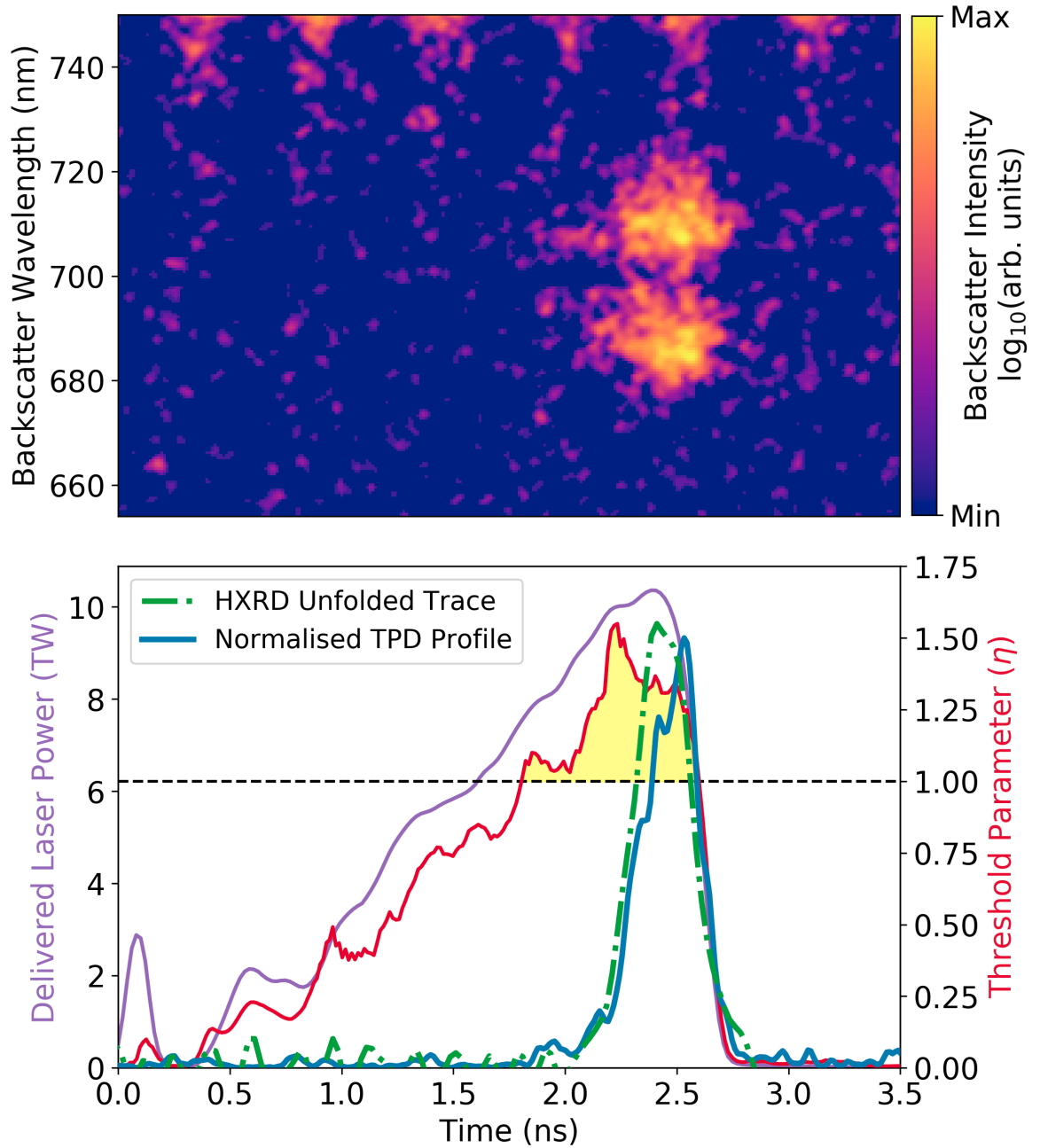


Figure 5.22: Upper image shows the backscatter signal for the two plasmon decay instability, with the intensity of a logarithmic scale. The lower graph shows the delivered laser power profile in purple with the left-hand axis, and the two plasmon decay instability threshold parameter in red on the right-hand axis. The incident laser power has been scaled to account for drive losses. The region where this threshold exceeds 1 is highlighted in yellow. The backscatter signal has been spectrally integrated and normalised, plotted as the solid blue line on the lower graph. The dot-dashed green line is the normalised and unfolded hot electron bremsstrahlung trace seen by HXR2 that has been scaled for this plot. Image inspired by [222].

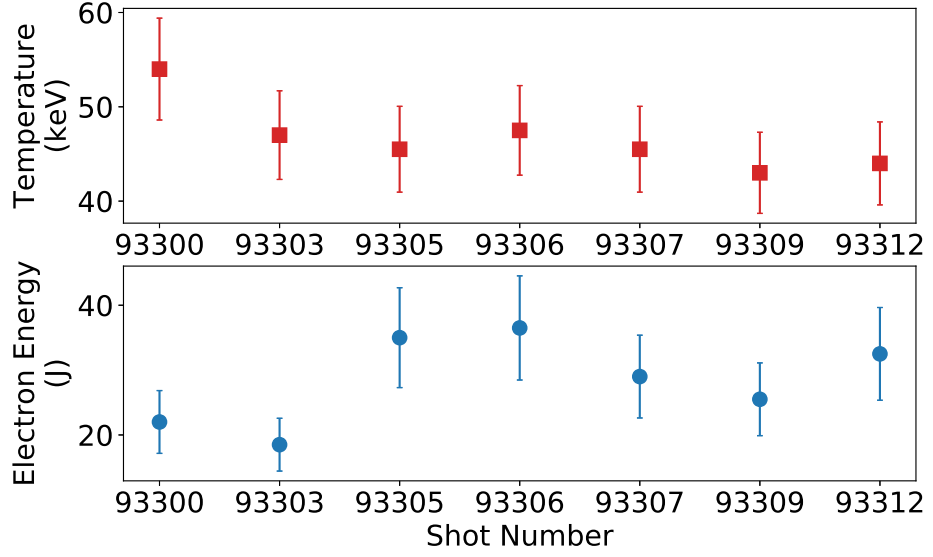


Figure 5.23: Hot electron temperatures and energies from HXR. Both parameters were very consistent and relatively low across all shots. The high temperature for shot 93300 is most likely due to the diagnostic having its sensitivity set too low which can increase the susceptibility to noise, this was corrected for the remaining shots.

The same method was used to find the hot electron energy and temperature as was outlined in Section 3.5.3. This method requires a bremsstrahlung source created by the hot electrons, that for this analysis was found from Geant4 simulations of the capsule density profile at peak intensity, as predicted by HYADES simulations. The fitted temperatures and energies are given in Figure 5.23, with temperatures remaining near constant at ~ 45 keV and energies in the range 20-40 J. This represents a 0.07-0.13% conversion efficiency of laser energy to hot electrons. Equation 5.9 was produced [285] from an analytic fit to experimental data that can be used to estimate the increase in adiabat for a given hot electron population with a temperature T_{hot} in keV and total energy E_{hot} in kJ.

$$\Delta\alpha = E_{hot} \left[\left(\frac{90}{T_{hot}} \right)^{4.7} + \left(\frac{650}{T_{hot}} \right)^{0.6} \right]^{-1} \quad (5.9)$$

Using the values for hot electron temperature and energy found from this experiment, the adiabat was expected to have increased by less than 0.002 indicating that hot electrons did not play a significant role in degrading the performance of these implosions and that low mode asymmetries can be assumed to be the primary degradation mechanism.

These implosions were in part designed to minimise the stimulation of parametric instabilities, so this result is unsurprising. The resulting low yield of hot electrons is important as

it enables the modelling of the implosion without the need to integrate hot electrons within them, and suggests that hot electrons will not disrupt fuel assemblies.

5.7 Discussion

The effect of target offset on the yield of direct drive implosions performed on Omega has been studied for warm and cryogenic implosions, both experimentally and with 2 or 3D simulations [50, 51, 281, 286]. Offsets of 10 μm and greater have been seen to be significantly detrimental to the performance of these implosions, producing neutron yield lower than what would have been achieved for an implosion with a perfectly aligned capsule. The relationship of the decrease in yield with the magnitude of the offset varies considerably across the referenced works. Grimble *et al.* [51] found that no YOC's greater than 0.5 were found for an ensemble of cryogenic-DT implosions that had offsets of $>20 \mu\text{m}$, with most having a YOC of $\lesssim 0.3$.

Future implosion designs that are to be used for high gain energy production must be robust against imperfect alignment. The high repetition rate of ~ 10 Hz means that no target mount can be used, with injection methods being proposed [287]. The implosion will need to be able to achieve high gain even with slight and unavoidable misalignments from any method of positioning the target to TCC.

Potential causes of target offsets and resulting low mode asymmetries seen in the experiment presented in this chapter might include a systematic misalignment of the capsule, lasers, or both from TCC greater than the nominal 5 μm alignment accuracy. The impact of a misalignment would be greatly increased if the misalignment was in the direction of the stalk [260], as was suggested by the XRPHC data. Further to this, an investigation by Edgell *et al.* [53] found that the distributed polarisation rotators [136] (DPR), a near field optical element that provides beam smoothing, that are in use on the Omega laser system resulted in low mode asymmetries.

DPRs use a wedge of birefringent material that is placed in each beam path prior to the phase plate. This produces two orthogonally polarised beams with a small 47 μrad difference in directions [53]. The resulting on target displacement of the high frequency intensity patterns from these two beams of 90 μm produces an instantaneous reduction in non-uniformity by a factor of $\sqrt{2}$ [136].

Regions at the edges of overlapped beams will be dominated by one single linear polarisation. The crossing of these linear polarisations in the coronal plasma has been shown to increase the beam-to-beam non-uniformity through its susceptibility to the CBET instability [53]. The transfer of energy between beams can lead to asymmetric drive and results in low mode asymmetries in the imploded capsule shape.

Modelling of an imploding capsule that implements the beam polarisation displacement from the DPRs with a 3D CBET code indicated that there were large $\sim 5\%$ peak-to-valley differences in the on target absorption [53]. When decomposed into the Legendre polynomials, the absorption distribution showed strong modes 1 and 2, with the largest being mode 10, that is thought to be the result of Omega's truncated icosahedron beam pattern [281]. It should be noted that no mode 10 was observed in the Legendre polynomial decomposition that was performed on the self-emission images that was predicted by the 3D modelling. The resolution of the detectors though means that modes this high are unlikely to as readily be observed as lower ones.

5.8 Improved Drive Multiplier

Changes in laser intensity or drive pressure due to CBET can be included in radiation-hydrodynamics codes with a time dependent multiplier on the laser intensity [203, 288] to replace more complex self-consistent CBET models. The laser pulse can be split into regions containing the picket, foot, rise, and peak power where each has its own empirically derived multiplication factor on the laser intensity. This collapses much of the complexity surrounding the changing laser overlaps, intensities, plasma conditions and much more into a far simpler model that can readily be included in implosion simulations without drastic increases in computation time. Additional loss mechanisms will be leading to a decreased drive, such as backscatter and reflections from other laser plasma instabilities, all of which will be incorporated into the multiplier, but it is believed that loss from CBET will be dominant.

In work performed by Robbie Scott, a potential issue with HYADES' drive model was found when comparing its simulation results with those of Lilac [259] and experimental data from an ensemble of cryogenic-DT implosions. In particular, the timing of the peak neutron emission, also known as bangtime, was consistently ~ 100 ps later than what was seen in

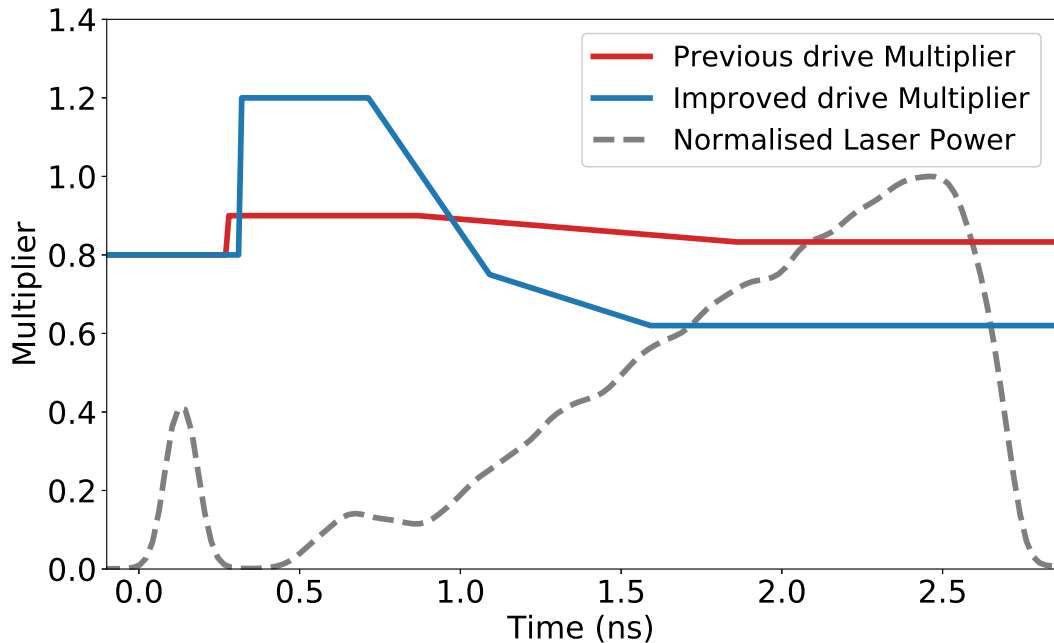


Figure 5.24: Time dependent drive multipliers for the various stages of an implosion. The previously used model is shown in red and the improved model shown in blue, improved with the data taken with SFC. The multiplier increasing above 1 might be explained with non-local transport effects.

both the experiments and the Lilac simulations. This discrepancy was attributed to the drive multiplier not sufficiently constrained by experimental data. Based on this, the radius of the ablation front determined from the SFC diagnostic was subsequently used to tune HYADES' calculations, and then to iteratively improve the drive multiplier model until an agreement was found.

The previous and new improved multipliers are shown in Figure 5.24, along with the laser profile. The new drive multiplier was found to have an increased value for the foot, increasing the drive pressure to 1.2, and a lower multiplier for the main part of the drive where it falls to ~ 0.6 . Increasing the drive multiplier to a value greater than 1 identifies the time of high non-local transport where the free streaming of the electrons was higher than the preset flux limiter. Similar characteristics have been seen in Lilac simulations that employ self-consistent drive models and non-local electron transport [289].

Figure 5.25 depicts the same data as Figure 5.7, that being the inner edge radius of the experimental data and the simulated implosions that used the improved drive multiplier, with the previously used un-optimised multiplier results shown for comparison. The lower initial drive of the previous multiplier initiates a slower implosion, hence why the radius is

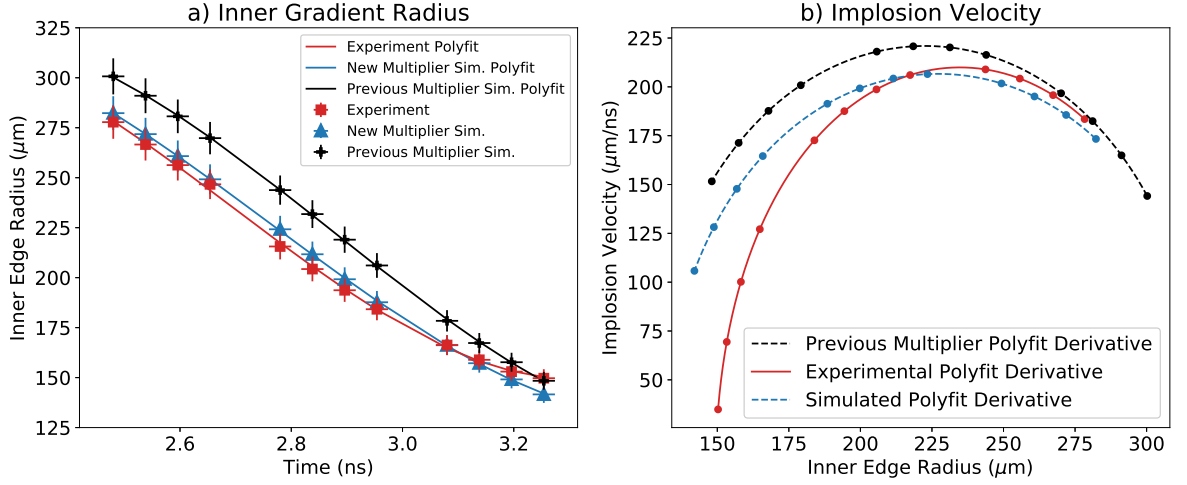


Figure 5.25: a) A comparison of the inner gradient shell radius against time of the experimental data with the simulated values produced from the previous and improved laser drive multiplier, plotted with 3rd order polynomial fits. b) The resulting implosion velocities were inferred from the differentiation of the fitted polynomials with respect to time.

initially too large. However, compared with the improved multiplier, the late time drive is too high which leads to a large over estimation of the implosion velocity that can readily be seen in the image b) of the figure.

The refined multiplier was able to produce an improved agreement with the cryogenic-DT ensemble, with the average difference in the bangtime for the ensemble being reduced to near zero. Other parameters such as areal density also fell much closer to the experimental data. Further experiments that explore these reduced adiabat designs are required if the multiplier is to be better constrained with additional tuning data. This can only be realised with time resolved trajectory and hot spot measurements from diagnostics with multiple lines of sight.

5.8.1 Cryogenic-DT Implosions

Motivated by high performance predictions, a cryogenic-DT implosion was performed using this reduced adiabat concept. The implosion took place soon after the experiment presented in this chapter, such that preliminary analysis had been performed but the drive multiplier had not yet been tuned. The pulse shape was similar to that presented in Figure 5.4, where the picket and foot powers of 6 and 1.2 TW were chosen based on the best performing shots from the warm-DD capsules. Simulations predicted that the implosion would achieve high neutron yields of $>10^{14}$ and large areal densities of $\sim 300 \text{ mg/cm}^2$.

When tested, the cryogenic-DT implosion under-performed compared with the simula-

Implosion Metric	Experimental Results	Previous Multiplier Simulation	Improved Multiplier Simulation
Neutron Yield ($\times 10^{14}$)	0.33	1.42	0.32
Areal density (mg/cm^2)	139	290	149
Ion temperature (keV)	2.73	2.3	2.25

Table 5.5: Implosion performance metrics from a cryogenic-DT implosion using a reduced adiabat concept, and two radiation-hydrodynamics simulations of the same implosions, one using the previous drive multiplier and the other using the improved multiplier. Both the areal density and the ion temperature are the burn-averaged calculated values. The uncertainty on the measured yield is $\sim 5\%$, on the areal density $\pm 10 \text{ mg}/\text{cm}^2$, and on the ion temperature $\pm 0.1 \text{ keV}$.

tions. Lower values for the neutron yield and areal density were recorded than what was predicted. This inability to accurately simulate the implosion demonstrates the importance of experiments for tuning the drive multiplier and highlights that codes such as HYADES are not sufficiently predictive to the reduced adiabat regime specifically. The previous multiplier values were tuned to an ensemble with implosion characteristics too dissimilar from this one, such that the reduced adiabat design fell outside the range of applicability for the previous multiplier and could not model the implosion accurately.

Once the drive multiplier had been tuned using the data and procedure outlined in Section 5.3, the implosion was re-simulated with the new laser drive coupling. The reduced performance of the cryogenic-DT shot is explained by these new simulations. They revealed that the differently scaled laser drive produced shocks that were mistimed for optimal performance. Table 5.5 shows some of the key performance metrics from the experimental implosion and two simulations, one using the previous multiplier and the other using the optimised values. It can be seen that neutron yield and areal density are reproduced well with the new multiplier, indicating that this tuning has incorporated previously uncaptured effects. At present, the reason for differences in ion temperatures is unclear.

The laser pulse was redesigned with the new multiplier and is shown in Figure 5.26, plotted with the previous laser pulse design and the delivered laser pulse for the cryogenic-DT shot, based on the previous design. The new design is again predicted to be highly performing, and is intended for further testing on cryogenic-DT implosions.

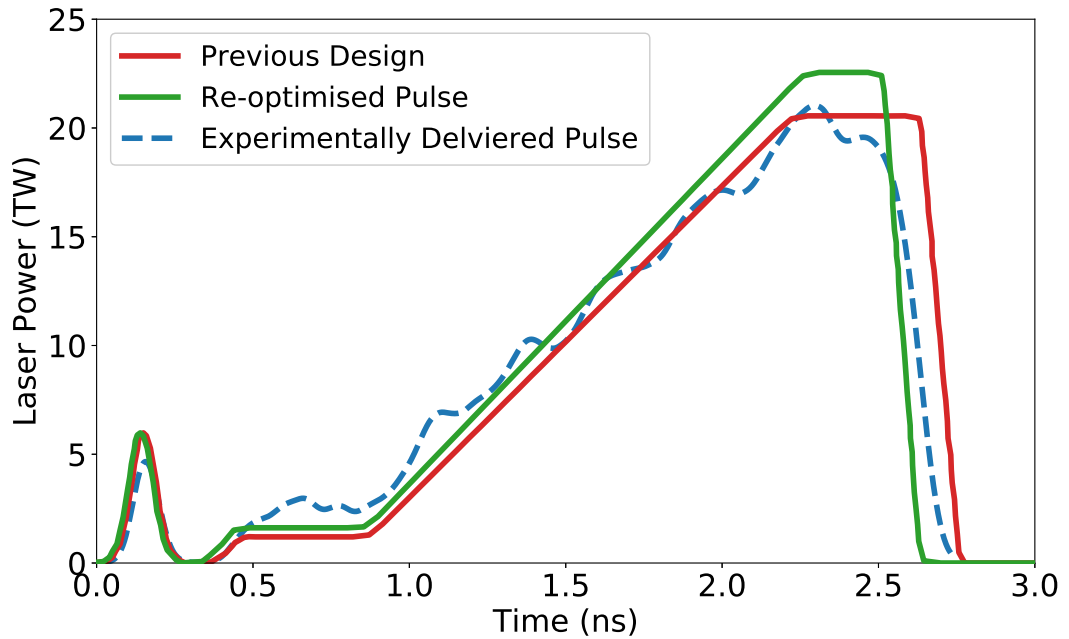


Figure 5.26: Laser pulses for reduced adiabat implosions. The previous design was based on the unoptimised drive multiplier and was used in a cryogenic-DT experiment. The design was re-optimised with the new multiplier values and is predicted to have high performance if implemented.

5.9 Conclusion

Detailed time and space resolved measurement are essential in moving forward the design of direct drive implosion experiment. Current simulation models do not include all the physics needed to capture the complexities of an implosion, yet together, experiments and simulation provide a potential route to realised ignition. In the experiment presented in this chapter, 12 direct drive implosions were performed on Omega-60. The focus was to demonstrate reduced fuel adiabat assembly relevant for shock ignition.

A significant mode 2 asymmetry was observed during the implosion of the capsule, and in the central hot spot formed at late time. This hot spot also displayed a mode 0 asymmetry where it was offset from the implosion centre. Despite this, predictions for the performance of pure plastic shelled capsules matched closely with one-dimensional simulations, a remarkable demonstration of the ability to accurately design and perform experiments. Comparatively, capsules with an additional Cu dopant layer under-performed, suggesting that higher dimensional effects were not captured in the simulations. The dominant laser-plasma instability was identified as two plasmon decay which induced a low conversion efficiency of laser energy into hot electrons of modest temperatures, suggesting that they did not impact the implosion

performance.

The implosion trajectory was accurately determined with a gated self-emission framing camera, and the results from this were used to tune an empirical drive multiplier. Implementing this tuned multiplier significantly improved the ability of the radiation-hydrodynamics code HYADES to predict key implosion metrics such as bangtime and areal density of a cryogenic-DT shot based on this concept.

With the capabilities of the improved drive multiplier, a reduced adiabat pulse shape has been redesigned and is intended to be tested on cryogenic-DT shots on Omega, aiming to demonstrate the high neutron yields that are predicted from simulations. Further work could include testing a low adiabat and purposefully sub-ignition implosion on kJ or MJ scale facilities that are not aiming for high yield specifically, but to demonstrate the ability to assemble the fuel as expected for shock ignition.

Chapter 6

Conclusions

The objective of this thesis is to study the fuel assembly and ignition stages needed to realise the shock ignition approach to direct driver inertial confinement fusion (ICF). To this aim, experiments were performed on the Omega-60 laser facility that isolated the physics of these two stages. The first experiment used a novel conical target design that accessed the laser-plasma conditions relevant for MJ-scale shock ignition implosions, in order to study the parametric instabilities and hot electrons generated by a high intensity spike. The second experiment characterised the implosion trajectory and hot spot formation for reduced adiabat implosions to tune a laser drive multiplier to account for the reduction in drive from instabilities, including the Cross-Beam Energy Transfer instability (CBET).

Inertial confinement fusion (ICF) involves the symmetric implosion and ignition of cryogenic fusion fuel capsules using highly shaped laser pulses. The central hot spot ignition approach requires large implosion velocities to impart the shell with enough kinetic energy to compress and heat a hot spot to trigger ignition. The large accelerations and high compressions result in the fuel being susceptible to detrimental hydrodynamic non-uniformities and instabilities that can degrade the coupling of energy to the hot spot and potentially break up the fuel.

Shock ignition is a variant of ICF that separates the fuel assembly and the triggering of ignition. It proposes a low velocity assembly of the fuel offering greater robustness against hydrodynamic instabilities, and larger fuel areal densities from lower implosions on a lower fuel adiabat. A late timed spike in laser intensity launches a strong shock into the compressed fuel that triggers ignition. The parameter space for interaction of the high intensity spike with the ablation plasma conditions was previously unexplored, and the low adiabat implosions

were not well modelled.

A novel large open angle conical target and beam repointing scheme was fielded on Omega that was able to access for the first time the ablation plasma conditions relevant for MJ-scale direct drive implosions on a sub-scale system. High temperature and long density scale length plasmas of up to 500 μm and 3 keV were achieved, similar to the conditions expected for shock ignition implosions. Laser intensities of up to $8 \times 10^{15} \text{ W/cm}^2$ illuminated the generated plasma to emulate the high intensity spike.

The laser-plasma instabilities were identified by the Full Aperture Backscatter (FABS) diagnostic that spectrally resolved and temporally streaked the light backscattered from instabilities. The dominant feature that was observed during the high intensity interaction was consistent with the convective stimulated Raman scattering (SRS) instability. A signature of the two plasmon decay (TPD) instability was observed during the formation of the ablation plasma only. It is inconclusive if these were the only LPI stimulated during the interaction as backscatter measurements were only available on beams with a single incidence angle. It has been previously observed that the angle the backscatter diagnostic has with the respect to the target normal can significantly impact the features that are recorded [224].

The hot electrons generated were characterised in terms of their temperature and total energy by bremsstrahlung radiation decomposition, and characteristic line emission detection from an embedded copper layer. Two hard x-ray spectrometers were fielded; the 9-channel time integrated Hard X-ray Image Plate (HXIP) diagnostic, and the 3-channel time resolved Hard X-Ray Detector (HXRD). The hot electron temperatures inferred with HXIP were found from a reduced χ^2 minimisation procedure to be between 35-50 keV, in agreement with HXRD once the disparity between their predictions is considered [186]. The total energy of the hot electrons was found with the Zinc von Hamos (ZVH) diagnostic, a spectrometer with a high detection efficiency for photons in the range 7-10 keV. The emitted K_α yield was compared against Monte-Carlo simulations of electron-target interactions. Hot electron energies found represented a conversion efficiency of $\sim 1 - 3\%$ of laser energy into hot electrons. Incorporating electrons with these characteristics into radiation-hydrodynamics simulations of a shock ignition implosion suggest they would impose minimal detriment to the shock pressure and areal density. Characterising these hot electrons is an essential step in assessing the viability of shock ignition, and the inferred properties provide an encouraging

outlook for the success of this approach.

High areal densities and greater energy gains can be achieved by imploding fuel capsules using shaped laser pulses that maintain a low fuel adiabat where the compressibility of the material is kept high. An experiment was performed to improve the ability to accurately model these implosions by tuning an empirically derived laser drive multiplier model to account for coupling inefficiencies, primarily due to CBET. An array of gated self-emission images were recorded with the Sydor Framing Camera diagnostic (SFC) that were used to infer the implosion trajectory of the capsule. The multiplier was tuned by comparison of the measurements with post-processed 1-dimensional radiation-hydrodynamics simulations. A cryogenic implosion was previously performed on Omega whose design was based on the reduced adiabat explored in this experiment. The implosion under-performed compared with predictions made with the previous unoptimised multiplier. The implosion characteristics however, were well reproduced when using the improved multiplier. The laser pulse has been re-optimised for a high yield implosion that is intended for testing on Omega.

Low mode asymmetries were identified during the implosion. Hot spot offsets and ellipticities were identified with the time integrated X-Ray Pinhole Camera diagnostic (XRPHC). Offsets of $\sim 20 \mu\text{m}$ from the implosion centre were observed.

The hot spot size, shape, and evolution were characterised with the near-orthogonally placed diagnostic Time Resolved X-ray Imager (TRXI) and Kirkpatrick-Baez Framed microscope (KBF). A strong elliptical shape that was described by a dominant mode 2 asymmetry was observed by the TRXI diagnostic. These elliptical hot spots indicated an asymmetric implosion that lead to worsened coupling of shell kinetic energy to the hot spot. Circular hot spots were observed by the KBF diagnostic suggesting that it was viewing the hot spot down the semi-major axis of the asymmetry, whereas TRXI was looking perpendicular to it. The minimum hot spot size and the timing of peak compression were well modelled by radiation-hydrodynamics simulations. Time integrated hot spot images recorded with the Gated Monochromatic X-ray Imager (GMXI) suggested strong hot spot flows were present that represent residual kinetic energy that did not aid in hot spot formation.

Multiple interconnected factors impacted the yield of the implosion, including the hot spot offsets, capsule ellipticity, target composition, and in-flight shell adiabat. The yield on a subset of shots was severely affected by the addition of embedded Cu doped layer that

resulted in increased surface roughness and necessitated a coating of Al_2O_3 . This impacted the ability to accurately assess the relationship of the adiabat with yield, as the magnitude of the other factors are not well known.

The work presented in this thesis represents a significant step forward in the understanding and modelling of physics relevant to ignition scale direct drive shock ignition. Two experiments have been presented that have focused on the assembly and ignition stages of shock ignition, each with numerous findings and conclusions. The key perspectives highlighted by this work include:

- It is necessary to characterise the laser-plasma interactions in ablation plasma and laser intensity conditions that are expected for an ignition scale shock ignition implosion. The parametric instabilities need to be identified from backscatter measurements at multiple angles. The hot electrons that are generated from these instabilities need to be fully characterised by multiple diagnostics that utilise different methods for analysis, for example bremsstrahlung and line emission measurements. This could be achieved with novel diagnostics that are designed for high repetition rate facilities, with well characterised and judiciously designed responses. It is essential that the hot electrons are well known for shock ignition to progress as their effect must be considered in implosion designs and that can only be realised with experimental characterisation. Further to this, reaching the relevant parameter space is a requirement due to the dependence of laser-plasma instabilities on the temperature and density scale length of the plasma.
- Shock ignition implosion designs that are informed by radiation-hydrodynamics codes must incorporate hot electron generation and propagation. The coupling of laser energy to hot electrons will reduce the laser drive energy on the capsule which will impact the implosion velocity and igniting shock strength. The hot electrons will preheat the fuel, reducing the peak areal density that can be reached, and limiting the gain of the implosion. By including these effects, a more accurate understanding of the laser and capsule requirements for shock ignition can be found, and strategies for mitigating these effects can be implemented. These include delaying the shock timing in order for more areal density to have built up or increasing the ablator layer thickness to increase

the shell stopping power.

- Reduced adiabat implosions offer the potential for high yields but require greater understanding if they are to be used for shock ignition fuel assembly. The improved modelling found here will greatly enhance the ability to model and design implosions. Further experiments must be performed to test the ability to accurately predict a low adiabat and sub-ignition fuel assembly. It needs to be demonstrated that the areal density and ion temperature profiles can be reproduced by simulations, and that the conditions that can be reached are sufficient for a shock ignition implosion to be primed to ignite.

Appendix A

n -dimensional Maxwell-Boltzmann Distribution Functions

The n -dimensional Maxwell-Boltzmann velocity distribution function is given by the following equation,

$$f(v).d^n v = \left(\frac{m}{2\pi k_B T} \right)^{n/2} \exp \left(-\frac{m|v|^2}{2k_B T} \right) .d^n v \quad (\text{A.1})$$

where v is the particle velocity, m is the particle mass, and T is the temperature. The subsequent energy distributions for the first three dimensionalities (1D, 2D & 3D) are given by the following equations,

$$f_{1D}(E).dE = \frac{2E_{Tot}}{k_B T} \times \frac{1}{2} \sqrt{\frac{1}{Ek_B T}} \exp \left(-\frac{E}{k_B T} \right) .dE \quad (\text{A.2})$$

$$f_{2D}(E).dE = \frac{E_{Tot}}{k_B T} \times \frac{1}{k_B T} \exp \left(-\frac{E}{k_B T} \right) .dE \quad (\text{A.3})$$

$$f_{3D}(E).dE = \frac{2E_{Tot}}{3k_B T} \times 2 \sqrt{\frac{E}{\pi k_B^3 T^3}} \exp \left(-\frac{E}{k_B T} \right) .dE \quad (\text{A.4})$$

where E is the particle energy and E_{Tot} is the total energy in the distribution.

The relativistic Maxwell-Jüttner energy distribution is given by the following equation,

$$f(E) \propto \left(1 + \frac{E}{mc^2} \right) \left[\left(1 + \frac{E}{mc^2} \right)^2 - 1 \right]^{\frac{n-2}{2}} e^{-E/k_B T} \quad (\text{A.5})$$

where mc^2 is the rest mass of the particle and n is the dimensionality.

Appendix B

Sydor Framing Camera Noise Removal Techniques

The Sydor Framing Camera diagnostic (SFC), outlined in Section 3.6.2, records gated self-emission images from an imploding capsule. Examples of the images recorded by SFC and the analysis method are given in Section 5.3. The susceptibility of the diagnostic to high frequency noise can be seen in Figure 5.2 which depicts all 16 images taken by the diagnostic, and Figure B.1 below where a single image is shown. This noise can affect the analysis of the images and characterisation of the capsule, therefore it must be removed.

The origin of this high frequency noise is likely to be high energy photons that bypass the micro-channel plate used to gate the images and which strike the imaging CCD directly. This saturates the pixel that the photon strikes, whose signal can then bleed over to the surrounding pixels. This bleeding denies the ability to simply remove all the saturated pixels, as it is not just the saturated pixels that are affected. The self-emission from the capsule can also cause saturation of CCD so a rudimentary removal of saturated pixels would also remove data.

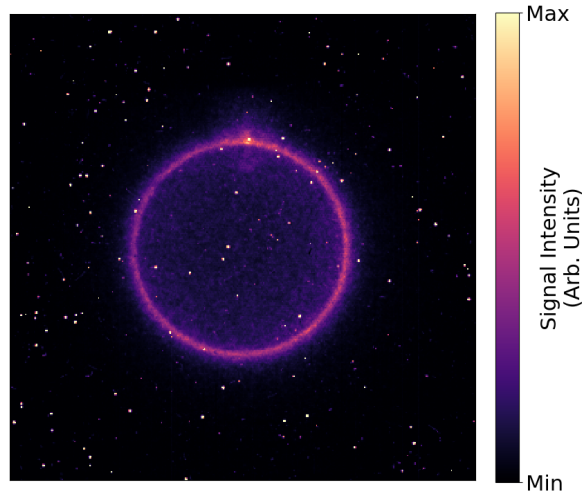


Figure B.1: An example image of Sydor framing camera data showing the self emission of an imploding capsule. The high frequency noise can be seen, likely caused by high energy radiation.

Methods for noise removal include a median pixel filter, a Gaussian blur, and a removal of the high frequency Fourier modes. A median pixel filter will replace each pixel by the median value of the surrounding pixels within a specified range, where a 5×5 region around the pixel is chosen for this data. A Gaussian blur convolves the data with a 2D Gaussian function for a specified value of the Gaussian standard deviation, chosen for this comparison to be 3 pixels. The high frequency Fourier modes are removed by performing a 2D Fourier transform on the data and only keeping a certain amount of the low frequency mode, where 10% are kept here. The cleaned data is then reconstructed by performing an inverse Fourier transform on the truncated frequency modes. Each of these methods will remove or change more than just the saturated pixels and will edit the self-emission data as well. A custom routine was written that was able to identify the saturated pixels while differentiating them from the self-emission data that was saturated. It was also able to identify the pixels where this saturation had bled over. All of the saturated pixels and their bleedings were replaced with the median value from the surrounding 5×5 pixel region.

The four noise removal techniques have been used on the data shown in Figure B.1, and the absolute difference between the raw data and the cleaned versions have been found. The custom routine's cleaned data is shown in Figure B.2, along with its absolute difference with the raw data, shown on a log scale for better comparison with the other techniques as it highlights all the pixels that have had their values changed. It can be seen that there are

only small regions that are changed corresponding to the noise.

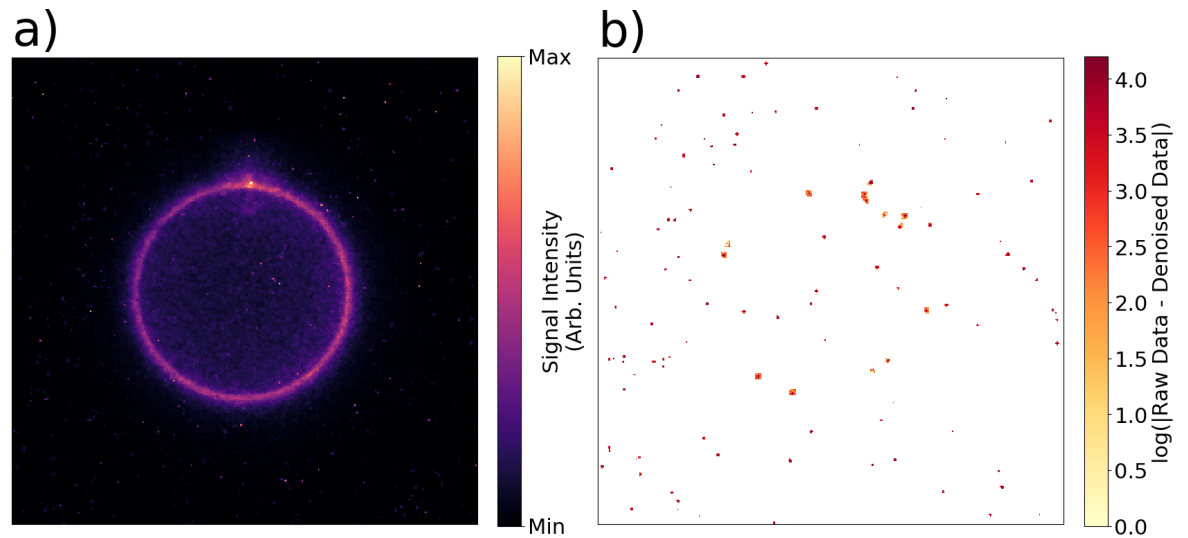


Figure B.2: A custom noise removal routine has been used on the data shown in Figure B.1, and the cleaned data is shown in image a). Image b) shows the absolute difference between raw data and the cleaned version, the bright spots are the identified noise and bleedings.

The Median Pixel Filter technique is shown in Figure B.3. The cleaned data shows that this technique does well at removing most if not all of the noise but it also changes the self-emission data as well. This can be seen as the ring in image b), indicating that these pixels have had their values changed.

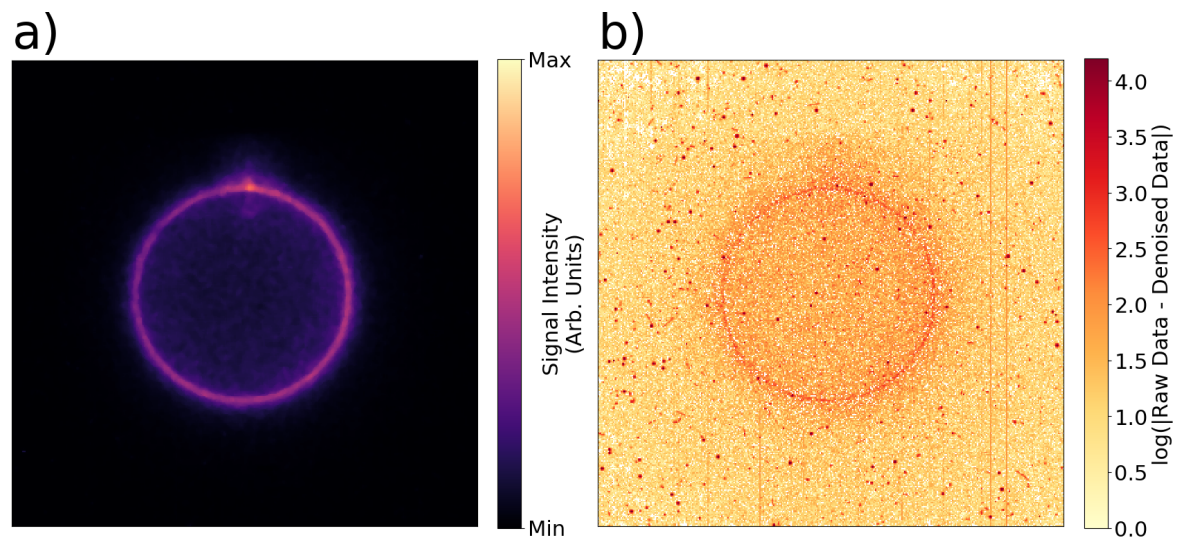


Figure B.3: a) SFC data that has been cleaned by a median pixel filter and b) the absolute difference between raw data and the cleaned version.

Figure B.4 shows the use of a Gaussian filter on the data. This technique does indeed reduce the effect of the high frequency noise by blurring the affected pixels but does not remove them. Similar to the median pixel filter, it significantly impacts the self-emission data, as can be seen from the ring in image b).

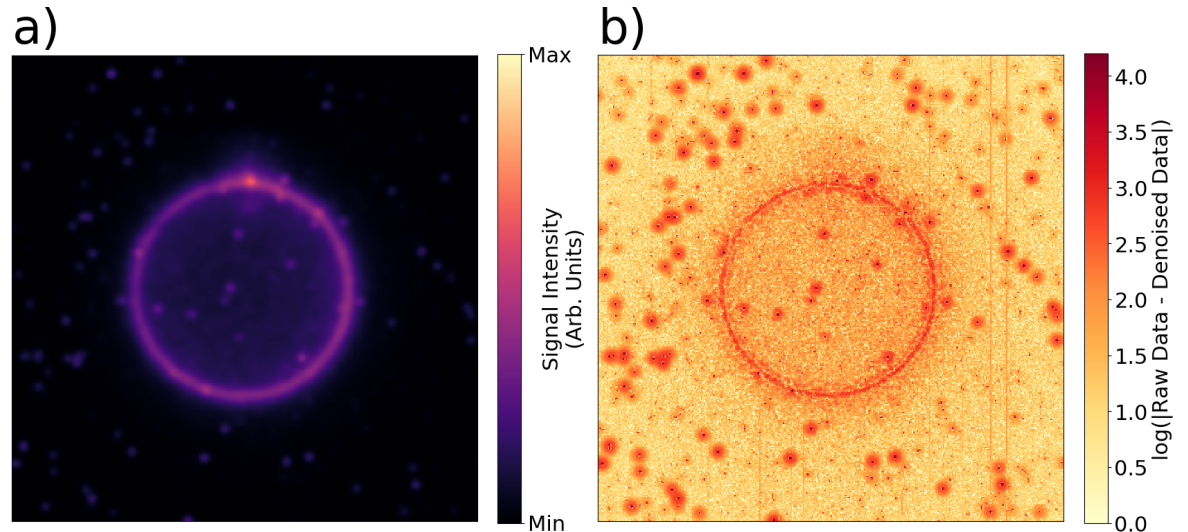


Figure B.4: a) SFC data that has been cleaned by a Gaussian blur filter and b) the absolute difference between raw data and the cleaned version.

The removal of the high frequency Fourier modes is shown in Figure B.5. This technique does not impact the self-emission data as much as the Gaussian blur but is less effective at removing the noise.

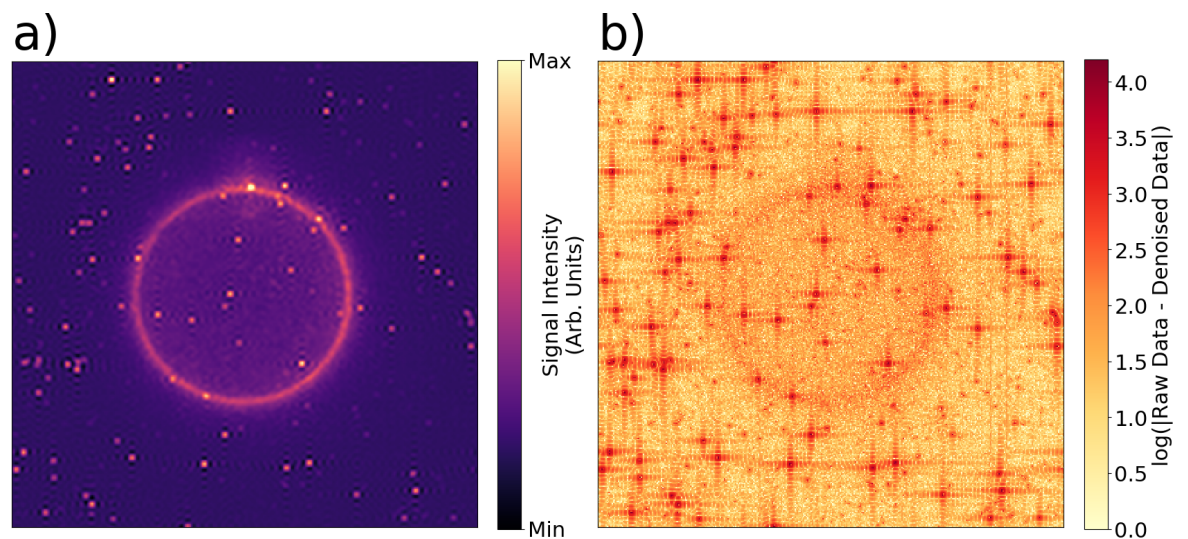


Figure B.5: a) SFC data that has been cleaned by a removing high frequency Fourier modes and b) the absolute difference between raw data and the cleaned version.

Using each of these noise removal techniques, the inner edge radius of the capsule's emission can be found. The inner edge radius is the location of the 65% intensity contour from the minimum emission at the centre of the image to the peak emission of the ring, as outlined in Section 3.6.2. Figure B.6a) shows the predicted radius against time for the 16 gated images of SFC from each of the techniques, as well as for the uncorrected or "raw" data. Figure B.6b) shows the inferred implosion velocities, found by fitting a 3rd order polynomial to the radius and taking the derivative. It can be seen that the custom routine and median pixel filter produce similar values of the radius and velocity to both each other and to the raw data. The Gaussian blur and the high Fourier mode removal both smear out the signal to such an extent that the inner edge is moved inwards.

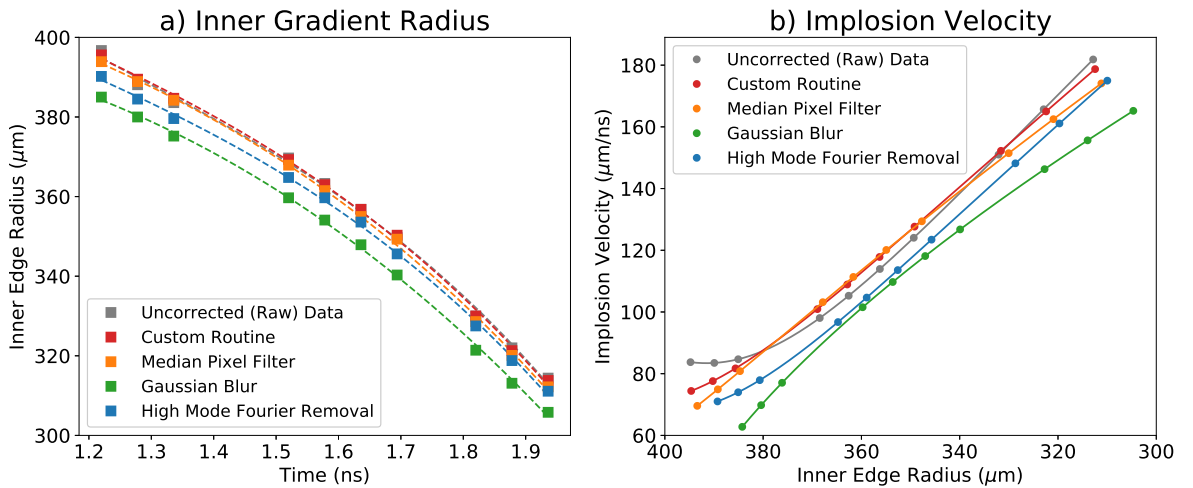


Figure B.6: The inner edge radius and inferred implosion velocity from the raw SFC data and various noise removal techniques. The implosion velocity is found by fitting and differentiating a 3rd order polynomial to the radius trajectory.

The custom routine is able to provide a high level of noise removal while maintaining the self-emission data in its entirety. This ensures that the radius determination method is able to be implemented efficiently and accurately. Other techniques for noise removal will comprise the data to varying degrees, producing different radius predictions.

List of References

- [1] I. P. O. C. Change. Climate change 2007: the physical science basis. *Agenda*, 6(07):333, 2007.
- [2] H. Chen, T. N. Cong, W. Yang, C. Tan, Y. Li, and Y. Ding. Progress in electrical energy storage system: A critical review. *Progress in natural science*, 19(3):291, 2009.
- [3] B. H. Association. England and Wales Hydropower Resource Assessment. Technical report, Department of Energy & Climate Change (DECC) & Welsh Assembly Government (WAG), 2010.
- [4] M. Holt, R. J. Campbell, and M. B. Nikitin. Fukushima nuclear disaster. Congressional Research Service Washington, DC, USA, 2012.
- [5] A. P. Møller and T. A. Mousseau. Biological consequences of Chernobyl: 20 years on. *Trends in ecology & evolution*, 21(4):200, 2006.
- [6] K. Rao. Radioactive waste: The problem and its management. *current science*, 81(12):1534, 2001.
- [7] E. Gibney. Nuclear-fusion reactor smashes energy record. *Nature*, pages 371–371, 2022.
- [8] J. Tollefson et al. US achieves laser-fusion record: what it means for nuclear-weapons research. *Nature*, 597(7875):163, 2021.
- [9] R. S. Craxton, et al. Direct-drive inertial confinement fusion: A review. *Physics of Plasmas*, 22(11):110501, 2015.
- [10] S. Atzeni and J. Meyer-ter Vehn. *The physics of inertial fusion: beam plasma interaction, hydrodynamics, hot dense matter*, volume 125 of *Oxford science publications*. OUP Oxford, 2004.

- [11] S. Pfalzner. *An introduction to inertial confinement fusion*. CRC Press, 2006.
- [12] J. Lindl. Development of the indirect-drive approach to inertial confinement fusion and the target physics basis for ignition and gain. *Physics of Plasmas*, 2(11):3933, 1995.
- [13] R. Betti, C. D. Zhou, K. S. Anderson, L. J. Perkins, W. Theobald, and A. A. Solodov. Shock ignition of thermonuclear fuel with high areal density. *Physical Review Letters*, 98(15):1, 2007.
- [14] J. Nuckolls, L. Wood, A. Thiessen, and G. Zimmerman. Laser compression of matter to super-high densities: Thermonuclear (CTR) applications. *Nature*, 239(5368):139, 1972.
- [15] T. Boehly, et al. Initial performance results of the OMEGA laser system. *Optics Communications*, 133(1-6):495, 1997.
- [16] M. A. Abdou. Tritium breeding in fusion reactors. In *Nuclear data for science and technology*, pages 293–312. Springer, 1983.
- [17] N. Ghahramany, S. Gharaati, and M. Ghanaatian. New approach to nuclear binding energy in integrated nuclear model. *Journal of Theoretical and Applied Physics*, 6(1):1, 2012.
- [18] G. Gamow and E. Teller. The rate of selective thermonuclear reactions. *Physical Review*, 53(7):608, 1938.
- [19] H.-S. Bosch and G. Hale. Improved formulas for fusion cross-sections and thermal reactivities. *Nuclear fusion*, 32(4):611, 1992.
- [20] J. Ongena. Fusion: A true challenge for an enormous reward. In *EPJ Web of Conferences*, volume 98, page 05004. EDP Sciences, 2015.
- [21] J. D. Lawson. Some criteria for a power producing thermonuclear reactor. *Proceedings of the physical society. Section B*, 70(1):6, 1957.
- [22] R. E. Tipton. Generalized Lawson criteria for inertial confinement fusion. Technical report, Lawrence Livermore National Lab.(LLNL), Livermore, CA (United States), 2015.

- [23] G. Fraley, E. Linnebur, R. Mason, and R. Morse. Thermonuclear burn characteristics of compressed deuterium-tritium microspheres. *The Physics of Fluids*, 17(2):474, 1974.
- [24] I. A. Richardson and J. Leachman. Thermodynamic properties status of deuterium and tritium. In *AIP Conference Proceedings*, volume 1434, pages 1841–1848. American Institute of Physics, 2012.
- [25] P. W. McKenty, et al. Direct-drive cryogenic target implosion performance on OMEGA. *Physics of Plasmas*, 11(5):2790, 2004.
- [26] F. J. Marshall, et al. Direct-drive, cryogenic target implosions on OMEGA. *Physics of Plasmas*, 12(5):056302, 2005.
- [27] O. Hurricane, et al. Beyond alpha-heating: driving inertially confined fusion implosions toward a burning-plasma state on the national ignition facility. *Plasma Physics and Controlled Fusion*, 61(1):014033, 2018.
- [28] O. Hurricane, et al. Approaching a burning plasma on the nif. *Physics of Plasmas*, 26(5):052704, 2019.
- [29] O. N. Krokhin and V. B. Rozanov. Escape of α Particles from a Laser-Pulse-Initiated Thermonuclear Reaction. *Soviet Journal of Quantum Electronics*, 2(4):393, 1973.
- [30] A. Zylstra and O. Hurricane. On alpha-particle transport in inertial fusion. *Physics of Plasmas*, 26(6):062701, 2019.
- [31] L. S. Brown, D. L. Preston, and R. L. Singleton Jr. Charged particle motion in a highly ionized plasma. *Physics Reports*, 410(4):237, 2005.
- [32] H. Scott and S. Hansen. Advances in nlte modeling for integrated simulations. *High Energy Density Physics*, 6(1):39, 2010.
- [33] P. Springer, et al. A 3d dynamic model to assess the impacts of low-mode asymmetry, aneurysms and mix-induced radiative loss on capsule performance across inertial confinement fusion platforms. *Nuclear Fusion*, 59(3):032009, 2018.
- [34] L. Spitzer. *Physics of fully ionized gases*. Courier Corporation, 2006.
- [35] P. Patel, et al. Hotspot conditions achieved in inertial confinement fusion experiments on the national ignition facility. *Physics of Plasmas*, 27(5):050901, 2020.

- [36] R. Craxton. High efficiency frequency tripling schemes for high-power Nd: Glass lasers. *IEEE Journal of Quantum Electronics*, 17(9):1771, 1981.
- [37] W. L. Kruer. *The physics of laser plasma interactions / William L. Kruer*. Frontiers in physics ; v. 73. Addison-Wesley, Redwood City, Calif., 1988.
- [38] J. T. Larsen and S. M. Lane. HYADES-A plasma hydrodynamics code for dense plasma studies. *Journal of Quantitative Spectroscopy and Radiative Transfer*, 51(1-2):179, 1994.
- [39] R. E. Kidder. The theory of homogeneous isentropic compression and its application to laser fusion. In *Laser Interaction and Related Plasma Phenomena*, pages 449–464. Springer, 1974.
- [40] W. Rankine. On the thermodynamic theory of waves of finite longitudinal disturbance [Philos. Trans. 160 (1870), part II, 277–288]. *Classic papers in shock compression science, High-press. Shock Compression Condens. Matter*, pages 133–147, 1998.
- [41] H. Hugoniot. Mémoire sur la propagation des mouvements dans les corps et spécialement dans les gaz parfaits (première partie). *Journal de mathématiques pures et appliquées*, 57:3, 1887.
- [42] H. Hugoniot. Mémoire sur la propagation des mouvements dans les corps et spécialement dans les gaz parfaits (deuxième partie). *Journal de mathématiques pures et appliquées*, 58:1, 1889.
- [43] D. Barlow. *Inertial Confinement Fusion: Energy Transport and Shock Ignition*. Ph.D. thesis, University of Warwick, 2021.
- [44] A. Zylstra, et al. Burning plasma achieved in inertial fusion. *Nature*, 601(7894):542, 2022.
- [45] A. Kritcher, et al. Design of inertial fusion implosions reaching the burning plasma regime. *Nature Physics*, 18(3):251, 2022.
- [46] J. Ross, et al. Experiments conducted in the burning plasma regime with inertial fusion implosions. *arXiv preprint arXiv:2111.04640*, 2021.

- [47] S. P. Regan, et al. The National Direct-Drive Inertial Confinement Fusion Program. *Nuclear Fusion*, 59(3):032007, 2019.
- [48] S. Banerjee, K. Ertel, P. Mason, J. Phillips, J. Greenhalgh, and J. Collier. DiPOLE: A multi-slab cryogenic diode pumped Yb:YAG amplifier. In G. Korn, L. O. Silva, and J. Hein, editors, *High-Power, High-Energy, and High-Intensity Laser Technology; and Research Using Extreme Light: Entering New Frontiers with Petawatt-Class Lasers*, volume 8780, pages 45 – 51. International Society for Optics and Photonics, SPIE, 2013.
- [49] A. Parker, R. Hansen, and A. Chen. Simulating Big Energy. *Science & Technology Review, March 2021 Issue*, 2021.
- [50] I. V. Igumenshchev, F. J. Marshall, J. A. Marozas, V. A. Smalyuk, R. Epstein, V. N. Goncharov, T. J. Collins, T. C. Sangster, and S. Skupsky. The effects of target mounts in direct-drive implosions on OMEGA. *Physics of Plasmas*, 16(8), 2009.
- [51] W. Grimble, F. J. Marshall, and E. Lambrides. Measurement of cryogenic target position and implosion core offsets on OMEGA. *Physics of Plasmas*, 25(7), 2018.
- [52] D. T. Michel, I. V. Igumenshchev, A. K. Davis, D. H. Edgell, D. H. Froula, D. W. Jacobs-Perkins, V. N. Goncharov, S. P. Regan, A. Shvydky, and E. M. Campbell. Subpercent-Scale Control of 3D Low Modes of Targets Imploded in Direct-Drive Configuration on OMEGA. *Physical Review Letters*, 120(12):125001, 2018.
- [53] D. H. Edgell, P. B. Radha, J. Katz, A. Shvydky, D. Turnbull, and D. H. Froula. Nonuniform Absorption and Scattered Light in Direct-Drive Implosions Driven by Polarization Smoothing. *Physical Review Letters*, 127(7):75001, 2021.
- [54] R. Epstein. Reduction of time-averaged irradiation speckle nonuniformity in laser-driven plasmas due to target ablation. *Journal of applied physics*, 82(5):2123, 1997.
- [55] R. Stephens, D. Olson, H. Huang, and J. Gibson. Complete Surface Mapping of ICF Shells. *Fusion Science and Technology*, 45, 2004.
- [56] B. M. Haines, et al. Detailed high-resolution three-dimensional simulations of OMEGA separated reactants inertial confinement fusion experiments. *Physics of Plasmas*, 23(7):072709, 2016.

- [57] A. Lees, et al. Experimentally Inferred Fusion Yield Dependencies of OMEGA Inertial Confinement Fusion Implosions. *Phys. Rev. Lett.*, 127:105001, 2021.
- [58] Rayleigh. Investigation of the Character of the Equilibrium of an Incompressible Heavy Fluid of Variable Density. *Proceedings of the London Mathematical Society*, s1-14(1):170, 1882.
- [59] J. D. Lindl and W. C. Mead. Two-Dimensional Simulation of Fluid Instability in Laser-Fusion Pellets. *Phys. Rev. Lett.*, 34:1273, 1975.
- [60] H. J. Kull. Theory of the Rayleigh-Taylor instability. *Physics Reports*, 206(5):197, 1991.
- [61] P. B. Radha, et al. Direct drive: Simulations and results from the National Ignition Facility. *Physics of Plasmas*, 23(5):056305, 2016.
- [62] S. X. Hu, D. T. Michel, A. K. Davis, R. Betti, P. B. Radha, E. M. Campbell, D. H. Froula, and C. Stoeckl. Understanding the effects of laser imprint on plastic-target implosions on OMEGA. *Physics of Plasmas*, 23(10):102701, 2016.
- [63] S. P. Regan, et al. Hot-Spot Mix in Ignition-Scale Inertial Confinement Fusion Targets. *Phys. Rev. Lett.*, 111:045001, 2013.
- [64] O. A. Hurricane, et al. An analytic asymmetric-piston model for the impact of mode-1 shell asymmetry on ICF implosions. *Physics of Plasmas*, 27(6), 2020.
- [65] H. Takabe, K. Mima, L. Montierth, and R. Morse. Self-consistent growth rate of the rayleigh-taylor instability in an ablatively accelerating plasma. *The Physics of fluids*, 28(12):3676, 1985.
- [66] S. E. Bodner. Rayleigh-Taylor Instability and Laser-Pellet Fusion. *Phys. Rev. Lett.*, 33:761, 1974.
- [67] M. S. Plesset and S. A. Zwick. The growth of vapor bubbles in superheated liquids. *Journal of applied physics*, 25(4):493, 1954.
- [68] G. I. Bell. Taylor instability on cylinders and spheres in the small amplitude approximation. Technical report, Los Alamos National Laboratory, 1951.

- [69] J. D. Lindl, P. Amendt, R. L. Berger, S. G. Glendinning, S. H. Glenzer, S. W. Haan, R. L. Kauffman, O. L. Landen, and L. J. Suter. The physics basis for ignition using indirect-drive targets on the National Ignition Facility. *Physics of plasmas*, 11(2):339, 2004.
- [70] R. Betti, et al. Progress in hydrodynamics theory and experiments for direct-drive and fast ignition inertial confinement fusion. *Plasma Physics and Controlled Fusion*, 48(12 B), 2006.
- [71] J. Lindl, O. Landen, J. Edwards, E. Moses, and N. team. Review of the national ignition campaign 2009-2012. *Physics of Plasmas*, 21(2):020501, 2014.
- [72] C. D. Zhou and R. Betti. Hydrodynamic relations for direct-drive fast-ignition and conventional inertial confinement fusion implosions. *Physics of Plasmas*, 14(7), 2007.
- [73] A. Vallet. *Hydrodynamic modeling of the shock ignition scheme for inertial confinement fusion*. Ph.D. thesis, Université de Bordeaux, 2014.
- [74] M. Herrmann, M. Tabak, and J. Lindl. A generalized scaling law for the ignition energy of inertial confinement fusion capsules. *Nuclear Fusion*, 41(1):99, 2001.
- [75] P. McKenna, D. Neely, R. Bingham, and D. Jaroszynski. *Laser-plasma interactions and applications*. Springer, 2013.
- [76] P. B. Radha, et al. Triple-picket warm plastic-shell implosions on OMEGA. *Physics of Plasmas*, 18(1), 2011.
- [77] H.-S. Park, et al. High-adiabat high-foot inertial confinement fusion implosion experiments on the National Ignition Facility. *Physical review letters*, 112(5):055001, 2014.
- [78] A. B. Zylstra, et al. Record Energetics for an Inertial Fusion Implosion at NIF. *Physical Review Letters*, 126(2):25001, 2021.
- [79] A. Kritcher, et al. Achieving record hot spot energies with large HDC implosions on NIF in HYBRID-E. *Physics of Plasmas*, 28(7):072706, 2021.
- [80] M. Tabak, J. Hammer, M. E. Glinsky, W. L. Kruer, S. C. Wilks, J. Woodworth, E. M. Campbell, M. D. Perry, and R. J. Mason. Ignition and high gain with ultrapowerful lasers. *Physics of Plasmas*, 1(5):1626, 1994.

- [81] S. Atzeni, A. Marocchino, A. Schiavi, and G. Schurtz. Energy and wavelength scaling of shock-ignited inertial fusion targets. *New Journal of Physics*, 15(4):045004, 2013.
- [82] D. Turnbull, A. Maximov, D. Edgell, W. Seka, R. Follett, J. Palastro, D. Cao, V. Goncharov, C. Stoeckl, and D. Froula. Anomalous absorption by the two-plasmon decay instability. *Physical Review Letters*, 124(18):185001, 2020.
- [83] X. Ribeyre, M. Lafon, G. Schurtz, M. Olazabal-Loumé, J. Breil, S. Galera, and S. Weber. Shock ignition: Modelling and target design robustness. *Plasma Physics and Controlled Fusion*, 51(12), 2009.
- [84] R. Nora, et al. Theory of hydro-equivalent ignition for inertial fusion and its applications to OMEGA and the National Ignition Facility. *Physics of Plasmas*, 21(5):056316, 2014.
- [85] S. Atzeni, X. Ribeyre, G. Schurtz, A. Schmitt, B. Canaud, R. Betti, and L. Perkins. Shock ignition of thermonuclear fuel: principles and modelling. *Nuclear fusion*, 54(5):054008, 2014.
- [86] X. Ribeyre, G. Schurtz, M. Lafon, S. Galera, and S. Weber. Shock ignition: An alternative scheme for HiPER. *Plasma Physics and Controlled Fusion*, 51(1), 2009.
- [87] M. Dunne. A high-power laser fusion facility for Europe. *Nature physics*, 2(1):2, 2006.
- [88] M. J. Rosenberg, et al. Origins and Scaling of Hot-Electron Preheat in Ignition-Scale Direct-Drive Inertial Confinement Fusion Experiments. *Physical Review Letters*, 120(5):55001, 2018.
- [89] A. Seaton and T. Arber. Laser-plasma instabilities in long scale-length plasmas relevant to shock-ignition. *Physics of Plasmas*, 27(8):082704, 2020.
- [90] J. F. Drake and Y. C. Lee. Temporally growing raman backscattering instabilities in an inhomogeneous plasma. *Physical Review Letters*, 31(19):1197, 1973.
- [91] C. S. Liu, M. N. Rosenbluth, and R. B. White. Raman and Brillouin scattering of electromagnetic waves in inhomogeneous plasmas. *Physics of Fluids*, 17(6):1211, 1974.
- [92] A. Simon, R. W. Short, E. A. Williams, and T. Dewandre. On the inhomogeneous two-plasmon instability. *Physics of Fluids*, 26(10):3107, 1983.

- [93] A. Colaitis, X. Ribeyre, E. Le Bel, G. Duchateau, P. Nicolaï, and V. Tikhonchuk. Influence of laser induced hot electrons on the threshold for shock ignition of fusion reactions. *Physics of Plasmas*, 23(7), 2016.
- [94] T. E. Fox, A. P. Robinson, and J. Pasley. Strong shock generation by fast electron energy deposition. *Physics of Plasmas*, 20(12), 2013.
- [95] W. L. Shang, R. Betti, S. X. Hu, K. Woo, L. Hao, C. Ren, A. R. Christopherson, A. Bose, and W. Theobald. Electron Shock Ignition of Inertial Fusion Targets. *Physical Review Letters*, 119(19):1, 2017.
- [96] P. Nicolaï, J. L. Feugeas, M. Touati, X. Ribeyre, S. Gus’Kov, and V. Tikhonchuk. Deleterious effects of nonthermal electrons in shock ignition concept. *Physical Review E - Statistical, Nonlinear, and Soft Matter Physics*, 89(3):1, 2014.
- [97] S. Tigik, L. Ziebell, and P. Yoon. Collisional damping rates for plasma waves. *Physics of Plasmas*, 23(6):064504, 2016.
- [98] J. Dawson. On landau damping. *The physics of fluids*, 4(7):869, 1961.
- [99] J. Trela. *Effect of hot electrons on the hydrodynamic of shocks and implosions for shock ignition*. Ph.D. thesis, Université de Bordeaux, 2019.
- [100] J. Freidberg, R. Mitchell, R. L. Morse, and L. Rudsinski. Resonant absorption of laser light by plasma targets. *Physical Review Letters*, 28(13):795, 1972.
- [101] D. Forslund, J. Kindel, and E. Lindman. Theory of stimulated scattering processes in laser-irradiated plasmas. *The Physics of Fluids*, 18(8):1002, 1975.
- [102] C. Liu and M. N. Rosenbluth. Parametric decay of electromagnetic waves into two plasmons and its consequences. *The Physics of Fluids*, 19(7):967, 1976.
- [103] A. Palmer. Stimulated Scattering and Self-Focusing in Laser-Produced Plasmas. *The Physics of Fluids*, 14(12):2714, 1971.
- [104] R. Craxton and R. McCrory. Hydrodynamics of thermal self-focusing in laser plasmas. *Journal of applied physics*, 56(1):108, 1984.
- [105] P. Kaw, G. Schmidt, and T. Wilcox. Filamentation and trapping of electromagnetic radiation in plasmas. *The Physics of Fluids*, 16(9):1522, 1973.

- [106] J. F. Drake, P. K. Kaw, Y.-C. Lee, G. Schmid, C. S. Liu, and M. N. Rosenbluth. Parametric instabilities of electromagnetic waves in plasmas. *The Physics of Fluids*, 17(4):778, 1974.
- [107] D. Forslund, J. Kindel, K. Lee, E. Lindman, and R. Morse. Theory and simulation of resonant absorption in a hot plasma. *Physical Review A*, 11(2):679, 1975.
- [108] C. Liu, M. N. Rosenbluth, and R. B. White. Raman and Brillouin scattering of electromagnetic waves in inhomogeneous plasmas. *The Physics of Fluids*, 17(6):1211, 1974.
- [109] J. Manley and H. Rowe. Some general properties of nonlinear elements-Part I. General energy relations. *Proceedings of the IRE*, 44(7):904, 1956.
- [110] H. Baldis, E. Campbell, and W. Kruer. *Laser-plasma interactions. Chapter 9.* Handbook of Plasma Physics, 1991.
- [111] D. S. Montgomery. Two decades of progress in understanding and control of laser plasma instabilities in indirect drive inertial fusion. *Physics of Plasmas*, 23(5), 2016.
- [112] C. Randall, J. R. Albritton, and J. Thomson. Theory and simulation of stimulated brillouin scatter excited by nonabsorbed light in laser fusion systems. *The Physics of Fluids*, 24(8):1474, 1981.
- [113] W. L. Kruer, S. C. Wilks, B. B. Afeyan, and R. K. Kirkwood. Energy transfer between crossing laser beams. *Physics of Plasmas*, 3(1):382, 1996.
- [114] T. D. Arber, et al. Contemporary particle-in-cell approach to laser-plasma modelling. *Plasma Physics and Controlled Fusion*, 57(11):113001, 2015.
- [115] W. Theobald, et al. Spherical shock-ignition experiments with the 40+20-beam configuration on OMEGA. *Physics of Plasmas*, 19(10), 2012.
- [116] R. Yan, J. Li, and C. Ren. Intermittent laser-plasma interactions and hot electron generation in shock ignition. *Physics of Plasmas*, 21(6), 2014.
- [117] A. G. Seaton and T. D. Arber. Laser-plasma instabilities in long scale-length plasmas relevant to shock-ignition. *Physics of Plasmas*, 27(8):082704, 2020.
- [118] D. Turnbull, et al. Impact of spatiotemporal smoothing on the two-plasmon-decay instability. *Physics of Plasmas*, 27(10):102710, 2020.

- [119] C. Stoeckl, W. Theobald, S. P. Regan, and M. H. Romanofsky. Calibration of a time-resolved hard-x-ray detector using radioactive sources. *Review of Scientific Instruments*, 87(11), 2016.
- [120] W. Theobald, et al. Spherical strong-shock generation for shock-ignition inertial fusion. *Physics of Plasmas*, 22(5), 2015.
- [121] R. Nora, et al. Gigabar spherical shock generation on the OMEGA laser. *Physical Review Letters*, 114(4):1, 2015.
- [122] A. A. Solodov, B. Yaakobi, D. H. Edgell, R. K. Follett, J. F. Myatt, C. Sorce, and D. H. Froula. Measurements of hot-electron temperature in laser-irradiated plasmas. *Physics of Plasmas*, 23(10), 2016.
- [123] C. Chen, et al. A bremsstrahlung spectrometer using k-edge and differential filters with image plate dosimeters. *Review of Scientific Instruments*, 79(10):10E305, 2008.
- [124] M. Hohenberger, et al. Time-resolved measurements of the hot-electron population in ignition-scale experiments on the National Ignition Facility (invited). *Review of Scientific Instruments*, 85(11), 2014.
- [125] W. Theobald, et al. Enhanced hot-electron production and strong-shock generation in hydrogen-rich ablaters for shock ignition. *Physics of Plasmas*, 24(12), 2017.
- [126] J. Trela, et al. The control of hot-electron preheat in shock-ignition implosions. *Physics of Plasmas*, 25(5), 2018.
- [127] C. Zhang, C. Yu, C. Yang, D. Xiao, J. Liu, and Z. Fan. A theoretical model for low-mode asymmetries in ICF implosions. *Physics of Plasmas*, 26(2), 2019.
- [128] J. Kelly, et al. OMEGA EP: High-energy petawatt capability for the OMEGA laser facility. In *Journal de Physique IV (Proceedings)*, volume 133, pages 75–80. EDP sciences, 2006.
- [129] G. H. Miller, E. I. Moses, and C. R. Wuest. The national ignition facility. *Optical Engineering*, 43(12):2841, 2004.

- [130] J. Miquel, C. Lion, and P. Vivini. The laser mega-joule: LMJ & PETAL status and program overview. In *Journal of Physics: Conference Series*, volume 688, page 012067. IOP Publishing, 2016.
- [131] J. Katz, W. Donaldson, R. Huff, E. Hill, J. Kelly, J. Kwiatkowski, and R. Brannon. 3ω beam-timing diagnostic for the OMEGA laser facility. In *Target Diagnostics Physics and Engineering for Inertial Confinement Fusion IV*, volume 9591, page 95910A. International Society for Optics and Photonics, 2015.
- [132] University of Rochester. *OMEGA Laser System, Omega Facility Users' Guide*.
- [133] S. Skupsky and R. S. Craxton. Irradiation uniformity for high-compression laser-fusion experiments. *Physics of Plasmas*, 6(5):2157, 1999.
- [134] D. Goodin, et al. Status of the design and testing of the OMEGA Cryogenic Target System (OCTS). In *20th Symposium on Fusion Technology (SOFT)*. 1998.
- [135] V. Gopalaswamy. personal communication.
- [136] T. R. Boehly, V. A. Smalyuk, D. D. Meyerhofer, J. P. Knauer, D. K. Bradley, R. S. Craxton, M. J. Guardalben, S. Skupsky, and T. J. Kessler. Reduction of laser imprinting using polarization smoothing on a solid-state fusion laser. *Journal of Applied Physics*, 85(7):3444, 1999.
- [137] T. J. Kessler, Y. Lin, J. J. Armstrong, and B. Velazquez. Phase conversion of lasers with low-loss distributed phase plates. In *Laser Coherence Control: Technology and Applications*, volume 1870, pages 95–104. International Society for Optics and Photonics, 1993.
- [138] OMEGA SG5/R80 Distributed Phase Plate. https://omegaops.lln.rochester.edu/etp/OMEGA_SG5.pdf. Accessed: 2022-04-27.
- [139] S. Skupsky, R. W. Short, T. Kessler, R. S. Craxton, S. Letzring, and J. M. Soures. Improved laser-beam uniformity using the angular dispersion of frequency-modulated light. *Journal of Applied Physics*, 66(8):3456, 1989.
- [140] S. P. Regan, et al. Performance of 1-THz-bandwidth, two-dimensional smoothing by spectral dispersion and polarization smoothing of high-power, solid-state laser beams. *JOSA B*, 22(5):998, 2005.

- [141] A. Babushkin, R. Craxton, S. Oskoui, M. Guardalben, R. Keck, and W. Seka. Demonstration of the dual-tripler scheme for increased-bandwidth third-harmonic generation. *Optics letters*, 23(12):927, 1998.
- [142] S. G. Gales and C. D. Bentley. Image plates as x-ray detectors in plasma physics experiments. *Review of Scientific Instruments*, 75(10 II):4001, 2004.
- [143] N. Izumi, R. Snavely, G. Gregori, J. A. Koch, H. S. Park, and B. A. Remington. Application of imaging plates to x-ray imaging and spectroscopy in laser plasma experiments (invited). *Review of Scientific Instruments*, 77(10), 2006.
- [144] A. L. Meadowcroft, C. D. Bentley, and E. N. Stott. Evaluation of the sensitivity and fading characteristics of an image plate system for x-ray diagnostics. *Review of Scientific Instruments*, 79(11):1, 2008.
- [145] B. R. Maddox, H. S. Park, B. A. Remington, N. Izumi, S. Chen, C. Chen, G. Kimminau, Z. Ali, M. J. Haugh, and Q. Ma. High-energy x-ray backlighter spectrum measurements using calibrated image plates. *Review of Scientific Instruments*, 82(2), 2011.
- [146] T. Bonnet, M. Comet, D. Denis-Petit, F. Gobet, F. Hannachi, M. Tarisien, M. Versteegen, and M. M. Aleonard. Response functions of Fuji imaging plates to monoenergetic protons in the energy range 0.6–3.2 MeV. *Review of Scientific Instruments*, 84(1):013508, 2013.
- [147] G. Boutoux, N. Rabhi, D. Batani, A. Binet, J. E. Ducret, K. Jakubowska, J. P. Nègre, C. Reverdin, and I. Thfoin. Study of imaging plate detector sensitivity to 5-18 MeV electrons. *Review of Scientific Instruments*, 86(11), 2015.
- [148] G. Boutoux, et al. Validation of modelled imaging plates sensitivity to 1-100 keV x-rays and spatial resolution characterisation for diagnostics for the “PETawatt Aquitaine Laser”. *Review of Scientific Instruments*, 87(4), 2016.
- [149] M. Stoeckl and A. A. Solodov. Readout models for BaFBr0.85I0.15:Eu image plates. *Review of Scientific Instruments*, 89(6):0, 2018.
- [150] M. J. Rosenberg, et al. Image-plate sensitivity to x rays at 2 to 60 keV. *Review of Scientific Instruments*, 90(1), 2019.

- [151] C. Dozier, D. Brown, L. Birks, P. Lyons, and R. Benjamin. Sensitivity of x-ray film. II. Kodak No-Screen film in the 1–100-keV region. *Journal of Applied Physics*, 47(8):3732, 1976.
- [152] B. Hidding, et al. Novel method for characterizing relativistic electron beams in a harsh laser-plasma environment. *Review of Scientific Instruments*, 78(8), 2007.
- [153] G. Jackson Williams, B. R. Maddox, H. Chen, S. Kojima, and M. Millecchia. Calibration and equivalency analysis of image plate scanners. *Review of Scientific Instruments*, 85(11):3, 2014.
- [154] V. V. Vistovsky, A. V. Zhyshkovich, Y. M. Chornodolsky, O. S. Myagkota, A. Gloskovskii, A. V. Gektin, A. N. Vasil'Ev, P. A. Rodnyi, and A. S. Voloshinovskii. Self-trapped exciton and core-valence luminescence in BaF₂ nanoparticles. *Journal of Applied Physics*, 114(19):1, 2013.
- [155] W. Mengesha, T. Taulbee, J. Valentine, and B. Rooney. Gd₂SiO₅(Ce³⁺) and BaF₂ measured electron and photon responses. *Nuclear Instruments and Methods in Physics Research Section A: Accelerators, Spectrometers, Detectors and Associated Equipment*, 486(1-2):448, 2002.
- [156] P. Dorenbos, J. de Haas, R. Visser, C. van Eijk, and R. Hollander. Absolute light yield measurements on BaF₂ crystals and the quantum efficiency of several photomultiplier tubes. *IEEE Transactions on Nuclear Science*, 40(4):424, 1993.
- [157] C. Stoeckl, V. Y. Glebov, D. D. Meyerhofer, W. Seka, B. Yaakobi, R. P. J. Town, and J. D. Zuegel. Hard x-ray detectors for OMEGA and NIF. *Review of Scientific Instruments*, 72(1 II):1197, 2001.
- [158] G. F. Knoll. *Radiation detection and measurement*. John Wiley & Sons, 2010.
- [159] H. Y. Cho, J. H. Lee, and C. S. Lee. Improvement of Time Resolution of BaF₂ Scintillator for Low-Energy Gamma Rays by Digital Pulse-Shape Method. *IEEE Transactions on Nuclear Science*, 57(3):1386, 2010.
- [160] S. Diehl, R. W. Novotny, B. Wohlfahrt, and R. Beck. Readout concepts for the suppression of the slow component of BaF₂ for the upgrade of the TAPS spectrometer at ELSA. *Journal of Physics: Conference Series*, 587(1):012044, 2015.

- [161] R. Wentink and J. Carbone. Charge Injection Device (CID) technology — A solution for photon and particle imaging applications. *Nuclear Instruments and Methods in Physics Research Section A: Accelerators, Spectrometers, Detectors and Associated Equipment*, 347(1-3):522, 1994.
- [162] R. Bailey, C. Damerell, R. English, A. Gillman, A. Lintern, S. Watts, and F. Wickens. First measurement of efficiency and precision of CCD detectors for high energy physics. *Nuclear Instruments and Methods in Physics Research*, 213(2-3):201, 1983.
- [163] M. P. Lesser. Improving CCD quantum efficiency. In *Instrumentation in Astronomy VIII*, volume 2198, pages 782–791. International Society for Optics and Photonics, 1994.
- [164] D. A. Baiko. *Design and development of a radiation hardened color video sensor charge injection device chip*. Master’s thesis, Rochester Institute of Technology, 2006.
- [165] S. Bhaskaran, T. Chapman, M. Pilon, and S. VanGorden. Performance based CID imaging: past, present, and future. In E. L. Dereniak, J. P. Hartke, P. D. LeVan, R. E. Longshore, and A. K. Sood, editors, *Infrared Systems and Photoelectronic Technology III*, volume 7055, pages 171 – 181. International Society for Optics and Photonics, SPIE, 2008.
- [166] N. E. Palmer, M. B. Schneider, P. M. Bell, K. W. Piston, J. D. Moody, D. L. James, R. A. Ness, M. J. Haugh, J. J. Lee, and E. D. Romano. Performance of CID camera X-ray imagers at NIF in a harsh neutron environment. In *Target Diagnostics Physics and Engineering for Inertial Confinement Fusion II*, volume 8850, page 885009. International Society for Optics and Photonics, 2013.
- [167] M. J. Haugh, M. R. Charest, P. W. Ross, J. J. Lee, M. B. Schneider, N. E. Palmer, and A. T. Teruya. Calibration of X-ray imaging devices for accurate intensity measurement. *Powder Diffraction*, 27(2):79, 2012.
- [168] J. Hubbell and S. Seltzer. Tables of X-Ray Mass Attenuation Coefficients and Mass Energy-Absorption Coefficients 1 keV to 20 MeV for Elements $Z = 1$ to 92 and 48 Additional Substances of Dosimetric Interest, 1995.

- [169] B. L. Henke, J. P. Knauer, and K. Premaratne. The characterization of x-ray photocathodes in the 0.1–10-keV photon energy region. *Journal of Applied Physics*, 52(3):1509, 1981.
- [170] G. A. Rochau, et al. Energy dependent sensitivity of microchannel plate detectors. *Review of Scientific Instruments*, 77(10), 2006.
- [171] D. K. Bradley, P. M. Bell, J. D. Kilkenny, R. Hanks, O. Landen, P. A. Jaanimagi, P. W. McKenty, and C. P. Verdon. High-speed gated x-ray imaging for ICF target experiments (invited). *Review of Scientific Instruments*, 63(10):4813, 1992.
- [172] L. R. Benedetti, et al. Advances in x-ray framing cameras at the National Ignition Facility to improve quantitative precision in x-ray imaging. *Review of Scientific Instruments*, 87(2):023511, 2016.
- [173] D. Bradley, P. Bell, O. Landen, J. Kilkenny, and J. Oertel. Development and characterization of a pair of 30–40 ps x-ray framing cameras. *Review of scientific instruments*, 66(1):716, 1995.
- [174] D. T. Michel, C. Sorce, R. Epstein, N. Whiting, I. V. Igumenshchev, R. Jungquist, and D. H. Froula. Shell trajectory measurements from direct-drive implosion experiments. *Review of Scientific Instruments*, 83(10):10E530, 2012.
- [175] F. J. Marshall. Compact Kirkpatrick-Baez microscope mirrors for imaging laser-plasma x-ray emission. *Review of Scientific Instruments*, 83(10):10, 2012.
- [176] J. Timothy and R. Bybee. Preliminary results with microchannel array plates employing curved microchannels to inhibit ion feedback. *Review of Scientific Instruments*, 48(3):292, 1977.
- [177] L. C. Jarrott, et al. Calibration and characterization of a highly efficient spectrometer in von Hamos geometry for 7-10 keV x-rays. *Review of Scientific Instruments*, 88(4):43110, 2017.
- [178] L. v. Hámos. Röntgenspektroskopie und Abbildung mittels gekrümmter Kristallreflektoren. *Naturwissenschaften*, 20(38):705, 1932.

- [179] L. Anklamm, C. Schlesiger, W. Malzer, D. Grötzsch, M. Neitzel, and B. Kanngießner. A novel von hamos spectrometer for efficient x-ray emission spectroscopy in the laboratory. *Review of Scientific Instruments*, 85(5):053110, 2014.
- [180] C. Stoeckl, G. Fiksel, D. Guy, C. Mileham, P. M. Nilson, T. C. Sangster, M. J. Shoup, and W. Theobald. A spherical crystal imager for OMEGA EP. *Review of Scientific Instruments*, 83(3), 2012.
- [181] C. Stoeckl, et al. Soft x-ray backlighting of direct-drive implosions using a spherical crystal imager on OMEGA. *Review of Scientific Instruments*, 83(10):10E501, 2012.
- [182] B. D. Guenther and D. Steel. *Encyclopedia of modern optics*. Elsevier, Amsterdam, the Netherlands, second edition edition, 2018.
- [183] E. Hecht. *Optics, 5e*. Pearson Education India, 2002.
- [184] K. U. Akli, et al. Temperature sensitivity of Cu $K\alpha$ imaging efficiency using a spherical Bragg reflecting crystal. *Physics of Plasmas*, 14(2):023102, 2007.
- [185] L. Jarrott, et al. Visualizing fast electron energy transport into laser-compressed high-density fast-ignition targets. *Nature Physics*, 12(5):499, 2016.
- [186] M. Stoeckl and A. A. Solodov. Refining instrument response functions with 3-D Monte Carlo simulations of differential hard x-ray spectrometers. *Nuclear Instruments and Methods in Physics Research, Section A: Accelerators, Spectrometers, Detectors and Associated Equipment*, 931(April):162, 2019.
- [187] J. Allison, et al. Recent developments in GEANT4. *Nuclear Instruments and Methods in Physics Research, Section A: Accelerators, Spectrometers, Detectors and Associated Equipment*, 835:186, 2016.
- [188] R. E. Sanders. Technology innovation in aluminum products. *Jom*, 53(2):21, 2001.
- [189] B. L. Henke, E. M. Gullikson, and J. C. Davis. X-ray interactions: photoabsorption, scattering, transmission, and reflection at $E= 50\text{-}30,000$ eV, $Z= 1\text{-}92$. *Atomic data and nuclear data tables*, 54(2):181, 1993.
- [190] J. Hubbell and S. Seltzer. NIST standard reference database 126. *Gaithersburg, MD: National Institute of Standards and Technology*, 1996.

- [191] W. C. Mead. Laser irradiation of disk targets at 0.53 μm wavelength. *Physics of Fluids*, 26(8):2316, 1983.
- [192] R. P. Drake, R. E. Turner, B. F. Lasinski, E. A. Williams, K. Estabrook, W. L. Kruer, E. M. Campbell, and T. W. Johnston. X-ray emission caused by Raman scattering in long-scale-length plasmas. *Physical Review A*, 40(6):3219, 1989.
- [193] G. H. McCall. Calculation of X-ray bremsstrahlung and characteristic line emission produced by a Maxwellian electron distribution. *Journal of Physics D: Applied Physics*, 15(5):823, 1982.
- [194] P. R. Bevington and K. D. Robinson. *Data Reduction and Error Analysis for the Physical Sciences*. McGraw-Hill, 2007.
- [195] M. Bonamente. *Statistics and analysis of scientific data*. Springer, 2017.
- [196] H. Habara, T. Iwawaki, T. Gong, M. Wei, S. Ivancic, W. Theobald, C. Krauland, S. Zhang, G. Fiksel, and K. Tanaka. A ten-inch manipulator (TIM) based fast-electron spectrometer with multiple viewing angles (OU-ESM). *Review of Scientific Instruments*, 90(6):063501, 2019.
- [197] F. J. Marshall, T. Ohki, D. McInnis, Z. Ninkov, and J. Carbone. Imaging of laser-plasma x-ray emission with charge-injection devices. *Review of Scientific Instruments*, 72(1):713, 2001.
- [198] R. Forties and F. Marshall. In situ characterization of high-intensity laser beams on OMEGA. *Review of scientific instruments*, 76(7):073505, 2005.
- [199] F. Marshall, J. Delettrez, R. Epstein, R. Forties, R. Keck, J. Kelly, P. McKenty, S. Regan, and L. Waxer. Direct-drive-implosion experiments with enhanced fluence balance on OMEGA. *Physics of Plasmas*, 11(1):251, 2004.
- [200] C. Thomas, G. Rehm, I. Martin, and R. Bartolini. X-ray pinhole camera resolution and emittance measurement. *Physical Review Special Topics-Accelerators and Beams*, 13(2):022805, 2010.
- [201] D. T. Michel, et al. Measurements of the ablation-front trajectory and low-mode nonuniformity in direct-drive implosions using X-ray self-emission shadowgraphy. *High Power Laser Science and Engineering*, 3:1, 2015.

- [202] A. K. Davis. *Laser Ablation and Hydrodynamic Coupling in Direct-Drive Experiments*. Ph.D. thesis, University of Rochester, 2017.
- [203] A. K. Davis, et al. Isolating and quantifying cross-beam energy transfer in direct-drive implosions on OMEGA and the National Ignition Facility. *Physics of Plasmas*, 23(5), 2016.
- [204] W. Theobald, et al. The single-line-of-sight, time-resolved x-ray imager diagnostic on OMEGA. *Review of Scientific Instruments*, 89(10), 2018.
- [205] K. Engelhorn, et al. Sub-nanosecond single line-of-sight (SLOS) x-ray imagers (invited). *Review of Scientific Instruments*, 89(10), 2018.
- [206] T. J. Hillsbeck, et al. Pulse-dilation enhanced gated optical imager with 5 ps resolution. *Review of Scientific Instruments*, 81(10), 2010.
- [207] L. R. Benedetti, et al. Timing characterization of fast hCMOS sensors. *Review of Scientific Instruments*, 92(4):044708, 2021.
- [208] P. Kirkpatrick and A. V. Baez. Formation of Optical Images by X-Rays. *J. Opt. Soc. Am.*, 38(9):766, 1948.
- [209] F. J. Marshall, R. E. Bahr, V. N. Goncharov, V. Y. Glebov, B. Peng, S. P. Regan, T. C. Sangster, and C. Stoeckl. A framed, 16-image Kirkpatrick-Baez x-ray microscope. *Review of Scientific Instruments*, 88(9), 2017.
- [210] F. J. Marshall, J. A. Oertel, and P. J. Walsh. Framed, 16-image, Kirkpatrick-Baez microscope for laser-plasma x-ray emission. *Review of Scientific Instruments*, 75(10 II):4045, 2004.
- [211] J. Moody, et al. Backscatter measurements for NIF ignition targets. *Review of Scientific Instruments*, 81(10):10D921, 2010.
- [212] L. Spitzer and R. Härm. Transport phenomena in a completely ionized gas. *Physical Review*, 89(5):977, 1953.
- [213] B. Bennett, J. Johnson, G. Kerley, and G. Rood. Recent developments in the Sesame equation-of-state library. Technical report, Los Alamos Scientific Lab., N. Mex.(USA), 1978.

- [214] J. J. MacFarlane, I. E. Golovkin, P. Wang, P. R. Woodruff, and N. A. Pereyra. SPECT3D - A multi-dimensional collisional-radiative code for generating diagnostic signatures based on hydrodynamics and PIC simulation output. *High Energy Density Physics*, 3(1-2):181, 2007.
- [215] R. H. H. Scott, et al. Shock Ignition Laser-Plasma Interactions in Ignition-Scale Plasmas. *Physical Review Letters*, 127(6):065001, 2021.
- [216] E. Campbell, et al. Laser-direct-drive program: Promise, challenge, and path forward. *Matter and Radiation at Extremes*, 2(2):37, 2017.
- [217] J. MacFarlane. VISRAD—A 3-D view factor code and design tool for high-energy density physics experiments. *Journal of Quantitative Spectroscopy and Radiative Transfer*, 81(1-4):287, 2003.
- [218] M. Mahdavi and B. Kaleji. Deuterium/helium-3 fusion reactors with lithium seeding. *Plasma Physics and Controlled Fusion*, 51(8):085003, 2009.
- [219] J. G. Chervenak and A. Liuzzi. Experimental thick-target bremsstrahlung spectra from electrons in the range 10 to 30 keV. *Physical Review A*, 12(1):26, 1975.
- [220] J. T. Larsen. Cascade Applied Sciences, Inc., 2020.
- [221] W. Seka, B. B. Afeyan, R. Boni, L. M. Goldman, R. W. Short, K. Tanaka, and T. W. Johnston. Diagnostic value of odd-integer half-harmonic emission from laser-produced plasmas. *Physics of Fluids*, 28(8):2570, 1985.
- [222] W. Seka, D. H. Edgell, J. F. Myatt, A. V. Maximov, R. W. Short, V. N. Goncharov, and H. A. Baldis. Two-plasmon-decay instability in direct-drive inertial confinement fusion experiments. *Physics of Plasmas*, 16(5), 2009.
- [223] M. N. Rosenbluth, R. B. White, and C. S. Liu. Temporal Evolution of a Three-Wave Parametric Instability. *Physical Review Letters*, 31(19):1190, 1973.
- [224] M. J. Rosenberg, et al. Stimulated Raman scattering mechanisms and scaling behavior in planar direct-drive experiments at the National Ignition Facility. *Physics of Plasmas*, 27(4), 2020.

- [225] T. Dewandre, J. R. Albritton, and E. A. Williams. Doppler shift of laser light reflected from expanding plasmas. *Physics of Fluids*, 24(3):528, 1981.
- [226] S. Perkins, D. Cullen, M. Chen, J. Rathkopf, J. Scofield, and J. Hubbell. Tables and graphs of atomic subshell and relaxation data derived from the LLNL Evaluated Atomic Data Library (EADL), $Z= 1-100$, 1991.
- [227] A. Tentori, et al. Experimental characterization of hot-electron emission and shock dynamics in the context of the shock ignition approach to inertial confinement fusion. *Physics of Plasmas*, 28(10):103302, 2021.
- [228] X. Llovet, C. J. Powell, F. Salvat, and A. Jablonski. Cross Sections for Inner-Shell Ionization by Electron Impact. *Journal of Physical and Chemical Reference Data*, 43(1):013102, 2014.
- [229] M. H. Mendenhall, A. Henins, L. T. Hudson, C. I. Szabo, D. Windover, and J. P. Cline. High-precision measurement of the x-ray Cu $K\alpha$ spectrum. *Journal of Physics B: Atomic, Molecular and Optical Physics*, 50(11):115004, 2017.
- [230] J. Scofield. Energies of hydrogen and helium like ions for Z 's from 6 to 54. Technical report, California Univ., 1975.
- [231] S. Zhang, et al. Experimental study of hot electron generation in shock ignition relevant high-intensity regime with large scale hot plasmas. *Physics of Plasmas*, 27(2), 2020.
- [232] P. Koester, et al. Bremsstrahlung cannon design for shock ignition relevant regime. *Review of Scientific Instruments*, 92(1):013501, 2021.
- [233] B. Yaakobi, et al. Fast-electron generation in long-scale-length plasmas. *Physics of Plasmas*, 19(1):012704, 2012.
- [234] V. T. Tikhonchuk, et al. Physics of laser-plasma interaction for shock ignition of fusion reactions. *Plasma Physics and Controlled Fusion*, 58(1):14018, 2015.
- [235] A. A. Solodov, et al. Hot-electron generation at direct-drive ignition-relevant plasma conditions at the National Ignition Facility. *Physics of Plasmas*, 27(5):052706, 2020.
- [236] T. Desjardins, C. Di Stefano, E. Merritt, K. Flippo, and F. Doss. Reducing direct drive preheat with dopants. *High Energy Density Physics*, 39(March):100937, 2021.

- [237] G. Cristoforetti, et al. Observation and modelling of Stimulated Raman Scattering driven by an optically smoothed laser beam in experimental conditions relevant for Shock Ignition. *High Power Laser Science and Engineering*, 9:1, 2021.
- [238] R. H. H. Scott, et al. Measuring fast electron spectra and laser absorption in relativistic laser-solid interactions using differential bremsstrahlung photon detectors. *Review of Scientific Instruments*, 84(8):1, 2013.
- [239] F. Jüttner. Das Maxwell'sche Gesetz der Geschwindigkeitsverteilung in der Relativtheorie. *Annalen der Physik*, 339:856 , 2006.
- [240] L. Antonelli, et al. Laser-driven strong shocks with infrared lasers at intensity of 10^{16} W/cm². *Physics of Plasmas*, 26(11), 2019.
- [241] W. Theobald, et al. Initial experiments on the shock-ignition inertial confinement fusion concept. *Physics of Plasmas*, 15(5), 2008.
- [242] E. Llor Aisa, X. Ribeyre, G. Duchateau, T. Nguyen-Bui, V. T. Tikhonchuk, A. Colaïtis, R. Betti, A. Bose, and W. Theobald. The role of hot electrons in the dynamics of a laser-driven strong converging shock. *Physics of Plasmas*, 24(11), 2017.
- [243] O. Klimo, S. Weber, V. T. Tikhonchuk, and J. Limpouch. Particle-in-cell simulations of laser-plasma interaction for the shock ignition scenario. *Plasma Physics and Controlled Fusion*, 52(5), 2010.
- [244] O. Klimo, J. Psikal, V. Tikhonchuk, and S. Weber. Two-dimensional simulations of laser-plasma interaction and hot electron generation in the context of shock-ignition research. *Plasma Physics and Controlled Fusion*, 56(5):055010, 2014.
- [245] L. Yin, et al. Trapping induced nonlinear behavior of backward stimulated Raman scattering in multi-speckled laser beams. *Physics of Plasmas*, 19(5), 2012.
- [246] O. Klimo, V. T. Tikhonchuk, X. Ribeyre, G. Schurtz, C. Riconda, S. Weber, and J. Limpouch. Laser plasma interaction studies in the context of shock ignition-Transition from collisional to collisionless absorption. *Physics of Plasmas*, 18(8), 2011.
- [247] R. K. Follett, J. F. Myatt, J. G. Shaw, D. T. Michel, A. A. Solodov, D. H. Edgell, B. Yaakobi, and D. H. Froula. Simulations and measurements of hot-electron gen-

- eration driven by the multibeam two-plasmon-decay instability. *Physics of Plasmas*, 24(10), 2017.
- [248] J. R. Fein, et al. Mitigation of hot electrons from laser-plasma instabilities in high-Z, highly ionized plasmas. *Physics of Plasmas*, 24(3), 2017.
- [249] J. Myatt, W. Theobald, J. A. Delettrez, C. Stoeckl, M. Storm, T. C. Sangster, A. V. Maximov, and R. W. Short. High-intensity laser interactions with mass-limited solid targets and implications for fast-ignition experiments on OMEGA EP. *Physics of Plasmas*, 14(5), 2007.
- [250] S. Baton, et al. Experiment in planar geometry for shock ignition studies. *Physical review letters*, 108(19):195002, 2012.
- [251] S. Baton, E. Le Bel, S. Brygoo, X. Ribeyre, C. Rousseaux, J. Breil, M. Koenig, D. Batani, and D. Raffestin. Shock generation comparison with planar and hemispherical targets in shock ignition relevant experiment. *Physics of Plasmas*, 24(9):092708, 2017.
- [252] G. Cristoforetti, et al. Measurements of parametric instabilities at laser intensities relevant to strong shock generation. *Physics of Plasmas*, 25(1):012702, 2018.
- [253] M. Hohenberger, et al. Time-resolved measurements of the hot-electron population in ignition-scale experiments on the national ignition facility. *Review of Scientific Instruments*, 85(11):11D501, 2014.
- [254] S. Atzeni, A. Schiavi, L. Antonelli, and A. Serpi. Hydrodynamic studies of high gain shock ignition targets: effect of low-to intermediate-mode asymmetries. *The European Physical Journal D*, 73(11):1, 2019.
- [255] T. Goffrey. *A cylindrical magnetohydrodynamic arbitrary Lagrangian Eulerian code*. Ph.D. thesis, University of Warwick, 2014.
- [256] C. J. Werner, et al. MCNP Version 6.2 Release Notes, 2018.
- [257] K. Anderson, et al. A polar-drive shock-ignition design for the National Ignition Facility. *Physics of Plasmas*, 20(5):056312, 2013.

- [258] V. Gopalaswamy, et al. Tripled yield in direct-drive laser fusion through statistical modelling. *Nature*, 565(7741):581, 2019.
- [259] T. R. Boehly, et al. Multiple spherically converging shock waves in liquid deuterium. *Physics of Plasmas*, 18(9), 2011.
- [260] M. Gatu Johnson, et al. Impact of stalk on directly driven inertial confinement fusion implosions. *Physics of Plasmas*, 27(3), 2020.
- [261] M. Gatu Johnson, et al. Impact of asymmetries on fuel performance in inertial confinement fusion. *Physical Review E*, 98(5):1, 2018.
- [262] N. P. Incorporated. Norland Optical Adhesive 68. <https://www.norlandprod.com/literature/68tds.pdf>. Accessed: 2022-04-27.
- [263] R. Lerche, D. Phillion, and G. Tietbohl. 25 ps neutron detector for measuring ICF-target burn history. *Review of scientific instruments*, 66(1):933, 1995.
- [264] O. Mannion, J. Knauer, V. Glebov, C. Forrest, A. Liu, Z. Mohamed, M. Romanofsky, T. Sangster, C. Stoeckl, and S. Regan. A suite of neutron time-of-flight detectors to measure hot-spot motion in direct-drive inertial confinement fusion experiments on OMEGA. *Nuclear Instruments and Methods in Physics Research Section A: Accelerators, Spectrometers, Detectors and Associated Equipment*, 964:163774, 2020.
- [265] C. Shulldberg. Private Communication. Inertial Fusion Technology, General Atomics.
- [266] R. Shah. personal communication.
- [267] L. Benedetti, et al. Advances in x-ray framing cameras at the National Ignition Facility to improve quantitative precision in x-ray imaging. *Review of Scientific Instruments*, 87(2):023511, 2016.
- [268] N. S. Krasheninnikova, et al. Development of a directly driven multi-shell platform: Laser drive energetics. *Physics of Plasmas*, 27(2), 2020.
- [269] R. N. Bracewell. *Two-dimensional imaging*. Prentice-Hall, Inc., 1995.
- [270] A. Bose, et al. Analysis of trends in experimental observables: Reconstruction of the implosion dynamics and implications for fusion yield extrapolation for direct-drive cryogenic targets on OMEGA. *Physics of Plasmas*, 25(6):1, 2018.

- [271] W. L. Shang, et al. Properties of hot-spot emission in a warm plastic-shell implosion on the OMEGA laser system. *Physical Review E*, 98(3), 2018.
- [272] R. Shah. personal communication.
- [273] R. Shah. personal communication.
- [274] F. J. Marshall and J. A. Oertel. A framed monochromatic x-ray microscope for ICF (invited). *Review of Scientific Instruments*, 68(1):735, 1997.
- [275] K. M. Woo, et al. Effects of residual kinetic energy on yield degradation and ion temperature asymmetries in inertial confinement fusion implosions. *Physics of Plasmas*, 25(5), 2018.
- [276] B. K. Spears, et al. Mode 1 drive asymmetry in inertial confinement fusion implosions on the National Ignition Facility. *Physics of Plasmas*, 21(4), 2014.
- [277] S. W. T. F.R.S. XLVI. Hydrokinetic solutions and observations. *The London, Edinburgh, and Dublin Philosophical Magazine and Journal of Science*, 42(281):362, 1871.
- [278] P. Helmholtz. XLIII. On discontinuous movements of fluids. *The London, Edinburgh, and Dublin Philosophical Magazine and Journal of Science*, 36(244):337, 1868.
- [279] O. M. Mannion, et al. Mitigation of mode-one asymmetry in laser-direct-drive inertial confinement fusion implosions. *Physics of Plasmas*, 28(4), 2021.
- [280] R. C. Shah, et al. Systematic Fuel Cavity Asymmetries in Directly Driven Inertial Confinement Fusion Implosions. *Physical Review Letters*, 118(13):1, 2017.
- [281] I. V. Igumenshchev, et al. Three-dimensional modeling of direct-drive cryogenic implosions on OMEGA. *Physics of Plasmas*, 23(5), 2016.
- [282] I. V. Igumenshchev, et al. Three-dimensional hydrodynamic simulations of OMEGA implosions. *Physics of Plasmas*, 24(5), 2017.
- [283] M. Gatu Johnson, et al. Impact of imposed mode 2 laser drive asymmetry on inertial confinement fusion implosions. *Physics of Plasmas*, 26(1), 2019.
- [284] A. Christopherson, et al. Direct measurements of DT fuel preheat from hot electrons in direct-drive inertial confinement fusion. *Physical Review Letters*, 127(5):055001, 2021.

- [285] S. W. Haan, et al. Point design targets, specifications, and requirements for the 2010 ignition campaign on the National Ignition Facility. *Physics of Plasmas*, 18(5), 2011.
- [286] K. S. Anderson, et al. Effect of cross-beam energy transfer on target-offset asymmetry in direct-drive inertial confinement fusion implosions. *Physics of Plasmas*, 27(11), 2020.
- [287] K. Schultz, D. Goodin, and A. Nobile Jr. IFE target fabrication and injection—achieving “believability”. *Nuclear Instruments and Methods in Physics Research Section A: Accelerators, Spectrometers, Detectors and Associated Equipment*, 464(1-3):109, 2001.
- [288] T. J. Collins and J. A. Marozas. Mitigation of cross-beam energy transfer in ignition-scale polar-direct-drive target designs for the National Ignition Facility. *Physics of Plasmas*, 25(7), 2018.
- [289] R. Scott. personal communication.